DEVELOPMENT OF A CONDITION MONITORING PHILOSOPHY FOR A PULVERISED FUEL VERTICAL SPINDLE MILL

André Govender

A dissertation submitted to the Faculty of Engineering and the Built Environment, University of the Witwatersrand, in fulfilment of the requirements for the degree of Master of Science in Engineering.

Johannesburg 2016

Declaration

I declare that this dissertation is my own, unaided work. It is being submitted for the Degree of Master of Science in Engineering to the University of the Witwatersrand, Johannesburg. It has not been submitted before for any degree or examination to any other University.

………………………………………………………………………………

(Signature of Candidate)

………………. day of …………….……………., ………………..

Abstract

The quantity and particle size distribution of pulverised coal supplied to combustion equipment downstream of coal pulverising plants are critical to achieving safe, reliable and efficient combustion. These two key performance indicators are largely dependent on the mechanical condition of the pulveriser. This study aimed to address the shortfalls associated with conventional time-based monitoring techniques by developing a comprehensive online pulveriser condition monitoring philosophy. A steady-state Mill Mass and Energy Balance (MMEB) model was developed from first principles for a commercial-scale coal pulveriser to predict the raw coal mass flow rate through the pulveriser. The MMEB model proved to be consistently accurate, predicting the coal mass flow rates to within 5 % of experimental data. The model proved to be dependent on several pulveriser process variables, some of which are not measured on a continuous basis. Therefore, the model can only function effectively on an industrial scale if it is supplemented with the necessary experiments to quantify unmeasured variables. Moreover, a Computational Fluid Dynamic (CFD) model based on the physical geometry of a coal pulveriser used in the power generation industry was developed to predict the static pressure drop across major internal components of the pulveriser as a function of the air flow through the pulveriser. Validation of the CFD model was assessed through the intensity of the correlation demonstrated between the experimentally determined and numerically calculated static pressure profiles. In this regard, an overall incongruity of less than 5 % was achieved. Candidate damage scenarios were simulated to assess the viability of employing the static pressure measurements as a means of detecting changes in mechanical pulveriser condition. Application of the validated pulveriser CFD model proved to be highly advantageous in identifying worn pulveriser components through statistical analysis of the static pressure drop measured across specific components, thereby demonstrating a significant benefit for industrial application.

Research Outputs and Accolades

Conference Proceedings

Podium Presentation

Govender, A., Schmitz, W., Naidoo, R., (2015). Development of a Condition Monitoring Philosophy for a Pulverised Fuel mill. *20th Southern African Conference on Research in Coal Science and Technology: Latest Research at Universities and R&D Organisations*, 24-25 November 2015, North-West University, Potchefstroom, South Africa. (Abstract presented in Appendix F).

Poster Presentation

Govender, A., Schmitz, W., Naidoo, R., (2015). Numerical studies on a Vertical Spindle Mill employed in the power generation industry. Abstract accepted for the *7th Cross Faculty Symposium,* 1-2 March 2016, University of the Witwatersrand, Johannesburg, South Africa. (Abstract presented in Appendix F).

Accolades

Winner of the Best Student Poster Presentation in the Faculty of the Engineering and Built Environment. University of the Witwatersrand 7th Cross Faculty Symposium, 1 March 2016, Johannesburg, South Africa.

Third runner-up of the Best Student Oral Presentation in the 7th Cross Faculty Symposium, University of the Witwatersrand, 2 March 2016, Johannesburg, South Africa.

Dedicated to my loving, supportive and inspirational wife,

Derusha

Acknowledgements

At the completion of this study, I am grateful to have walked this journey with the unremitting guidance and support of several individuals.

Firstly, to the one who remains at the centre of my focus, The Almighty: Thank you for providing me with the strength and discipline to persevere through all aspects of this study.

To my Wife, Derusha: For your unconditional love and unwavering support during the most difficult of times. Thank you for always believing in me. Your patience, understanding and continuous encouragement has given me the confidence to push boundaries. Thank you for tirelessly listening to my complaints and problems and for continuously providing me with valuable insight. I could not have accomplished this challenging yet rewarding task without you by my side.

I would like to convey my gratitude to Eskom, Muzi Myeza, Sibusiso Nxumalo and the Eskom Power Plant Engineering Institute for affording me this once in a lifetime opportunity to pursue my Master's degree and for the financial support.

To my academic supervisor, Professor Walter Schmitz: For the invaluable role played during the course of this dissertation. Your support, guidance, insights, opinions and words of encouragement were always appreciatively received. Thank you for constantly challenging my abilities and for stimulating my mind, it has resulted in me wanting to be better, both personally and professionally.

To my academic co-supervisor, Reshendren Naidoo: For generously sharing your knowledge in the field of computational fluid dynamics. Thank you for providing advice, direction and assistance when needed.

To Christiaan De Wet: Thank you for providing guidance, support and mentorship. For the time you have taken to provide lengthy explanations to all my questions and for your patience in ensuring I fully understand the concepts of CFD, I am eternally grateful.

A special thank you to a host of Eskom staff who have guided me and to those that went beyond the call of duty to assist me in achieving my outcomes: Norman Crowe, Bonny Nyangwa, Waleed Moses, Anton Hart, Matthew Muller, Hlono Malatsi, Simon Phala, Mafika Mkwanazi, Khutso Ledwaba, Thandi Mkhize, Ntombi Mkwanazi, Hussein Manzana, Candice Stephens, Jolandie Kruger, Hamresin Archary, Christo Van Der Merwe, Avinash Maharaj, Lesigen Moodley, Tom Keyser and Thembinkosi Shange.

My sincerest appreciation to the Steinmuller boiler maintenance department: Tawande Mashiri and Team for assisting with the mechanical aspects of my experimental work.

To my colleagues from Wits Combustion Group 3, Dheshan Naran, Dewan Smit, Amanda Pantsi, Kyle Enslin and Ayodimejilab Biobaku: Thank you for always listening, providing guidance and advice when needed.

Last but not least, my sincerest appreciation to all my family and friends for their continuous support and encouragement.

Contents

List of Figures

List of Tables

List of Symbols

A	Area	(m^2)
B	Duct width	(mm)
C_p	Heat capacity	kJ/kgK
D	Diameter	(mm)
d	Probe diameter	(mm)
daf	Dry ash free basis	-
db	Dry basis	-
d_h	Hydraulic diameter	(m)
E	Heat loss due to drying coal	(kW)
H	Duct height	(mm)
Δh	Enthalpy	(kJ/kg)
h	Heat transfer coefficient	(W/m^2K)
I	Current	(A)
k	Thermal conductivity	(W/mK)
L	Length	(mm)
M	Mass of pulverised fuel	(g)
$\dot{m}$	Mass flow rate	(kg/s)
N	Number of sample points	-
Nu_D	Nusselt number	-
OD	Outer diameter	(mm)
ΔP	Pressure drop	(Pa)
P	Pressure	(Pa)
pf	Power factor	-
P_i	Pulveriser power input	(kW)
Pr	Prandtl number	-
P_w	Wetted perimeter	(m)
Q	Energy loss rate	(kW)
$\dot{q}$	Heat transfer rate	(kg/s)
R	Resistance	(Ω)
Re	Reynolds number	-
R_o	Universal gas constant (8.314)	(J/mol.K)
r_1	Radius of mill body	(mm)

r_2	Radius of classifier region	(mm)
T	Temperature	(^oC)
t	Time	(s)
V	Voltage	(V)
VM	Volatile matter of coal	(%)
v	Velocity	(m/s)
w	Relative uncertainty of an independently measured quantity	-
w_o	Raw coal moisture content	(kg/kg)
w_1	Pulverised fuel moisture content	(kg/kg)
x_1	Air humidity fraction	(kg/kg)
x_{ash}	Percentage ash in coal	(%)
x	Measurement of independent variable	-

Greek Symbols

μ	Dynamic Viscosity	(Pa.s)
ρ	Density	(Kg/m^3)

Subscripts

amb	Ambient conditions
avg	Average
bulk	Bulk property of raw coal
calculated	Calculated fluid property
coal	Raw coal
conv	Convection
DCS	Digital control system
duct	Raw coal duct
evap	Evaporation of raw coal moisture
grind	Grinding of coal
i	Input
max	Maximum

measured	Experimentally determined parameter
min	Minimum
o	Output
PA	Primary air
PF	Pulverised fuel
pipe	Pulverised fuel pipe
SA	Seal air
simulated	Simulated outcome
static	Static pressure
segment	Area segment
total	Total air flow rate
w	Water

Chapter 1: Introduction

1.1 Research background

Coal has, for more than a century, been the largely relied upon resource required by fossil fuelled power plants to produce electricity economically and viably. In electricity generation, coal accounts for over 40 % of the total fuel consumed worldwide (International Energy Agency, 2015). From the various technologies employed to produce power, which include coal-fired, nuclear, hydro, gas turbine and pumped storage, the dominance of coal-fired power generation in the energy sector is evident, with approximately 93 % of Eskom's electricity generated from coal-fired power plants (Eskom, 2014). In 2004, state owned power utility Eskom embarked on a capacity expansion program which led the return to service of three power stations that were formerly decommissioned in the late 1980's. This added an additional 3.65 Gigawatts electric (GWe) to the utility's installed capacity. The power utility has a net maximum generating capacity of 42 GWe and is in the process of increasing its coal-fired power generation capacity by 9.6 GWe to meet the energy requirements of South Africa (SA) (Eskom, 2014).

A coal-fired power station converts the chemical energy stored in coal into electrical energy. There are several systems that operate collectively at a power station to produce electricity. The key systems, as identified in Figure 1.1, typically include the fuel handling plant, coal pulverisation, a steam generator (boiler) and combustion, turbine-generator plant, environmental protection plant and heat rejection plant (condenser and cooling tower).

Raw coal, obtained from local mines, is conveyed from the power station stockyard to the coal bunkers where it is stored temporarily. From the bunkers, coal is supplied to the coal pulverisation plant where it is pulverised following which it is pneumatically conveyed to the boiler to be combusted. The heat energy released inside the boiler during coal combustion is used to convert high pressure water, inside an array of boiler tubes, into superheated steam. The superheated steam is thereafter supplied to the turbine-generator plant. In the turbine-generator plant, the superheated steam drives a steam turbine which is coupled to a generator that produces electricity. Thereafter the steam is condensed and recycled into the water-steam circuit.

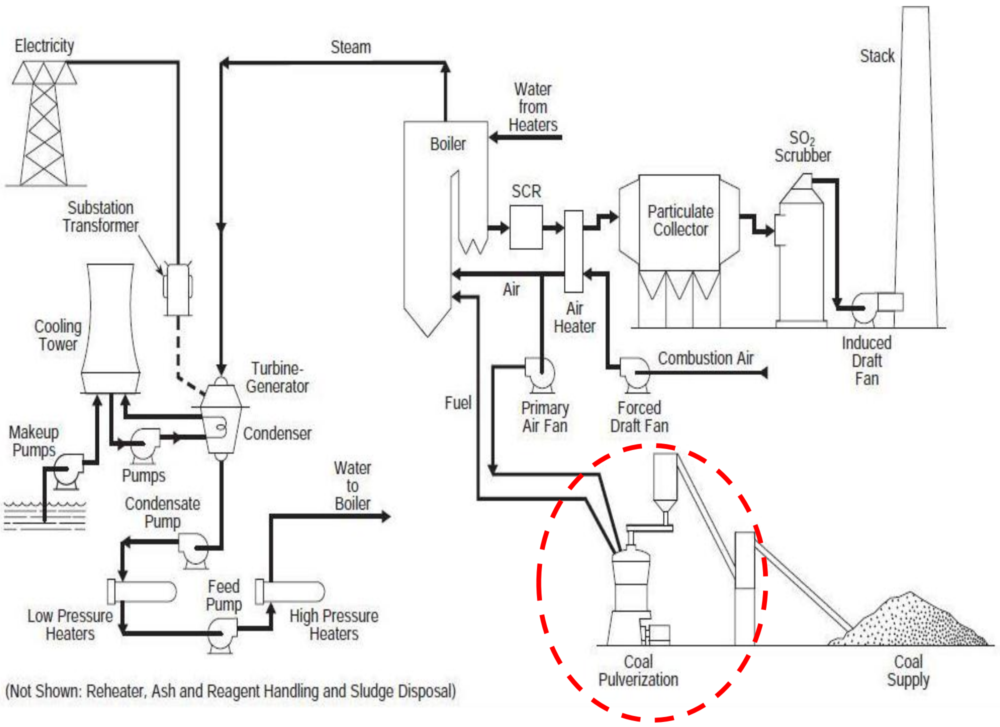

Figure 1.1 System arrangement of a typical coal-fired power plant (Kitto and Schultz, 2005)

Coal pulverising systems, the location of which is highlighted in Figure 1.1, are found in all pulverised fuel-fired power plants to finely grind, dry and preheat, classify as well as pneumatically transport the pulverised coal particles to the furnace for combustion. The pulverisers are generally classified under the boiler plant system. A succinct description of a direct-fired coal pulverisation process is given hereafter.

A pulveriser system typically comprises of the mechanical components as illustrated in Figure 1.2. Hot primary air is utilised to dry and transport pulverised coal particles during the grinding process. The pulveriser receives hot primary air from the air preheater. The temperature of the primary air entering the pulveriser is controlled using tempering air in order to maintain a fixed air/coal temperature at the pulveriser outlet. In the pulveriser, raw coal is mechanically reduced from a nominal size of about 40 mm to a fineness in the range of approximately 70 % (by mass) passing a 200 mesh sieve (75 μm). The dried and ground coal is then pneumatically conveyed to the burners for combustion.

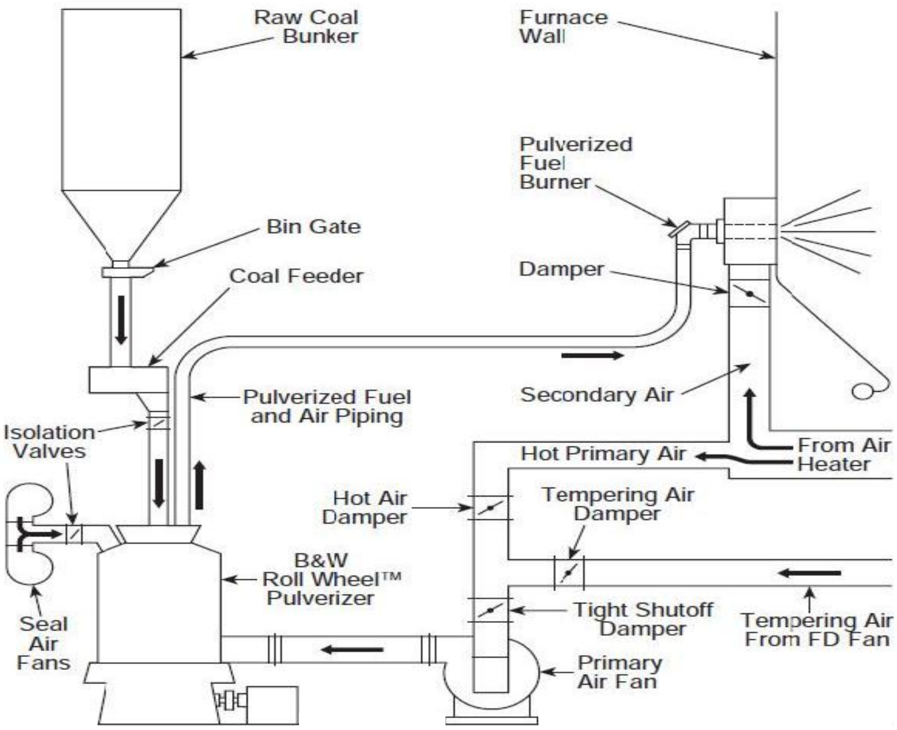

Figure 1.2 Schematic illustration of a coal pulverisation plant (Kitto and Schultz, 2005)

One of the major key performance indicators at coal-fired power plants is the thermal efficiency. Vuthaluru et al. (2005) mention that coal pulveriser's are one of the first mechanical components in the power generation process which have a major influence on boiler plant efficiency. The fine coal particles produced by the pulveriser ensure maximum energy release from coal thereby improving combustion efficiency and stability. Additionally, reliable coal pulveriser performance is required to achieve and sustain full and partial load operation of the boiler in a modern pulverized coal-fired electric generating station (Kitto and Schultz, 2005)

Over the years, significant financial resources have been invested and extensive research has been conducted in the field of coal-fired power generation in pursuit of cleaner, more efficient and optimised processes. The recent implementation of stringent environmental legislation which demand environmentally friendly coal-fired power production, as well the growing interest in renewable energy technologies, provides a strong impetus to stimulate technological changes through research primarily aimed at improving coal-fired power generation processes for the future.

1.2 Classification of pulverisers

Pulverisers are generally classified as being low, medium or high speed. SA power stations employ a combination of low and medium speed pulverisers. These are typically ball and tube mills and vertical spindle mills (VSM), respectively. Over 200 VSM's in Eskom are employed to produce 46 % of the utilities total coal-fired power generation capacity. At the completion of the current new build coal-fired projects, this value is set to increase by 11 %. A summary of Eskom pulverisation plants is tabulated in Appendix A. For the purpose of this dissertation the terms pulveriser and mill are used interchangeably and emphasis is placed on the VSM (ball and ring type).

1.2.1 Horizontal air-swept pulverisers

The low-speed ball and tube mill is a frequently employed horizontal air-swept pulveriser. Figure 1.3 displays the general arrangement of a typical double ended ball and tube pulveriser. This pulveriser design incorporates a horizontal cylinder charged with small steel grinding balls having a diameter of 50 mm. About 30 % of the cylinder volume is occupied by the grinding balls and grinding action is achieved by rotational movement of the cylinder. This consents the hardened steel balls to rise up and tumble onto coal particles, thereby pulverising them on impact. The ball and tube mill is arranged for either single or double ended operation. In the former, coal and air are fed through one end of the pulveriser and are extracted at the opposite end. In double ended operation, coal and air enter from both ends of the mill and the pulverised coal/air mixture is removed from both ends. In both types, oversized coal particles are rejected by externally fitted classifiers, thereby ensuring the desired coal fineness is achieved (EPRI, 2006).

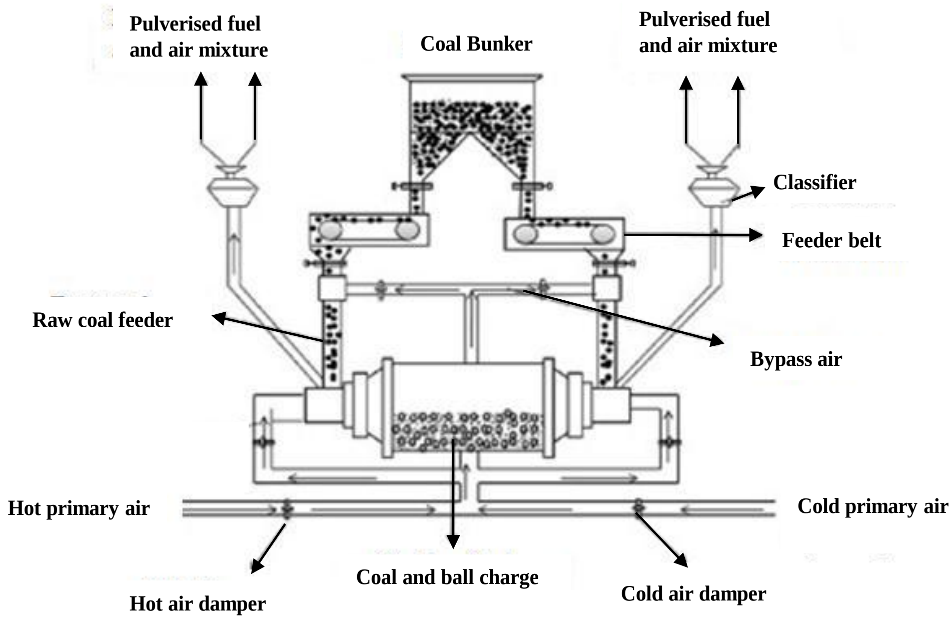

Figure 1.3 Schematic diagram of a low speed ball and tube mill (Adapted from Agrawal et al., 2015)

1.2.2 Vertical air-swept pulverisers

In a typical vertical air-swept pulveriser, there are two input streams, coal and air, and the pulverised coal/air mixture is extracted through two or more (up to 4) mill outlet pipes. Its main mechanism of particle size reduction relies on the rolling action of grinding elements which pass over a layer of granular material, compressing it against a moving table, as schematically highlighted in Figure 1.4. A cushioning effect caused by the compressed granular layer retards grinding effectiveness whilst simultaneously reducing grinding component wear rates. The classification of coal is analogous to horizontal air-swept pulverisers, however, the static or dynamic classifier installed is designed within the mill body (Kitto and Schultz, 2005). In contrast to the ball and tube mill, coal drying is more effective in a vertical air-swept mill as a result of the increased height which permits longer residence times for coal particles to lose moisture. Furthermore, VSM's enjoy lower specific power consumption (Kitto and Schultz, 2005). As of late, newer Eskom power stations employ ergonomically acceptable VSM's perhaps due to the aforementioned benefits.

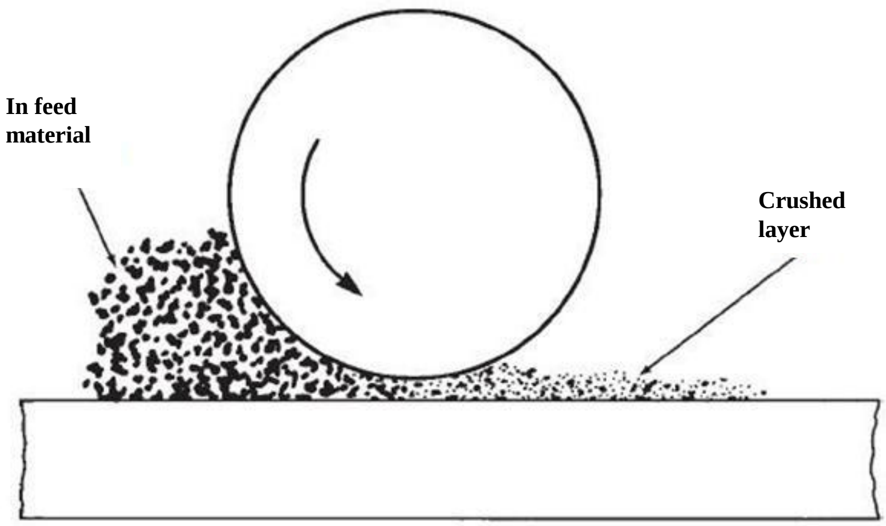

Figure 1.4 Vertical air-swept mill grinding mechanism (Adapted from Kitto and Schultz, 2005)

Vertical air-swept coal pulverisers wear in a similar manner to the horizontal air-swept type. Wear results from the combined effects of abrasion[I] and erosion[II]. The mechanism which dominates in the wearing process of a particular pulveriser component depends largely on the designed function of that specific component and on the properties of coal being pulverised (Kitto and Schultz, 2005).

1.2.3 Vertical Spindle Mill (ball and ring)

VSM's are generally characterised by three different designs. These are bowl mills, ring roll mills, and ball and ring mills. Since the principle of operation of these designs is similar, only a description of the 8.5E VSM (ball and ring type) will be provided. Figure 1.5 represents a simplified schematic diagram of a typical VSM. The pulveriser consists of nine hollow steel balls (730 mm in diameter) which are located freely between two grinding rings. The bottom grinding ring is

[I] Abrasion refers to the removal of a material by friction due to relative motion of two surfaces in contact.
[II] Here erosion is defined as the progressive removal of material from a component on which a fluid borne stream impinges.

connected to a shaft and is designed to rotate at 40 rpm. The top grinding ring remains stationary and is spring loaded during normal pulveriser operation. Coal enters through the central pipe from a volumetric or gravimetric feeder and settles on a rotating table. The volume feed flow is controllable as the feeder speed is variable. Whilst on the table, coal is radially displaced outward onto the grinding path (bottom ring) by means of centrifugal forces. The raw coal is ground as it passes under the grinding balls. Preheated primary air is introduced through primary air ports or throat gaps located around the periphery of the bottom grinding ring. As the primary air emerges through the equally spaced throat gap area it captures ground coal particles and effectively forms a fluidized bed region directly above the throat. Site tests performed at Arnot Power Station revealed that a large percentage of moisture in coal is removed in this region during the drying process (De Wet Krüger, 1977).

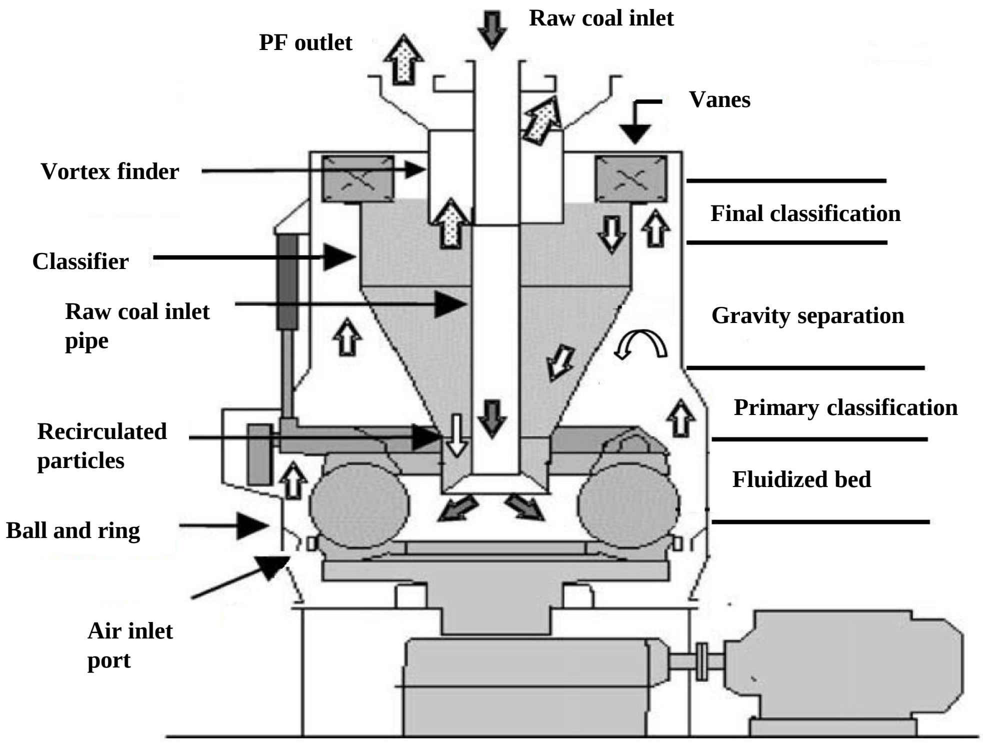

Figure 1.5 Schematic representation of a vertical spindle mill with static classifier, showing air and coal flow paths (Adapted from Parham et al., 2003)

Figure 1.6a displays the geometrical configuration of a typical throat gap in a VSM. The size of the throat gap plays an important role in ensuring the primary air enters the pulveriser at a sufficiently low velocity to entrain only fine particles. The narrower the gap the higher the primary air velocity. Heavier particles, those generally having densities greater than 2500 kg/m^3 fall into the air plenum chamber and are rejected by the pulveriser. This step in the pulverisation process is considered as the primary or initial stage of particle size classification. As the air/coal mixture rises along the height of the pulveriser, the primary air velocity decreases due to the subsequent increase in pulveriser area. This forces coal particle separation by gravity. Heavier particles then fall out of suspension and are recirculated to the grinding zone for further size reduction. The terminology used to describe this stage of particle separation is termed secondary classification.

Figure 1.6b illustrates the classifier which is located in the higher region of the pulveriser and consists of 18 static classifier blades set at 37^o. Additionally, to aid classification a classifier cone and reject return skirt is fitted, as highlighted in Figure 1.6c. During pulveriser operation, larger coal particles that impinge onto the classifier, lose momentum, drop out of suspension and are returned to the grinding zone by the classifier cone. This is the final stage of particle size classification. Only the very fine coal particles pass through the vortex finder and are discharged by the pulveriser into pulverised fuel (PF) pipes leading to the PF burners (Kitto and Schultz, 2005). The particle size separation zones were outlined in Figure 1.5.

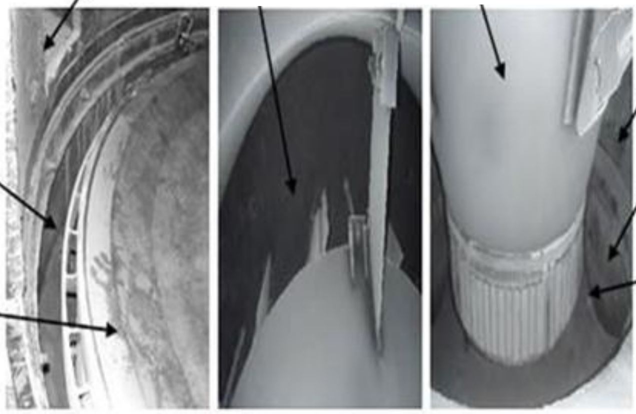

Figure 1.6 Digital images exposing pulveriser internal components

1.3 Coal flow

The coal flow rate to pulverisers at most Eskom coal-fired power stations is generally regulated by a volumetric feeder. Using this method of operation, the quantity (kg/s) of coal supplied to the pulveriser is determined through approximation methods and varies significantly. The consequences arising from operating with variations in raw coal feed rates are furnace air/fuel imbalances. This is brought about by pulverisers that deliver the air/fuel mixture to the PF burner with inconsistent air/fuel ratios (AFR). High[III] AFR's (typically >1.6) lead to a scenario where there are elevated levels of oxygen in the boiler. This case also causes the PF burners to become more susceptible to flame outs due to unstable pulverised burner flames at lower than normal pulveriser operating loads (Van Wyk, 2008). Flame outs lead to pulveriser trips and in most cases a loss of electrical output from a generating unit. This necessitates the use of fuel oil burner firing during normal boiler operation to stabilise coal burner flames, as observed at many SA power stations, and at a high operational cost. Conversely, Low AFR's (<1.4), produce fuel-rich PF burner operation resulting in longer burnout time of coal particles and a high percentage of unburned carbon (UBC) in ash

[III] High air/fuel ratios refer to a scenario when a higher mass flow rate of air is used in relation to the mass flow rate of coal which leads to fuel-lean pulverised fuel burner operation.

(Van Wyk, 2008). Obtaining a balanced PF flow distribution in PF pipes exiting the pulveriser is equally important in preventing fuel-rich or fuel lean burner operation. However, that area of research is outside the scope of this research project.

During normal operation, the coal recirculation rate within the pulveriser is dependent on several variables. These variables include the raw coal size, the mechanical condition of the pulveriser, the classifier blade angle settings as well as coal quality (especially, moisture content and Hardgrove Grindability Index (HGI)). Currently, there appears to be no viable method available to establish in real time the wear rate of pulveriser internal components. Due to these complex pulveriser process dynamics, the coal feed rate or pulveriser throughput cannot be accurately ascertained from the currently monitored process parameter indications such as the pulveriser differential pressure, primary air differential pressure or pulveriser current consumed (Messerschmidt, 1972).

Several researchers are in agreement that the accurate measurement and control of coal flow into a furnace is important in ensuring optimum power plant performance, combustion stability and efficiency is achieved (Fan and Rees, 1997; Millen et al., 2000; Kitto and Schultz, 2005; Andersen et al., 2006; Odgaard and Mataji, 2006). Coal flow measurement devices are available on the market, however, they are not easily employable in practice, require frequent calibration and come at a considerable cost (Andersen et al., 2006; Niemczyk, 2010).

Eskom power stations are currently operated with low-grade coal. The major characteristics that define low-grade coal are coal that contains low calorific value (MJ/kg), high moisture, high ash and low volatile content (Peta, 2014). This means that the pulverisers nowadays are required to grind, dry and classify a higher quantity (kg/s) of coal in order to achieve the equivalent boiler energy output that is specified by design. Aside from the challenges that operating with higher coal flow rates have on processes downstream of coal pulverisation such as ash handling and flue gas cleaning, this is likely to have a negative bearing on the wear rate of the mechanical components inside the pulveriser.

The coal pulverisation process is described as being highly nonlinear and uncertain (Fan and Rees, 1997). The probability of burning coal with improved qualities in SA in the future is not anticipatable and therefore, attention has shifted towards improving pulveriser performance. The expectation through research and testing is to improve the grinding process by developing models that can provide accurate coal flow estimations (Andersen et al., 2006).

1.4 Pressure drop

The static pressure drop in a pressurised coal pulveriser is usually determined by measuring the difference in static gauge pressure between the pulveriser inlet (highest pressure) and the pulveriser outlet (lowest pressure). The pressure drop is dependent on frictional flow resistance, mass flow rates of air/coal as well as the quantity of heat energy lost during the pulverisation process (Flynn, 2003). A significant contributor to frictional flow resistance is the geometrical configuration of the pulveriser hence there is a distinct relationship between pressure drop and the pulveriser geometry (Lindsley, 2000). Miller and Tillman (2008) mention that the pulveriser pressure drop is directly proportional to the pulveriser air/coal throughput. Moreover, the pressure losses increase with a decrease in coal HGI and classifier opening percentage (Miller and Tillman, 2008). Another factor which affects the pressure drop is the mechanical condition of pulveriser internal components (Flynn, 2003). Worn components lead to poor grinding capability thereby increasing the coal recirculation load inside the pulveriser which subsequently intensifies the pressure drop. Figure 1.7 schematically highlights the magnitude of the pressure drop with variations of coal and air mass flow rates.

In industry, the pressure drop is a ‘general indication’ of the quantity of coal present in the pulveriser (recirculating load) and not the coal feed rate or throughput (Flynn, 2003). For safe pulveriser operation, the pressure drop is maintained within a specified range. For the 8.5E VSM (ball and ring), normal operating pressure drop ranges between 3 – 4.5 kPa. However, this threshold is pulveriser load, condition as well as coal quality dependent (Fan and Rees, 1997).

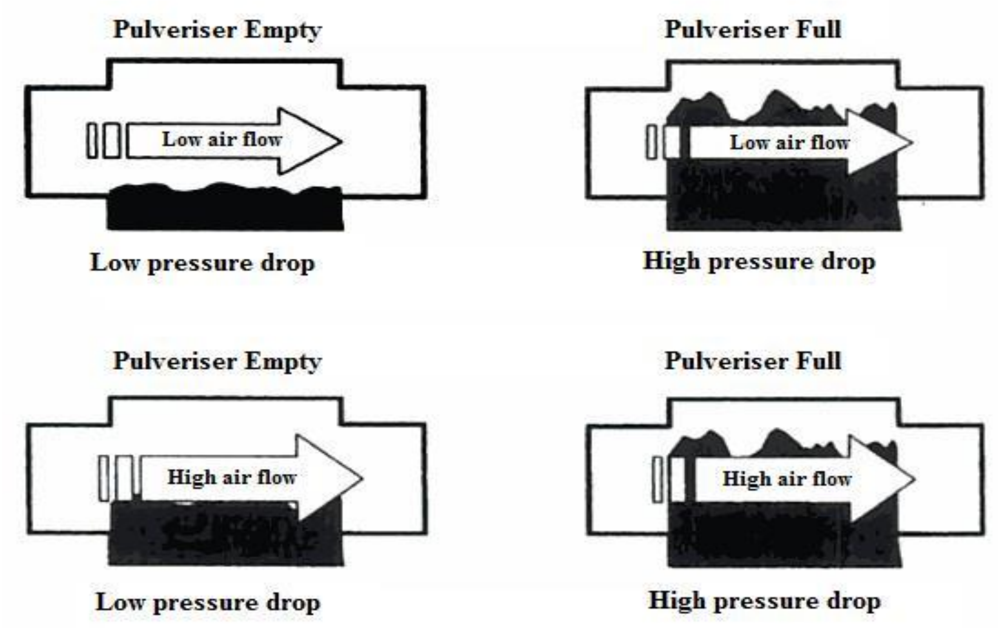

Figure 1.7 Effect of coal loading and air flow on the pulveriser differential pressure (Adapted from Lindsley, 2000)

1.5 Operational concerns

Most pulverisers in service today are at least 25 years old and experience similar operational, maintenance, performance and safety concerns. In a typical coal-fired power generating unit, there are between 3 and 6 pulverisers fitted per boiler. Currently, there is still a high degree of difficulty experienced in accurately measuring the input mass flow rate of coal into pulverisers from volumetric coal feeders for optimum operation and control (Niemczyk, 2010). Varying coal qualities e.g. calorific value (MJ/kg), Abrasion Index (AI) and moisture content lead to operational challenges such as wear, choking and blockages. This subsequently results in a reduction of throughput as well as frequent pulveriser shutdown.

Moisture in coal is considered a dead weight and causes severe handling difficulties leading to pulveriser performance and availability challenges. Typically, coals with higher moisture content require a pulveriser to operate with primary air at a higher temperature in order to sufficiently dry the coal. Furthermore, higher moisture content coals require increased residence time for effective drying thereby increasing the pulveriser recirculation load and reducing throughput. The effect of increased raw coal moisture content on pulveriser throughput is presented in Figure 1.8.

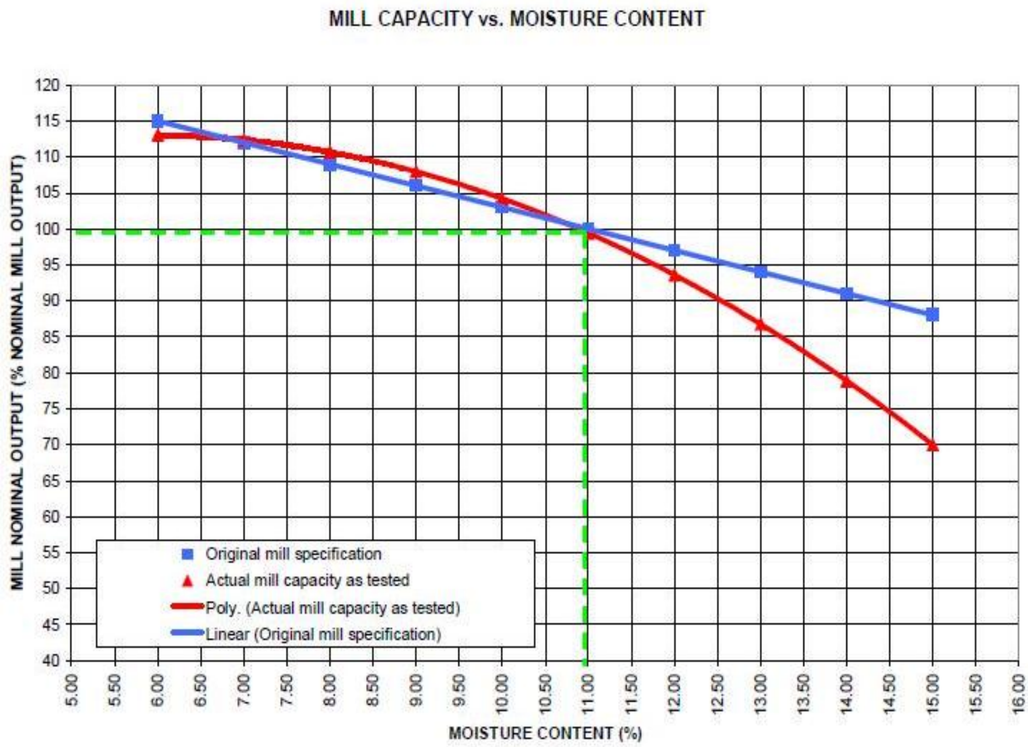

Figure 1.8 Graphical illustration highlighting the effect of coal moisture content on mill throughput (Van Wyk, 2008)

As mentioned in section 1.2.2, wear in a coal pulveriser is caused by either abrasion or erosion. Apart from valuable elements in coal, there are also undesirable constituents such as iron pyrite (FeS_2). The presence of these constituents causes significant wear on pulveriser components due to the abrasive action of a continuous stream of coal particles. The AI of coal is assessed using the Yancey-Geer Price apparatus and the higher the AI the higher the wear rate (Kitto and Schultz, 2005). The AI of coal consumed by Eskom ranges between 100 and 1100 mg Fe / kg coal (Van Wyk, 2008). The HGI of coal is also an important parameter in the pulverisation process as it is a measure of the general hardness of the coal. Coals with a HGI value below 50 require more energy to grind. For a given combination of particles and pulveriser components, factors that enhance the erosion rate are (1) an increase in primary air velocity, (2) coal particle size and (3) quantity of solids in the fluid stream (Kitto and Schultz, 2005). The throat gap region, inner cone and classifier zone are areas within the pulveriser which are most susceptible to erosion.

An important pulveriser performance requirement is the size of the coal particles leaving the pulveriser. The size fractions most frequently referenced as suitable for combustion is outlined Table 1.1. This size distribution promotes complete combustion and reduces levels of UBC in ash. Pulverisers operating with worn components affect the particle size distribution at the pulveriser output, thereby reducing the boiler combustion efficiency.

Table 1.1 Eskom standard PF size distribution (CMP, 2003)

Sieve size (µm)	Percentage passing (by mass)
300	99 - 99.6
150	86 - 95
106	76 - 85
75	65 - 75

Pulveriser fires are not uncommon and they usually develop in the high temperature air zones of the pulveriser or the in the fuel rich low temperature areas. The accumulation of coal in the air plenum chamber, due to a worn throat gap or low primary air velocity, can often lead to ignition of the coal by the high temperature primary air if it is not rejected. A common and reliable pulveriser fire indicator is the pulveriser outlet temperature indication (Wang et al., 2009). Pulveriser fires may be prevented by removing coal rejects promptly (Kitto and Schultz, 2005) and by setting a high temperature limit for the primary air (Fan and Rees, 1997).

Maintenance on coal pulveriser’s at Eskom is carried out using conventional, time-based maintenance strategies. Thus far, there is no sufficiently effective system for online monitoring of the coal pulverisation process thereby promoting largely suboptimal pulveriser performance.

1.6 Research motivation

The lack of pulveriser condition monitoring techniques is perhaps a primary determinant of poor pulveriser performance leading to unstable and inefficient combustion, high emissions as well as reduced power plant efficiency. An inherent aspect of pulveriser operation is the wearing process of pulveriser components. The mechanical condition of internal components such as the throat gap, classifier and inner cone are critical as they aid in achieving the operative purposes of the pulveriser especially with regards to grinding efficiency. Conventional strategies employed to identify worn components are ineffective as they are performed on a time-based mode as opposed to being predictive or condition-based. Developing a condition monitoring philosophy is beneficial as the challenges associated with conventional monitoring techniques may be circumvented by online monitoring of critical components. Since the poor condition of the aforementioned components compromise the PF size distribution at the pulveriser exit and subsequently exacerbate the combustion performance of a power generating unit, techniques to identify mechanical deterioration of these components must be instituted.

Additionally, the frequent shutdown of pulverisers for inspection due to poor performance places strain on power utilities to deliver the required power output. Online pulveriser component monitoring will allow for early elucidation of poor mechanical condition thereby providing a means to maintain satisfactory pulveriser performance. Hence, the efficiency of the coal combustion process will be substantially increased while the power generating load constraints due to pulveriser shutdowns may be significantly reduced.

1.7 Aim and Objectives of this study

Fan and Rees (1997) mention that although pulverisers play an important role in the overall power generation process it is one area that has enjoyed very little attention in terms of mathematical modelling. The reason for this relates largely to the idea that modelling pulverisers are very difficult. The implied difficulty stems from a combination of conditions that are inherent in the pulverisation process, such as wear, choking as well as operating with unknown coal properties (Fan and Rees, 1997)

The aim of the present research study was to develop a Mill Condition Monitoring Philosophy (MCMP) for a PF VSM employed in the power generation industry. The MCMP to be developed was a standalone philosophy and it was not anticipated to intervene in the pulveriser control system.

In order to achieve the aim the following objectives were identified:

- To gain a thorough understanding of the coal pulverisation process.
- Establish the raw coal feed rate (kg/s) to a grinding mill by developing and validating a mathematical model, a MMEB from first principles. This will incorporate the fundamental theories pertinent to the conservation of mass and energy as well as heat transfer.
- Experimentally determine the static pressure loss across the vertical height of critical components inside a commercial-scale VSM.
- Develop and validate a CFD model of the 8.5E VSM (ball and ring type) to predict the static pressure losses inside the pulveriser as a function of single-phase flow (air) and two-phase flow (air and coal).
- Establish a relationship, if any, between the static pressure drops (ΔP) across critical mill internal components determined computationally and the mechanical condition of the components thereof.
- Highlight the effect of worn components on the coal particle size distribution at the pulveriser exit through CFD application.

The mass and energy balance model, as well as the computational domain considered for the CFD calculation, was based on an 8.5E VSM (ball and ring type). Consequently, experimental studies were performed at an Eskom power plant that employed the associated pulveriser. Figure 1.9 clearly outlines the research method developed for this study.

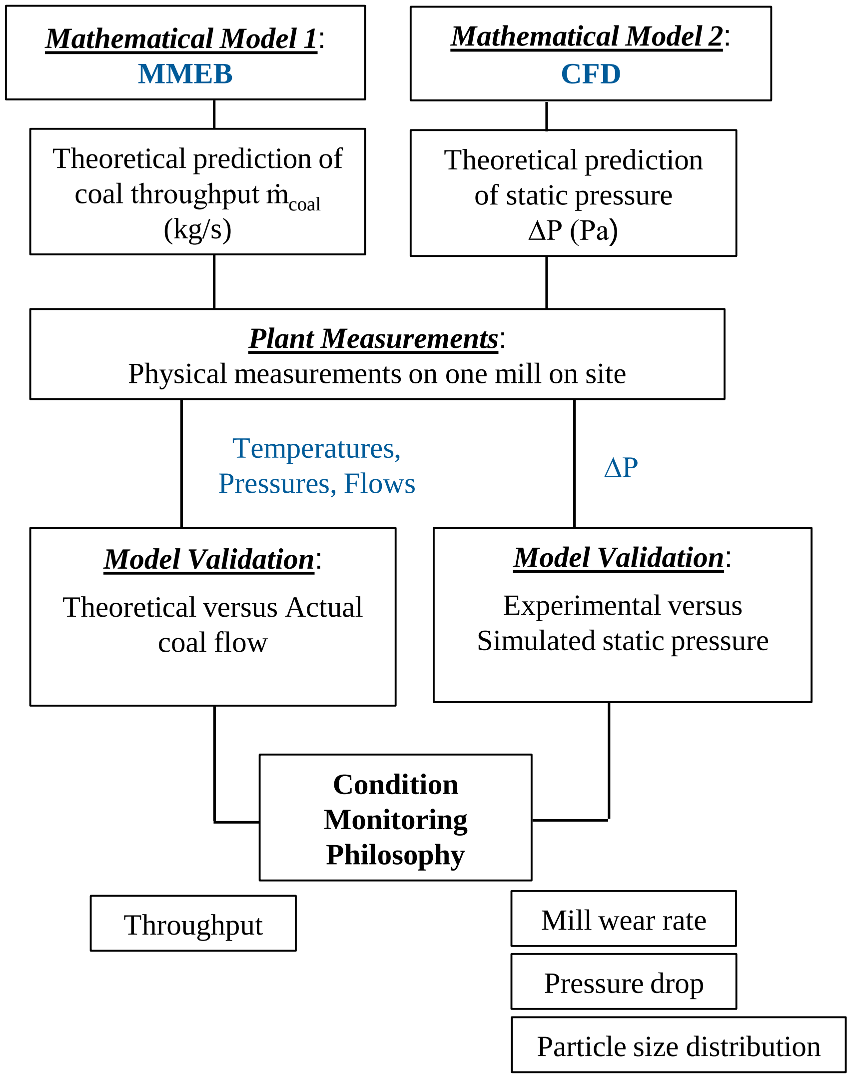

Figure 1.9 Summary schematic outlining the relationship between mathematical models, experimental and model outputs

1.8 Hypotheses

- Quantification of coal mass flow rate in a commercial-scale pulveriser (VSM) may be predicted using the principles of conservation of mass and energy.
- Static differential pressures measured on a commercial-scale VSM may be predicted using CFD.
- Static differential pressure measurements taken across critical components inside the pulveriser may be correlated to the condition of the component.

- The mechanical condition of pulveriser internal components is related to grinding efficiency.

1.9 Synopsis of this dissertation

Chapter 1 provides a succinct background into coal-fired power generation processes. Description of coal pulverisers, as well as the pulverisation processes used within Eskom, is outlined herein. It delineates the challenges and operational concerns associated with coal pulverisation and it highlights the impetus for the present study. Furthermore, the aim, objectives and research method are included in this chapter.

Chapter 2 presents a comprehensive literature review, focusing on work conducted previously in the area of coal pulverisation. Analytical approaches used to develop pulveriser models to predict process parameters are outlined. Additionally, numerical models created to establish the pulveriser flow behaviour have been highlighted. Finally, the use of analytical and numerical approaches in developing condition monitoring techniques is discussed.

Chapter 3 focuses on the experimental investigations performed to quantify several pulveriser process dependent variables highlighted through literature. A selection of experimental tests planned and executed for the development and validation of two mathematical models is presented. Moreover, the measurement locations, experimental instrumentation used as well as the experimental results obtained are outlined herein.

Chapter 4 presents the derivation and validation of a mass and energy balance model created to predict the coal throughput in a commercial-scale vertical spindle mill. The model, developed from first principles, is validated through correlation with experimental data described in Chapter 3.

Chapter 5 presents the development and validation of a highly detailed, commercial-scale vertical spindle mill model established numerically through CFD. The numerical model is validated through correspondence with experimental data presented in Chapter 3.

Chapter 6 outlines a candidate wear scenario matrix developed and presents the measured outcomes of typical damage scenarios predicted through numerical simulation whilst providing a comparison to a base case scenario. The viability of employing the static pressure measurements to highlight variations in the mechanical condition of pulveriser components is explored in relation to the aim of this study. Furthermore, this chapter delineates the relationship between poor mechanical condition and the particle size distribution at the pulveriser exit.

Chapter 7 highlights the conclusions of this study and the recommendations for future work.

Chapter 2: Literature Review

2.1 Current status of VSM research in Eskom

Eskom’s reliance on pulveriser supplier companies to assess and improve the performance of the pulverisers has resulted in very little collaboration between the power utility and academic institutions in SA. This is noticeable by the limited number of research projects which have been undertaken to date with the aim of improving power plant efficiency through optimisation of the pulverisation process. The focal point of previous research projects has concentrated on improving the coal pulverisation process by investigating parameters which affect the design of the VSM, condition monitoring techniques and performance optimisation. The impetus behind these research topics relates largely to depleting coal qualities, ageing power plants as well as stringent emission legislation in SA. Global acknowledgement that pulverisers are a key component in fossil fuel power generation is rising and will be highlighted through the studies reviewed in this chapter.

De Wet Krüger (1977) conducted field tests on a Loesche LM 18 pressure type roller pulveriser to investigate the operating and design parameters of the VSM. A range of different throat configurations was tested. The tests performed were carried out at an Eskom power station. The results of De Wet Krüger (1977) highlighted the importance of the throat gap area on overall pulveriser performance and on pulveriser wear rates. The static pressure drop across the throat gap was measured and it revealed that it constituted a large proportion of the total mill pressure drop for air only.

De Wet Krüger (1977) determined experimentally that the temperature gradient within the pulveriser is very steep directly above the throat gap area. This suggested that a significant portion of the coal drying takes place in this region. Figure 2.1 displays the measured temperatures within the VSM tested.

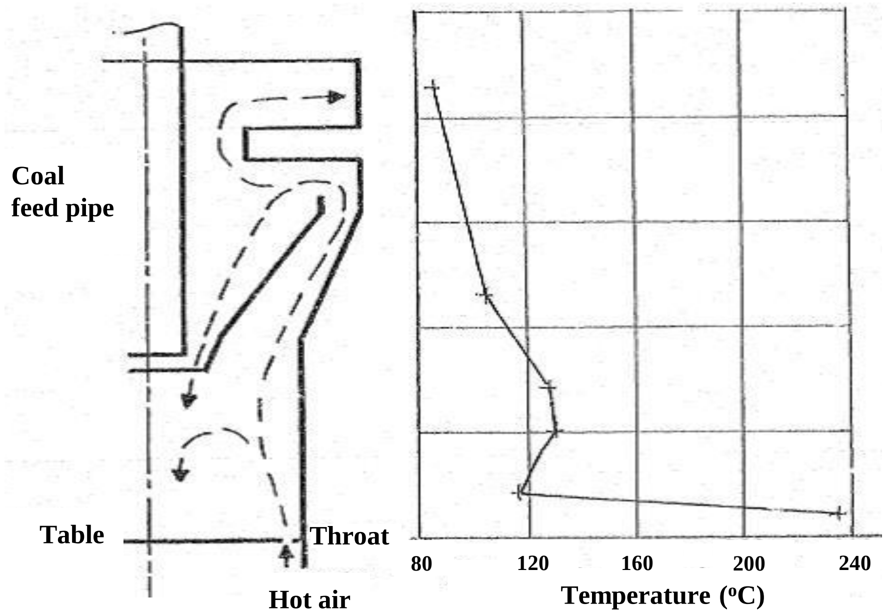

Figure 2.1 Experimentally determined temperature profile in a VSM (Adapted from De Wet Krüger, 1977)

Additionally, by employing fluidized bed theory and experimentally determined static pressure drop values along the pulveriser height, De Wet Krüger (1977) calculated a series of pulveriser operational voidage[IV]. From the voidage profile, highlighted in Figure 2.2, it is evident that the voidage changes markedly over a short distance within the pulveriser and there is an upward trend in voidage with increased pulveriser height. Although not explicitly highlighted in Figure 2.2, the operational voidage was additionally calculated at a distance of 450 mm above the throat, yielding a value of 0.8. The results of this study strongly suggests the region above the throat gap is densely packed with coal and closely resembles a fluidised bed in relation to the regions in the upper parts of the pulveriser (De Wet Krüger, 1977).

De Wet Krüger (1977) also conducted pitot traverses in the classifier region. These tests suggested that the air velocity distribution in the classifier can lead to high wear rates in this zone of the pulveriser. However, results of this finding were not explicitly presented.

[IV] Here voidage refers to the fraction of the bed volume occupied by the voids, a low voidage value is indicative of an area that contains fewer voids and is more densely packed.

An investigation performed by Holtshauzen (2008) assessed the operational impact of a rotating throat assembly in relation to the traditional stationary throat gap assembly. A comparative analysis was carried out by completing a series of standard pulveriser performance tests on two 10.8E VSM's installed at an Eskom power station. The pulveriser fitted with the rotating throat assembly demonstrated a lower overall pressure loss, lower coal reject rate and higher power consumption.

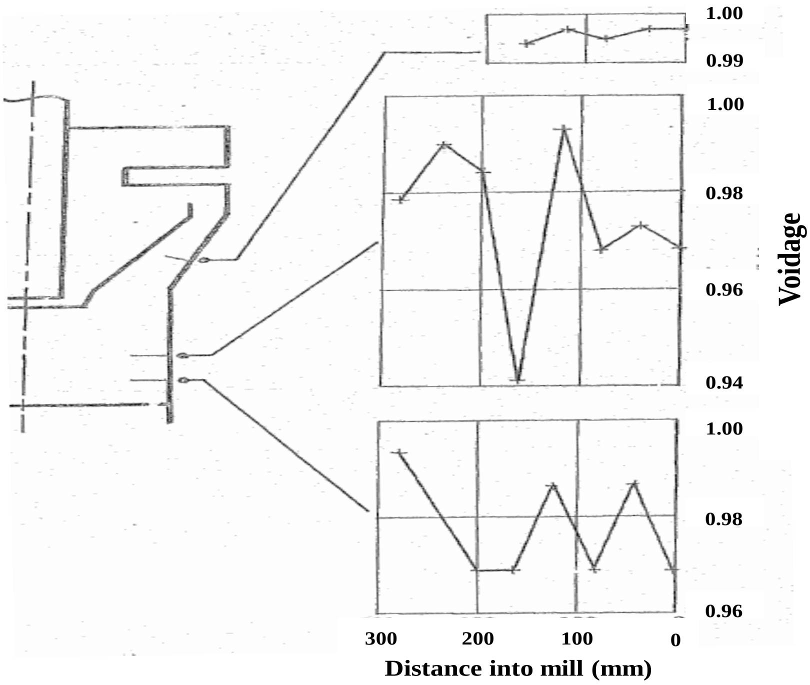

Figure 2.2 Voidage profile in a VSM (Adapted from De Wet Krüger, 1977)

Archary (2014) prepared an energy balance model to predict the coal mass flow rate in a VSM (roller type). The model accounted for convective energy losses to the environment and predicted the coal flow rate to within 2.33 % of a calibrated feeder. The model validations performed by Archary (2014) were carried out at an Eskom power station.

With the intention of improving pulveriser throughput without sacrificing PF fineness, Archary (2014) also established a relationship between throughput, classifier speed and air/fuel ratio, as well as particle fineness. The study concluded with the following findings:

- PF fineness increased with classifier speed.
- A higher pulveriser loading, as well as higher air/fuel ratios, circumvented correct PF fineness.

The investigation was performed on a pilot scale VSM, which incorporated a dynamic classifier, installed at Eskom's Research Testing and Development (RT&D) department. The scalability of the experimental results obtained on the pilot scale pulveriser was not compared to a commercial-scale pulveriser.

2.2 Mass and energy balance theory employed in pulveriser modelling

Odgaard and Mataji (2006) simplified and linearized a non-linear pulveriser energy balance model developed by Fan and Rees (1997). The aim of this research study was to develop a pulveriser monitoring system capable of detecting emerging faults in a pulveriser. A fault in a pulveriser was identified as 'extra energy input' into the model or as a residual. The model was developed to detect its ability to predict the pulveriser output temperature by employing the energy flows into and out of a predefined control volume of the pulveriser.

The model developed by Odgaard and Mataji (2006) employed existing pulveriser measured variables and the installation of additional instrumentation was therefore not required. The model was solved under steady state conditions as it assumed the pulveriser inlet and outlet coal flow to be equal. However, the quantification of coal mass flow rate was not explicitly mentioned and the pulveriser motor power consumption was neglected as an input in the balance. Evaporation of moisture from coal was accounted for in the model however, a static estimate of the moisture content of raw coal was utilised as the moisture content of raw coal was not measured online. The model output was compared to historical data recorded during a common pulveriser fault such as a blocked raw coal inlet pipe. The results of the model exhibited promising sensitivity in highlighting the occurrence of a fault through the temperature prediction.

Coal pulverisers dry the ground coal before they are blown into the furnace. The coal throughput in a pulveriser is significantly influenced by the moisture content of the raw coal, as explicated in section 1.5. The moisture content of raw coal is one of the many variables which are not measured online at the majority of Eskom power stations. Recent developments in infrared technology have allowed for the online determination of coal properties prior to the pulverisation process. However, these online coal analysers are only operational at a few Eskom coal-fired stations and will be implemented at all Eskom power stations in future.

Flynn (2003) presented a global input/output mass and energy balance model that was similarly derived to calculate the temperature profile of a pulveriser. Energy inputs and outputs of the model were accounted for from the primary air, raw coal and moisture in raw coal and PF streams. The model assumed the pulveriser temperature was measured in the pulveriser outlet pipe and that this temperature was representative of the pulveriser body and coal and air mass temperatures inside the pulveriser. The effects of coal drying were modelled by considering the latent heat of vaporisation for water.

In the pulveriser model presented by Flynn (2003), several pulveriser process parameters were not considered in the global energy balance. These parameters are highlighted below:

- The mass flow rate of seal air in/out of the pulveriser.
- The power input from the pulveriser motor.
- The energy consumed for grinding the coal.
- Air humidity factor.
- Convective and radiative heat losses from the pulveriser body to the environment.

Archary (2012) adapted and extended the model presented in Flynn (2003) to derive a new energy balance model aimed at predicting the coal throughput of a pulveriser under steady state conditions. Archary (2012) incorporated the mass flow rate of seal air, the pulveriser motor power input, air humidity and the convective heat losses to the environment. The model was developed for an

Eskom Lopulco LM143 VSM (tyre/table type) which was designed to grind coal at a nominal capacity of 25 tons/hr.

A review of isokinetic PF sampling reports obtained from Eskom power stations revealed that PF is not completely dry at the pulveriser exit. This is consistent with the findings of Coal Milling Projects (CMP) who have reported the moisture content (by mass) of PF to range between 1 and 3 percent (CMP, 2003). In the model derived by Archary (2012), the effects of moisture in the PF were excluded. Fan and Rees (1997) mention that when the moisture content of raw coal is higher than normal, the mass percentage of moisture in the PF will increase. This is primarily due to the high temperature limit imposed on the primary air entering the pulveriser (Fan and Rees, 1997).

During the coal drying process, the temperature of the air/coal mixture exiting the pulveriser is on average 60 percent lower than the primary air inlet temperature. Archary (2012) assumed average and constant heat capacity constants, for air and moisture. Furthermore, the model utilised the heat capacity of coal on a dry-ash free basis, whereas coal entering a pulveriser contains ash. Nonetheless, the model predicted the mass flow of raw coal to within 2.33 % of a calibrated feeder. The correspondence achieved between the models predicted coal mass flow rates and the experimental values are illustrated by the bar graph in Figure 2.3. In addition, the study highlighted the primary air temperature to be the most influential parameter on the model-predicted coal mass flow rate.

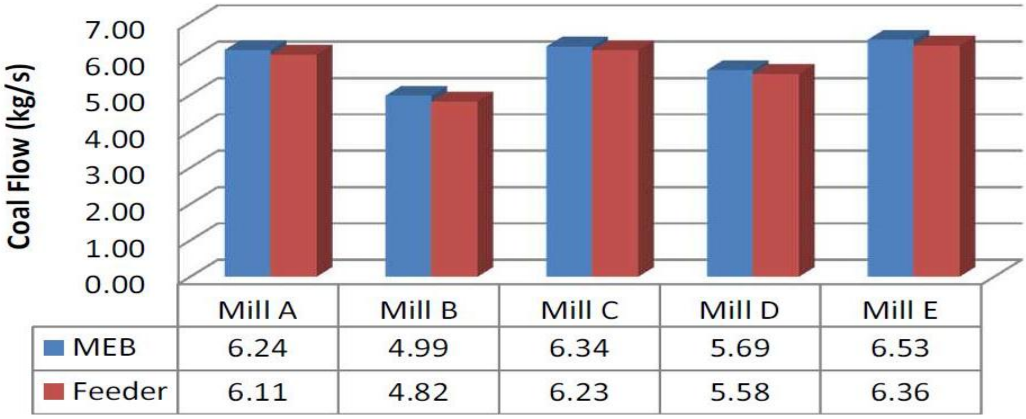

Figure 2.3 Graphical illustration of the model-predicted coal mass flow rate in comparison to the measured coal flow rate (Archary, 2012)

While the current outlook for pulveriser process parametric quantification using mass and energy balance techniques looks promising, all the variables surrounding the pulverisation process has not been comprehensively considered previously, and is therefore not yet fully understood. With that said, and for the purposes of this dissertation, the mass and energy balance developed by Archary (2012) to estimate the raw coal mass flow rate in a pulveriser will be assessed, adapted and enhanced in an attempt to ascertain the applicability of the mass and energy balance model for the 8.5E VSM (ball and ring) pulveriser employed at Power Station A.

2.3 Numerical studies of multiphase flow in coal pulverisers

Multiphase flow generally refers to any fluid flow consisting of two or more phases or components. Studies involving multiphase flows generally arise from the need to accurately predict the behaviour of these flows and the phenomena that they manifest within processes. Research into multiphase flow models usually fall into three categories, (1) experimentally, using laboratory sized models, (2) analytically, employing mathematical equations, and to a larger extent in recent years, (3) numerically, using CFD.

There appears to be limited literature highlighting the experimental investigation of two-phase flow in pulverisers. Few studies describe laboratory-scale experiments undertaken at restricted mill operating conditions while other teams described commercial-scale experiments undertaken at a narrow range of classifier vane angle settings (De Wet Krüger, 1977; Shah et al., 2009). Other researchers applied a limited number of conventional experimental techniques to investigate the mass flow distribution in coal pulveriser outlet pipes (Dodds et al., 2011). Solving complex flow problems theoretically or experimentally are not always achievable due to time, cost and accessibility constraints leaving numerical methods as the most viable option. However, investigation of flow patterns and coal particle trajectories in VSM's have also not been comprehensively undertaken with there being only a handful of publications available on the subject.

The earliest application of CFD in coal pulverisers, pioneered by Bhasker (2002) was performed on a geometrically simplified model of a VSM (roller/tyre type). Mechanical components excluded from the computational domain were the grinding rollers and journal assembly. The model was solved using commercially available CFD software TASCFlow, which is based on the finite volume method. A fully three-dimensional model was simulated. The model employed the standard κ-ε turbulence model which satisfied the Reynolds Averaged Navier-Stokes equations of motion for an incompressible fluid flow. Coal particles having a constant particle size of 25 μm were injected into the converged continuous air flow phase. The model was simulated using air and coal flow rates of 29.6 kg/s and 8.3 kg/s, respectively, indicating a higher than normal AFR.

The results of the CFD model were qualitative and produced distribution plots of velocity and static pressure as well as particle trajectories. Bhasker (2002) concluded that the presence of solid components inside the pulveriser, as well as particle drag forces, influence the air-coal path resulting in unequal air and coal flow distribution at the pulveriser exit.

Vuthaluru et al. (2005) utilised a granular Eulerian-Eulerian approach to generate the parametric behaviour of multiphase flows in a simplified VSM (tyre and table) model. The flow domain of the three-dimensional model was restricted to the areas between the pulveriser casing and the classifier cone, hence, the grinding zone, classifier and mill outlet pipes were not captured. Tetrahedral cells were used to discretize the three-dimensional computational domain and the trajectories of two different sized particles were simulated, 100 µm and 500 µm. Best practice guidelines suggest operating the VSM with an AFR of between 1.4 and 1.6. A higher than normal AFR has once again been utilised in this model, with air and coal flow rates of 31.5 kg/s and 5.6 kg/s respectively, AFR: 5.62. The CFD results, obtained through commercial code FLUENT, showed that the flow field within the pulveriser was slightly symmetric and demonstrated that the two different particle sizes injected followed different trajectories. The 100 µm particles were carried by the air flow to the top of the pulveriser while the 500 µm remained at the bottom, perhaps due to gravitational separation. No quantitative validation data was provided and the solution domain lacked satisfactory mesh resolution as it was populated with less than 500 000 volume cells.

In the Eulerian-Eulerian approach employed by Vuthaluru et al. (2005) the fluid dynamics equations for momentum and continuity were solved separately for the air and particle phases. Best practice guidelines suggest that when using this approach, modelling particle size distributions are complex and the hydrodynamics of each particle cannot be adequately represented. Furthermore, the modelling of turbulence for each phase has a substantial impact on computational costs and the strong coupling present between the individual phases renders it immensely difficult to achieve solution convergence. Hence the approach can be considered to be non-viable for large complex models.

To address the above-mentioned shortcomings, Vuthaluru and colleagues (2006) expanded on their previous research study by employing the Eulerian-Lagrangian approach to model a coal pulveriser. The focal point of this study was based on investigating the effect of air flow distribution on the wear pattern inside the pulveriser (Vuthaluru et al., 2006). Simulated solutions were calculated through the employment of commercially available CFD code FLUENT. Model input variables that were incorporated included the pulveriser static pressure and total pressure, velocity direction and turbulence intensity. As turbulence can greatly influence the results of the simulation, turbulence was modelled using the default

κ-ε turbulence model and the segregated numerical solver was employed. The dispersed phase was simulated with coal particles of a single size (250 µm), introduced at a rate of 0.00025 kg/s to simplify the solution. The findings of this research study, succinctly summarised in section 2.4.2, highlights the versatility of employing CFD calculations to develop condition monitoring systems.

In the Euler-Lagrangian approach used by Vuthaluru et al. (2006), the model solves the Navier-Stokes equations for the continuous phase using the Euler method by default. The equations of motion for individual particles in the particulate phase are solved under the Lagrangian framework. Best practice guidelines suggest that in utilising this approach comprehensive information can be obtained for individual particles such as:

- Particle-particle interaction, particle impact on wall boundaries in the computational domain.
- Particle size distribution analysis.
- Modelling of heat and mass transfer between particles and the surrounding fluid.

However, the fundamental drawbacks of the Euler-Lagrangian approach are that it requires more computational power to solve complex models and it is limited to smaller concentrations of particles. Up to 60 % of a cell volume can be occupied by particles using this approach. Whilst in the Euler-Euler approach, up to 100 % of a cell volume can be occupied by either the particle or continuous phases (CD-Adapco, 2014).

As previously mentioned, the classifier in a pulveriser plays an important role in the classification of pulverised coal particles after grinding. The classifier imposes a swirl onto the air/coal flow and separates pulverised coal particles using centrifugal action into two fractions. These are the fine product which exits the pulveriser and the coarse rejects which are recirculated to the grinding zone for further processing. To perform its function effectively, the classifier is equipped with multiple vanes. These vanes are set at an optimised angle in order to achieve an acceptable particle size distribution at the pulveriser exit. Classifier vanes operate between 0-100 percent, where 100 percent indicates a fully open classifier. At a classifier vane setting of 100 percent, the throttling effect of the vanes will be minimum resulting in negligible pressure drop across the classifier. When the vanes are throttled, the finer the PF product at pulveriser exit and the higher the coarse reject fraction. This promotes a higher recirculation load and reduces the throughput of the pulveriser. If the classifier is not in good mechanical condition, larger coal particles may exit the pulveriser and due to the weight of these larger particles, it leads to PF settling in the horizontal sections of the PF pipes on route to the PF burners. Therefore, it is important to pay special attention to the classifier vane angle settings and to monitor their mechanical condition.

Shah and co-workers (2009) developed a full scale multi-outlet CFD model of a bowl type VSM for the evaluation of classifier efficiency and to quantitatively determine the influence of classifier vane angle settings on the pulveriser output. Five geometrically modified classifier vane scenarios were assessed between 100 % and 45 %. The results of the simulations succinctly illustrated the unprecedented influence of the vane position on the air flow resistance in the classifier region. By evaluating the particle size distribution at the pulveriser exit, this team was able to demonstrate that an optimal PF fineness could be achieved at a classifier opening of 65 % (Shah et al., 2009). Additionally, coal mass balances were performed and presented as a percentage deviation from the mean. The simulated results demonstrated good accuracy and correlated well within a 7 % error when compared to physical plant measurements, emphasizing the viability of employing CFD to accurately predict flow phenomena in coal pulverisers. A highlight of this study to be noted was the exclusion of the Two-Way coupling model, as a result the interaction of the forces present between coal particles and the continuous air-phase was not considered.

Bhambare et al. (2010) expanded on the previously developed pulveriser CFD models by including Two-Way coupling between air and coal as well as moisture evaporation from coal. The findings of this study correlated well to results presented by Vuthaluru et al. (2006) which highlighted the uneven air flow distribution at the throat region. This team aimed at determining whether the non-uniform air flow distribution at the throat had any relation to the non-uniform air and particle size distribution in the pulveriser outlet pipes. A hypothetical case of even air flow distribution was created at the throat region. Coal and air mass flow in the pulveriser outlet pipes were expressed as a percentage deviation from the mean for before and after the hypothetical test scenario simulated. Although the standard deviation of the primary air flow in the pulveriser outlet pipes improved from 3.8 % to 0.3 % with the modification, the non-uniformity of the coal flow only improved from 3.5 % to 2.8 %, emphasizing a poor correlation between the two measured outcomes.

The focus of this section was placed on reviewing pulveriser models derived numerically through CFD. The application of CFD to coal pulverisers has demonstrated great potential in highlighting the flow dynamics rife within the pulveriser environment. Rather than acting exclusively to predict flow behaviour, CFD provides comprehensive information and detailed visualisation of the phenomena that manifests in a pulveriser, in comparison to data attainable through experimental methods. Previous pulveriser numerical studies were predominantly performed on geometrically simplified models of an MPS tyre and table VSM design. The most commonly employed numerical approaches, including the selection of physical models, were briefly discussed. Based on the reviewed literature, it is evident that a comprehensive understanding of the physics involved, as well as their impact on the results of pulveriser models generated thereof, has not been studied in its entirety. With the advancement in computational and CFD technology, research should, therefore, be focused on developing more refined pulveriser models that incorporate advanced physics models that define the fluid flow more accurately.

With that said, the present work anticipates exploring the complexities associated with the Babcock 8.5E ball and ring VSM design. Although the principle of operation between the ball/ring and the tyre/table is relatively similar, the fundamental distinction arises in the geometry creation, physical models defined, as well as the domain over which the pulveriser is simulated.

2.4 Condition Monitoring

2.4.1 Online condition monitoring systems for coal pulverisers

Fan and Rees (1997) developed a knowledge based monitoring system for a pulveriser to aid plant operators in monitoring pulveriser process parameters online. The monitoring system developed was an extension and application of a mathematical pulveriser mass and energy balance model developed in their previous study. The system was designed to achieve the following functions:

- Acquire and process real time mill process data.
- Online process parameter estimation and pulveriser performance prediction.
- Fault diagnosis and prognosis.
- Early alarming and problem analysis.

The system was designed to identify process variable abnormalities and developed incipient alarm signals when the error calculated between the models predicted variable and measured variable exceeded a predefined limit. However, the study stipulated that the expert knowledge data base required for such a system must be large and the inter-relationship between all associated variables must be well established. Furthermore, the application of the model on a full-scale pulveriser was not explored, hence qualitative data was not provided.

Satisfactory operation of the system developed by Fan and Rees (1997) in the Eskom environment is not expected due to the utilities operation with variable coal qualities, hence constructing inter-relationships between all variables may be extremely difficult. Nonetheless, the capability of employing mass and energy balances techniques to quantify process variables was accentuated.

The use of mathematical models for online monitoring of pulverisers has also been proposed by Zhang et al. (2002), Wei et al. (2007) as well as Wang et al. (2010). These models use pattern recognition techniques to learn the behaviour of pulveriser variables under normal operating conditions. For example, under normal pulveriser operation there is an existing relationship between mill differential pressure and the amount of power consumed by the mill. In this case, the model will learn that specific relationship and if, at any point while the monitoring system is active, the mill differential pressure exceeds a predefined limit for mill power consumed, it will raise an alarm.

In order to accurately monitor pulveriser performance, measurement of pulveriser throughput and fineness of PF produced is necessary. Since measurement of coal throughput and PF fineness is currently not measured online, continuous online monitoring of pulveriser performance is omitted from coal-fired power plants.

The conventional method of ensuring satisfactory pulveriser performance is to set up pulveriser characteristic curves supplied by pulveriser manufacturer companies at the time of commissioning and conduct periodic isokinetic PF sampling. These conventional performance methods will be briefly explained hereafter.

Characteristic curves are commonly referred to as clean air and load line curves in the power generation industry. The clean air curve (CAC) is an indication of the system resistance through the pulveriser as a function of the airflow passing through the pulveriser. The load line (LL) of a pulveriser is a representation of the relationship between the quantity of air and coal introduced into the pulveriser (CMP, 2003). The characteristic curves are a basic X-Y plot of the pulveriser differential pressure and the primary air differential pressure. Figure 2.4 depicts a typical clean air curve and load line for a VSM. The method of acquiring of the mill differential pressure and the primary air differential pressure was highlighted previously. The LL curve is programmed into the Distributive Control System (DCS) of a power station. Adjustments to the pulveriser LL curves are required when there is an appreciable increase in moisture content of coal, when the slope of the clean air curve changes and when the performance of the pulveriser deteriorates due to wear (Messerschmidt, 1972). However, there are no means to monitor these conditions online hence, adjustments are not undertaken timeously.

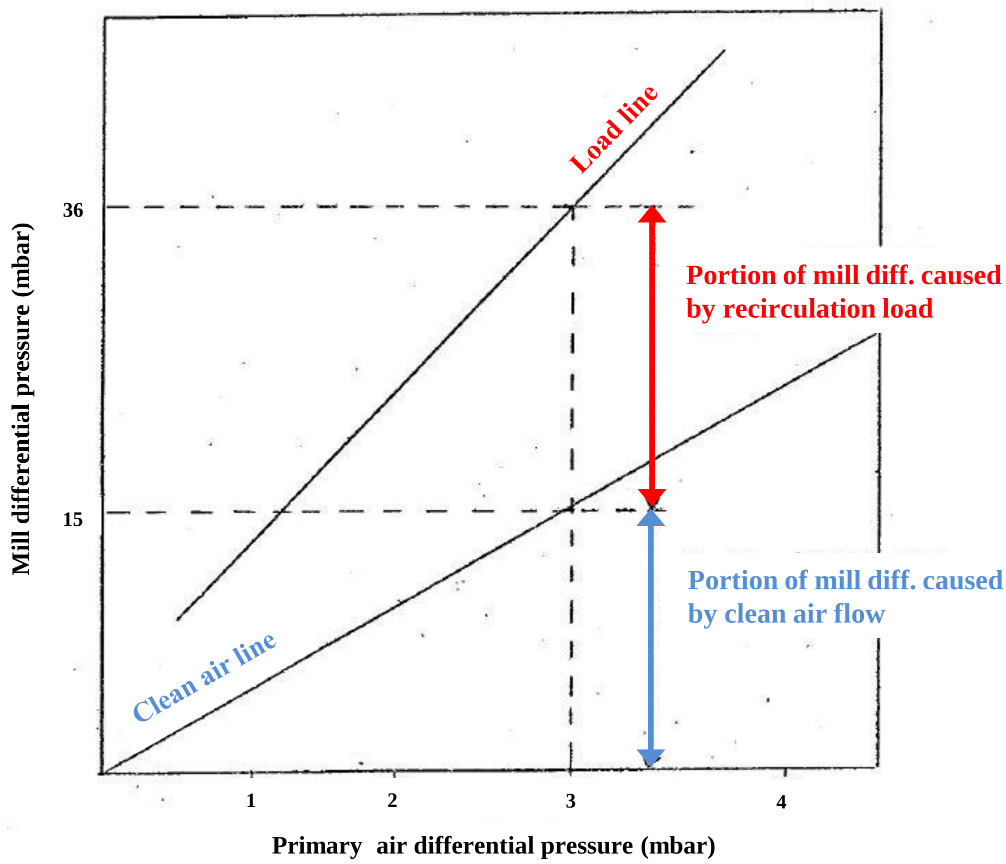

Figure 2.4 Typical clean air and load line curve for a VSM (Adapted from Messerschmidt, 1972)

Isokinetic[V] sampling of PF in pulveriser outlet pipes is the predominant method employed at Eskom power plants to obtain a representative sample of PF. Samples are collected by plant performance personnel and subsequently, a PF mass flow and size distribution analysis is performed. Isokinetic sampling is a tedious process and requires great care to be taken in order to ensure accuracy of the sample obtained. In general, common conditions that impair the accuracy of the sample are outlined below:

- When sample point locations are positioned close to pipe bends, restrictions or in the horizontal run of piping.

[V] Isokinetic refers to a process of capturing particles from a process stream without disturbing the path of the particle. The sample is extracted at the same velocity as it is flowing in the stream.

- Roping[VI] of PF in the PF pipe.
- Low air velocities in PF pipes leads to PF settling in horizontal pipes.
- Utilizing a smaller number of sampling points than the recommended standard.
- By not balancing the suction pressure of the sampling instrument, thereby failing to fulfil isokinetic conditions.

2.4.2 Application of CFD to condition-based monitoring

Rehman and colleagues (2013) prepared a three-dimensional numerical model of a single-stage centrifugal pump. The steady-state model was developed to predict the performance of the centrifugal pump as well as study the flow conditions conducive to prevent cavitation. Validation of the CFD model was accomplished using experimental results of pump head over a wide range of flow rates. Rehman et al. (2013) predicted the appearance of cavitation to occur when the pump head decreased by more than 3 % from its original value when plotted against the net positive suction head (NPSH). This team also mentioned that cavitation can be identified by monitoring the water vapour volume fraction in the flow domain. The study concluded that condition monitoring of the centrifugal pump can be achieved using CFD by modelling the NPSH of the centrifugal pump and the vapour volume fraction development on the pump impellor for different flow conditions (Rehman et al., 2013).

Due to depleting fossil fuels and stringent environmental legislation, alternate efficient energy sources are frequently pursued. Wind energy is one of these energy sources. Park et al. (2013) state that condition monitoring of wind turbines is fundamental to the continuous operation wind turbines. Park et al. (2013) applied the principles of fluid dynamics using commercially available CFD software to numerically model, in two dimensions, flow conditions in a wind turbine. Under this research study, four turbine blade configurations were tested within the computational domain of a vertical axis wind turbine and the differences in torque outputs obtained were compared to a base case. Simulation

[VI] Here roping refers to the agglomeration of ground coal particles in PF pipes (Van Der Merwe, 2013).

results showed a reduction in the turbine generated output as the number of turbine blades that were broken or missing from the vertical axis wind turbine increased. A 6.84 % decrease in turbine power output was noted with three blades missing from the wind turbine when compared to the base case, being no blades missing (Park et al., 2013). The CFD based condition monitoring technique developed in this study successfully predicted the faults in the turbine blades by monitoring the torque and turbine power output.

Structural degradation of critical pulveriser components due to wear is inevitable due to the harsh environment the coal pulverisers function in under normal operating conditions. This leads to several pulveriser performance issues with the combustion of PF being the first process directly affected. Knowledge of the performance of pulverisers is fundamental in achieving safe, reliable and economic boiler operation.

Vuthaluru et al. (2006) used a three-dimensional numerical model for multiphase flow in a pulveriser from a previous study as a basis for a study of the wear pattern in a commercial-scale coal pulveriser. The numerical model was expanded to investigate the air flow profile through the pulveriser as well as the coal particle trajectories within the computational domain.

The model investigated by Vuthaluru et al. (2006) simulated the air velocity in the pulveriser for a given mass flow of primary air input. High velocity zones within the pulveriser are undesirable. Extremely high air velocities in the throat region can result in excessive wear of the throat region due to the swirling effect of the air/coal mixture. High velocities in the throat region allow for the undesired larger particles to be entrained in the air. In addition, high air flow velocities reduce the particle residence time required to achieve satisfactory drying. Feeding PF burners with larger coal particles that are not sufficiently dry to ignite and combust completely is a primary cause for the noticeable decrease in combustion stability as well as boiler plant efficiency. This team also highlighted that low air velocity in lower parts of the pulveriser can cause a build-up of coal in that area and lead to mill fires (Vuthaluru et al., 2006). Therefore, it can be seen as an essential prerequisite to have an equal air flow distribution at the throat region and to monitor the throat gaps mechanical condition.

The geometry created for the development of the CFD model of Vuthaluru et al. (2006) was based on a VSM (roller type). The model only considered the throat and classifier region in detail and the pulveriser PF pipes. The results of the CFD model produced contour plots of air velocity over the entire computational domain. The air flow distribution was found to be uneven at the throat region. The contour plot (Figure 2.5) depicting the velocity profile in a VSM demonstrates that the model has good fluid mobility and highlights zones with increased velocity gradients. A noteworthy observation highlighted by this team was that the increased velocity was attributed to tangential air input streams that passed through the narrow throat gap. The velocity vector plot presented in Figure 2.5(b) demonstrates areas of air recirculation to be prominent in the classifier zone.

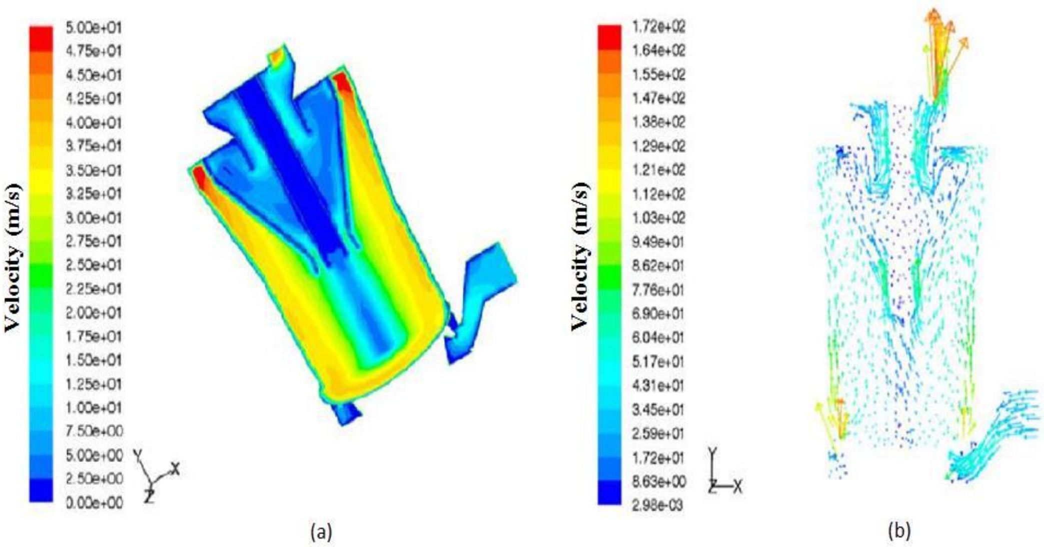

Figure 2.5 Cross sectional view of the pulveriser showing (a) Contour plot of velocity distribution (b) Velocity vector plot, from mill inlet to outlet (Adapted from Vuthaluru et al., 2006)

Vuthaluru et al. (2006) proposed a solution to reduce uneven air flow distribution by introducing a split in the primary air duct. Different combinations of air inlet mass flows were applied to the two different sides of the duct until even air flow distribution was achieved. The data obtained from this study, before and after the modification of the primary air duct are displayed as contour plots in Figure 2.6. The team concluded that by implementing a flow split in the primary airflow duct, the air flow distribution may be improved thereby reducing the possibility of wear in the throat region (Vuthaluru et al., 2006). It was mentioned that further studies should focus on particle carryover with different airflow velocities, particle size effects and the effect of the classifier on pulveriser output.

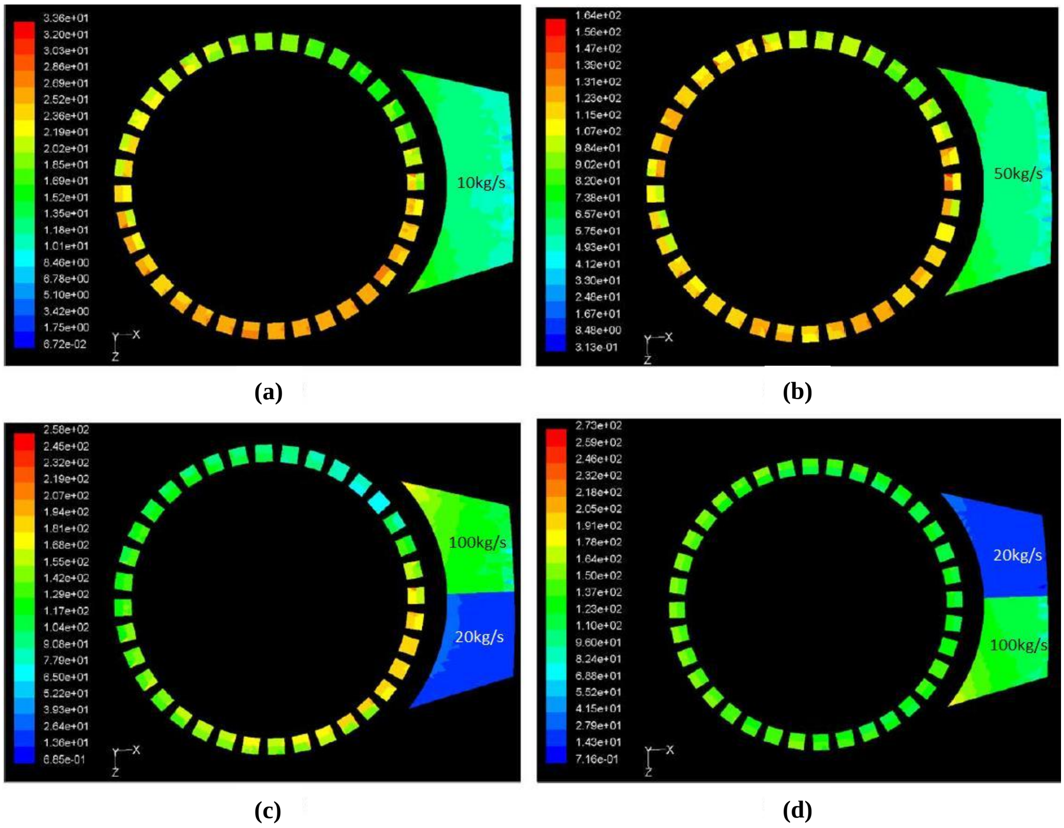

Figure 2.6 Contour plots of velocity magnitude (m/s) before and after duct modification (Adapted from Vuthaluru et al., 2005)

Modern power plants are equipped with standard instrumentation that is utilised to monitor the main process variables (temperatures, pressures, flows, etc.) in order to keep power generating units operating safely and within specific operating limits. There is, however, no specific monitoring of actual structural degradation of important components available (Michelis, 2011). The quantity and quality (fineness) of PF supplied to combustion equipment downstream of coal pulverising plants are critical to achieving safe, reliable and efficient combustion. These two key performance indicators are largely dependent on the condition of the pulveriser. Section 2.4 sought to highlight and review condition monitoring techniques employed to enhance industrial processes. The analytical approaches used from a control perspective, as well as the challenges associated thereof, have been briefly outlined. The challenges prohibiting effective online condition monitoring of the pulveriser has also been succinctly described. Additionally, the concept of employing numerical techniques for condition monitoring, pioneered by Rehman et al. (2013), Park et al. (2013) and Vuthaluru et al. (2006), was introduced.

The necessity to develop pulveriser condition monitoring techniques, as reported in the literature, is accentuated and is by far incomplete. Research should, therefore, be aimed at developing pulveriser condition monitoring techniques, with enhanced capabilities, to detect poor pulveriser condition. For the overarching purposes of this study, corroboration between analytical, experimental and numerical approaches encompassing the pulveriser operation will be explored in an attempt to achieve the aim.

Chapter 3: Vertical Spindle Mill Experiments

3.1 An overview of Power Station A

Power Station A is an Eskom coal-fired power station that was decommissioned in 1990 due to an excess amount of power available at the time. As a result of the energy crisis in SA, the power station was recommissioned. Table 3.1 provides a brief overview of the main design features of Power Station A.

Table 3.1 An overview of Power Station A design features

Coal Quality	**Design**		
Calorific Value	19.46 – 21.88 MJ/kg		
Ash	18.8 – 25.92 %		
Total Moisture	9.76 %		
Pulveriser Plant			
Manufacturer	**Unit**	**Type**	
Babcock and Wilcox	1,2,3,4,6	Ball and ring	
Loesche	5	Tyre and table	
Boiler Plant			
Unit	1,6	2,3,4	5
Manufacturer	Babcock and Wilcox		Steinmuller
Type	Tower	Elpaso	Elpaso
Steam flow	770 ton/hr		828 ton/hr
Firing type	Front and rear wall		Front wall
Final steam temperature	540 ^{o}C		
Final steam pressure	11 MPa		
Turbine Plant			
Manufacturer and Speed	M.A.N, 3000 rpm		
Heat Extraction Plant			
Unit	1,2,3,4	5	6
Cooling tower type	Wet	Dry (direct)	Dry (indirect)

3.2 Design specifications of a commercial-scale pulveriser

Each of the six coal-fired boilers at Power Station A is fitted with six pulverisers. The boiler of each unit was designed to achieve a maximum steam flow rate of 218 kg/s with four pulverisers in service. This makes provision for one pulveriser to be on standby for emergencies and the other for maintenance. However, due to frequent variation in the coal quality as well as the age of the pulverisers, five pulverisers are currently required to be operational to achieve maximum steam flow.

For the purpose of this dissertation, design details will only be supplied for the Vertical Spindle Mill (VSM) ball and ring type which are fitted to units 1 - 4 and 6 at Power Station A. Given that thirty of these pulverisers are identical, the specifications for one are succinctly outlined in Table 3.2.

Table 3.2 VSM (ball and ring) design specifications

Pulveriser Specification	
Type	8.5E VSM (ball and ring)
Number per boiler	6
Nominal capacity	28.8 ton/hr
Classifier type	Static
Number of classifier blades	18
Rotating throat speed	40 rpm
Number of throat vanes	72
Angle of throat vanes	60 degrees
Grinding ball dimensions, quantity	730 mm, 9
Number of PF outlet pipes, outer diameter	2, 560 mm
Number of primary air inlet ducts	2
Height of pulveriser	5333 mm
Diameter of pulveriser body	3175 mm
Classifier diameter	2895 mm

Each pulveriser is supplied with primary air from a designated primary air fan. The mass flow rate of primary air input to the pulveriser is controlled using a louvre damper located upstream of the pulveriser. Figure 3.1 outlines the major air flow streams, as well as the flue gas path at Power Station A. Air temperatures and flow rates depicted, are indicative of normal operating conditions. The pulverisation process has been described in detail in Chapter 1, section 1.2.3.

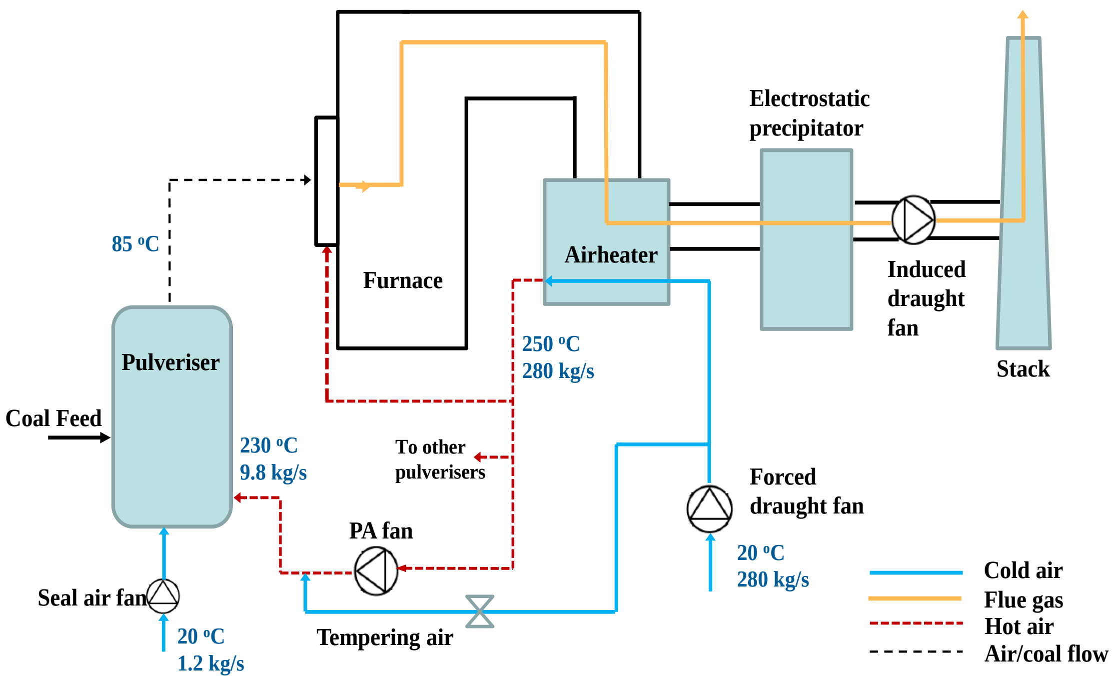

Figure 3.1 Process flow schematic illustrating air and flue gas path of Unit 4 at Power Station A

The temperature at which the primary air enters the pulveriser ranges from 220 °C to 250 °C. Drying of pulverised coal causes a significant reduction in temperature across the pulveriser resulting in the temperature at which the air/coal mixture exits the pulveriser to range from 70 °C to 90 °C. In order to maintain a safe air/coal exit temperature, a supply of cold tempering air is available from the forced draught (FD) fan. The path of the primary air and tempering air supplied to the pulverisers were outlined in Figure 3.1.

Additionally, a list of measured and unmeasured pulveriser process variables at Eskom coal-fired power plants is succinctly summarised in Appendix A.

3.3 Experimental investigation

A thorough literature review highlighted several process variables as significantly influential in the coal pulverisation process. In an attempt to facilitate further understanding, and moreover, quantify dependant variables accurately, selected experimental investigations were performed. The ensuing sections, presenting the experimental work conducted, have been divided into three parts. Each part comprehensively describes the test performed, the test locations, measuring instruments employed, test procedures engaged as well as a discussion of the results attained.

3.3.1 Primary air flow traverse

The quantity of air supplied to the pulveriser is calculated by employing the difference in static pressure measured before and after an orifice plate located in the ducting between the primary air fan and the pulveriser. The primary air duct carrying the air subsequently splits into two equal ducts prior to entering the pulveriser. An air flow traverse test was conducted on pulveriser 4A to accurately ascertain the quantity of primary air (and associated temperature) supplied to the pulveriser in relation to the DCS recorded value.

3.3.1.1 Measurement and sampling point location

For the primary air flow measurement, existing measurement points were located on each duct supplying the pulveriser. A three dimensional view of the primary air duct highlighting the location of the measurement points is presented in detail in Figure 3.2. Primary air flow traverse tests were conducted for the left hand (LH) and the right hand (RH) ducts. The LH and RH ducts, as well as the measurement point location on each duct, are identical. All four measurement points that were available on each duct were utilised for the traverse measurement.

When performing an air flow traverse, British Standard (BS) 15259:2007 recommended that several measurements be taken across the cross sectional area of a duct to improve the accuracy of the traverse measurement. Additionally, a prerequisite for rectangular ducts demands the division of the cross sectional area of the measurement plane into equal segments. The centre of each segment was then identified as the sampling location. Furthermore, measurements of pressure and temperature must be recorded simultaneously at each sampling location.

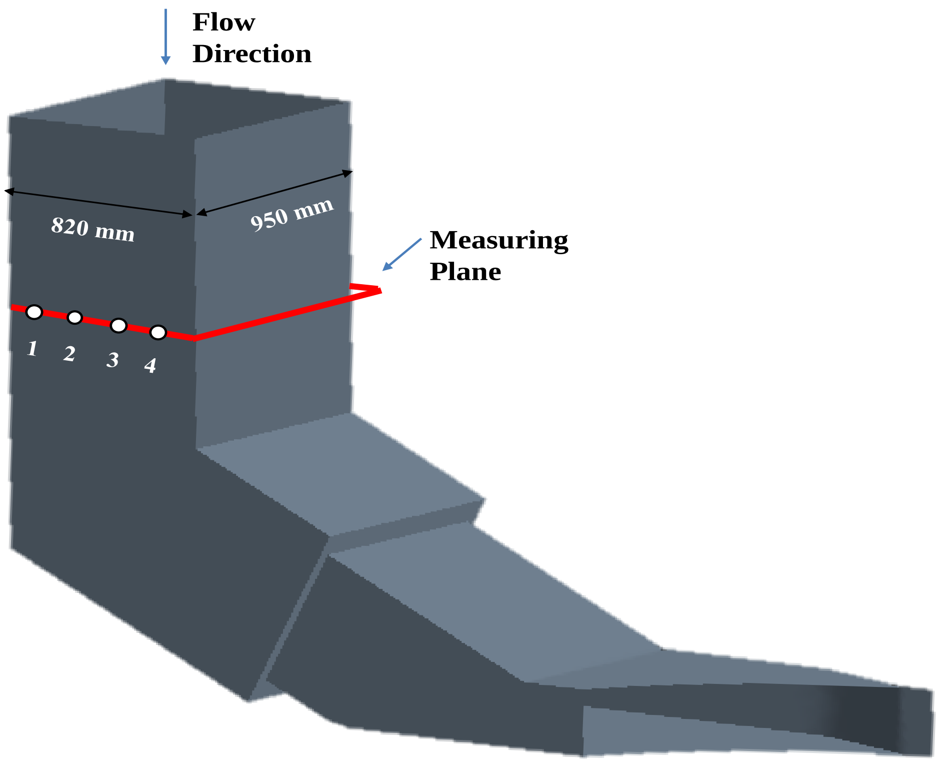

Figure 3.2 Perspective view of LH primary air duct revealing location of traverse sampling points

The size of the duct, as well as the position of the existing measurement points, dictated whether equal sampling segments could be attained. In the case of the primary air duct, it was not possible to achieve equal square segments for each sampling location. Figure 3.3 schematically illustrates the traverse measurement plane created over the cross sectional area of the LH primary air duct. The shaded region highlights the sampling segment created. The intersections of orange dotted lines indicate a sampling point for the respective measurement point. The measuring instrument insertion depth required for each sample point was subsequently calculated. Five sampling points were created for each of the four measurement points, fulfilling the value of at least four sample points per measurement point as recommended in BS 15259:2007. The measurement plane for the RH duct is identical and is therefore not presented.

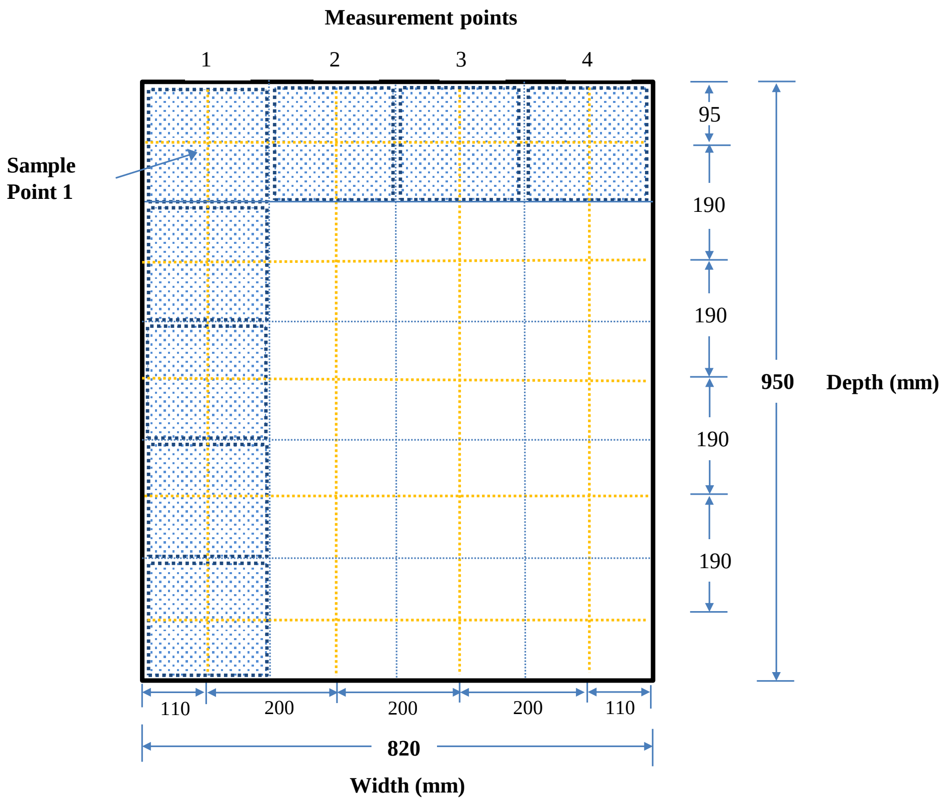

Figure 3.3 Schematic of the cross sectional area of LH primary air duct illustrating the sampling point locations

3.3.1.2 Measurement instrumentation

Figure 3.4 succinctly describes the L-type Pitot static tube which was employed to measure the static pressure and the total pressure in the primary air duct. The dynamic pressure (velocity pressure) was then calculated as the difference between these two pressures sensed in the primary air duct. The dynamic pressure (ΔP) can be measured directly by using a differential pressure manometer as shown in the illustration (Figure 3.4). When the Pitot static tube was inserted into the fluid stream, the total pressure measurement port was placed in the direction of the fluid flow, and the static pressure measurement ports were aligned perpendicular to the flow direction. For the primary air temperature measurement, a separate thermocouple was attached the Pitot static-tube during the traverse.

Instrument calibration certificates for the L-type Pitot-tube and digital thermometer are presented in Appendix B.

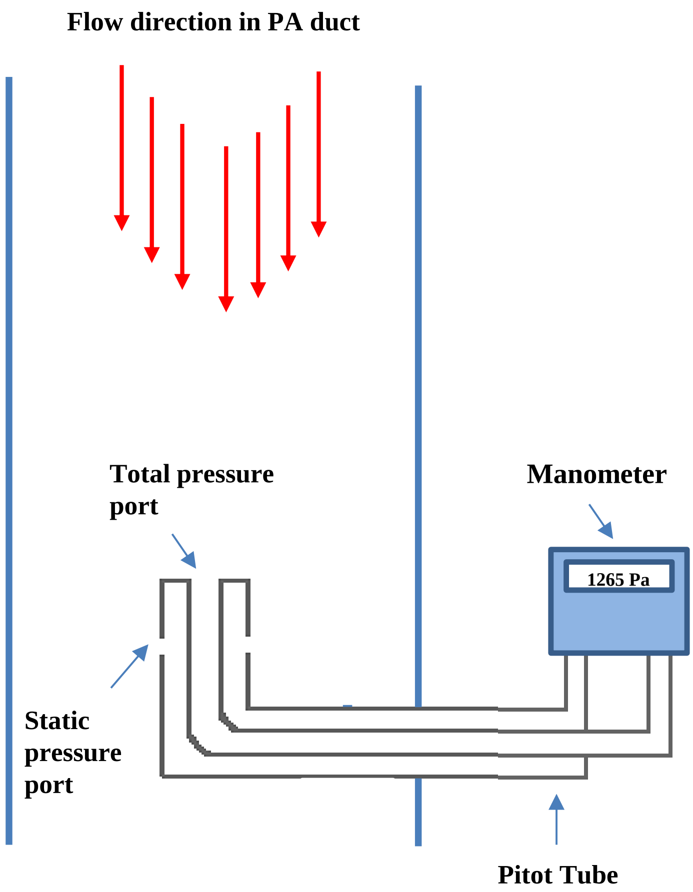

Figure 3.4 Schematic illustration of the L-Type Pitot used to measure the total pressure and static pressure in the primary air duct (Drawing is not to scale)

3.3.1.3 Measurement results

At each sample point (depicted in Figure 3.3), the static pressure, dynamic pressure (Δp) and temperature were measured. For constant density fluids, given (Δp) and density (ρ), Benedict (1977) provides a relationship to calculate the velocity of air (v_{air}) from the measured data, as indicated in Equation 3.1.

$$\frac{\Delta p}{\rho} = \frac{1}{2}\, v_{air}^2$$

$$v_{air} = \sqrt{\frac{2\Delta p}{\rho}} \tag{3.1}$$

Maharaj (2014) provides a relationship, based on the ideal gas law, to calculate the local air density at test conditions by employing the standard values of temperature and pressure, as highlighted in Equation 3.2.

$$\rho_2 = \rho_1 \times \frac{P_2}{P_1} \times \frac{T_1}{T_2} \tag{3.2}$$

Where condition 1 refers to air at standard temperature and pressure (STP) and condition 2 is air properties recorded during the test. The STP values employed for air were as follows:

ρ_1 = 1.293 kg/m^3

P_1 = 101 325 Pa

T_1 = 273.15 K

The mass flow rate of a fluid is delineated as the mass of fluid passing a point in the system per unit time. Benedict (1977) provided a relationship to approximate the mass flow rate of fluids in a stream by the product of the density, measured velocity (v_{air}) and the segment area ($A_{segment}$), as described in Equation 3.3. The sum of the mass flow rates calculated for each segment equates to the total mass flow rate in the duct.

$$\dot{m}_{air} = \rho \times A_{segment} \times v_{air} \tag{3.3}$$

As a significant amount of data was measured and calculated during the traverse, measured data and calculated results will only be presented for the LH duct, measurement point 1. A full report of measured data and calculated results for all sampling points can be viewed in Appendix C. Table 3.3 and Table 3.4 present the measured and calculated results determined for the LH primary air duct measurement point 1.

Table 3.3 Measured data for measurement point 1, LH Duct

Duct Depth (mm)	P_{static} (Pa)	Δp (Pa)	$T_{measured}$ (°C)
95	2532	19.68	24.70
285	2755	20.67	25.50
475	2986	19.61	24.60
665	1983	20.58	25.20
855	2485	19.88	24.90

Table 3.4 Calculated results for measurement point 1, LH Duct

Duct Depth (mm)	ρ (kg/m^3)	v_{PA} $(\mathrm{m/s})$	$A_{segment}$ (m^2)	$\dot{m}_i$ $(\mathrm{kg/s})$	$\sum_{i=95mm}^{855} \dot{m}_i$ $(\mathrm{kg/s})$
95	1.02	6.19	0.039	0.253	1.280
285	1.02	6.34	0.039	0.259	
475	1.03	6.16	0.039	0.254	
665	1.01	6.35	0.039	0.258	
855	1.02	6.22	0.039	0.255	

From the data calculated for measurement point 1, it was evident that the velocity is appreciably constant throughout the duct depth. This resulted in a uniform mass flow rate in each segment, as displayed in Table 3.4.

3.3.1.4 Summary and Discussion of primary air flow results

The primary air flow rate, as well as its temperature, is measured by fixed plant instrumentation. This allows for continuous monitoring of these parameters while the pulveriser is operational. Since the fixed primary air flow rate plant instrumentation is located before the primary air duct splits, it measures the total primary air flow rate. Therefore, the sum of the measured primary air flow rates in the LH and RH duct must be computed to compare with the value logged by the

DCS. A summary of the primary air flow traverse measurements is provided in Table 3.5.

Table 3.5 Summary of primary air flow traverse measurements

	Units	LH Duct	RH Duct
ρ_{avg}	kg/m^3	1.024	1.025
μ_{PA}	Pa.s	1.84e-05	
$v_{PA,\ avg}$	m/s	6.19	6.09
$T_{measured}$	^{o}C	25.2	25.0
T_{DCS}	^{o}C	24.72	25.38
$\dot{m}_{PA,\ measured}$	kg/s	4.94	4.86
$\dot{m}_{PA,\ measured,\ total}$	kg/s	9.80	
$\dot{m}_{PA,\ DCS}$	kg/s	10.5	
Difference	%	7	

The primary air flow traverse test was performed for one primary air flow rate ($\dot{m}_{PA,\ DCS}$ = 10.5 kg/s). The primary air flow rates calculated for the LH and RH duct were within 1.6 % of each other. The similarity between the primary air flow measured in the LH and RH ducts suggests equal air flow distribution at the entrance to the pulveriser. A comparison of the measured and DCS recorded value for the overall primary air flow rate revealed a discrepancy of 7 %. This may be attributed to the DCS recorded value excluding any air leakage from the primary air duct between the DCS measurement point and the traverse location point. The traverse measurement point location is closer to the pulveriser inlet. Therefore, the measured primary air flow rate was assumed as the true mass flow rate of primary air entering the pulveriser, given that the tests were performed using calibrated instrumentation and in accordance with best practice guidelines. The results tabulated in Table 3.5 enable a correction factor to be applied to the DCS recorded primary air flow rate value for all further calculations.

Additionally, the dissimilarity in air temperature between the measured value and the DCS recorded value for the LH and RH ducts were, on average, 0.43 ^{o}C and was therefore considered to be negligible, thereby indicating the DCS recorded values for temperature to be sufficiently accurate.

3.3.2 Global pulveriser performance tests

The second part of the experimental tests conducted involved a global analysis of the pulveriser performance. Pulveriser performance tests and measurements were performed on pulveriser 4A. The global pulveriser performance tests completed comprised of the following sub-tests:

- Coal quality analysis of raw coal fed to the pulveriser.
- Measurement of raw coal temperature.
- Measurement of seal air mass flow rate and temperature.
- Measurement of PF moisture content and PF mass flow rate using isokinetic PF sampling methods.
- Measurement of raw coal mass flow rate using the Drop Ball Method (DBM).
- Measurement of the pulveriser external body temperature.
- Measurement of the ambient air velocity and temperature at the pulveriser location.

These tests were conducted simultaneously to obtain a comprehensive analysis of the performance of the pulveriser. Additionally, the pulveriser performance tests were performed in triplicate over a three day period.

3.3.2.1 Measurement locations and test description

For a coal quality analysis, raw coal samples were obtained from raw coal sampling ports. These sampling ports are located 300 mm above each raw coal feeder, as highlighted in Figure 3.5. The measurement of the raw coal temperature was also taken at this location.

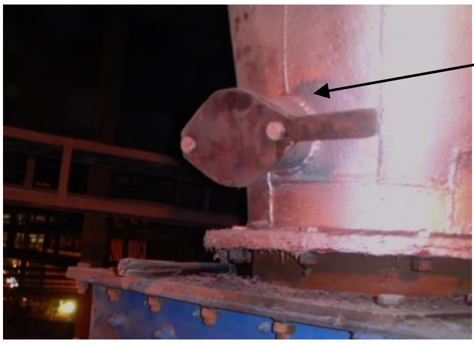

Figure 3.5 Digital image highlighting the location of raw coal sampling port at coal feeder, 4A

International Organisation for Standardisation (ISO) 18283: 2006 was used as a guide for the raw coal sampling. Representative raw coal samples were obtained by collecting approximately 10 kg of raw coal every 20 minutes over a four hour test period. Approximately 120 kg of coal was sampled for each of the three test days. Samples were placed in a plastic bag and sealed at the sampling point location to maintain the integrity of the sample.

Van Wyk (2008) explains that a proximate analysis is a chemical analysis in which the four main constituents of coal are identified. These four constituents are water (moisture content, as %), mineral impurity (ash content, as %), volatile matter (volatile content, as %) and fixed carbon (carbon content, as %) (Van Wyk, 2008). Eskom power stations have coal laboratories which perform proximate analyses of coal. The twelve raw coal samples collected each day were transported to the onsite coal laboratory at Power Station A for a proximate analysis. The analyses were conducted in accordance with Eskom approved methods (refer to Appendix A). Monthly composite samples are sent from Eskom power utilities to RT&D for an ultimate[VII] analysis, however in this study, data obtained from the proximate analysis proved sufficient for the intended mass and energy balance application.

Each pulveriser has a designated seal air fan. The seal air fan takes suction from ambient air and is located within close proximity to the pulveriser. It is considered

[VII] An ultimate analysis is more comprehensive than a proximate analysis and provides the elemental composition of oxygen, hydrogen and nitrogen present in the coal tested.

impractical to have fixed flow meters to measure the seal air mass flow rate and temperature. Hence, there was no seal air mass flow rate or temperature indication available on the DCS. Additionally, no measurement points were available on the seal air duct to perform an air flow traverse test. In such a case, the mass flow rate of seal air can be calculated by measuring the air flow velocity across the suction side of the seal air fan system (Burgess et al., 2014). Consequently, velocity measurement points were created on the suction side of the seal air fan and the approach employed in this undertaking was analogous to the method outlined for the primary air flow traverse measurement. However, in this instance, the divisions of the seal air fan suction area were calculated to ensure the measurement point fell precisely at the midpoint of each segment, as schematically presented in Figure 3.6. Twenty velocity measurement points were created which are represented as red dots on the illustration (Figure 3.6). A preliminary inspection of the suction area revealed it to be free of obstructions that could potentially affect the seal air suction velocity measurements. Since the seal air fan takes suction from ambient air, the temperature of the seal air was at ambient temperature. The temperature of the ambient air was measured at the seal air fan suction point.

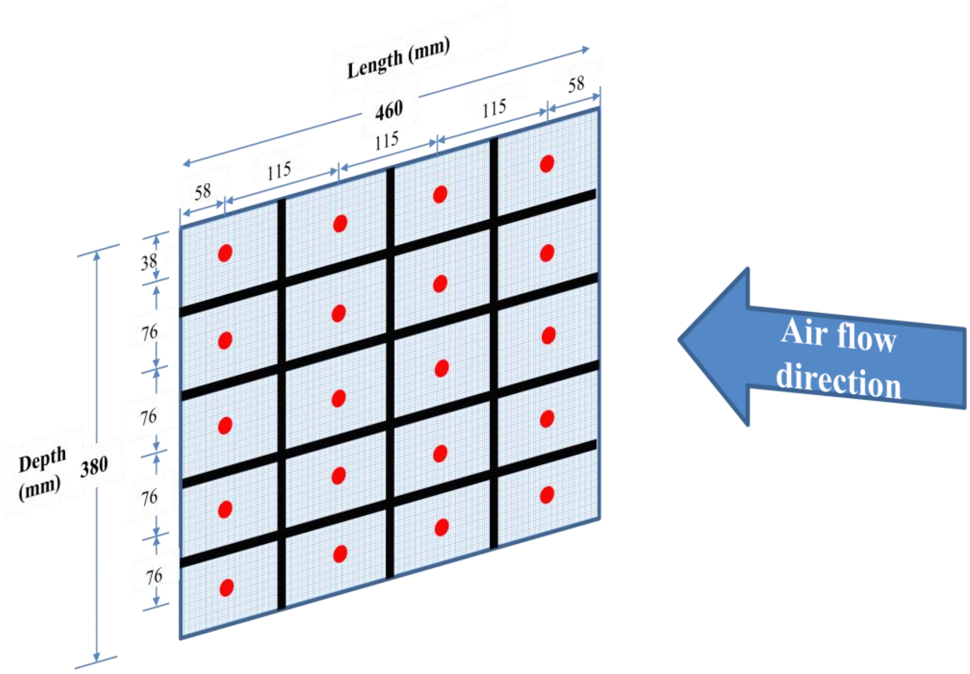

Figure 3.6 Cross section of seal air fan suction area illustrating the velocity measurement point locations (Drawing is not to scale)

For the measurement of the PF mass flow rate and moisture content, isokinetic[VIII] PF sampling was performed. PF sampling is routinely performed at Eskom power stations and measurement points were available. During this sampling method, the pulveriser was required to be operated on manual mode to circumvent variations in raw coal feed flow. Sampling takes place on the PF pipework between the pulveriser and the PF burners. Due to stratification in pipe bends as well as in horizontal sections of the PF pipework, best practice guidelines recommend that the locations of sample ports be on the vertical rise of the PF pipe. The sample ports available satisfied these recommendations. Depending on the VSM configuration, there are between two and four PF pipes that exit directly from a VSM. These pipes split further into four and eight, respectively. In the case of pulveriser 4A at Power Station A, PF is discharged into two PF pipes, following which each pipe splits into two. Therefore four PF pipes had to be sampled. PF sampling in all four pipes permits a PF mass balance to be completed in order to

[VIII] Isokinetic sampling refers to a process of sampling where the PF sample is extracted with minimal disturbance to the air flow in a PF pipe. The isokinetic sampler extracts coal particles at the same velocity as that in the PF pipe.

compute the total PF mass flow rate supplied from the pulveriser. The PF mass flow rate was then compared to the mass flow rate of raw coal entering the pulveriser (established through the method highlighted in the following paragraph). The positions of the PF sample extraction points within a PF pipe depend on the diameter of the PF pipe and are determined in accordance with BS 893:1978. Figure 3.7 displays the 32 locations in the cross sectional area of a PF pipe from where the PF samples were extracted. PF samples were obtained and graded according to Eskom standard PF sampling procedure (refer to Appendix A). Additionally, the air/coal temperature in each PF pipe was measured during PF sampling.

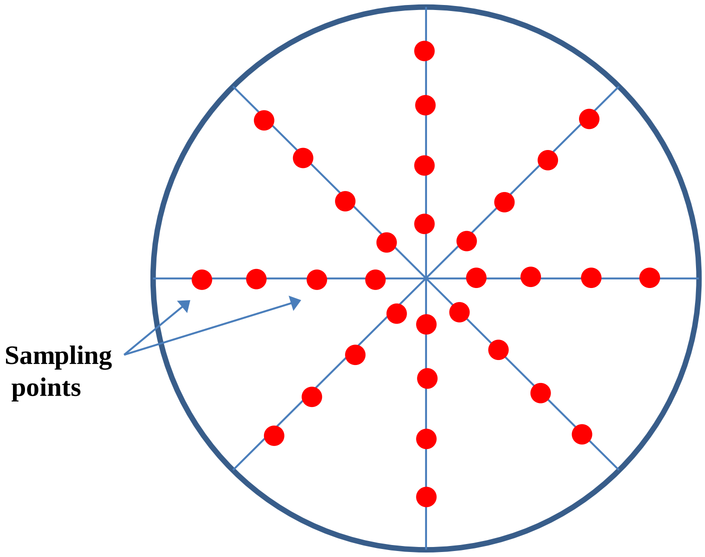

Figure 3.7 Cross section of PF pipe illustrating 32 sampling point locations

Niemczyk et al. (2012) and Pradeebha et al. (2013) mention that it is difficult to measure the raw coal flow rate into a pulveriser. Furthermore, raw coal flow rate approximation methods have not been explicitly explicated in literature. Aside from a few Eskom power stations that make use of gravimetric[IX] raw coal feeders, the majority of power stations have volumetric raw coal feeders. The raw coal mass flow rate approximation method employed by plant performance teams at

[IX] Gravimetric feeders compensate for the variation in bulk density of coal and deliver a fixed weight of coal to the pulveriser. The gravimetric feeder’s ability to accurately weigh the coal makes it significantly better than volumetric feeders.

the power utilities that use volumetric coal feeders is the DBM. Since this test is usually performed in conjunction with isokinetic sampling, measurement ports were available. The location of the measurement port is highlighted in Figure 3.8. Given that there is no procedure available to explain the method, a description of the test is attempted hereafter.

Consider the DBM technique illustrated in Figure 3.8. Coal flow is directed from the storage bunker to the feeder. A wooden ball, approximately 40 mm in diameter (to resemble a piece of raw coal) is attached to a 4000 mm length string. The wooden ball is then inserted through the port hole to the midpoint of the duct. Given that the coal flow is influenced by gravity, the wooden ball is allowed to travel freely through the raw coal chute. Once 500 mm of the string enters the duct, a stop watch begins recording the time (when point A enters the port hole). As the length of the string is marked accordingly, the time is recorded until 3000 mm of the string has fully entered the duct (when point B enters the duct). This time essentially indicates the duration (in seconds) that the wooden ball travelled a height of 3000 mm. Since the dimensions of the duct are known, the volume of the duct can be calculated. By utilising the time measured and standard techniques, the volumetric flow rate of the coal can be obtained. In addition, a sample of the coal was collected to ascertain the coal bulk density experimentally (refer to Appendix D), following which the coal mass flow rate may be calculated. The coal sample required for the bulk density test was obtained further downstream in the duct at the location highlighted previously (Figure 3.5).

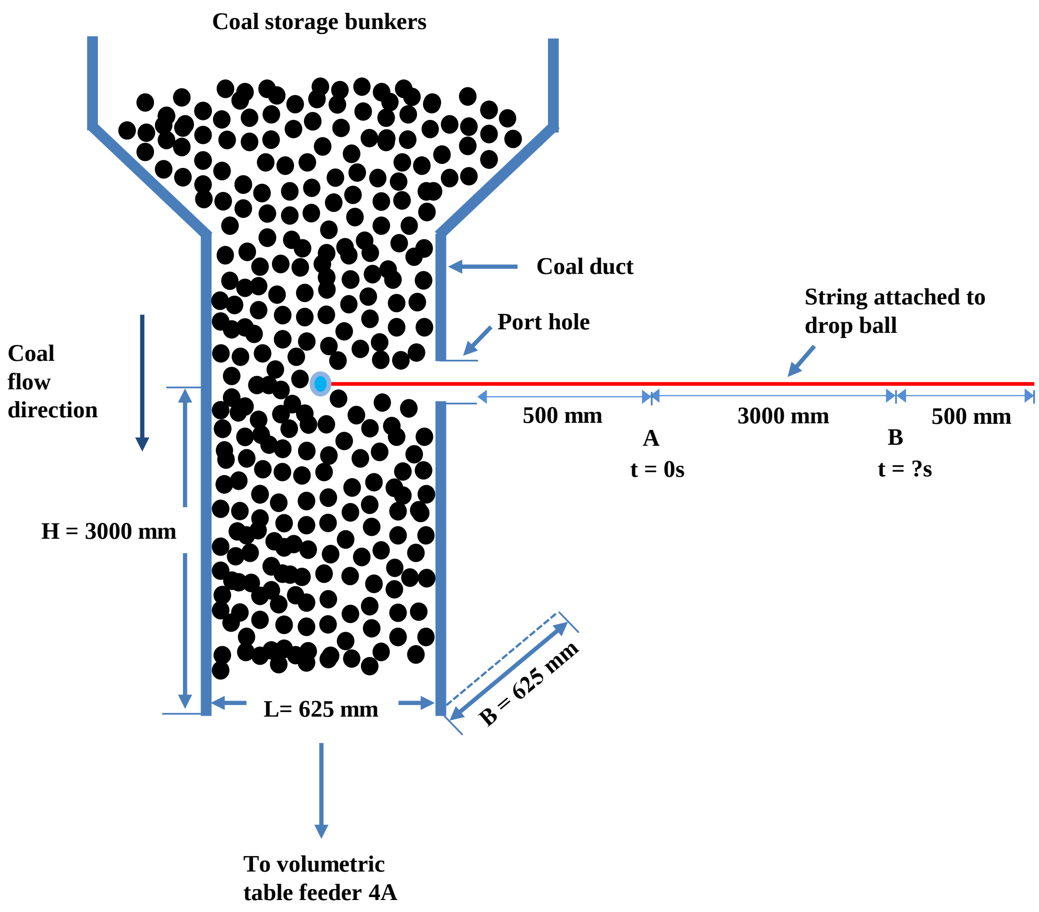

Figure 3.8 Illustration of DBM used at the raw coal duct between the coal storage bunkers and the coal feeder (Drawing is not to scale)

Energy losses through conduction, convection and radiation are common in a pulveriser system (Kapakyulu, 2007). In this study, only convective heat loss to the environment was considered. Heat flows from an area of higher temperature to an area of reduced temperature. Therefore, in the case of the pulveriser, heat transfers from the inside of the pulveriser through the pulveriser casing to the external environment which was at ambient conditions. The measurement of the ambient air temperature and velocity was measured in the vicinity of the pulveriser. Furthermore, the temperature of the external pulveriser casing was measured. In this instance, several measurements were taken along the vertical height of the pulveriser, as identified in Figure 3.9, at points marked A to H. These measurements were recorded in order to calculate the overall heat transfer coefficient required to estimate the convective heat loss to the environment (Incropera et al., 2006).

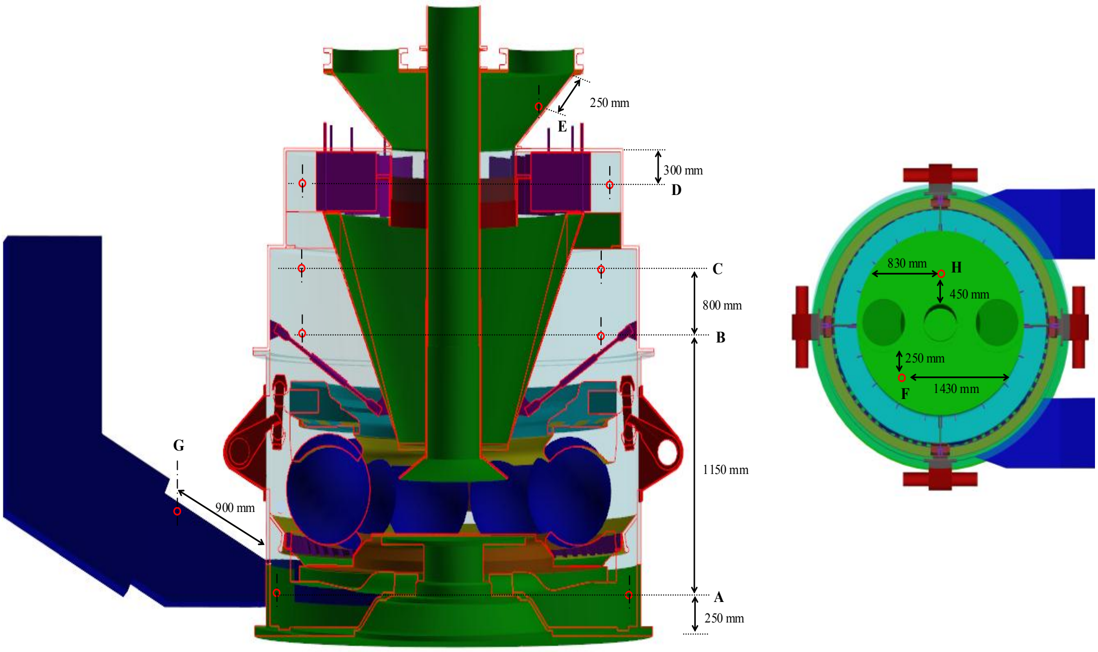

Figure 3.9 Schematic identifying the location of the external pulveriser casing temperature measurement points, A to H

3.3.2.2 Measurement instrumentation

In order to determine the seal air mass flow rate, the seal air velocity had to be measured. A vane anemometer was used to measure the air velocity across the seal air fan suction plane (depicted in Figure 3.6). In principle a vane anemometer functions like a windmill, air flowing pass the vanes causes rotation of the spindle at a rate that is proportional to the velocity of the air passing it (Mohanty, 1994). Furthermore, the thermo-vane anemometer was also used to measure the ambient air temperature and velocity in the vicinity of pulveriser 4A.

For the raw coal and pulveriser casing temperature measurement, an infrared thermometer was used. The type and model of the vane anemometer, as well as the infrared thermometer employed is identified in Figure 3.10a and Figure 3.10b, respectively. Instrument calibration certificates for the thermo-vane anemometer and the infrared thermometer may be viewed in Appendix B.

(a) (b)

Figure 3.10 Thermo-vane anemometer (a) and infrared thermometer (b) used in the global pulveriser performance tests

In order to determine the PF mass flow rate and moisture content, isokinetic sampling was performed to obtain a PF sample following which assessment of the sample was undertaken. The isokinetic sampling instrumentation architecture is schematically illustrated in Figure 3.11. An isokinetic sampling probe is configured such that it allows for the measurement of the static pressure in the measurement probe and in the PF pipe being measured. The static differential pressure between these two pressures is measured using a U-tube manometer. Isokinetic sampling conditions is considered to be achieved when the differential pressure reading on the U-tube manometer is 0 Pa. This balance in pressure was realized by regulating the extraction pressure in the centrally located extraction tube using compressed air at approximately 600 kPa. Additionally, the extraction tube provides a means to obtain the PF sample (cross section of probe head depicted in Figure 3.11). To obtain a representative sample, a guide plate was used to direct the sampling probe to each of the 32 sampling points locations (as highlighted in Figure 3.7) along the cross sectional area of the PF pipe.

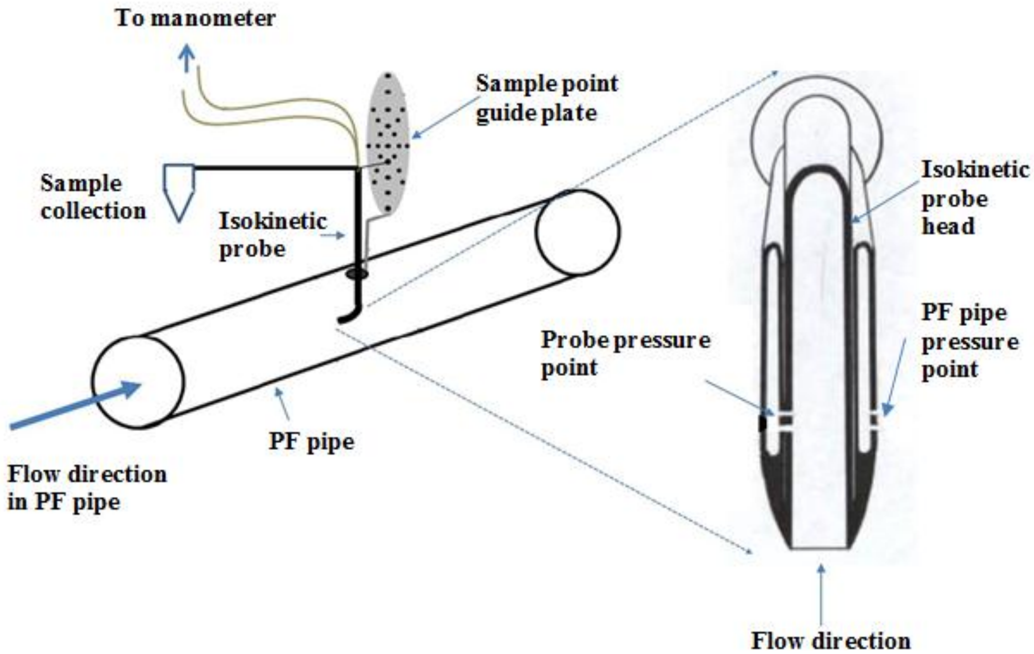

Figure 3.11 Isokinetic sampling system architecture (Adapted from Van Der Merwe, 2013)

For the DBM test, the only resources required were wooden balls, string and a stopwatch.

3.3.2.3 Global pulveriser performance test results

The global pulveriser performance tests comprised of several sub-tests (highlighted in section 3.3.2). Apart from the seal air mass flow rate determination, these sub-tests were performed in triplicate, over a three day period, in order to assess the variability of the measured results. Due to the large volume of data measured and calculated over the three day test period, measured and calculated results will only be presented for day one. Albeit a brief summary is provided in section 3.3.2.4, a full report of measured and calculated results for day two and three can be viewed in Appendix C.

A proximate analysis was performed on the raw coal composite sample. Table 3.6 displays the measured parameters, reported on an 'air dried' basis.

Table 3.6 Proximate analysis results, day one

Measured Parameter	Units	Value
Calorific Value	MJ/kg	20.63
Total moisture	%	8.76
Volatiles	%	21.61
Ash	%	31.30
HGI	-	57
AI	-	161

For the seal air mass flow rate, the velocities measured at each point (highlighted in Figure 3.6) was used to calculate the average air velocity over the seal air fan suction area. Following which the mass flow rate of the seal air was calculated by employing Equation 3.3. The local density at test conditions was established by employing the relationship described in Equation 3.2. These tests were undertaken in triplicate on day one to determine the reproducibility of the results. The measured and calculated results are presented in Table 3.7.

Table 3.7 Measured data and calculated results for the seal air mass flow rate, day one

Test number	$\boldsymbol{\rho}$ $(\mathbf{kg}/\boldsymbol{m}^{\mathbf{3}})$	$\boldsymbol{v}_{\boldsymbol{SA},\ \boldsymbol{measured}}$ $(\mathbf{m/s})$	$\boldsymbol{A}_{\boldsymbol{SA\ suction}}$ $(\boldsymbol{m}^{\mathbf{2}})$	$\dot{\boldsymbol{m}}_{\boldsymbol{SA},\ \boldsymbol{calculated}}$ $(\mathbf{kg/s})$
01	1.03	6.85	0.175	1.23
02	1.03	7.16	0.175	1.29
03	1.03	6.84	0.175	1.23
Average	1.03	6.89	0.175	1.24

In order to establish the mass flow rate of pulverised fuel exiting the pulveriser as well as the moisture content thereof, isokinetic PF sampling was performed. The isokinetic sampling probe (depicted in Figure 3.11) was used to extract a sample of PF from four PF pipes.

The manufacturer of the isokinetic sampling probe provides a relationship to estimate the mass flow rate of pulverised fuel in each PF pipe sampled, as outlined in Equation 3.4.

$$\dot{m}_{PF,\ calculated} = \frac{M_{PF}}{N \times t} \times \left(\frac{D_{pipe}}{d_{probe}}\right)^2 \qquad (3.4)$$

Where:

M_{PF} = Mass of PF sample extracted (kg)

N = Number of sample points per PF pipe (32)

t = Time sampled at each sample point (15 seconds)

D_{pipe} = PF pipe diameter (387 mm)

d_{probe} = Isokinetic extraction probe diameter (12.5 mm)

Isokinetic sampling was performed according to best practice guidelines, which suggested sampling for 15 seconds at each of the 32 points. Furthermore, 'isokinetic conditions' were maintained by constantly adjusting the suction pressure to ensure the pressure in the PF pipe and the sampling probe was equal.

Presented herein, Table 3.8 provides the measured data and calculated results obtained for the PF mass flow rate. It must be noted that the sum of the PF mass flow rates from each of the four pipes tested has been computed to yield the total PF mass flow rate supplied from the pulveriser.

Table 3.8 Measured data and calculated results for PF mass flow rate, day one

PF Pipe	M_{PF} (kg)	N	t (s)	D_{pipe} (mm)	d_{probe} (mm)	$\dot{m}_{PF,\ calculated}$ (kg/s)	$\sum_{i=1}^{4} \dot{m}_{PF,\ calculated}$ (kg/s)
1	0.768	32	15	387	12.5	1.53	6.76
2	0.917	32	15	387	12.5	1.83	
3	1.012	32	15	387	12.5	2.02	
4	0.688	32	15	387	12.5	1.37	

For the PF moisture content analysis, Eskom standard procedure (refer to Appendix A) aligned to conform to BS 893:1978 was diligently applied. The extracted PF sample (from each PF pipe) was reduced to a representative 60 g sample using cone and quartering reduction techniques. Thermal drying was accomplished by placing the 60 g sample in an oven, set at 105 ^{o}C, for 60 minutes. Thus the moisture in PF, expressed as mass fraction, was quantified through weighted difference by employing Equation 3.5. Table 3.9 highlights the measured and calculated results obtained for the PF moisture content analysis.

$$w_1 = \left(\frac{Mass\ of\ sample\ before\ drying - Mass\ of\ sample\ after\ drying}{Mass\ of\ sample\ before\ drying}\right) \quad (3.5)$$

Where:

w_1 = Mass fraction of moisture in PF

Table 3.9 Measured data and calculated PF moisture content results, day one

PF Pipe	Mass of sample before drying (g)	Mass of sample after drying (g)	w_1 (g/g)
1	60	58.50	0.025
2	60	59.40	0.010
3	60	58.41	0.010
4	60	58.79	0.020
		Average	0.016

The second method employed to ascertain the raw coal mass flow rate was the DBM experiment. In order to calculate the raw coal mass flow rate, the time taken for the wooden ball to travel a height of 3000 mm was measured. With the volume of the duct and bulk density of coal known, the mass flow rate of raw coal was approximated using the relationship defined in Equation 3.6.

$$\dot{m}_{coal,\ calculated} = \frac{V_{Duct}}{t} \times \rho_{bulk} \tag{3.6}$$

Where:

V_{duct} = Duct volume (m^3)

t = Recorded drop ball time (s)

ρ_{bulk} = Bulk density of raw coal (kg/m^3)

Table 3.10 presents the measured data and the calculated results for the DBM tests performed at the drop ball location port. In Table 3.10, the length, width and height represented by L, B and H (as depicted in Figure 3.8), respectively, was employed to calculate the volume of the duct. It must be noted that in order to calculate the internal duct volume, the duct wall thickness of 6.32 mm was accounted for. The DBM test was executed in triplicate in order to assess the variability in the measured results.

Table 3.10 Measured data and calculated results for the DBM test, day one

Test number	L (m)	B (m)	H (m)	V_{duct} (m^3)	$t_{measured}$ (s)	ρ_{bulk} (kg/m^3)	$\dot{m}_{coal,\ calculated}$ $(\mathrm{kg/s})$
1	0.63	0.63	3	1.17	183	946.28	6.05
2					174		6.36
3					169		6.55
						Average	6.32

As previously outlined, the DBM test is an approximation method. This necessitated an experimental investigation to be conducted to ascertain the validity of this method in quantifying the raw coal flow rate to the pulveriser. A prerequisite for this brief investigation was a power station that utilised a gravimetric feeder in addition to the port holes on the raw coal duct required to initiate the DBM test. A comparison of the results obtained from the DBM and the gravimetric feeder readings could then be employed to assess the validity of the method. A review of pulverisers within the Eskom Fleet identified two power stations to be suitable, as these stations employ gravimetric coal feeders. However, the necessary port holes required were only available at Power Station B. Therefore, the experimental investigation was concluded at Power Station B. The method employed and results obtained for this investigation is presented in detail in Appendix E.

Finally, the ambient air velocity, as required for convective heat loss calculations, was measured to be 1.9 m/s.

3.3.2.4 Summary and Discussion of the global pulveriser performance test results

Table 3.11 presents a summary of the proximate coal analysis results obtained over the three day test period. For comparison purposes, the coal quality as specified in the boiler design data is presented alongside the current proximate analysis results. It was evident that the ash content and HGI fall outside the prescribed specification, highlighting poor quality coal. As previously discussed, a combination of high ash and low HGI is indicative of pulverisers having to operate with substandard coal quality leading to suboptimal performance. In addition, these results outline that all other parameters of the coal consumed during the tests were in fair agreement with the design specification of the boiler plant. The size of the raw coal tested during the proximate analysis ranged from 3 mm to 40 mm.

Table 3.11 Summary of raw coal proximate analysis results, air dried basis

		Day one	**Day two**	**Day three**	**Design Range**
Measured Parameter	**Units**	**Value**	**Value**	**Value**	**Value**
Calorific Value	MJ/kg	20.63	20.21	20.85	19.46 - 21.88
Total moisture	%	8.76	8.36	8.17	< 9.76
Volatiles	%	21.61	20.89	23.84	18.80 - 24
Ash	%	31.30	31.27	29.08	18.80 – 25.95
HGI	-	57	58	57	> 62
AI	-	161	160	161	< 350

The seal air suction flow velocity was recorded during a series of measurements following which the average velocity was calculated to approximate the total seal air mass flow rate. As outlined in Table 3.7, the average velocities were consistently reproducible highlighting precision and accuracy of the measurements. Evidently, the total primary air mass flow rate (summarised in Table 3.5), in comparison to the seal air mass flow rate (reported in Table 3.7) was significantly higher. However, in determining the seal air mass flow rate, quantification of the total air flow into the pulveriser was achieved, thereby reducing the total number of unknown variables when completing a MMEB. The seal air mass flow was only measured on day one of the test program and a value of 1.24 kg/s was utilised for all calculations in the MMEB model validation in Chapter 4.

Conventional tests such as the DBM and isokinetic PF sampling techniques were employed to establish the raw coal and PF mass flow rate, respectively. Table 3.12 succinctly summarises the results obtained for each of these tests. Relative to the coal mass flow rate results attained through isokinetic sampling, the DBM consistently under-predicted the coal mass flow rate by an average of about 6 %.

Briefly, the results of the DBM investigation conducted at Power Station B (refer to Appendix E), highlighted the discrepancy between the results of the DBM and gravimetric feeder readings to be consistent. Although the DBM under-predicted the coal mass flow rate by an average of 8.74 %, the general trend was noteworthy. The findings of this investigation corroborate the DBM results experienced at Power Station A. The discrepancy obtained can be largely attributed to several assumptions made during the DBM as presented in Appendix E.

Additionally, Table 3.12 highlights the measured moisture content of pulverised fuel to range between 1.5 % and 2.3 %. This is in agreement with the literature as outlined in Chapter 2, section 2.2. Lastly, Table 3.12 depicts the comparison between the DCS recorded value for the pulveriser exit temperature and the PF pipe temperature (average of four pipes), highlighting an average difference of 0.9 ^{o}C. This demonstrates that the fixed plant instrument accurately measures the pulveriser outlet temperature. Although this variance was trivial, MMEB calculations completed in Chapter 4 will employ the value obtained through measurement.

Table 3.12 Summary of DBM and Isokinetic sampling results

Measured Parameter	Units	Day one	Day two	Day three
$\dot{m}_{coal,\ calculated}$	kg/s	6.32	6.46	6.24
$\dot{m}_{PF,\ calculated}$	kg/s	6.76	6.84	6.63
Discrepancy	%	6.51	5.56	5.88
$w_{1,\ average}$	kg/kg	0.016	0.023	0.015
$T_{PF,\ measured,\ average}$	^{o}C	89	87.5	85
$T_{PF,\ DCS}$	^{o}C	88	86.2	84.6
$T_{PA,\ DCS}$	^{o}C	229	225	230

The pulverisation process temperatures measured at various locations have been summarised and tabulated in Table 3.13. The variables T_A to T_H represent the pulveriser external casing temperatures that were measured at the locations highlighted in Figure 3.9. Notably, the temperatures measured over the three day period are comparable. This can be attributed to moderately variable pulveriser operating conditions and coal qualities over the said period.

Table 3.13 Summary of pulveriser temperature measurements

		Day one	Day two	Day three
Description	**Variable**	**$T_{measured}$ (°C)**	**$T_{measured}$ (°C)**	**$T_{measured}$ (°C)**
Raw coal	$\boldsymbol{T}_{coal}$	11	12	9
Seal air	$\boldsymbol{T}_{SA}$	19	22	20.5
Ambient	$\boldsymbol{T}_{amb}$	19	22	20.5
Air plenum	$\boldsymbol{T}_{A}$	173	176	175
Above top ring	$\boldsymbol{T}_{B}$	84	83	86
Below classifier	$\boldsymbol{T}_{C}$	84	83	85
Classifier	$\boldsymbol{T}_{D}$	83	82	82
Outlet plenum Side	$\boldsymbol{T}_{E}$	83	81	84
Pulveriser outlet	$\boldsymbol{T}_{F}$	83	83	82
Primary air inlet duct	$\boldsymbol{T}_{G}$	180	186	181
Pulveriser outlet (2)	$\boldsymbol{T}_{H}$	83	83	82

3.3.3 Static pressure measurements

Lipták (2003) explains that the static pressure of fluids in a stream is generally measured by (1) through taps in the wall, (2) static probes inserted into the fluid stream, or (3) small apertures located on an aerodynamic body immersed in the fluid stream. In a coal-fired power plant, a typical pulveriser has only two static pressure measurement points and these are employed to calculate the static differential pressure across the pulveriser for purposes of pulveriser control. Due to the location of this two wall measurement points, it was not possible to establish an accurate picture of the pressure profile within the pulveriser with these points alone.

An application to install additional wall static pressure measurement test points on one pulveriser was prepared and presented to the Engineering Change Management (ECM) Committee at Power Station A on 29 October 2014. Approval of this test modification, obtained on 18 November 2014, allowed for the installation of ten additional static pressure measurement points along the vertical height of one pulveriser. Of the six VSM (ball and ring) pulverisers installed on Unit 4, the selection of the pulveriser to be utilized for the test purposes was based on the following criteria:

- A VSM (ball and ring) that is usually in service 90 % of unit operation time. This narrowed down the options to pulveriser 4A and 4E. The reason for this requirement was to ensure a high probability that the pulveriser would be in service for test purposes. For instance, pulveriser 4B and 4D, 4C and 4F supply the middle and top burner rows of the furnace respectively and are in operation interchangeably for about 75 % of unit operation time.
- 4A had recently been overhauled and was replaced with new rings and nine new grinding balls. This prompted the selection of pulveriser 4A for test purposes so that the static pressure profile in a 'new' pulveriser could be attained as opposed to a worn pulveriser.

The static pressure tapping points were planned for and installed in February 2015, the date of which was selected based on the availability of pulveriser 4A and boiler maintenance personnel.

3.3.3.1 Measurement locations

Fox et al. (2009) mention that for internal fluid flow the transition of the flow regime to turbulence occurs for Reynolds numbers (*Re*) larger than 2300. Consider the cross section of the LH primary air duct depicted in Figure 3.3. The cross sectional area and hydraulic diameter may be computed as highlighted in Equation 3.7 and Equation 3.8, respectively.

$$A = 0.82\,m \times 0.95\,m = 0.779\,m^2 \tag{3.7}$$

$$d_h = \frac{4A}{P_w} = \frac{4 \times 0.779}{2(0.82+0.95)} = 0.883\,m \tag{3.8}$$

Typical properties of primary air recorded and calculated during the primary air traverse test were summarised in Table 3.5. Hence, *Re* may be approximated as outlined in Equation 3.9.

$$Re = \frac{\rho_{corrected,\ avg} \times v_{PA,\ avg} \times d_h}{\mu_{PA}} = \frac{1.024 \times 6.19 \times 0.883}{1.83 \times 10^{-5}} = 3.058\ \times 10^5 \qquad (3.9)$$

$Re\ > 2300$, therefore the viscous flow regime dominating the pulveriser domain may be categorised as being turbulent.

Shaw (1960) investigated the influence of tapping point shape and dimensions on the static pressure measured by determining the error in static pressure measurements of incompressible turbulent fluid flow. The results demonstrate that the flow profile close to the wall is disturbed by the static tapping point hole (Shaw, 1960). This phenomenon is schematically illustrated in Figure 3.12.

The results of Shaw (1960) highlight that the error in static pressure measurements is the least when the following conditions are followed:

- The tapping point diameter, d, (identified in Figure 3.12), must be as small as possible, be perpendicular to the flow direction and be greater than 0.5 mm to avoid blockages.
- The tapping points must be free from burrs and as smooth as possible.
- To counter-effect the flow deflection near the hole, the tapping point length to diameter ratio should meet the following criteria: 1.5 < (L/d) < 6.

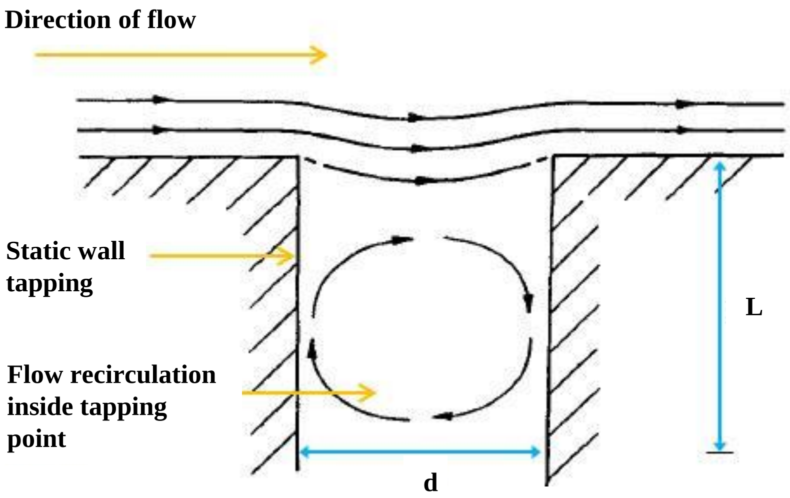

Figure 3.12 Illustrative representation of the flow behaviour at a typical static pressure tapping point (Adapted from Shaw, 1960)

Benedict (1977) mentions that although square-edged holes created for static pressure measurement introduce small positive errors to the static pressure sensed, radius-edged holes introduce additional positive errors whereas chamfer-edged holes introduce small negative errors. A range of geometries and orientations displaying the effect of orifice edge form on the resultant static pressure sensed in a fluid stream is depicted in Figure 3.13. Square-edged holes are indicated as the reference form.

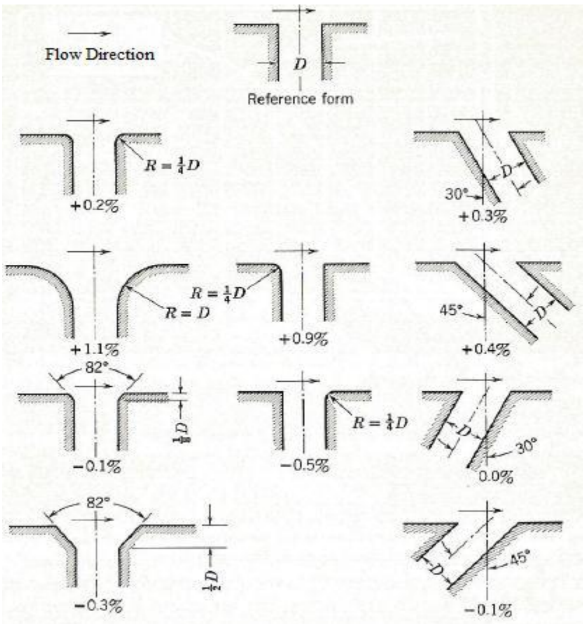

Figure 3.13 The effect of orifice edge form on static pressure measurements (Adapted from Benedict, 1977)

The recommendations provided by Shaw (1960) and Benedict (1977) were applied as a guideline for the additional tapping points that were installed on pulveriser 4A. Aside from recirculation in certain areas within the pulveriser, the flow direction is predominantly from the bottom to the top.

For the static pressure measurement, 9 mm square-edged holes were drilled by a skilled labourer through the pulveriser walls. The thickness of the casing was measured to be 35 mm. The (L/d) ratio was calculated to be 3.89 hence, the recommended value stipulated by Shaw (1960) was satisfied. The holes drilled were inspected to ensure that they were free of any obstructions that could negatively influence the static pressure measurement. Half inch steel nipples were subsequently welded onto the external surface of the pulveriser casing, following which a half inch ball valve was fitted to the free end of the steel nipple. Each of the ten static pressure tapping point installations was identical and the architecture followed is schematically presented in Figure 3.14.

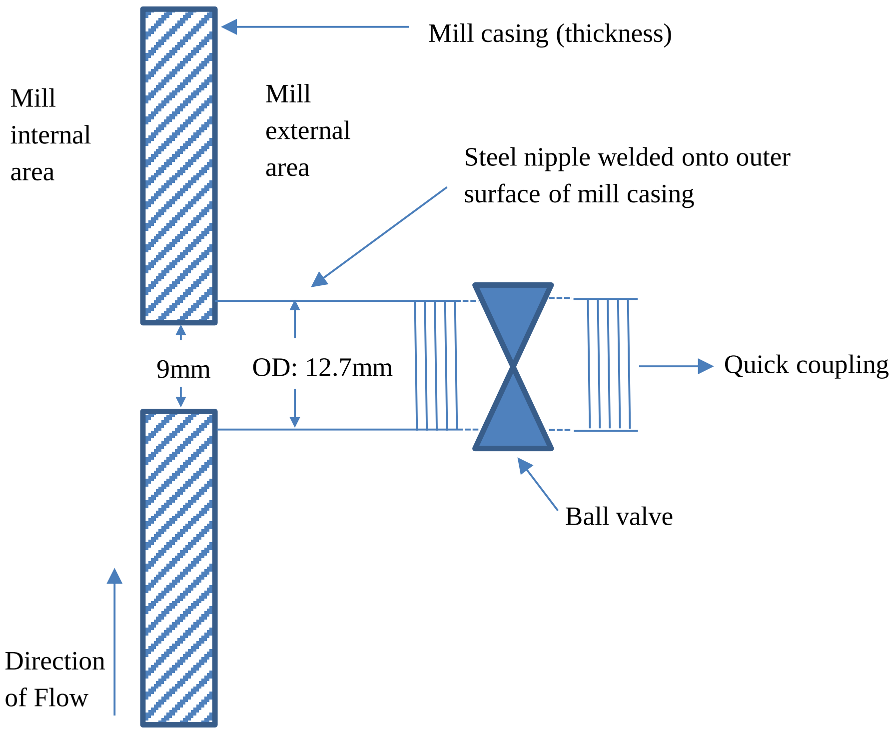

Figure 3.14 Cross section of pulveriser wall showing the tapping point installation architecture (Drawing is not to scale)

An assessment of the internal geometrical characteristics of the pulveriser allowed for a strategic selection of new tapping point locations. Ten tapping points were drilled, one at each location identified.

In general, the following criteria were adhered to:

- Measurement points were installed away from mechanical components inside the pulveriser that could affect the static pressure measured, these included pulveriser internal support structures.
- Measurement points were installed away from mechanical obstructions on the exterior side of the pulveriser to ensure accessibility during testing, these included hydraulic pressure loading equipment, primary air inlet ducting, access platforms and inspection doors.

Represented herein, Figure 3.15 and Figure 3.16, schematically highlight the locations of the ten new static pressure measurement points as well as existing measurement points. With reference to the aforementioned figures, tapping points were installed below the throat gap (A), above the top grinding ring (B), below the classifier (C), inside the classifier (D) and at two locations at the pulveriser exit (E and F). It was initially planned to install a tapping point directly above the throat gap, however due to the presence of ceramic lining in this region, it was not possible. Therefore, this tapping point allocated to an area further up along the vertical height of the pulveriser to the next suitable location, this point being above the top grinding ring (B). Only six (A, B, C, D, E, F) of the ten newly installed points were used for measurements due to a limitation of pressure measuring equipment. Existing points (G and H) representing the pulveriser inlet and outlet static pressure measurement points, respectively, were used in conjunction with the new points installed.

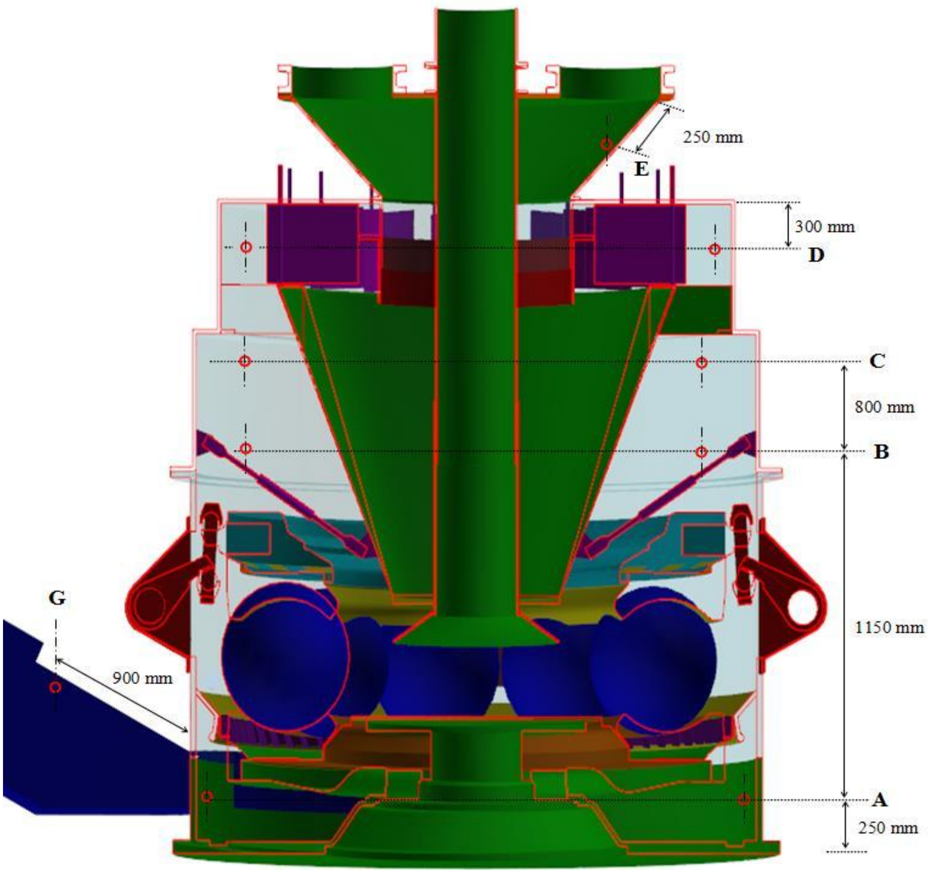

Figure 3.15 Cross section of pulveriser showing location of static pressure tapping points

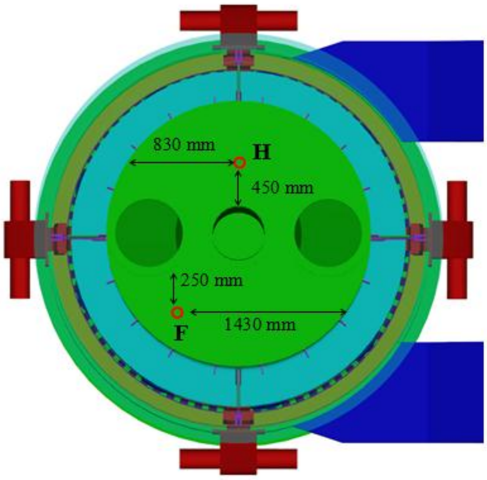

Figure 3.16 Top view of pulveriser showing location of static pressure measurement points F and H

3.3.3.2 Measurement instrumentation

Van Der Merwe (2013) measured the wall static pressure in PF pipes downstream of a coal pulveriser. The test procedure followed by Van Der Merwe (2013) was used as a guide to measure and record the static pressures inside the pulveriser. Six Siemens differential pressure transducers were used to measure the static pressure at the various locations depicted previously.

An impulse line is a small pipe that is used to connect a point at which pressure is to be measured to an instrument (Reader-Harris et al., 2005). The correct use of impulse lines prevents measurement inaccuracies. Best practice guidelines recommend that impulse lines be as short as possible from the point of measurement to the measuring devices, be free from blockages and free of leakages (Reader-Harris, 2005). For two-phase flows, especially in the dust laden pulveriser environment, periodic purging of the impulse line with high pressure air is recommended to keep the impulse lines clear of dust build up. Furthermore, the number of connection points on an impulse line must be kept to a minimum to prevent leakages at couplings. Impulse line diameters typically used for static pressure measurement range from 4 mm to 25 mm. ISO 2186: 2007 (2) recommends a minimum impulse line diameter of 6 mm. In accordance with best practice guidelines, 6 mm impulse lines were then connected to a quick coupling that was fitted to the open end of the ball valve.

The static pressure at each of the new tapping points (highlighted in Figure 3.15 and Figure 3.16) were measured as the differential pressure between the static pressure at the measurement point on the pulveriser and atmospheric pressure. On each of the differential pressure transducers, the wall static pressure measurement was connected to the positive terminal. The negative terminal of each pressure transducer was left open to atmosphere.

The Siemens differential pressure transducers employed are loop powered and the transducers regulate the amount of current it draws proportional to the static pressure it measures (Van Der Merwe, 2013). A USB-6008 National Instruments (NI) Data Acquisition System (DAS) was used to record the measured data for each of the six pressure transducers using the NI Signal Express software. The static pressure measurement instrumentation architecture followed for each of the six transducers used is schematically outlined in Figure 3.17.

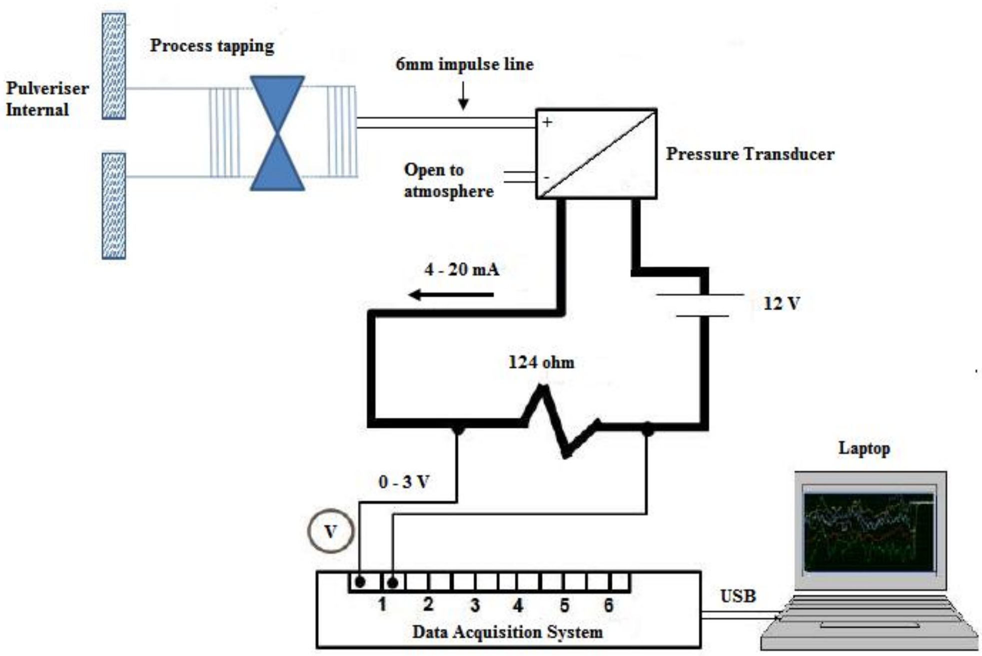

Figure 3.17 Static pressure measurement instrumentation architecture (Adapted from Van Der Merwe, 2013)

The NI DAS can only measure and record voltage signals. Therefore, a 124 Ω resistor was added to the power circuit across which the USB-6008 NI measured the voltage signals. The current was maintained between 4 mA and 20 mA during the test. The operating range for each pressure transducer was set to -500 Pa and 10 000 Pa using the instructions provided in the user manual (Siemens Energy and Automation, 2008). The minimum and maximum operating voltages were calculated to be between 0.496 V and 2.48 V, respectively by employing the relationship described in Equation 3.10 and Equation 3.11. The voltage range on the NI DAS software was then set accordingly.

$$V_{min} = I_{min}R = (4\,mA)(124\Omega) = 0.496\,V \tag{3.10}$$

$$V_{max} = I_{max}R = (20\,mA)(124\Omega) = 2.48\,V \tag{3.11}$$

The ability of the NI DAS to measure and record only voltage signals necessitated the construction of a curve that enabled the corresponding pressure to be attained from the voltage measurement. The linear curve, created between pressure, voltage and current, is graphically illustrated in Figure 3.18.

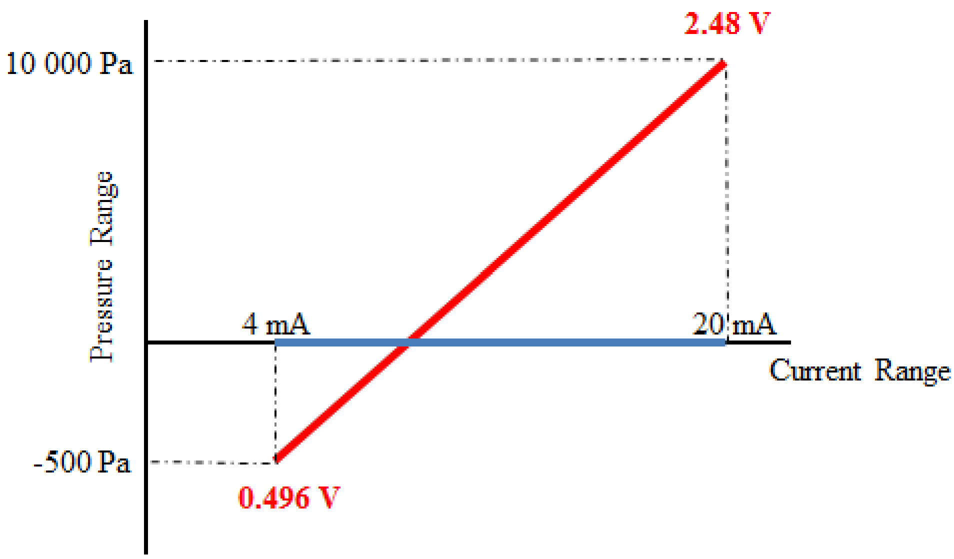

Figure 3.18 Graphical illustration of the relationship between pressure, voltage and current (Adapted from Van Der Merwe, 2013)

3.3.3.3 Measurement results

Prior to the start of each test, each tapping point and impulse line was purged with high pressure air to clear any blockages. Static pressure measurements were taken for single-phase flow (air only) and for two-phase flow (air and coal). Recall from section 3.3.1, the primary air flow traverse highlighted the DCS reading to be 7 % higher than the experimentally determined primary air flow rate hence from this point forward reference will be made to the corrected primary air flow rate values.

All pressure transducers were calibrated by a South African National Accreditation System (SANAS) approved laboratory. The uncertainty of measurement reported for each pressure transducer was ±25 Pa. Instrument calibration certificates for the pressure transducers are presented in Appendix B.

3.3.3.3.1 Single-phase static pressure measurements

For single-phase flow, static pressure measurements were recorded for three different mass flow rates of primary air while the pulveriser was on standby mode. The primary air used during these tests was obtained from the FD fan through the tempering air supply line (illustrated in Figure 3.1). This air bypassed the air heater and was therefore at ambient temperature. For the duration of this test, the seal air fan and pulveriser motor were not required to be in operation. For each of the tested mass flow rates of primary air, voltage measurements at each static pressure measurement point were taken simultaneously using the NI DAS. Once the required air flow rate applied was stable, the voltage was recorded every second over a three minute period.

During this test a substantial amount of data was recorded, therefore measured data and calculated results will only be presented for one mass flow rate of primary air tested. A full report of measured data and calculated results for all static pressure measured for each air flow rate tested as well as the unit operating conditions can be viewed in Appendix C.

A pressure transducer was connected to each measurement point. Voltage measurements were then fitted into the relevant calibration curve to enable static pressure quantification. For example, at measurement point A, pressure transducer 6 was used. The linear relation for transducer 6, highlighted in Equation 3.12, was employed to calculate the static pressure at point A from the average voltage measured over the three minute test period. This procedure was analogously applied to all voltage measurements recorded at each measurement point. (Appendix B displays the linear relationship constructed for each pressure transducer). Table 3.14 presents the measured data and calculated results for primary air mass flow rate of $\dot{m}_{PA,\ measured}$ = 9.8 kg/s.

$$P_{static,\ calculated} = (5.5034 V_{measured,\ avg} - 3.3269) * 1000 \tag{3.12}$$

Table 3.14 Measured data and calculated static pressure results for primary air mass flow rate 1, 9.8 kg/s

Measurement point	Pressure transducer	$\mathbf{V}_{measured,\ avg}$ $(\boldsymbol{V})$	$\boldsymbol{P}_{static,\ calculated}$ $(\boldsymbol{Pa})$
A	6	1.024	2309.10
B	5	0.843	1288.83
C	2	0.842	1301.05
D	4	0.850	1298.14
E	3	0.778	952.95
F	4	0.789	1007.42
G	1	1.052	2454.39
H	2	0.797	1056

3.3.3.3.2 Two-phase flow static pressure measurements

For the two-phase flow condition, the static pressure measurements were recorded during normal operation of the pulveriser. The primary air supplied to the pulveriser was obtained from the FD fan through the air heater (flow path illustrated in Figure 3.1). Since this air does not bypass the air heater, the primary air is at a much higher temperature in comparison to the temperature of the air used during the single-phase static pressure measurements.

The procedure, analogous to that explicated in section 3.3.3.3.1, was followed to measure the voltage signals and correlate the corresponding static pressure results. Unlike the single-phase flow tests, this test was restricted to one mass flow rate of primary air, ($\dot{m}_{PA,\ corrected}$ = 9.8 kg/s, $\dot{m}_{PA,\ DCS}$ = 10.5 kg/s). This had an associated raw coal flow rate of $\dot{m}_{coal,\ calculated}$d = 6.32 kg/s (highlighted in Table 3.12). For two-phase flow, data was recorded every second over a 15 minute interval. Table 3.15 presents the measured data and calculated static pressure results obtained for the two-phase flow test condition.

Table 3.15 Measured data and calculated static pressure results for two-phase flow condition

Measurement point	Pressure transducer	$V_{measured,\ avg}$ (V)	$P_{static,\ calculated}$ (Pa)
A	6	1.808	6623.60
B	5	1.345	4048.35
C	2	1.334	4010.65
D	4	1.327	3954.76
E	3	1.125	2854.77
F	6	1.168	3104.28
G	1	2.014	7940.07
H	2	1.205	3302.51

3.3.3.4 Summary and Discussion of pulveriser static pressure results

On a typical coal pulveriser in industry, only the overall static differential pressure across the pulveriser is measured and recorded on the DCS. Plant performance teams use the existing measurement test points at these locations (highlighted in Figure 3.15 and Figure 3.16 as points G and H, respectively) to verify the pulveriser differential pressure using portable manometers. The limited number of fixed pulveriser pressure measuring instruments only endorsed a comparison for the overall pulveriser pressure drop. The comparison between the overall pulveriser pressure drop measured experimentally and recorded on the DCS, for both single and two-phase flows are summarised in Table 3.16. For the single-phase flow condition, although three primary air flow rates were tested, the data was only compared for $\dot{m}_{PA,\ measured}$ = 9.8 kg/s.

Table 3.16 Comparison between measured and DCS recorded values for the overall pulveriser pressure drop

	Units	**Single-phase flow**	**Two-phase flow**
Primary air flow	kg/s	9.8	9.8 *(corrected)*
G, $P_{static,\ measured}$	Pa	2454.39	7940.07
H, $P_{static,\ measured}$	Pa	1056	3302.52
$\Delta P_{GH,\ measured}$	Pa	1398.39	4637.55
$\Delta P_{GH,\ DCS}$	Pa	1321.58	4427.09
Difference	%	5.49	4.54

As outlined in Table 3.16, there was a less than 6 % difference between the measured and DCS recorded values for both phase conditions. The individual measurements of static pressure used to calculate $\Delta P_{GH,\ measured}$ were taken at the same location as the fixed plant instrumentation. Therefore, the only possible explanation for the discrepancy between the two values can be attributed to a non-calibrated fixed plant instrument.

Presented herein, schematic diagrams indicating the measurement point locations is represented alongside the measurement results graphically illustrated in Figure 3.19. The measurement points in conjunction with the graphical representation allow for better interpretation of the pressure profile within the pulveriser. Each of the three primary air flow rates tests, although different in magnitude, exhibited a similar static pressure profile. The static pressure was observed to decrease from the pulveriser inlet to the outlet. As previously highlighted, it was not possible to measure the static pressure directly above the throat gap region due to the presence of ceramic lining. The pressure drop across the throat gap region was therefore considered to be across points A and B. As expected from literature, the highest pressure drop was evident across the throat gap region. A value of

1165 Pa was calculated for the maximum primary air flow rate tested. This was anticipated due to the small area of the throat gap which increases the resistance of the system.

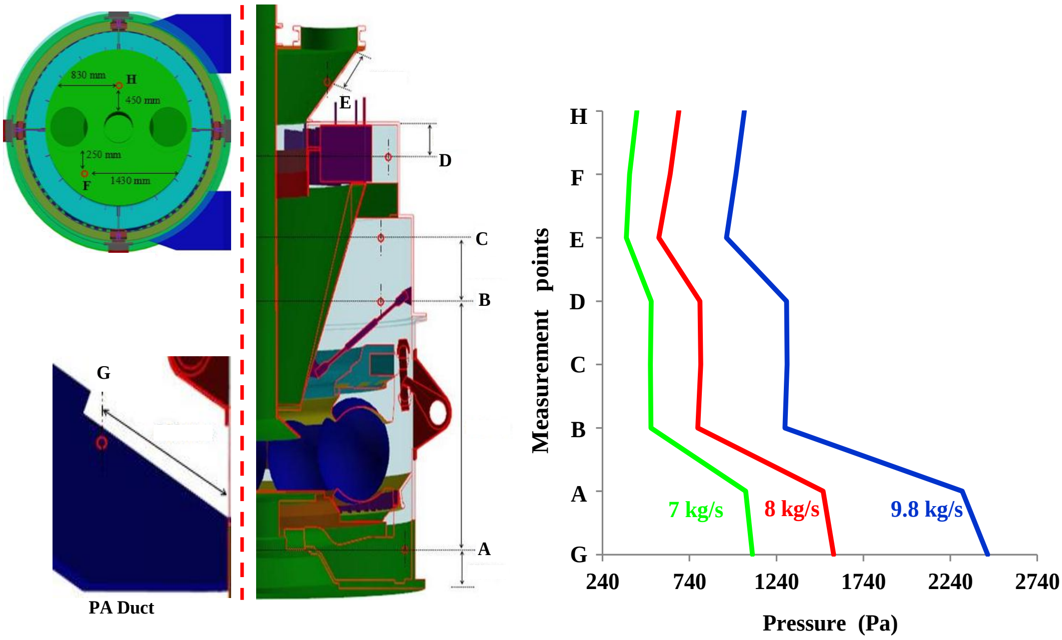

Figure 3.19 Illustrative summary of measured static pressure results obtained for three primary air mass flow rates tested

Notably, the static pressure at points B, C and D are relatively uniform. This may be attributed to insignificant geometrical variation in the area between these points. Although the area at point D, representing the classifier, decreased slightly, noteworthy change in static pressure was not observed. The pressure drop across the classifier (points D-E) for each flow was calculated to be, on average, 28 % lower than the pressure drop across the throat gap region. The pressure drop across the throat gap amounts to 70 % of the total pressure drop in the pulveriser. As previously mentioned, no plant data or explicit literature was available to compare with the other static pressure measurements taken along the vertical height of the pulveriser (highlighted as points A, B, C, D and E in Figure 3.19). However the general trend of the static pressure profile for each of the three primary air mass flow rates was similar, confirming the precision of the instrument, accuracy of analysis and reproducibility of the measured outcome trends.

While the static pressure measurements for the single-phase flow (air) were performed with relative ease, the measurement of the static pressure for two-phase flow required considerably more effort. This was primarily due to blockage of the tapping holes and impulse lines during measurement with PF. This necessitated frequent purging of the aforementioned points to enable measurements to be recorded. It must be noted that the global pulveriser performance tests (presented in section 3.3.2) were performed simultaneously with the static pressure measurements (presented in section 3.3.3.3.2). Due to the magnitude of the tests performed and challenges experienced thereof, static pressure measurements could only be obtained for the one mass flow rate of primary air under two-phase flow conditions.

Figure 3.20 presents the static pressure profile acquired for the two-phase flow test condition. It must be noted that this test was performed during normal operating conditions of the pulveriser. In comparison to Figure 3.19, the presence of coal is observed to significantly increase the static pressure values within the pulveriser, and consequently the overall pulveriser pressure drop. This observation was not entirely unexpected as the presence of coal, a higher primary air temperature and moisture evaporation from coal increases the air flow resistance through the pulveriser. Furthermore, this result corroborates well with literature (outlined in Figure 1.7). Notably, the static pressure profile for two-phase flow exhibits a similar trend to the single-phase flow profile and similarly, the pressure drop across the throat gap was observed to contribute significantly to the overall pressure drop across the pulveriser.

Aside from measurement uncertainty in the pressure transducers itself, little opportunity exists for large measurement errors, in both the single and two-phase flow scenarios since these tests were performed with calibrated instrumentation and in accordance with best practice guidelines. Therefore, it can be concluded that the static pressure measured at all locations was accurately quantified.

Additionally, the pulveriser external casing temperature profile, reported in section 3.3.2 at points A to H, is represented alongside the two-phase static pressure results displayed in Figure 3.20. The steep temperature gradient, evident across points G-B, may be attributed to the effect of drying coal. The external primary air duct casing temperature at point G, as compared to the DCS value (displayed in Table 3.12) for primary air flow temperature is markedly lower, mainly due to thermal insulation in the primary air duct. The temperature of the casing from point C to point H was observed to be uniform. Rationally, one can expect the temperature within the pulveriser to be slightly higher than the external casing temperature. However, the close resemblance between the correspondingly measured pulveriser external casing temperature at point H (83 ^{o}C) to the DCS recorded value at point H (88 ^{o}C), was an indication that the measured results are sufficiently accurate.

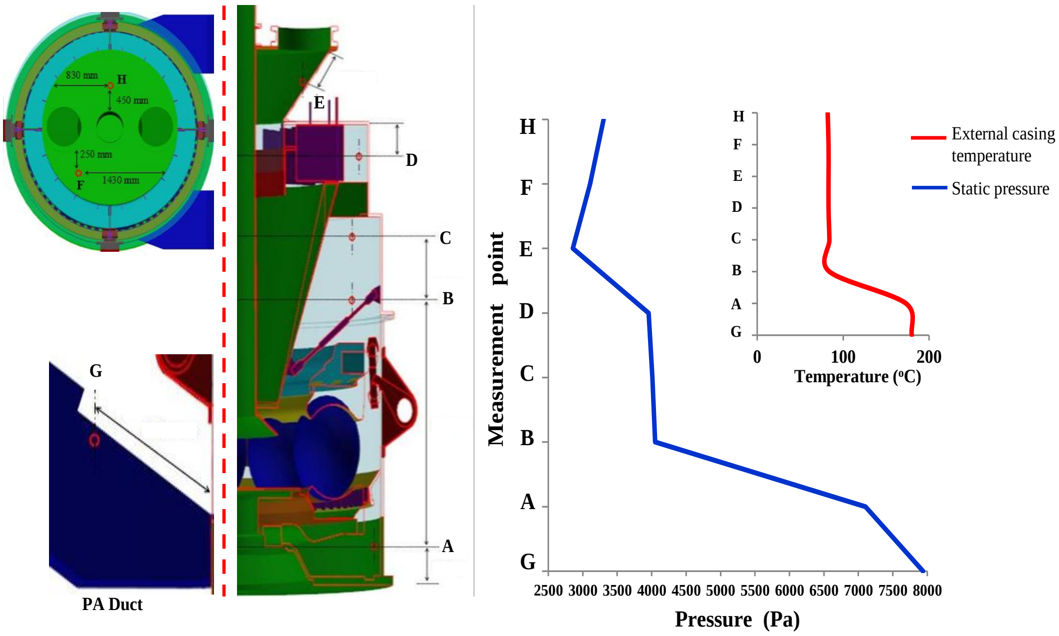

Figure 3.20 Two-phase static pressure and inset external pulveriser temperature profile of the 8.5E VSM, (Air flow: 9.8 kg/s; Coal flow: 6.32 kg/s)

3.4 Concluding remarks

A comprehensive literature review culminated in the selection of appropriate pulveriser process variables for investigation. Previous studies provided a framework to quantify pertinent process variables through acceptable experimental methods and measurement. This necessitated the explication of the various methodologies and strategies employed to achieve the measured outcomes. The effects of erroneous experimental results were further minimized through engagement with best practice guidelines. Overall, satisfactory quantification of several pulveriser process variables was accomplished experimentally and forms a prerequisite through which the mathematical models, developed in Chapter 4 and Chapter 5, will be subsequently assessed and validated.

Chapter 4: Development and Validation of the MMEB model

4.1 An introduction to mass and energy balances

The laws of conservation of mass and energy have formed the foundation of all process design activities since its existence. A mass balance can be performed for any process step and it is known that the input mass will be equal to the output mass at steady state. It follows from the first law of thermodynamics that energy can exist in many forms, such as heat, work, electrical energy, and it is the total energy that is conserved in a system (Coulson and Richardson, 1999). The general mass and energy balance equation, which can be written for any process, and is generally the starting point for any system analysis is highlighted in Equation 4.1.

$$Energy\ in + Generation - Consumption - Accumulation = Energy\ out \qquad (4.1)$$

The application of mass and energy balances to particularly model and predict process variables surrounding the coal pulverisation process has been researched previously. A range of simple models has been derived for purposes of process parameter monitoring or fault detection, while comprehensive models have been explored for the purposes of dynamic pulveriser simulation and control (Fan and Rees, 1997; Odgaard and Mataji 2006; Kapakyulu, 2007, Archary, 2012). The general approach to model the pulveriser often involves steady state modelling of the process variables as this readily reduces the complexity of the variables delineated by the process. Additionally, modelling the dynamic process of a coal pulveriser is mathematically complex which warrants simplifying assumptions to be imposed to develop a more tractable model (Zhang et al., 2002).

4.2 Model Derivation

To apply the concept of mass and energy balances, an understanding and identification of the key variables associated with a process is required. For the pulveriser system, the control volume highlighting the key variables considered in the derivation of the MMEB model was simplified and is schematically presented in Figure 4.1.

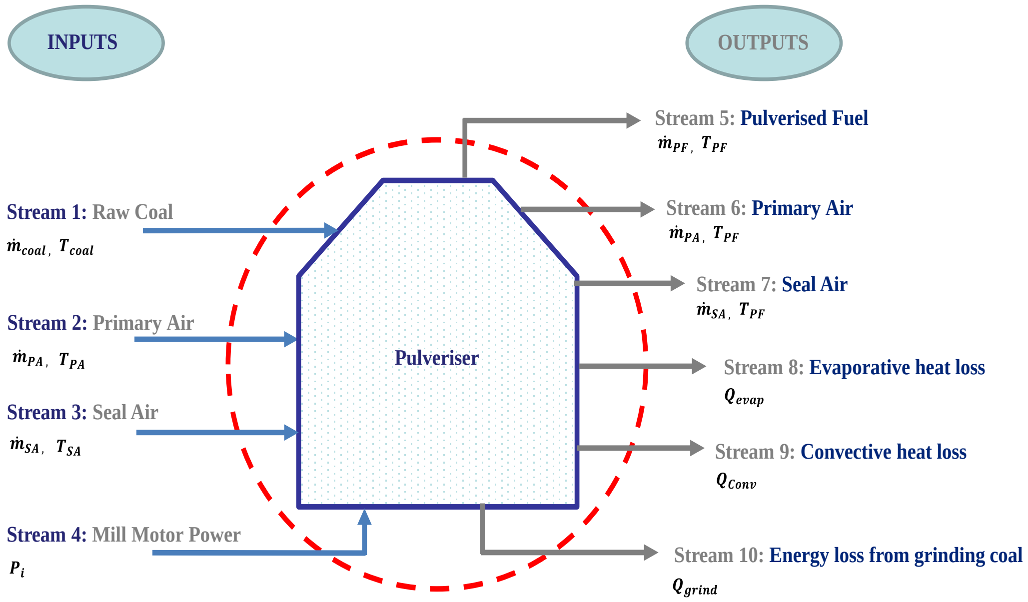

Figure 4.1 Global MMEB model control volume

4.2.1 Model assumptions

The following assumptions were necessary for the derivation of the model:

1. Although coal pulverisation is a transient process, the derivation was completed in steady state.
2. The total mass of coal entering the pulveriser is equivalent to the total mass of PF exiting the pulveriser. This implies that the internal coal recirculation rate is constant.
3. The total mass of the primary air and seal air entering the pulveriser is equivalent to the total mass of primary air and seal air exiting the pulveriser.
4. The primary air, seal air, and PF exit the pulveriser at the same temperature.
5. PF exiting the pulveriser is not completely free of moisture (CMP, 2003).
6. Air ingress to and leakage from the pulveriser is negligible.
7. Kitto and Schultz (2005) highlight that the quantity of coal rejected by the pulveriser during normal operation is about 0.25 % of the coal feed rate. Due to this relatively small amount, the quantity of coal rejected by the pulveriser has been omitted.

8. The temperature of the pulveriser external body exposed to ambient conditions is uniform.
9. The actual energy used for physical particle breakage is approximately four percent of the total energy consumed by the pulveriser (Stamboliadis, 2002).
10. Heat energy absorbed by the pulveriser internal metal components is considered to be small and since it is relatively difficult to quantify experimentally it was neglected (Zhang et al., 2002).
11. As radiation heat transfer is usually considered in processes were the temperatures are significantly higher than those commonly existent during pulveriser operation, heat energy loss to the environment through radiation is not considered (Kapakyulu, 2007).

4.2.2 Model equations

With reference to Figure 4.1, a steady state, global mass and energy balance model may be derived from first principles. Effectively, a mathematical representation describing the mass and energy balance model derived is depicted in Equation 4.2.

$$\dot{q}_{coal_i} + \dot{q}_{PA_i} + \dot{q}_{SA_i} + P_i = \dot{q}_{PF_o} + \dot{q}_{PA_o} + \dot{q}_{SA_o} + Q_{evap} + Q_{conv} + Q_{grind} \quad (4.2)$$

Where:

$\dot{q}$ = Input and output heat energy (kJ/s)

P_i = Pulveriser power input (kJ/s)

Q_{evap} = Energy lost through evaporation of moisture from coal (kJ/s)

Q_{conv} = Energy lost through convective heat transfer to the environment (kJ/s)

Q_{grind} = Energy consumed by the pulveriser to physically grind coal (kJ/s)

Expanding the terms of the inlet streams presented in Equation 4.2 yields Equation 4.3 to Equation 4.6.

$$\dot{q}_{coal_i} = (1 - w_o)\dot{m}_{coal}Cp_{coal}\,T_{coal} + w_o\dot{m}_{coal}Cp_w\,T_{coal} \tag{4.3}$$

$$\dot{q}_{PA_i} = (1 - x_1)\dot{m}_{PA}\,Cp_{air}T_{PA} + x_1\dot{m}_{PA}\,Cp_wT_{PA} \tag{4.4}$$

$$\dot{q}_{SA_i} = (1 - x_1)\dot{m}_{SA}\,Cp_{air}T_{SA} + x_1\dot{m}_{SA}\,Cp_wT_{SA} \tag{4.5}$$

During pulveriser operation, the pulveriser power consumption is not measured directly however the current drawn by the pulveriser motor is measured and recorded on the DCS. Eccles (2011) provides a relationship to calculate the power consumed by the pulveriser motor as described in Equation 4.6.

$$P_i = \sqrt{3}\ \times pf\ \times V\ \times I \tag{4.6}$$

Where:

pf = Power factor

V = Voltage (V)

I = Current (A)

Expanding the terms of the outlet streams presented in Equation 4.2 yields Equation 4.7 to Equation 4.12.

$$\dot{q}_{PF_o} = (1 - w_1)\dot{m}_{coal}Cp_{coal}\,T_{PF} + w_1\dot{m}_{coal}Cp_w\,T_{PF} \tag{4.7}$$

$$\dot{q}_{PA_o} = (1 - x_1)\dot{m}_{PA}\,Cp_{air}T_{PF} + x_1\dot{m}_{PA}\,Cp_wT_{PF} \tag{4.8}$$

$$\dot{q}_{SA_o} = (1 - x_1)\dot{m}_{SA}\,Cp_{air}T_{PF} + x_1\dot{m}_{SA}\,Cp_wT_{PF} \tag{4.9}$$

Flynn (2003) provides a relationship to calculate the heat loss due to evaporation of moisture from raw coal as highlighted in Equation 4.10.

$$Q_{evap} = \Delta h\ \times\ \dot{m}_{coal}\ \times (w_o - w_1) \tag{4.10}$$

Incropera et al. (2006) provides Equation 4.11 to approximate the rate of heat loss through convective heat transfer from the external pulveriser casing to the environment. In order to calculate the heat transfer surface area (A_{mill}), dimensions of the pulveriser casing were obtained from the as-built drawings.

$$Q_{conv} = \mathrm{h}\,\mathrm{A}_{mill}(T_{mill} - T_{amb}) \tag{4.11}$$

Equation 4.12 provides a relationship to approximate the energy loss as a result of physically grinding raw coal (Stamboliadis, 2002).

$$Q_{grind} = 0.04 \times P_i \tag{4.12}$$

Since the prediction of the coal mass flow rate is central to the derivation of the global MMEB model, substitution of Equations 4.3 to Equation 4.12 into Equation 4.2 and rearranging yields Equation 4.13 from which the mass flow rate of coal may be predicted.

$$\dot{m}_{coal} = \frac{(1-x_1)\dot{m}_{PA}\,(Cp_{air}T_{PF} - Cp_{air}T_{PA}) + x_1\dot{m}_{PA}\,(Cp_wT_{PF} - Cp_wT_{PA}) + (1-x_1)\dot{m}_{PA}\,(Cp_{air}T_{PF} - Cp_{air}T_{PA}) + x_1\dot{m}_{PA}\,(Cp_wT_{PF} - Cp_wT_{PA}) + Q_{conv} + Q_{grind} - P_i}{(1-w_o)Cp_{coal}T_{coal} + w_oCp_w T_{coal} - (1-w_1)T_{PF} - w_1Cp_w T_{PF} - \Delta h(w_o - w_1)} \tag{4.13}$$

4.2.3 Model constants

Equation 4.13 highlights the employment of heat capacity constants. While the specific heat capacity of dry air and water is readily available from data books, the specific heat capacity of coal is predominantly reported as approximately 1.26 kJ/kgK dry ash free (daf) basis (Miller and Tillman, 2008; Khan, 2011). Postrzednik (1981) developed a correlation which relates the specific heat of coal as a function of temperature and volatile matter content of the coal. For temperature values lower than 100 ^{o}C, the heat capacity of coal may be approximated using Equation 4.14.

$$Cp_{coal}(daf) = 1015.32 + 812.26VM^{daf} \tag{4.14}$$

Where:

VM^{daf} = Volatile matter of coal on a dry ash free basis (%)

As the raw coal entering the pulveriser contains ash, the employment of this correlation posed by Postrzednik (1981) was also deemed unsatisfactory. This necessitated the approximation of the specific heat of coal on a dry basis (db). The ash present in coal is comprised primarily of silica. Using a weighted percentage of ash present in coal, an attempt to approximate the specific heat capacity of coal on a dry basis was used as shown in Equation 4.15.

$$Cp_{coal}(db) = \left[\left((1 - x_{ash}) \times Cp_{coal}(daf)\right) + \left((x_{ash}) \times Cp_{silica}(daf)\right)\right] \qquad (4.15)$$

Where:

x_{ash} = Percentage of ash in coal, db (%)

Cp_{silica} = Specific heat of silica (kJ/kgK)

4.2.4 Convective heat loss

Incropera et al. (2011) define convective heat transfer as the transference of heat by way of the motion of a fluid moving past a solid surface which is ideally at a different temperature than that of the fluid. The expression presented by Incropera et al. (2011) to calculate the overall convective heat transfer rate was described in Equation 4.11.

For simplification purposes, the pulveriser may be considered as a 'cylinder' subjected to a cross flow of ambient air as illustrated in Figure 4.2. With reference to Figure 4.2, the pulveriser body was divided into two areas, where r_1 and r_2 refer to the radius of pulveriser body and classifier sections respectively. The convective heat transfer was therefore investigated separately for these areas as they exhibited different temperatures during the full-scale experiment.

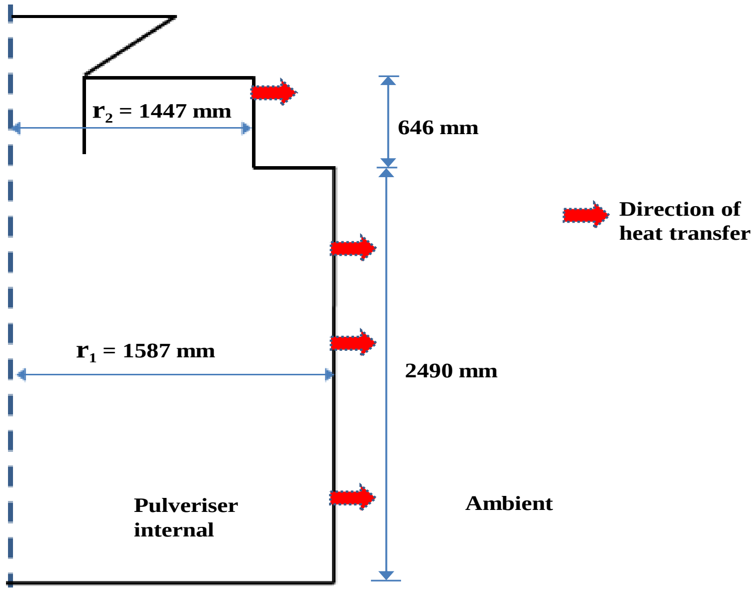

Figure 4.2 Schematic representation of the convective heat transfer in an 8.5E VSM (drawing is not to scale)

Presented herein, Equation 4.16 to Equation 4.18 highlight the correlations employed to compute the overall heat transfer coefficient (h) for a circular cylinder subjected to a cross flow of fluid as required by the correlation depicted in Equation 4.11 (Incropera et al., 2011).

$$Nu_D = 0.3 + \frac{0.62 Re^{1/2} Pr^{1/3}}{\left[1+\left(\frac{0.4}{Pr}\right)^{2/3}\right]^{1/4}} + \left[1 + \left(\frac{Re}{282000}\right)^{5/8}\right]^{4/5} \qquad (4.16)$$

Where Nu_D represents the dimensionless Nusselt number. Re is a dimensionless constant correlated through Equation 4.17. The Prandtl number (Pr) is a constant which may be obtained from data books for a specified ambient air temperature.

$$Re = \frac{\rho_{air} v_{amb} D}{\mu_{air}} \qquad (4.17)$$

The convective heat transfer coefficient can thereafter be quantified through the employment of Equation 4.18.

$$Nu_D = \frac{hD}{k} \qquad (4.18)$$

Where, D and k represent the diameter of the pulveriser section considered and the thermal conductivity of ambient air, respectively.

4.3 Mass and Energy balance model input data

In Chapter 3, section 3.3.1 and 3.3.2, experimental results obtained during the primary air flow traverse and global pulveriser performance tests were presented. These results were used as input to the Mass and Energy Balance model derived in order to quantify the coal mass flow rate. As tests were performed repeatedly over a three day period, Figure 4.3 schematically represents a comprehensive view of the pulveriser performance test results in conjunction with the two-phase flow static pressure measurement results acquired during day one of the global performance test program. The sketch displays the measurement points and the results obtained thereof. In addition, the major mass and energy flow streams encompassing the pulveriser process are displayed. It must be noted that the static pressure data presented herein is for information purposes and are not required for the mass and energy balance input. Furthermore, the PF sampling and DBM results depicted are included for MMEB model validation.

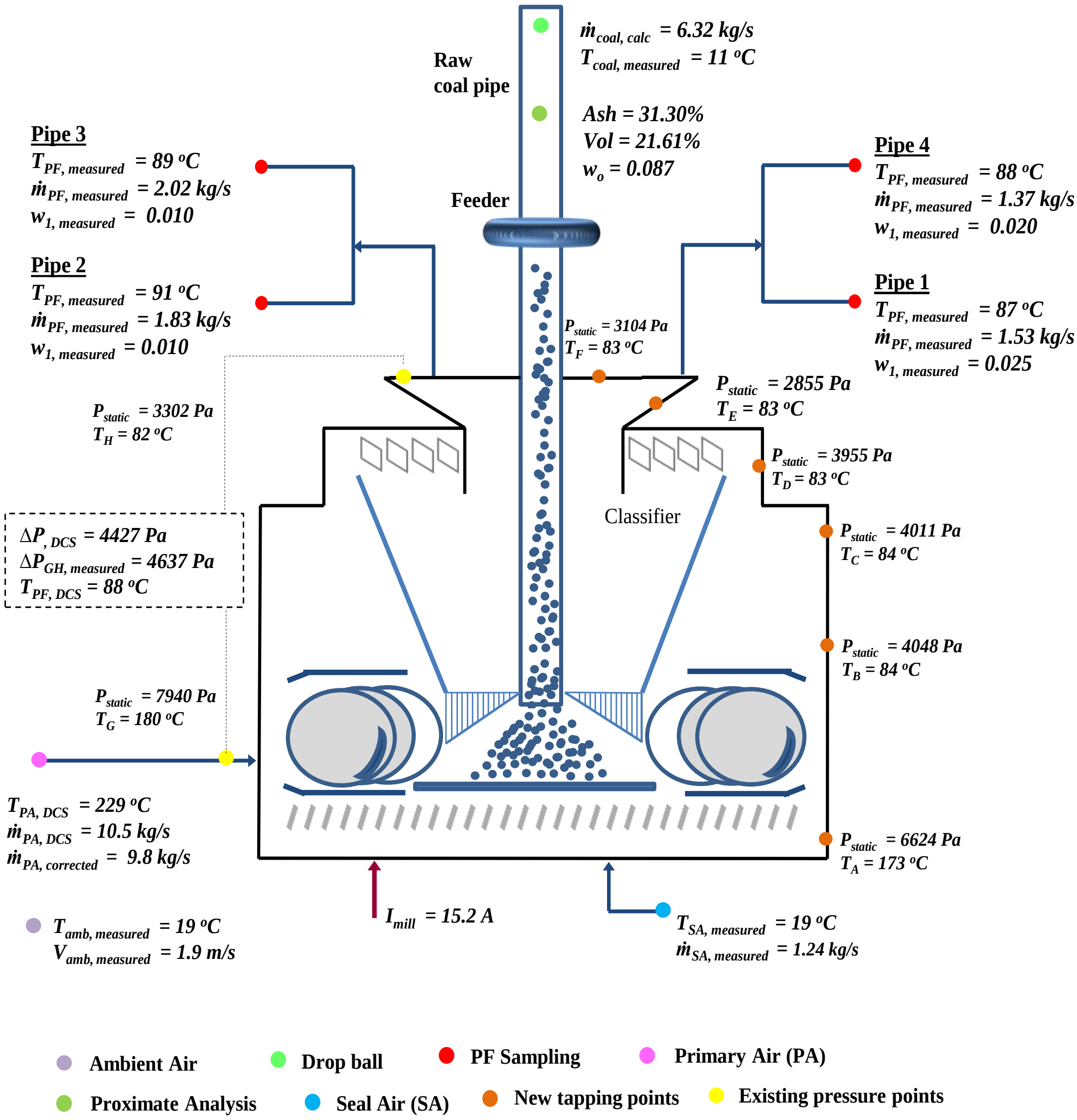

Figure 4.3 A comprehensive system sketch highlighting pulveriser process variables, day one

4.4 Results and Validation of the MMEB model through experimental correlation

Flynn (2003) highlights that mathematical models are only as good as how well they fit the physical data recorded during plant measurements. The fidelity of the derived model to predict the coal mass flow rate may be assessed through the intensity of the correlation between experimentally determined and model-predicted coal mass flow rates.

Recall from Chapter 3, section 3.3.2, the DBM and isokinetic PF sampling tests yielded the coal mass flow rates, as summarised in Figure 4.3 for day one of the test program. Since it was postulated that neither of these experimentally ascertained mass flow rates are more accurate than the other, confidence in the predictive capability of the derived model may be achieved by comparison to both sets of experimental results, as depicted in Figure 4.4.

The coal mass flow rate predicted by the MMEB model demonstrates a close correlation to the experimental results attained through isokinetic sampling and serves to validate the model derived. Although the MMEB model-predicted results are slightly higher, the correlation displayed is still adequate, achieving an average variance of less than 5 % (depicted in Table 4.1).Conversely, the coal mass flow rate predicted by the MMEB model demonstrates a poor correlation to the experimental results attained through the DBM experiment, achieving an average variance of 10.03 % (depicted in Table 4.1). This variance may be attributed to the inaccuracies associated with the DBM measurement technique and coal bulk density measurement as highlighted in Appendix E.

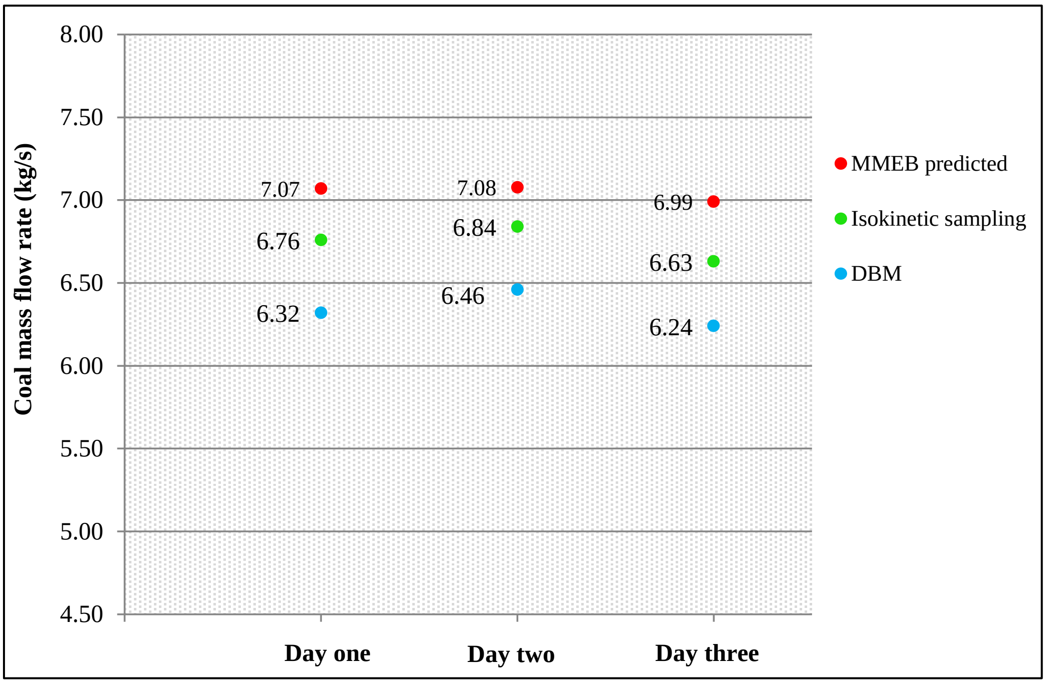

Figure 4.4 Comparison of coal mass flow rates between MMEB model-predicted, isokinetic sampling and the DBM

Table 4.1 Variance between experimentally determined and model-predicted coal mass flow rates

	Coal flow rate (kg/s)				
	Predicted (1)	**DBM (2)**	**Isokinetic Sampling (3)**	**Variance (%) (1, 2)**	**Variance (%) (1, 3)**
Day one	7.07	6.32	6.76	10.61	4.38
Day two	7.08	6.46	6.84	8.76	3.39
Day three	6.99	6.24	6.63	10.73	5.15
			Average	10.03	4.31

4.5 Propagation of uncertainty

Experiments are performed to ascertain some physical property and theoretically every measurement has an associated uncertainty. This necessitated an uncertainty analysis to be performed on all measured values to determine errors, precision and the general validity of experimental measurements (Rathakrishnan, 2007; Holman, 2012). Additionally, the propagation of uncertainty in calculated results must be expressed.

Holman (2012) provides an approach to express the propagation of uncertainty in a computed result caused by the cumulative effect of the uncertainties in all independently measured variables, as outlined by Equation 4.19.

$$w_R = \pm\left[\left(\frac{\partial R}{\partial x_1} w_{x_1}\right)^2 + \left(\frac{\partial R}{\partial x_2} w_{x_2}\right)^2 + \left(\frac{\partial R}{\partial x_3} w_{x_3}\right)^2 + \cdots + \left(\frac{\partial R}{\partial x_n} w_{x_n}\right)^2\right]^{\frac{1}{2}} \qquad (4.19)$$

Where:

R = Result dependent on independent variables $(x_1, x_2, \dots, x_n)$

w_R = Uncertainty in result, R

x_i = Independent measured variable

w_{x_i} = Uncertainty in independent variable

A step-wise approach was adopted to determine the propagation of uncertainty. Recall from Chapter 3, the primary air and seal air mass flow rates were not measured directly but computed using Equation 3.2. Since these variables are a precursor in determining the cumulative uncertainty in the predicted coal mass flow rate, the approach provided by Holman (2012) was applied here initially.

Briefly, for the seal air mass flow rate, the substitution of Equation 4.20 into Equation 3.2 yields Equation 4.21, through which the seal air mass flow rate was calculated. By rearranging Equation 4.21 to the form of Equation 4.19, the propagation of error in the seal air mass flow is determinable, as highlighted by Equation 4.22.

$$\rho_{corrected} = \frac{P}{R_0 T} \tag{4.20}$$

$$\dot{m}_{SA} = \frac{P}{RT} \times A_{segment} \times v \tag{4.21}$$

$$w_{\dot{m}_{SA}} = \pm\left[\left(\frac{\partial \dot{m}_{SA}}{\partial \mathrm{T}} w_{\mathrm{T}}\right)^2 + \left(\frac{\partial \dot{m}_{SA}}{\partial \mathrm{v}} w_v\right)^2\right]^{\frac{1}{2}} \tag{4.22}$$

Equation 4.23 and 4.24 were employed to determine the relative uncertainties in the temperature and velocity measurements using data obtained from instrument calibration certificates.

$$w_{\mathrm{T}} = \frac{0.5\ ℃}{T_{measured}} \tag{4.23}$$

$$w_v = \frac{0.25\ m/s}{v_{measured}} \tag{4.24}$$

With reference to the calculated and measured seal air flow data tabulated in Table 3.7 and Table 3.13 respectively, the results obtained for the propagation of uncertainty in the seal air mass flow rate is displayed in Table 4.2.

Table 4.2 Propagation of uncertainty in the seal air mass flow rate measurements

	w_T	w_v	$w_{\dot{m}_{SA}}$
Test 1	2.63 e-02	3.65 e-02	6.49 e-03
Test 2	2.63 e-02	3.49 e-02	6.21 e-03
Test 3	2.63 e-02	3.65 e-02	6.49 e-03
Average	2.63 e-02	3.59 e-02	6.39 e-03

Table 4.2 highlights that the relative influence of the temperature and velocity measurements on the seal air mass flow rate computed was small. The uncertainty in the seal air mass flow rate was calculated to be on average 0.64 %. Evidently, the uncertainty in the velocity measurement appeared to be the largest contributor to the overall uncertainty.

Similarly, the uncertainty in the primary air mass flow rate calculated was determined. With reference to measured data and calculated results outlined in Table 3.3, the propagation of uncertainty results obtained for the primary air mass flow rate is tabulated in Table 4.3.

Table 4.3 Propagation of error in the primary air mass flow rate measurement point 1, LH Duct

Duct Depth (mm)	$w_{PA_{static}}$	$w_{\Delta P}$	$w_{T_{measured}}$	$w_{\rho_{corrected}}$	$w_{v_{PA}}$	$w_{\dot{m}_{PA}}$
95	3.95e-04	5.08e-02	8.09e-03	8.10e-03	2.57e-02	1.06e-03
285	3.63e-04	4.84e-02	7.82e-03	7.83e-03	2.45e-02	1.01e-03
475	3.35e-04	5.10e-02	8.12e-03	8.13e-03	2.58e-02	1.07e-03
665	5.04e-04	4.86e-02	7.95e-03	7.97e-03	2.46e-02	1.00e-03
855	4.02e-04	5.03e-02	8.02e-03	8.03e-03	2.55e-02	1.05e-03
Average	4.00e-04	4.98e-02	8.00e-03	8.01e-03	2.52e-02	1.04e-03

Table 4.3 highlights that the relative influence of the measured variables on the primary mass flow rate computed is small. The average uncertainty of the primary air mass flow rate was 0.1 % and the velocity measurements appeared to be the largest contributor to the overall uncertainty.

For complex models, such as the coal mass flow rate model derived, analytical computation of the partial differential equations proposed for Equation 4.19 would be extremely tedious. Holman (2012) provides an adaptation to the general routine, whereby the partial differential equations given in Equation 4.19 may be elucidated through the relationship identified in Equation 4.25.

$$\frac{\partial R}{\partial x_i} \approx \frac{\left(R_{x_i+\Delta x_i}\right)-\left(R_{x_i}\right)}{\Delta x_i} \tag{4.25}$$

Where:

Δx_i = Perturbed variable

Moffat (1988) mentions that the value of Δx_i must be taken arbitrarily small in order to obtain the true value of the partial derivative. Alternatively, the use of $\Delta x_i = w_{x_i}$ is acceptable and was therefore employed in this analysis (Moffat, 1988).

With reference to Equation 4.13, the model derived is a function of ten experimentally determined variables, as highlighted by Equation 4.26. However, in the propagation of uncertainty in the coal mass flow rate calculation, the contribution of w_o and w_1 were excluded due to the unavailability of uncertainty data for these variables. Table 4.4 presents the independent variables along with their respective local uncertainties.

$$\dot{m}_{coal,predicted} = \dot{m}_{coal,\ predicted}(\dot{m}_{PA}, \dot{m}_{SA}, T_{coal}, T_{PA}, T_{SA}, T_{PF}, T_{amb}, T_{mill}, w_o, w_1) \tag{4.26}$$

Table 4.4 Relative uncertainties for each of the independently measured variables

Independent variable	Units	$\boldsymbol{x_i}$	Uncertainty[X]	$\boldsymbol{w_{x_i} = \Delta x_i}$
$\dot{m}_{PA}$	kg/s	9.80	± 1.04e-03	1.06e-04
$\dot{m}_{SA}$	kg/s	1.24	± 6.39e-03	5.15e-03
T_{coal}	^{o}C	11	± 5	4.54e-01
T_{PA}	^{o}C	229	± 0.2	8.73e-04
T_{SA}	^{o}C	19	± 0.5	2.63e-02
T_{PF}	^{o}C	89	± 0.2	2.25e-03
T_{amb}	^{o}C	19	± 0.2	2.63e-02
$T_{mill,\ avg}$	^{o}C	115	± 5	4.35e-02
w_o	%	8.76	Not available	-
w_1	%	1.63	Not available	-

The propagation of measurement uncertainty in the predicted coal mass flow rate was subsequently determined using the method explicated previously. Table 4.5 succinctly summarises the final results obtained.

[X] Aside from the uncertainties of primary and seal air mass flow rates, these uncertainties were obtained directly from the respective calibration certificates.

Table 4.5 Propagation of measurement uncertainty in the coal mass flow rate predicted

Independent variable	Units	$\dot{m}_{coal_{x_i}}$	$\dot{m}_{coal_{x_i+\Delta x_i}}$	$\frac{\partial \dot{m}_{coal_{x_i}}}{\partial x_i}$	Contribution to uncertainty
$\dot{m}_{PA}$	kg/s	7.0704	7.0716	1.14e01	1.46e-06
$\dot{m}_{SA}$	kg/s	7.0704	7.0699	-1.01e-01	2.72e-07
T_{coal}	^{o}C	7.0704	7.0925	4.88e-02	4.90e-04
T_{PA}	^{o}C	7.0704	7.0716	1.35	1.38e-06
T_{SA}	^{o}C	7.0704	7.0717	4.96e-02	1.70e-06
T_{PF}	^{o}C	7.0704	7.0713	4.17e-01	8.79e-07
T_{amb}	^{o}C	7.0704	7.0705	5.68e-03	2.23e-08
$T_{mill,\ avg}$	^{o}C	7.0704	7.0703	-1.15e-03	2.49e-09
				$w_{\dot{m}_{coal}}$	0.023

Table 4.5 highlights that the relative contribution to uncertainty by each independent variable was extremely small. However, the propagation of uncertainty in the predicted coal mass flow rate was calculated to be 2.3 %. Notably, the main contributors to the uncertainty were the raw coal temperature and seal air temperature measurements.

4.6 Sensitivity analysis

While the uncertainty analysis presented in the preceding section sought to ascertain the variables whose individual uncertainty had a substantial effect to the uncertainty in the predicted coal mass flow rate, variables which pose the most influence to model output variability must also be identified. This task was achieved by completing a sensitivity analysis. Conceptually, a less time consuming approach to obtain a sensitivity ranking was to vary each input parameter, one at a time, by a given percentage while all other parameters remain unchanged. Following which the model input/output relationship may be quantified and assessed (Hamby, 1994).

In order to elucidate the potential of their effects on the model-predicted outcome, each input variable was increased by ten percent. Following which, the model output was calculated and gauged against the originally calculated coal mass flow rate. Figure 4.5 presents the sensitivity analysis results, highlighting the magnitude of the disparity in the coal mass flow rate for each input parameter.

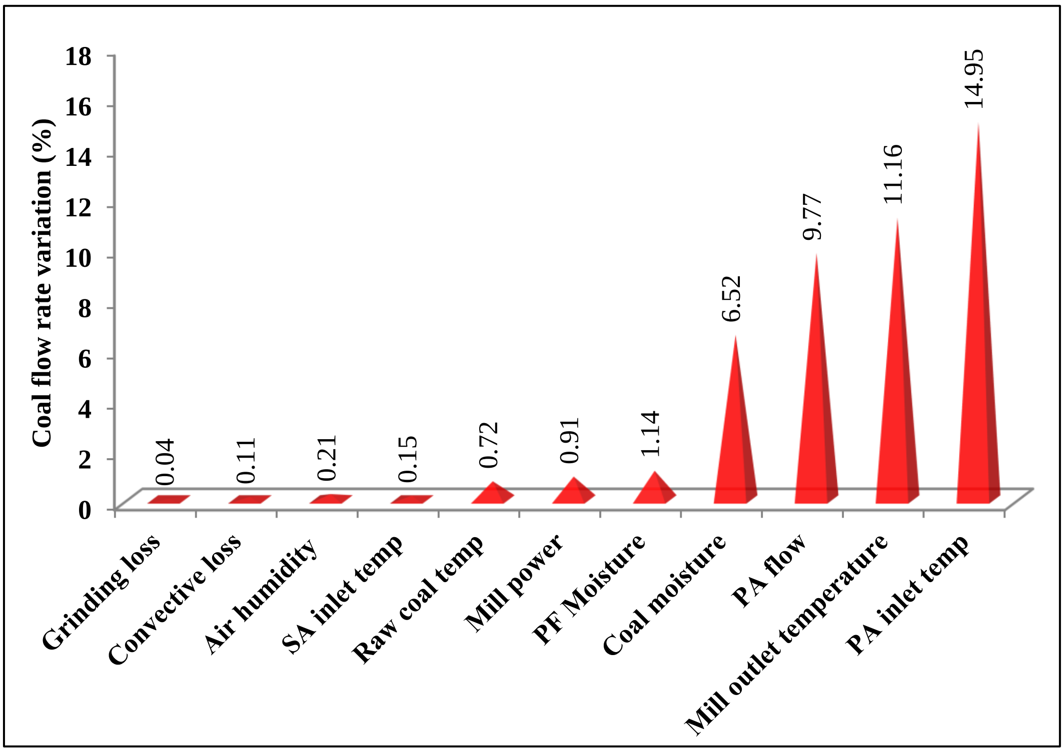

Figure 4.5 Graphical representation of the MMEB model input parameter sensitivity analysis

Evidently, a ten percent increase in the respective quantities of the primary air inlet temperature, mill outlet temperature, primary air flow rate and coal moisture had a significant influence on the model-predicted coal mass flow rate. The primary air inlet temperature had the largest influence affecting a change of approximately 15 % in the model-predicted coal mass flow rate. The graphical plot further demonstrates a statistically insignificant variation (<1 %) in the coal mass flow rate for input variables such as the pulveriser power input, raw coal temperature, seal air temperature, air humidity, grinding energy loss and convective heat loss.

The results of this sensitivity study are congruent with the outcomes presented by Archary (2012) and serves to verify the pulveriser model developed. With this information obtained, experimental emphasis can be narrowed down during the testing phases of future research endeavours by acquiring model inputs exhibiting a greater influence on model predictions to a higher degree of certainty.

In addition, recall from section 4.2.3 the heat capacity of raw coal (dry basis) was highlighted to be dependent on the volatile matter content and, moreover, it was corrected for ash content (refer to Equation 4.14 and Equation 4.15). Hence, a brief sensitivity analysis was undertaken to establish the effect of ash content correction on the MMEB model-predicted coal mass flow rate. In this analysis, a range of coal with varying ash content, and its respective volatile matter content, was employed to calculate the heat capacity of coal on a dry ash free basis and a dry basis. The heat capacity of coal on a dry basis is much lower than the respective heat capacity of coal on a dry ash free basis, as presented in Table 4.6.

Table 4.6 Effect of ash content on the heat capacity of coal

Ash Content (%)	**Volatile matter (%)**	$\boldsymbol{Cp_{coal}(daf)}$	$\boldsymbol{Cp_{coal}(db)}$
17.96	23.93	1.252	1.198
21.69	21.29	1.236	1.174
24.60	22.51	1.257	1.182
27.06	21.64	1.256	1.173
31.42	21.51	1.270	1.170
36.55	20.23	1.274	1.156
42.22	20.39	1.302	1.153

Figure 4.6 highlights the error associated with the MMEB model-predicted coal mass flow rate when the heat capacity of coal excludes the ash content correction. Notably, when the ash content was included the coal mass flow rate predicted was higher. An average discrepancy of 3.63 % was computed (not shown) between the two coal mass flow rate results, thereby highlighting the significance of incorporating the ash content in the raw coal heat capacity constant determination.

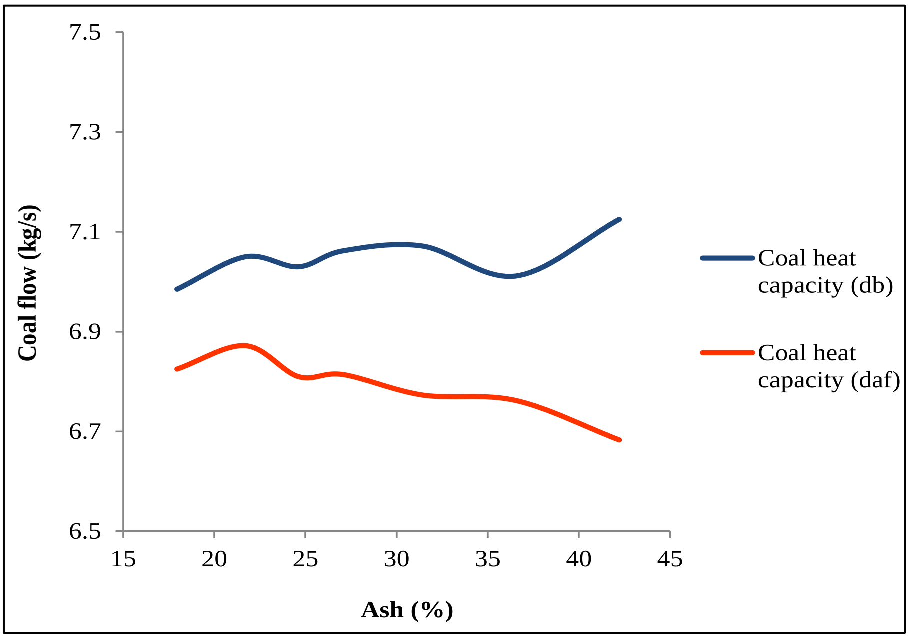

Figure 4.6 Effect of ash content correction on MMEB model-predicted coal mass flow rate

4.7 Concluding remarks

The MMEB model derived to predict the coal mass flow rate through a commercial-scale pulveriser has been successfully developed. The experimental (isokinetic results only) and model-predicted coal mass flow rates achieved significant correlation. The derived model demonstrated great potential in predicting the coal mass flow rate to within 5 % in relation to the isokinetic PF sampling experimental data, which serves to validate the model derived. Uncertainty effects of independent model input parameters were quantified and the propagation of uncertainty on the model-predicted output was established. Additionally, this chapter demonstrated the sensitivity ranking of model input parameters, highlighting significantly influential parameters on the predictive model output, thereby providing useful information for future research efforts. Moreover, rather than acting exclusively to predict the coal mass flow rate, the versatility of the validated MMEB model provides an unequivocal benefit in quantifying other pulveriser process variables defined in the model, provided the coal mass flow rate can be accurately measured.

Chapter 5: Development and Validation of the CFD model

5.1 An introduction to CFD

CFD combines the fields of fluid dynamics, mathematics and computer science to provide a unique and simplified numerical simulation environment that has the potential to solve complex, multi-disciplinary engineering problems economically. The fundamental principles constructed into commercial CFD codes are governed by the Navier-Stokes equations for fluid flow. In recent years, the evolution of CFD simulations in the power generation industry has exhibited immense potential in elucidating physical phenomenon in many processes that would otherwise not be explicitly understood. Numerous benefits of CFD simulations are related to the ability of the numerical method to predict physical phenomenon of full-scale models in a fraction of the time and cost as compared to conventional methods that use physical prototyping. Although, experimental methods and analytical models are far from being obsolete, they play a significant role in validating the baseline solutions acquired through CFD simulation. Additionally, the versatility of validated CFD models provides an unequivocal advantage in exploring infinite designs and the conceptualisation of the fluid behaviour in the designs thereof, allowing more efficient solutions to be achieved. The continued development in computing power, as well as innovative methods to enhance the capability of CFD, is expected to extend the applicability of the numerical based approach to provide more amenable solutions for power generation processes in the future.

The generic approach to simulating and solving problems in CFD, as adhered to in this dissertation, comprises of six basic phases as outlined schematically in Figure 5.1. The process begins with geometry creation which is intrinsically followed by mesh generation. For complex geometries, completion of these two initial phases is often a formidable task and is therefore categorised as the most time consuming (highlighted in Figure 5.1). This is primarily due to the geometry fidelity and quality of mesh that is required in order to ascertain credible numerically simulated results (Kitto and Schultz, 2005).

For the overarching purpose of this dissertation, numerical simulation of the 8.5E VSM (ball and ring) was accomplished using StarCCM+ version 9.02. The selection of this CFD code was based on its ability to handle large complex models. Additionally, the anticipated pulveriser geometrical modifications required to evaluate various condition scenarios could be achieved with relative ease. The innovative, intuitive simulation tools, complemented by a streamlined workflow, were an added benefit.

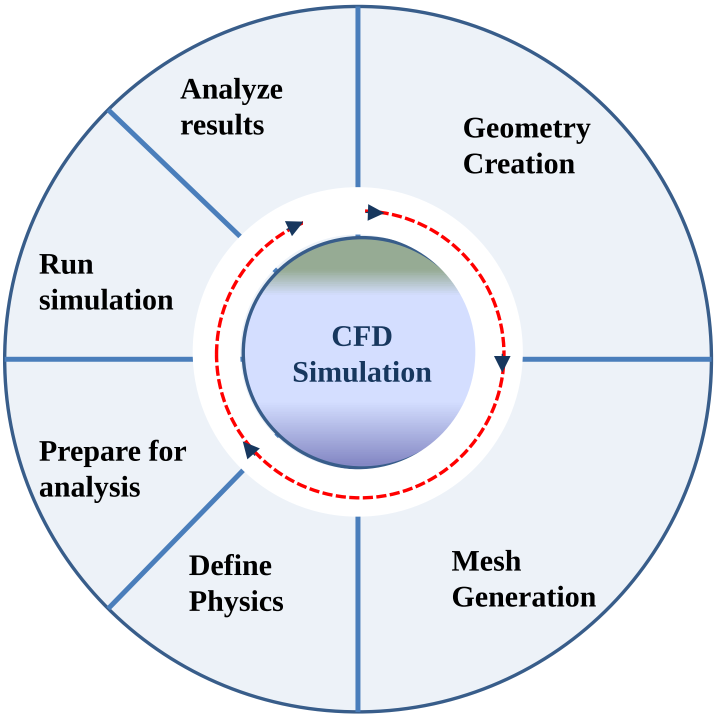

Figure 5.1 Illustrative summary of the generic approach employed to solve problems using CFD simulation (Derived from CD-Adapco, 2015)

5.2 Geometry creation

The first phase of CFD pre-processing involves the preparation of the computational domain over which a solution is sought. In this regard, there are three critical prerequisites that necessitated conscientious decisions to be made. The prerequisites included (1) the scope of the pulveriser geometry to be considered, (2) identification of inlet and outlet flow boundaries, and (3) the computational hardware available to obtain a credible solution.

The geometrical characteristics of a commercial-scale VSM (ball and ring) comprise of several complex shapes and angles (illustrated in Figure 1.5). The specific shapes and angles are fundamental to the precise operation of the pulveriser in controlling the PF throughput. The Computer Aided Design (CAD) model prepared for CFD simulation, therefore, needed to satisfactorily capture the effects of these geometrical complexities. A thorough literature review of coal pulverisers culminated in the identification of several features that are significantly influential on the flow dynamic pattern exhibited within the pulveriser domain considered.

Messerschmidt (1972) emphasised the significance of the throat gap size and angle in achieving the required flow velocities in the pulveriser. Bhasker (2002) highlighted that the presence of components inside the pulveriser affects the particle paths followed and hence the particle size distribution at the pulveriser exit. Vuthaluru et al. (2005) highlighted that various components fitted in the grinding chamber lead to secondary and tertiary swirl motions of different intensities. Vuthaluru et al. (2006) presented contours of velocity which outline the non-uniform air flow distribution at the throat gap and ascertained the primary air duct configuration to be influential on the primary air flow distribution at the throat gap region. Shah et al. (2009) reported that the classifier vane angles are important to achieve the desired particle size distribution. Bhambare et al. (2010) related the non-uniform air flow velocity from the throat region to be influential on the particle size distribution at the pulveriser outlet.

Additionally, the throat blade vane angles, as well as the classifier blade angles, impart a swirl to the fluid flow which can be considered to affect the pulveriser throughput. Although not considered previously, the presence of grinding media is anticipated to increase the flow resistance inside the pulveriser and affect the overall static pressure losses as well as the particle trajectories in the system. Therefore, the level of detail for the geometrical characteristics of the 8.5E VSM considered in the global full-scale CAD model prepared for the CFD simulation was influenced by the aforementioned factors.

Figure 5.2 illustrates an isometric view of the three dimensional domain considered for the numerical simulation. This model, referred to as the base case, was prepared in accordance to the existing VSM design as installed at Power Station A.

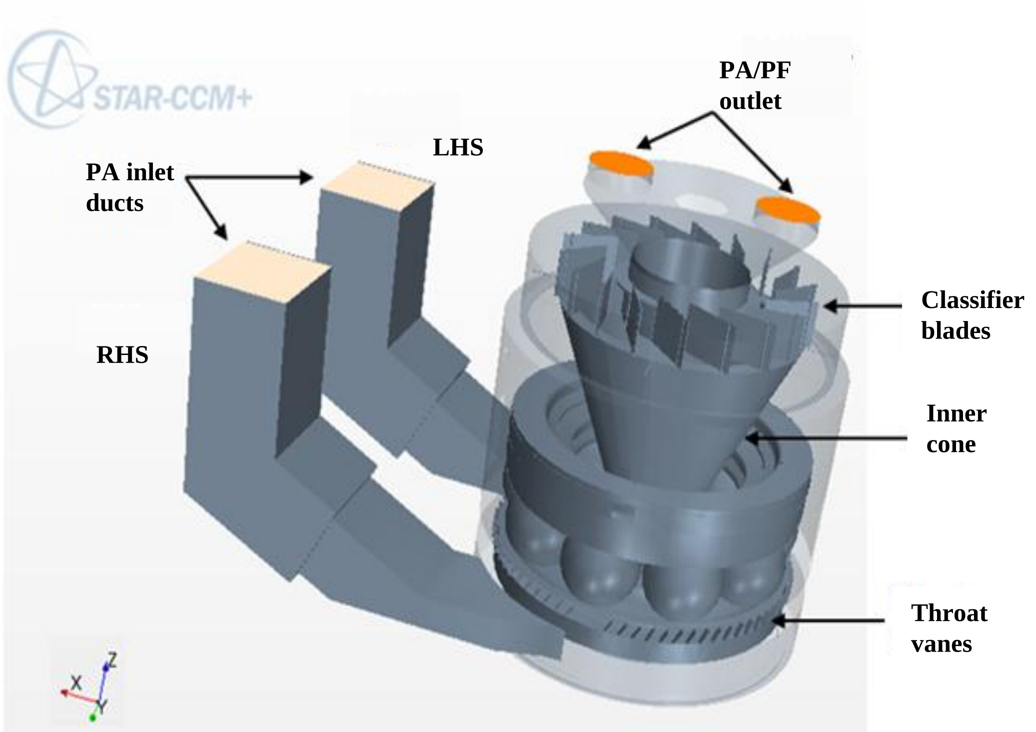

Figure 5.2 Perspective view illustrating the pulveriser domain

To demonstrate the high level of detail considered, closer views of the geometry prepared are depicted in Figure 5.3 to Figure 5.5.

Best practice guidelines suggest selecting boundary locations at areas where the fluid flow is adequately defined or can be reasonably approximated (Ansys, 2012). Therefore, the choice of inlet and outlet boundary locations was limited to the primary air (PA) inlet duct and the PA/PF outlet pipes. A holistic approach was taken to model the pulveriser by extending the domain further upstream of the pulveriser PA inlet to include both the LH and RH primary air ducts. The inclusion of these components sanctions for a more representative flow profile to be attained at the pulveriser inlet. Additionally, to assess the static pressure profile and particle size distribution at the pulveriser outlet, both PF pipe outlet turrets were considered. However, the PF pipe configuration subsequent to each of these pipes was deemed not necessary.

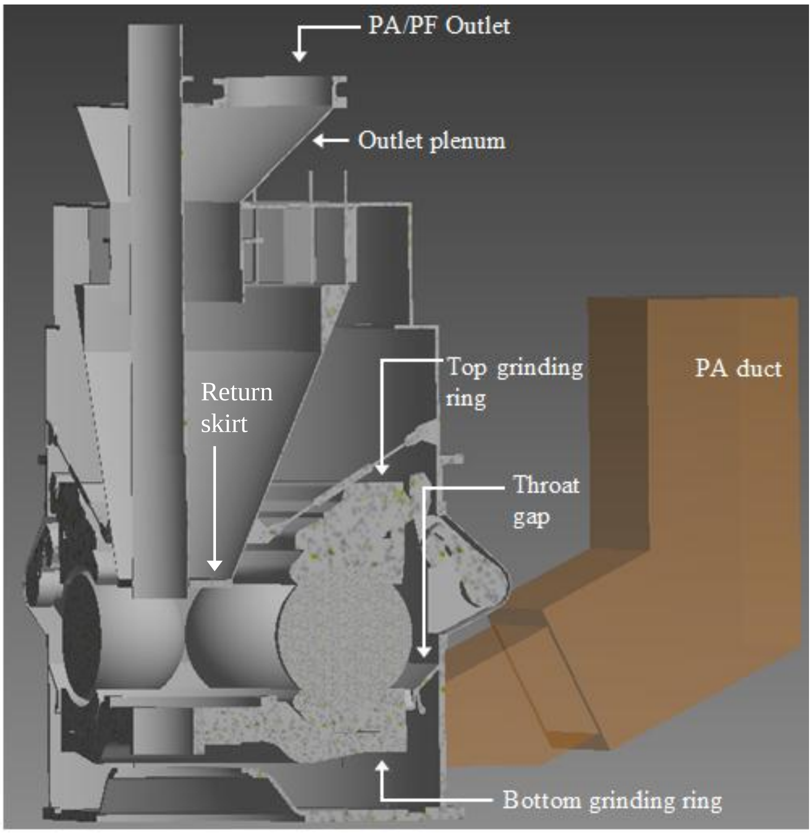

Figure 5.3 A quarter section view of the computational domain considered highlighting the pulveriser internal components and PA ducting

With complex geometry, best practice guidelines suggest evaluating the validity of the prepared and imported geometrical surface prior to generating a surface mesh. A wide range of *Surface Preparation* tools available in StarCCM+ was employed to provide diagnostic assessments of the geometry created. This necessitated manual surface repair or manipulation to be performed accordingly. However, the modifications effected were incorporated scrupulously to maintain the integrity of the geometric design.

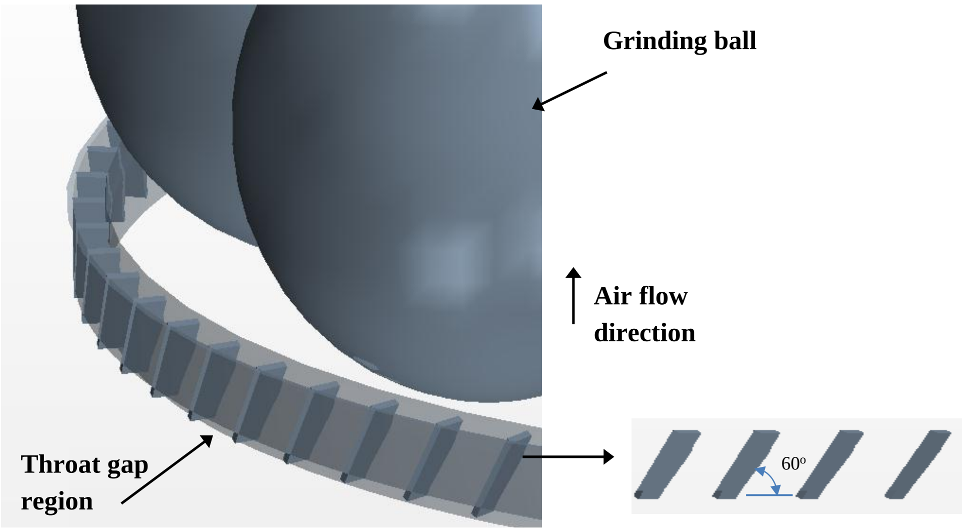

Figure 5.4 Schematic highlighting throat gap configuration with emphasis on throat gap vane angle

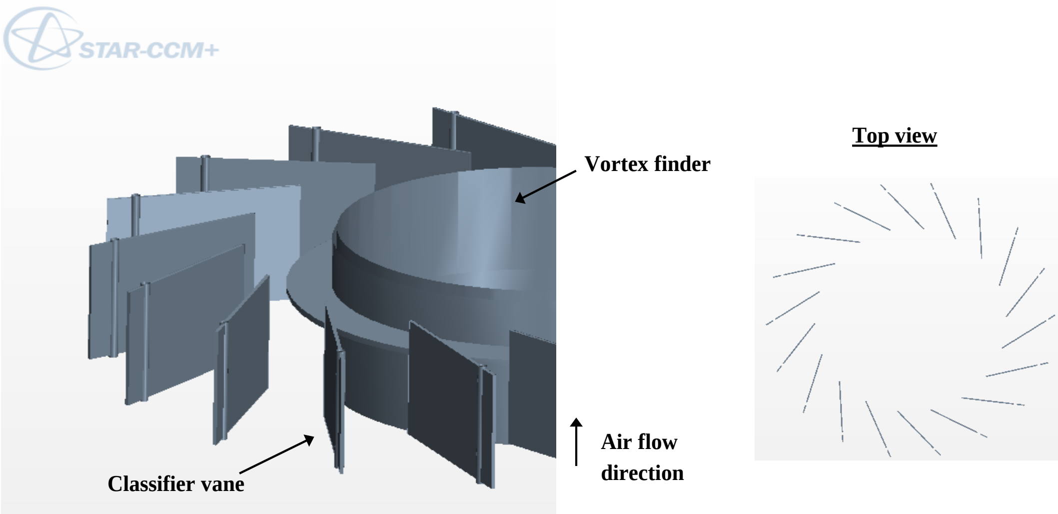

Figure 5.5 Schematic displaying classifier vane blades and vortex finder

It must be noted that simplification of the pulveriser domain using symmetry was not pursued primarily due to the anticipated swirl effects from the throat vane and classifier blade angle configurations. However, in an attempt to save on cell count, conscientious decisions to omit the raw coal feed pipe, loading gear arrangement, specifics of the classifier return skirt and brush ploughs in the air plenum chamber from the simulated domain were taken based on an assumption that these components have trivial effect on the static pressure profile or particle trajectories.

5.3 Boundary conditions

In order to facilitate the meshing process, the geometric parts created must be assigned to one or more region. A mesh is then generated for the region/s created, with each region defined by one or several boundaries. Consequently, interfaces are required to connect boundaries associated with different regions to ensure a conformal mesh is generated between regions. In a volume mesh, interfaces permit the transfer of mass and energy from one region to the other (CD-Adapco, 2014).

For the pulveriser simulation, two fluid regions and one porous region were created with their associated boundaries and necessary *in-place* interfaces. The pulveriser in its entirety and the throat region are considered fluid regions, associated with air as a continuum. The classifier rejects return skirt (highlighted in Figure 5.2 and Figure 5.6) was modelled as a porous region to enable the permeation of the fluid continuum (air).

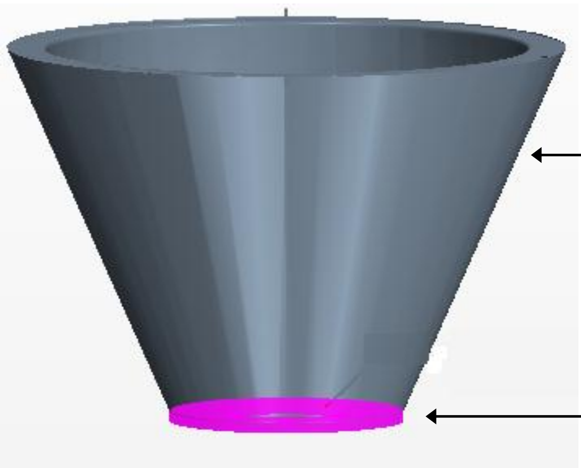

Figure 5.6 Schematic illustrating the porous region created at the classifier return skirt

Numerical solutions require boundary conditions to be explicitly assigned to all boundaries created. For the pulveriser simulation, the PA inlet mass flow rate and the static pressure outlet conditions are known. StarCCM+ suggests using a mass flow inlet boundary in combination with a pressure outlet boundary. Therefore, the PA inlet was modelled as a mass flow inlet boundary and the PA/PF outlet was modelled as a pressure outlet boundary, as highlighted in Figure 5.2. Additionally, the use of these boundary conditions requires the fluid temperature at the pulveriser inlet and outlet to be specified. For all other boundaries, a *wall type* boundary was specified. Wall type boundaries represent an impermeable surface and are ideally used to bound fluid regions.

5.4 Meshing

A mesh can be explicated as a discretized representation of a geometric domain. StarCCM+ employs the finite volume discretization technique to divide the computational domain into a finite number of control volumes. The partial differential equations that govern fluid flow are then integrated across these control volumes in order to obtain a solution (CD-Adapco, 2014).

An important challenge in mesh generation is to create a volume mesh of suitable quality. The creation of the volume mesh is influential on the rate of convergence and accuracy of a numerical solution. It must be noted that there is no set method explicitly explicated in literature to generate volume meshes for coal pulverisers. However, best practice guidelines recommend commencing with a good quality surface mesh. Additionally, volume mesh generation should be strategic to ensure regions with high velocity gradient are designed with satisfactory mesh resolution (CD-Adapco, 2014).

For the pulveriser simulation, Surface Preparation Tools were employed to optimize the geometry surfaces imported in StarCCM+, as previously outlined. CAD packages are not designed to produce models that are directly conducive to the CFD environment, therefore, this process ensured that all surfaces were closed, manifold and non-intersecting thereby permitting volume meshing to begin. Areas within the pulveriser, such as those surrounding the throat gap, classifier and vortex finder (depicted in Figure 5.4 and Figure 5.5) are anticipated to have higher velocity gradients. This was considered when the volume mesh was generated. Conversely, extended boundaries such as the PA inlet duct (illustrated in Figure 5.2) and PA/PF outlet (highlighted in section 5.4.1 hereafter), which were primarily included in the computational domain to minimize the effects of the boundary conditions imposed, were populated with a coarser mesh to prevent unnecessary computational time. Furthermore, the pulveriser created in CAD modelled the solid parts of the pulveriser that surrounded the fluid flow. Therefore, extraction of the fluid volume was undertaken in StarCCM+.

5.4.1 Selection of meshing models

For the pulveriser simulation, the option of unstructured mesh generation was selected based on the high degree of accuracy achievable with this meshing strategy for complex geometries (Khare et al., 2009). Meshing models control the type of surface and volume mesh generated. Surface and volume mesh models were selected and modelled in conjunction with each other. The models chosen included the surface remesher, polyhedral, prism layer and extruder.

While the tetrahedral mesher model is the fastest mesh generator which consumes the least amount of memory, the polyhedral mesher model was selected based on its ability to generate a numerical solution with equivalent accuracy by using up to eight times less cells. Additionally, populating a computational domain with polyhedral cells is especially beneficial were recirculation is anticipated. The arbitrary shaped polyhedral cells have an average of 14 cell faces thereby improving the approximation of gradients to neighboring cells in a domain (CD-Adapco, 2014).

The associated improvement in solution accuracy obtained from a simulated domain compacted with polyhedral cells is typically enhanced by including the Prism Layer model. Prism layers allow the physics solvers to approximate the flow profile near wall boundaries (defined within regions) more accurately. For large volumes like the pulveriser, where only the gross flow features are required, the flow profile near wall boundaries can be solved using a high y+ type mesh. This technique requires the construction of only a few prism layers to achieve acceptable results (CD-Adapco, 2014).

Recall from section 5.3, a pressure outlet boundary was chosen for the PA/PF outlet. The use of this boundary condition makes the solution susceptible to reverse flow at the boundary. In an attempt to circumvent the effects of reverse flow, by extending the computational domain further downstream of the specified boundary, the Extruder mesh model was selected to create orthogonal extruded cells at the PA/PF outlet boundary surfaces. The extrusion is produced by user allocated values for the number of layers, direction and magnitude. The selection of this model to extend the PF outlet boundary in StarCCM+, as opposed to using the CAD package, was based on the relative ease at which the optimum extrusion magnitude (and hence, fewer cells) could be identified to counter effect the reverse flow condition.

5.5 CFD analysis of single-phase flow

5.5.1 Physics models selection

The appropriate selection of physical models is essential to define the primary variables as well as the mathematical formulation that will govern how the physical phenomenon is characterized for a given numerical solution. Physical model selection is independent of the meshing models (CD-Adapco, 2014).

The Three-Dimensional model is designed to model the space of three dimensional meshes. Since the pulveriser domain was prepared in three dimensions (illustrated in Figure 5.2), a three dimensional mesh was generated, prompting the selection of the Three-Dimensional model to define the space.

The pulverisation process is time dependent. However, time varying solutions for such processes are rarely performed largely due to the limitations of the computational hardware. A review of relevant literature revealed that steady state models provided sufficiently detailed information required to elucidate the gross flow profile within the pulveriser domain. Therefore, the pulveriser flow field was modelled in steady state.

Typically, coal pulverisers are subjected to two major flow input streams, coal and air. The selection of a material model is required to manage the thermodynamic and transport properties relevant to the fluid being simulated. For the initial part of the CFD simulation, single-phase flow (only air) was simulated, therefore, the Single-Component Material model was selected to model the gas (air). A different approach was used for the inclusion of solid material (coal) during two-phase flow modelling and this will be elaborated on in section 5.6.

The viscous flow regime for the pulveriser simulation was considered to be turbulent, as highlighted in Chapter 3 by Equation 3.9. This flow regime classification is in consensus with previous studies and the velocity and hydraulic diameter, as required to estimate *Re*, was similarly derived from the mass flow rate of PA and the dimensions of the inlet PA duct, respectively (Vuthaluru et al., 2006).

The Ideal Gas Model was used to derive the density of the continuous phase (air) using the ideal gas law. Additionally, the Gravity Model was selected to account for gravitational acceleration in the simulated domain. When these two models are used in combination, the gas density becomes a function of the absolute pressure. This necessitated appropriate specification of the system operating pressure.

Since the air flow velocity encountered in the pulveriser domain is not significantly high (<200 m/s), it results in a low Mach number (< 0.3) and, therefore, the flow was categorised as being incompressible (Vuthaluru et al., 2006). Two approaches exist in StarCCM+ to model flow and energy. These approaches are Coupled and Segregated. However for incompressible flows as is present in the pulveriser domain, best practice guidelines recommend the use of the Segregated Flow Model, therefore, the Segregated Flow Model was selected. Using this approach, the flow equations for pressure and velocity are solved sequentially (as opposed to simultaneously in the coupled approach) in a segregated manner. The linkage between the momentum and continuity equations is achieved with a predictor-corrector approach (CD-Adapco, 2014).

Turbulent flows are characterised by rapid deviations in flow velocity. These flows often exhibit irregular, small-scale and high frequency variations in both space and time. It is possible to simulate turbulent flow directly however, it is computationally expensive. In this case a modified version of the Reynolds Averaged Navier-Stokes (RANS) equations is required. However, this modification results in additional unknown variables. Consequently, StarCCM+ has built-in sub-turbulent models that can be applied to approximate these unknown variables (Cd-Adapco, 2014).

For the pulveriser simulation, two of the four sub-turbulent models built into StarCCM+ were applicable. These were the Realizable K-Epsilon Model (RKE) and the Reynolds Stress Turbulent Model (RST). Best practice guidelines highlight that the RKE model provides a good compromise between robustness, accuracy and computational cost and is suitable for flow domains prevalent with recirculation. Alternatively, the RST Model is better suited for domains where high swirling flows are anticipated, although it is considered to be more computationally expensive. Additionally, obtaining a fully converged solution using the RST Model may require more iterations than the RKE (CD-Adapco, 2014).

An attempt to compare the results produced by employing each of these models was undertaken during initial simulations of single-phase flow (air). While a converged solution could be attained relatively quickly with the RKE model, the RST model appeared very mesh sensitive and the solution diverged within 50 iterations. A comparative analysis of model-predicted outcomes achieved through the use of selected turbulent models was undertaken by Afolabi (2012). In relation to experimental results, the discrepancy highlighted between the velocity profiles predicted between the RST and RKE models was marginal. At the additional computer expense, the study concluded that the use of the RST model was unjustified. With that said, the RKE Model was selected in this present study for all subsequent simulations performed over the pulveriser domain.

In numerical simulations, turbulent flows are significantly affected by the presence of walls, where the viscosity affected regions have large gradients in the solution variables This necessitates the use of a suitable wall treatment model to effectively capture the flow profile of wall bounded flows. The wall y+ value is a non-dimensional distance used to describe how coarse or fine a mesh is for a particular flow (Salim and Cheah, 2009). For the pulveriser simulation, a combination of coarse and fine meshes has been used. The All y+ wall treatment is a hybrid treatment that emulates the high y+ wall treatment for coarse meshes, and the low wall treatment for fine meshes. Consequent to the above-mentioned considerations, the All y+ wall treatment model was determined the preferred model and was used in conjunction with the RKE model.

5.5.2 Physics input data

In Chapter 3, experimental results obtained during the primary air flow traverse and static pressure measurement tests were presented. The results obtained were selectively employed as inputs to the CFD calculation. As the experiments were undertaken with varying PA flow rates, the relevant input data was applied to each simulation, as outlined in Table 5.1. As previously highlighted, the primary air flow traverse was only conducted for one primary air flow rate. Therefore, a 7 % correction factor was applied to DCS measured primary air flow rates for the other two primary air mass flow rates simulated. In each simulation, the static gauge pressure measured experimentally at the pulveriser outlet (point F, depicted in Figure 3.19), was employed to calculate the absolute pressure at the pressure outlet boundary. Additionally, since the dissimilarity between the LH and RH primary air flow was revealed to be negligible (refer to Table 3.5), equal primary air flow rates were applied to each primary air duct in the simulation. It must be noted that the single-phase flow simulations were performed with air at ambient temperature.

Table 5.1 Input physics data for the pulveriser simulation

	Units	Simulation 1	Simulation 2	Simulation 3
$T_{measured}$	^{o}C	25.10	-	-
T_{DCS}	^{o}C	-	25.05	25.12
$\dot{m}_{PA,\ measured}$	kg/s	9.80	-	-
$\dot{m}_{PA,\ corrected}$	kg/s	-	8	7
F, $P_{static,\ measured}$	Pa	1007.42	628.41	396.58
Atmospheric Pressure	Pa	85000		
Absolute Pressure	Pa	86007.42	85628.41	85396.58

5.5.3 Mesh refinement study

In order to gain confidence in the adequacy of the mesh resolution, a mesh refinement study must be performed. Durbin and Medic (2007) and Tu et al. (2008) recommend computing the numerical solution on a sequence of finer and finer meshes until further mesh refinement causes a negligible change in the simulated results. Once achieved, it can be concluded that the discretization error has been reduced to an acceptable error and the computed solution is independent of the mesh.

An iterative approach was adopted for the mesh refinement study. Prior to polyhedral mesh generation, a characteristic base size that provided adequate core mesh density throughout the computational domain was selected. This necessitated a few preliminary simulations to be executed, using a range of base sizes. In determining the optimum base size, areas within the pulveriser domain that experienced high velocity gradients were simultaneously identified. These areas were the throat gap and the vortex finder.

As previously outlined, best practice guidelines suggest a higher mesh resolution be applied to areas displaying high velocity gradients in order to resolve the flow characteristics within those areas accurately. For the pulveriser simulation, this has a direct impact on solution run time however, the subsequent increase in model fidelity is crucial to attaining accurate static pressure measurements which are central to this study. Strategic shapes (created to avoid increased cell count unduly) were employed to define volumetric controls applied to high velocity gradient areas. Following which several simulations were required to identify the most plausible cell size for these volumetric controls. For each simulation, a progressively smaller cell size was applied to each volumetric control (one at a time). The iterative process concluded when the discrepancy in static pressure calculated between one iteration and the succeeding iteration was insignificant.

With reference to the measurement points highlighted in Figure 3.15, Table 5.2 presents the static pressure loss results calculated for a range of cell sizes defined in the throat gap area (GB). Notably, the discrepancy in static pressure drop predictions observed between simulation 3 and 4 appears to be trivial. Hence, a cell size of 8 mm was chosen to discretize the throat gap area. Figure 5.7 displays mesh generated in the throat gap region.

Table 5.2 Summary of pressure drop results across the throat gap region for varying mesh densities in the throat gap region

Simulation	**Cell size (mm)**	ΔP_{GB} **(Pa)**	**Discrepancy (%)**
1	25	1409.19	-
2	15	1250.83	10.92
3	10	1177.91	5.83
4	8	1165.56	1.05

Analogous to the analysis performed in the throat gap area, and with reference to Figure 3.14 and Figure 3.15, Table 5.3 presents the static pressure loss results calculated for a range of cell sizes defined in the vortex finder (DF). The variation in pressure drop results was insignificant after the cell size was reduced from 50 mm to 10 mm. A compromise between solution accuracy and total cell count was justified in this instance and 50 mm was selected as the most plausible cell size for the vortex finder. Figure 5.8 illustrates the final mesh generated for the vortex finder in relation to adjacent cells.

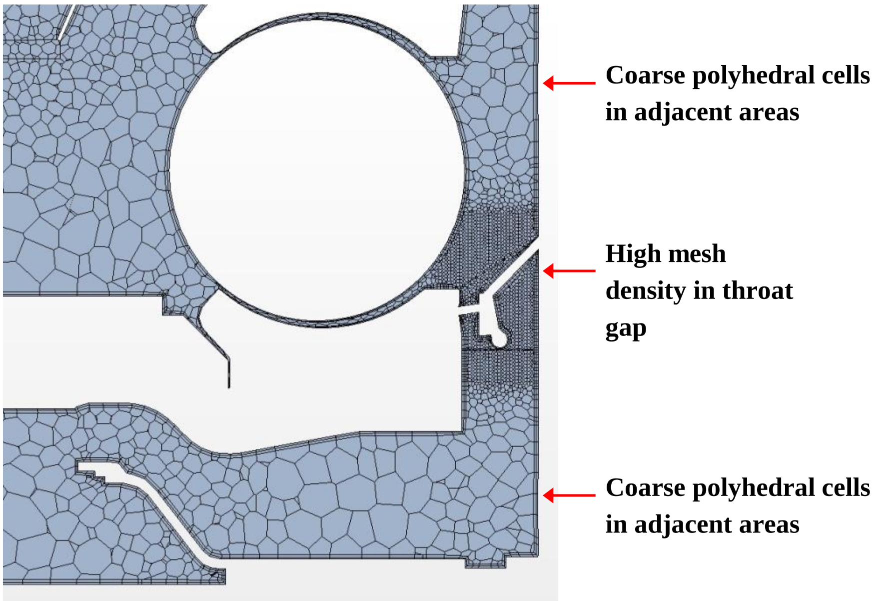

Figure 5.7 Cross sectional view of the pulveriser highlighting finer cell generation in the throat gap

Table 5.3 Summary of pressure drop results calculated across the vortex finder for varying mesh densities in the vortex finder

Simulation	**Cell size (mm)**	**ΔP_{DF} (Pa)**	**Discrepancy (%)**
1	100	332.82	-
2	80	302.71	9.05
3	50	290.72	3.96
4	10	288.19	0.87

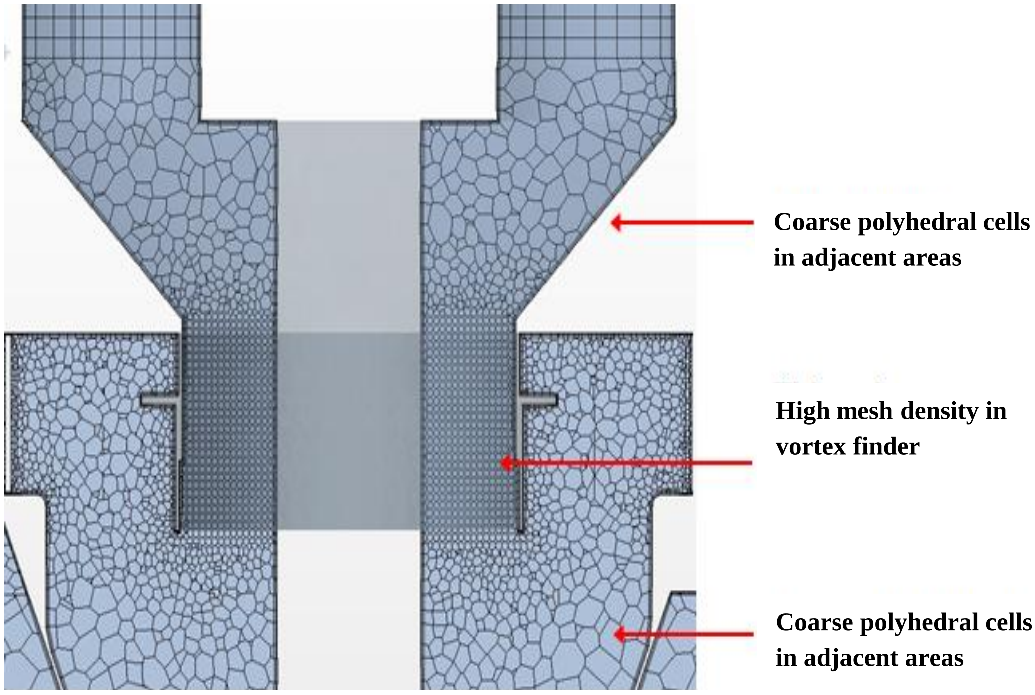

Figure 5.8 Cross sectional view of the pulveriser highlighting finer cell generation in the vortex finder

Recall from Chapter 3, section 3.3.3, the pulveriser *wall* static pressure profiles were ascertained experimentally. In order to perform a comparative analysis between experimental and numerical results, the near wall static profile must also be resolved accurately. Therefore, a concerted effort to realize a reasonable number of prism layers near boundary walls was undertaken. With reference to Figure 3.19, the largest pressure drop was observed across the throat gap. Therefore, the static pressure drop across this region was selected to be analysed for the rational identification of a suitable number of boundary layers for all walls in the pulveriser domain.

Table 5.4 presents the predicted static pressure results attained from several simulations. Two prism layers were selected for all wall boundaries as additional layers demonstrated insignificant variation in the measured outcome.

Table 5.4 Summary of simulated pressure drop results measured across the throat gap region for a range of wall boundary layers created in the pulveriser domain

Simulation	Wall boundary layers	ΔP_{GB} (Pa)
1	2	1156.65
2	5	1155.72
3	10	1155.70

Figure 5.9 presents a scalar plot of wall boundaries defined within the pulveriser domain, highlighting the wall y+ values to be less than 300 which are in consensus with best practice guidelines (CD-Adapco, 2015). This intimated the mesh generated to be highly satisfactory for the physics, turbulence and wall treatment models selected. Table 5.5 succinctly summarises the final mesh settings employed in the simulation.

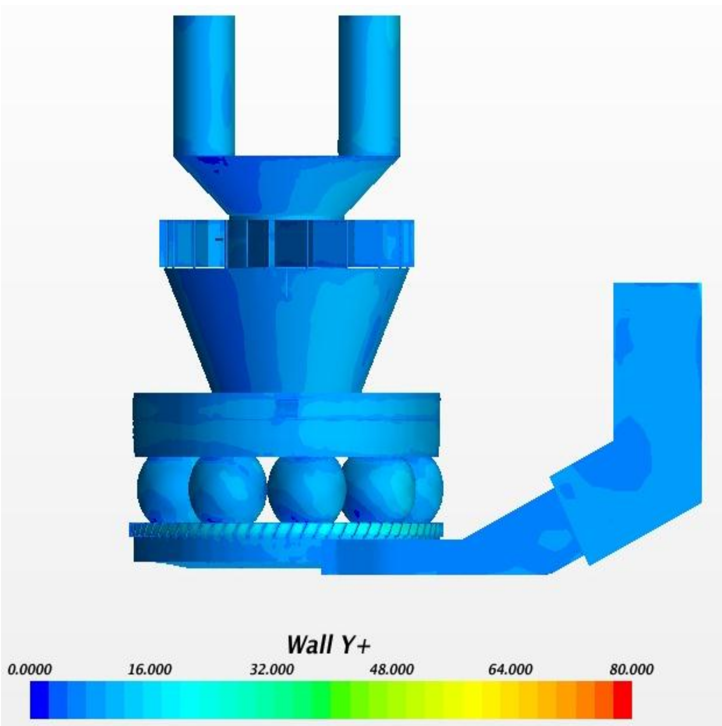

Figure 5.9 Scalar plot showing y+ values for final mesh settings

Table 5.5 Final mesh settings for the pulveriser simulation

<table>
<tr><th colspan="2">Mesh characteristic</th><th colspan="2">Value</th></tr>
<tr><td colspan="2">Base size</td><td colspan="2">100 mm</td></tr>
<tr><td colspan="2">Number of prism layers</td><td colspan="2">2</td></tr>
<tr><td colspan="2">Prism layer stretching</td><td colspan="2">1.3</td></tr>
<tr><td colspan="2">Prism layer thickness</td><td colspan="2">10 mm</td></tr>
<tr><td colspan="2">Surface growth rate</td><td colspan="2">1.3</td></tr>
<tr><td colspan="2">PF pipe extrusion length</td><td colspan="2">1000 mm</td></tr>
<tr><td>Region</td><td>Boundary part</td><td>Minimum cell size</td><td>Target cell size</td></tr>
<tr><td rowspan="9">Pulveriser</td><td>Grinding balls</td><td rowspan="9">10 mm</td><td rowspan="9">100 mm</td></tr>
<tr><td>Casing</td></tr>
<tr><td>Primary air ducts</td></tr>
<tr><td>Inner cone</td></tr>
<tr><td>Outlet plenum</td></tr>
<tr><td>Top ring</td></tr>
<tr><td>Bottom ring</td></tr>
<tr><td>Classifier vanes</td></tr>
<tr><td>Vortex finder</td></tr>
<tr><td rowspan="4">Throat</td><td>Casing</td><td>10 mm</td><td>100 mm</td></tr>
<tr><td>Throat vanes</td><td rowspan="3">5 mm</td><td rowspan="3">10 mm</td></tr>
<tr><td>Inner ring</td></tr>
<tr><td>Outer ring</td></tr>
<tr><td rowspan="2">Volumetric control (Continuum)</td><td>Vortex</td><td colspan="2">50 mm (absolute)</td></tr>
<tr><td>Throat gap</td><td colspan="2">8 mm (absolute)</td></tr>
<tr><td>Total cell count</td><td colspan="3">3531775</td></tr>
<tr><td>Mesh Generation time</td><td colspan="3">32 minutes</td></tr>
</table>

5.5.4 Assessing solution convergence

Analysis of solution convergence was undertaken through evaluation of five residual plots. Each residual, generated in StarCCM+ as the solution progresses, is a measure of the overall imbalances associated with the conservation of flow properties delineated in the model. The downward trend of these residuals, to an order of magnitude between 10^{-3} and 10^{-4}, suggest a converged solution (Tu et al., 2008). Best practice guidelines suggest monitoring engineering parameters of interest in addition to residuals, thereby collectively allowing a comprehensive assessment of solution convergence.

In the pulveriser simulation, an engineering parameter of interest was the static pressure at specific locations along the vertical height of the pulveriser. Therefore, a derived part was placed at the locations of interest in the computational domain. X-Y plots were subsequently defined for each derived part to highlight the variation in the static pressure results during solution iteration. Convergence was said to be reached once the fluctuation in the engineering parameter monitored inclined to a trivial value (CD-Adapco, 2014).

Based on the aforementioned criteria, analysis of the residual plots supplemented by the static pressure monitor plots intimated a fully converged solution was generated.

5.5.5 Single-phase (cold) pulveriser simulation results and discussion

The construction of scalar and vector contour plots in StarCCM+ proved particularly useful as they provided a visual representation of the overall flow phenomenon that exists in the simulated domain. Presented in Figure 5.10 and Figure 5.11, are contour plots generated to conceptualize the effect of the pulveriser internal components on the magnitude of the air flow velocity along the height (Z direction) of the pulveriser. The velocity profile was discernibly affected by both the throat gap and vortex finder region. The highest air flow velocity is observed across the throat gap region. This is congruent with results from previous studies conducted by Vuthaluru et al. (2006).

Figure 5.11a presents a top view of the throat gap region depicting the magnitude of the velocity around the throat gap. The angled vanes in the throat gap impart a swirl to the air flow, as highlighted by the direction of the red vectors in Figure 5.11b. The air flow distribution reasonably distributed throughout the circumference of the throat gap region, as outlined in Figure 5.11c. It must be noted that areas that exhibit high air flow velocities are more susceptible to wear during two-phase flow (air and coal) conditions.

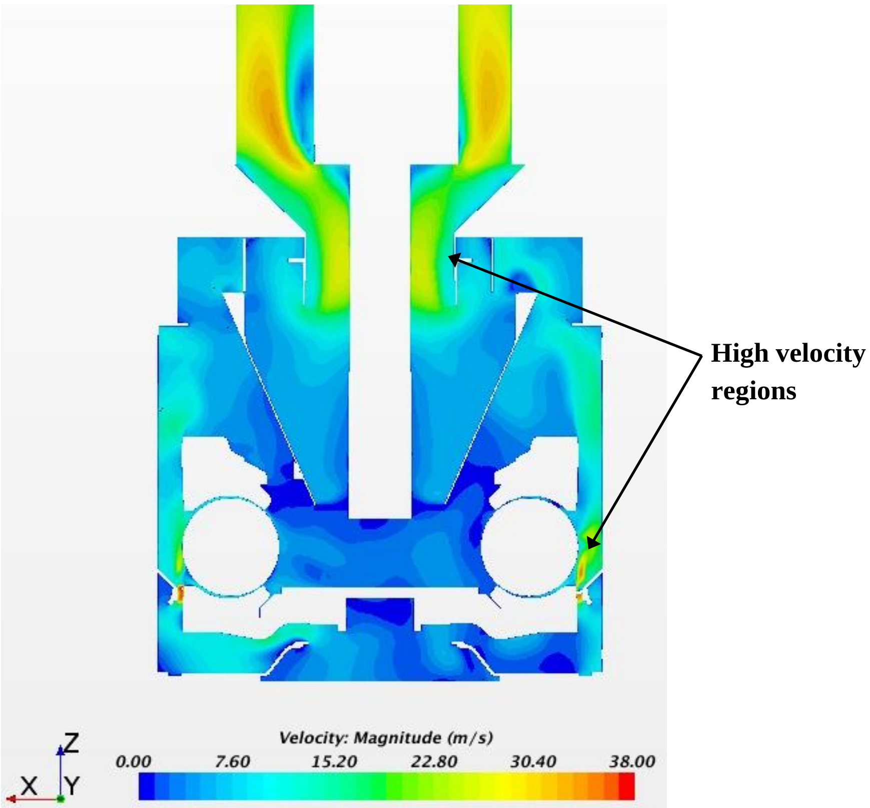

Figure 5.10 Contour plot depicting the influence of pulveriser internal components on the velocity profile

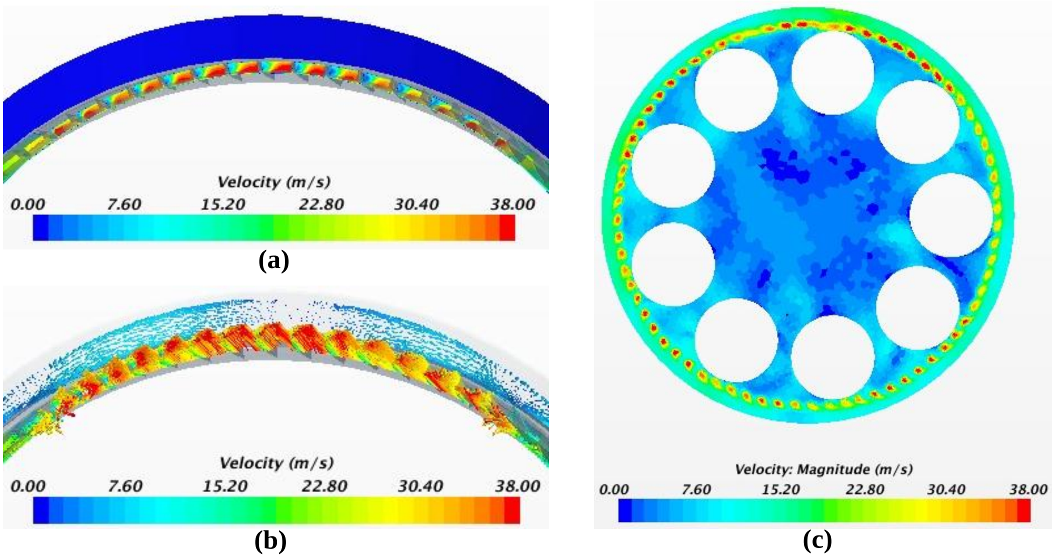

Figure 5.11 Scalar contour plot (a) highlighting the magnitude of the air velocity in the throat gap, (b) vector contour plot illustrating the effect of the angled vanes and (c) scalar contour plot depicting even air flow distribution at throat gap

Presented herein, Figure 5.12 and Figure 5.13 are the scalar contour plots exposing the effect of the pulveriser internal components on the static pressure distribution pattern along the same central plane generated for the velocity analysis.

The highest static pressure was observed in the primary air duct, with a slight reduction as the air enters the air plenum chamber region. The contour plot highlights a higher pressure at the far RH side of the air plenum chamber. This could be related to the arrangement of the PA ducts, as the primary air enters at the LH side, which may cause the flow to be forced towards the far right end, resulting in a higher pressure. A significant reduction in the static pressure was evident across the throat gap region and based on literature, this observation was not entirely unexpected. Notably, the static pressure above the throat gap up to the classifier is relatively consistent, thereby highlighting components in this region to have a smaller effect on the overall static pressure losses in the system. Analogous to the higher velocity gradient evident in the vortex finder, there appeared to be a similar trend with a higher pressure gradient observed in this area.

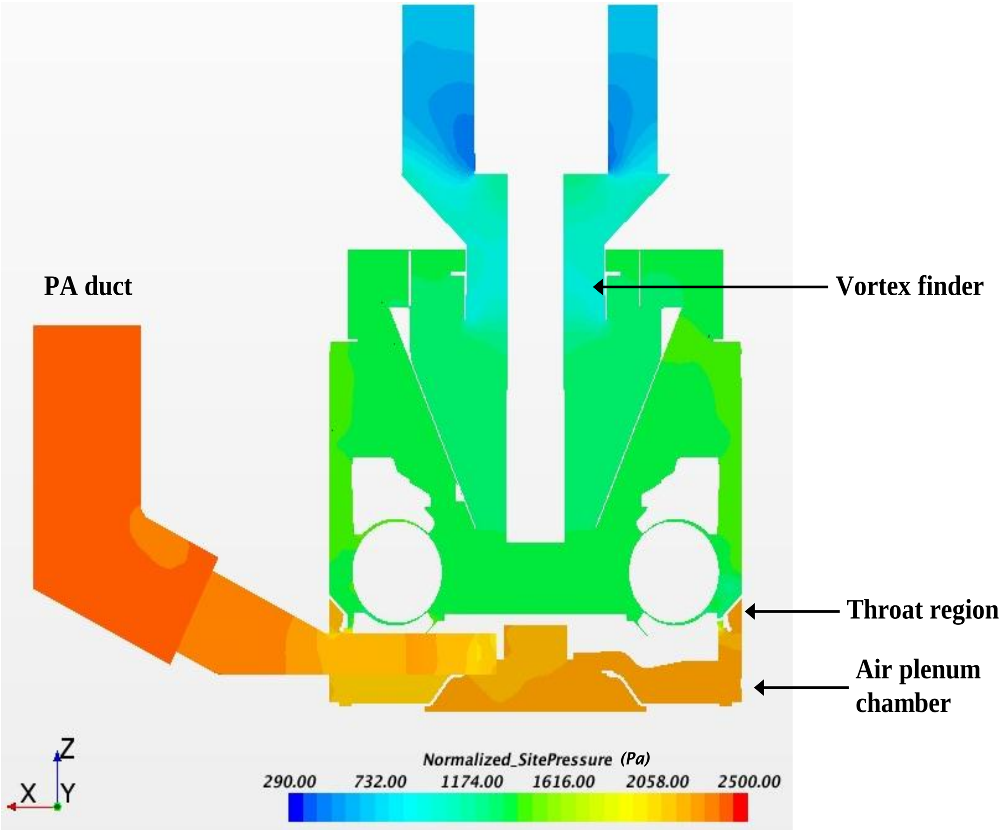

Figure 5.12 Contour plot depicting the influence of pulveriser internal components on the static pressure profile

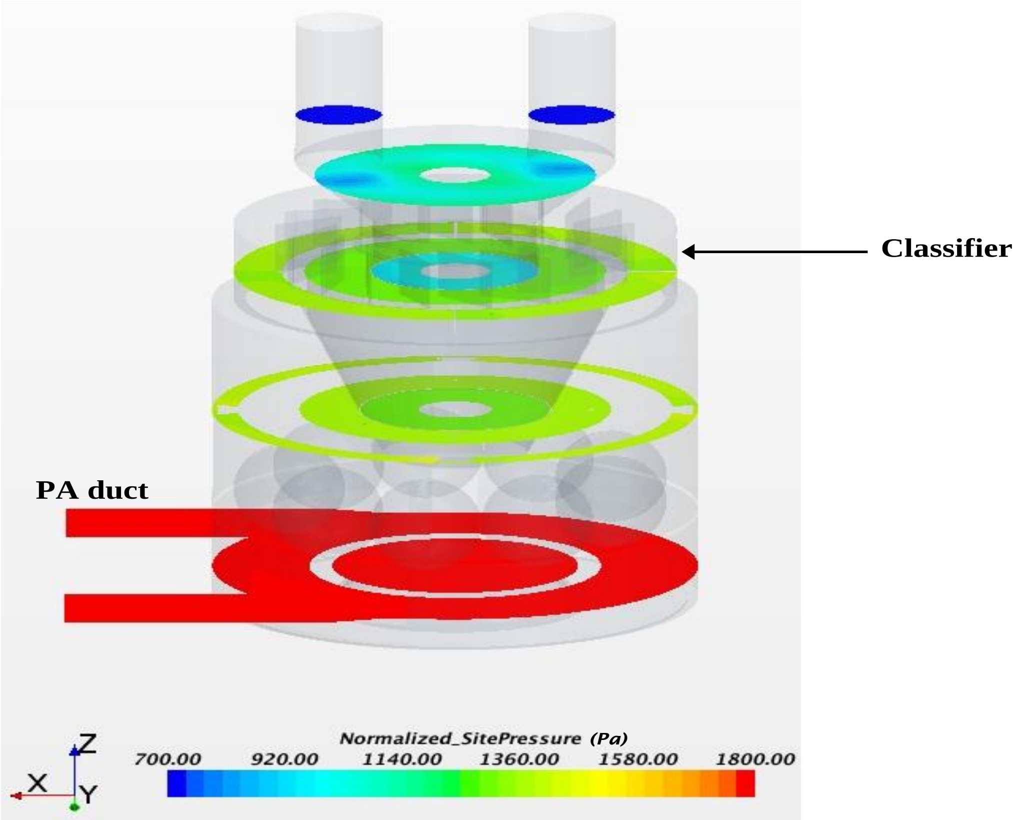

Figure 5.13 Contour plot depicting the static pressure profile in the pulveriser

Table 5.6 summarises the static pressure measurements, obtained for three PA mass flow rates, recorded at specific points within the simulated domain. The location of the measurement points is referenced in Figure 3.14 and Figure 3.15.

Table 5.6 Summary of static pressure simulation results obtained for three mass flow rates of primary air

	Simulation 1	**Simulation 2**	**Simulation 3**
	7 kg/s	**8 kg/s**	**9.8 kg/s**
Measurement point	$P_{static,\ simulated}$ (Pa)	$P_{static,\ simulated}$ (Pa)	$P_{static,\ simulated}$ (Pa)
A	1030.53	1457.61	2243.84
B	584.90	876.63	1378.45
C	590.04	883.27	1390.97
D	569.38	860.15	1356.28
E	350.64	569.09	919.62
F	395.58	628.41	1007.42
G	1119.50	1517.35	2412.25

5.5.6 Validation of the single-phase CFD model through experimental correlation

CFD validation refers to the establishment of a correspondence between fluid flow profiles predicted numerically through computation and actual fluid flows depicted in real life. The conventional approach to CFD validation requires relevant experimental work to be performed in order to establish a standard form of reference (Marvin, 1995).

Recall from Chapter 3, section 3.3.3, the installation of several static pressure ports along the vertical height of the pulveriser provided a means for a fundamental validation of the numerical model to be performed. The results obtained from the experimental work pertinent to the validation of the CFD model were graphically illustrated in Figure 3.19. The ability of the numerical model to accurately predict the static pressure profile in the pulveriser can be evaluated by the intensity of the correlation between the experimentally determined and numerically predicted static pressure values. As previously outlined, the measurement points created in CFD were positioned at the same location as in the physical experiment by employing a derived part.

The excellent correlation demonstrated between the static pressure profiles obtained experimentally and the static pressure profiles predicted through computational modelling as presented in Figure 5.14, serves to validate the CFD model developed. The numerical correspondence established between the experimental and predicted results at points (BCD), although visibly higher, is still satisfactory. The best fit was attained across points (GA) and (EF). The overall incongruity (not shown) between the experimental and numerically predicted static pressure results was calculated to be less than 5 % for each scenario, thereby highlighting the accuracy of the model and reproducibility of the simulated results.

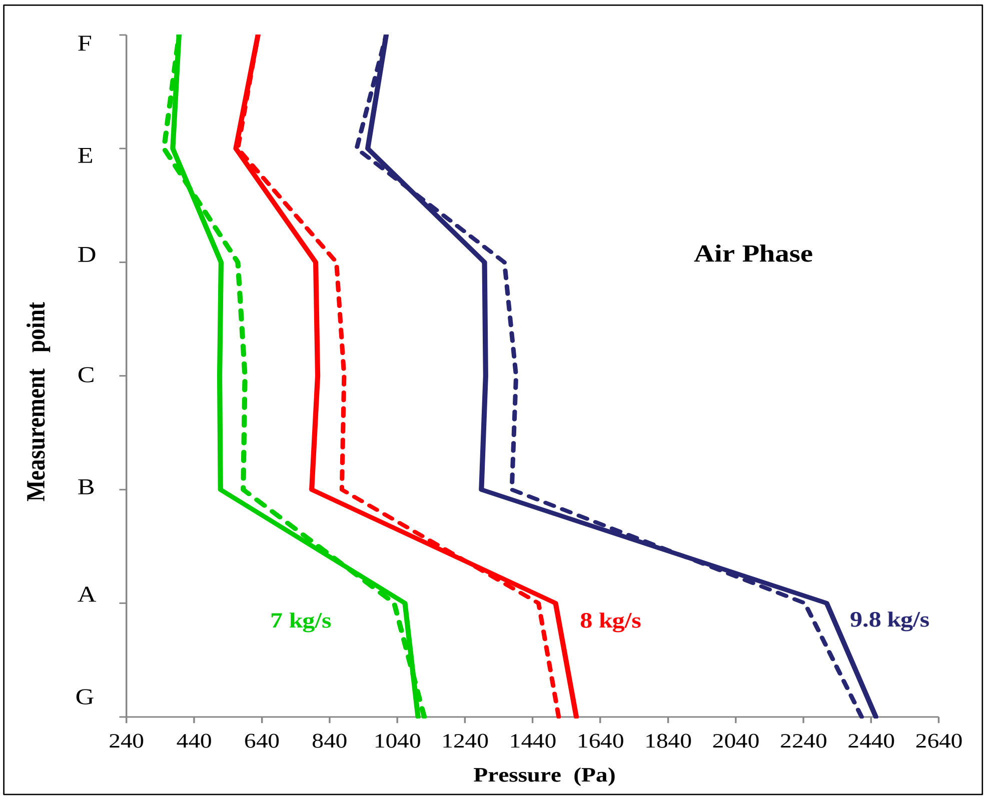

Figure 5.14 Experimental (solid) and simulated (dashed) static pressure profile for three PA mass flow rates (7 kg/s, 8 kg/s and 9.8 kg/s)

To this end, the CFD model developed has only considered single-phase flow (air) at ambient air temperature. In actual operating conditions, a pulveriser is subjected to two major input streams, a hot fluid stream (air) and a cold solid stream (coal). Hence, coal pulverisation can be categorised as a multiphase flow process with heat transfer. As previously demonstrated experimentally, the presence of coal particles has a significant effect on the magnitude of the static pressure sensed within the pulveriser. Therefore, employment of the numerical model to predict the two-phase static pressure profile necessitates the inclusion of coal and heat transfer in the computational domain. The ensuing section presents the introduction of the solid-phase into the pulveriser domain.

5.6 Solid-phase modelling

Prior to the inclusion of solid particles, a widely employed approach to enhance stable multiphase flow simulations requires initially a fully converged and valid solution for the air phase (Bhasker, 2002; Vuthaluru et al., 2006; Afolabi, 2012). This approach was adopted in this study and a fully converged solution obtained for the continuous phase was presented in section 5.5.

In general, two models exist for solid-phase modelling in StarCCM+. These are the Eulerian and Lagrangian models. Recall from Chapter 2, section 2.3, the main advantages and disadvantages of each model were briefly outlined. As previously mentioned, the coal particle size distribution at the pulveriser exit is a key performance indicator through which the pulveriser internal condition may be evaluated. Apart from assessing the mechanical condition of the pulveriser through the use of the static pressure drop measurements, the particle size distribution may provide a basis to evaluate the mechanical condition. Given the shortcomings posed by the Eulerian framework to provide detailed information about particle trajectories, the Lagrangian framework emerged as the most suitable approach to model the particulate phase for the pulveriser considered in this study.

5.6.1 Coupled approach

5.6.1.1 Physics models selection

Analogous to the physics model selection process completed to define the single-phase flow condition, appropriate models must be selected to define the Lagrangian framework chosen to model the solid-phase.

Since the pulveriser is subjected to coal particles which are generally a pure substance in solid form, the selection of a Solid, Single-Component Material model was necessary. A material model was required to manage the thermodynamic properties of the coal particles simulated in the pulveriser domain. Additionally, the shape of coal particles was considered to be spherical, this prompted the selection of the Spherical Particles model (CD-Adapco, 2015). As the quantity of moisture evaporated from raw coal during normal pulveriser operation accounts for a relatively small percentage of the total mass of coal supplied to the pulveriser, the density of coal particles was assumed to be invariant throughout the computational domain, this culminated in the selection of the Constant particle density model and a coal density of 1200 kg/m^3 was employed.

In the Lagrangian framework, the influence of solid particles on the continuous phase may be modelled by employing the Coupled or Uncoupled approach. Briefly, when the coal mass loading is relatively small, the solid-phase can be characterized by a finite number of particles, whose trajectories can be computed from a pre-calculated velocity field generated for the continuous phase. This is referred to as the *uncoupled* approach. In contrast, the *coupled* approach demands the simultaneous computation of the particle trajectories and the flow field, as each particle contributes to the momentum, mass and energy of the continuous phase (Tu et al., 2008). Since the particles are expected to reduce the momentum of the air phase as well as increase the turbulence in the domain, the Two-Way coupling model was selected.

Forces exerted on the coal particles due to its velocity relative to the continuous air phase were considered through the selection of the Drag force model. The selection of a drag coefficient is subsequently required to formulate the drag forces acting on the particle when Two-Way coupling is activated. Best practice guidelines suggested the Schiller-Naumann correlation to most accurately define the drag coefficient for spherical particles (CD-Adapco, 2014).

As previously outlined in section 5.5.1, the flow regime of the continuous air phase is characterised as turbulent and as can be expected, coal particles injected into a turbulent flow field will not exhibit a deterministic motion. Alternatively, each particle will have their own random path as a result of their interaction with the fluctuating turbulent velocity flow field (CD-Adapco, 2014). To account for this phenomenon, the Turbulent Dispersion model was chosen.

Optional models such as the Boundary Sampling model and the Track File model were selected as they proved beneficial in providing valuable information relating to particle interaction with selected boundaries and visualisation of particle trajectories, respectively.

5.6.1.2 Lagrangian boundary conditions

The choice of boundary interaction modes determines the behaviour of solid particles when they interact with physical boundaries defined within the computational domain. In the pulveriser domain, the mass flow inlet and pressure outlet boundaries (highlighted in Figure 5.2) were set to Escape mode, once the particle impinges on the said boundary it is allowed to escape from the domain. All other wall boundaries were set to Rebound mode, once a particle impinges on a wall, it rebounds into the domain with a reduced velocity (CD-Adapco, 2014).

5.6.1.3 Physics input data

Experimental results pertaining to two-phase flow conditions were presented in Table 3.12 (graphically in Figure 3.20). Selected results, used as input to the two-phase flow CFD calculation, have been succinctly represented in Table 5.7.

Table 5.7 Physics input data for two-phase flow

Variable	Units	Value
T_{PA}	^{o}C	229
T_{PF}	^{o}C	89
$\dot{m}_{PA,\ corrected}$	kg/s	9.80
$\dot{m}_{Coal}$	kg/s	6.32
H, $P_{static,\ measured}$	Pa	3303
Atmospheric Pressure	Pa	85000
Absolute Pressure	Pa	88303

The specification of the absolute pressure at the pressure outlet boundary was analogous to that explicated in section 5.5.2 however, the pulveriser outlet static pressure value was modified to the two-phase flow condition. Additionally, StarCCM+ default thermodynamic properties were employed for the coal particles, such as the coal density.

5.6.1.4 Injectors

The introduction of the solid-phase into the computational domain is accomplished through the use of injectors in StarCCM+. Injectors are responsible for defining the location, size, and direction at which solids particles enter the domain (CD-Adapco, 2014). Since it is currently not possible to simulate the physical grinding process in any commercial CFD code, assumptions pertaining to the location and size of the particles injected have to be generated.

Consider the grinding mechanism of the 8.5E VSM, as highlighted in Figure 5.15a. Since the coal flows from the grinding table outward radially onto the grinding track, it is postulated that ground coal particles are at the location highlighted. This necessitated a field function code to be written in StarCCM+ to group all the cells along the perimeter of the bottom grinding ring, the injector location selected is depicted as a threshold part in Figure 5.15b. A ‘part’ injector type was deemed most suitable for this application. When a part injector is employed, particles are injected from the centroid of every cell defined in the part.

Additionally, the selection of this location for particle seeding is congruent with previous studies (CD-Adapco, 2015).

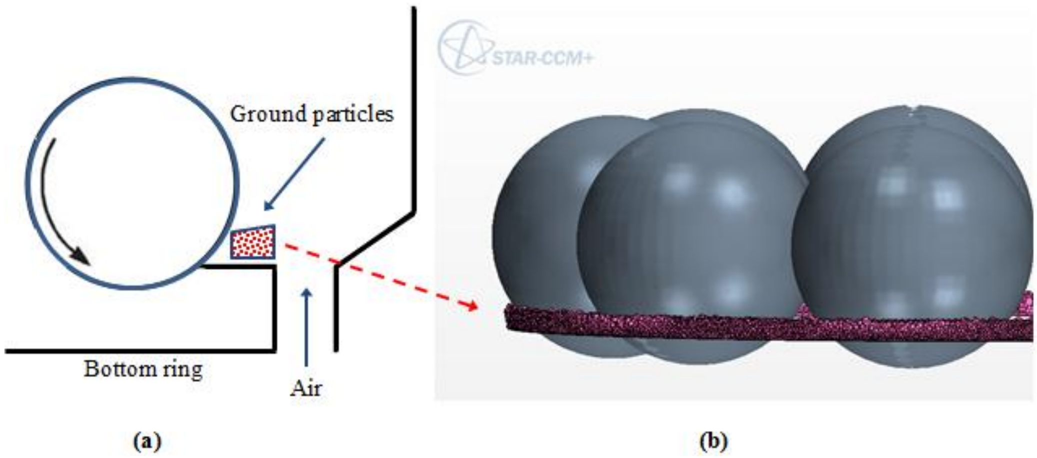

Figure 5.15 Schematic highlighting the injection location of ground coal particles

As previously outlined, the size of the raw coal entering the pulveriser is approximately 40 mm. For a given mass of PF, the Eskom standard with regards to acceptable PF sizes post pulverisation was presented in Table 1.1.

Using the Eskom standard as a guide, it is evident that a large portion of the ground particles are 75 μm and less in size. Therefore, one injector was initially set up in StarCCM+ to seed coal particles with a constant particle size of 75 μm.

5.6.1.5 Modelling the pulveriser temperature profile

As section 5.5 presented the investigation undertaken for the single-phase (air) flow dynamics in the pulveriser, modelling of pulveriser temperature profile was not considered. Raw coal has a moisture content ranging from 5 to 15 %. As previously discussed, an additional function of coal pulverisers is to dry the ground coal before it leaves the pulveriser. Coal drying is a function of the primary air mass flow rate and temperature, surface area of the coal particles as well as the particle residence time within the pulveriser. In favour of the drying process, primary air flows into the pulveriser at a high temperature (CMP, 2003).

Following the drying process, the primary air loses heat energy and exits the pulveriser at a much lower temperature. This heat loss increases the air density. Additionally, lower air temperature provides a decreased air viscosity, which is expected to influence the pressure drop across the pulveriser. Hence, energy lost due to drying must be considered in StarCCM+ in order to accurately calculate the static pressure for the two-phase flow scenario.

The energy source option provided in StarCCM+ is a viable option to model constant heat addition or extraction from a simulated domain. Prerequisites for the energy source option are a user-defined volumetric heat source/extraction in W/m^3 as well as a suitable location for the extraction (CD-Adapco, 2014).

In the case of the pulveriser, the primary air inlet temperature and pulveriser outlet temperature was measured to be 229 ^{o}C and 89 ^{o}C respectively, as presented in Table 3.12. Additionally, the primary air flow rate employed was 9.8 kg/s. CMP (2003) provides a relationship to determine the heat consumed during the coal drying process, as illustrated in Equation 5.1.

$$E = \dot{m}_{PA} C_p (T_{PA} - T_{PF}) \quad (5.1)$$

By employing Equation 5.1, the energy consumed during the drying process was calculated to be 1413160 W.

Additionally, heat loss through convective heat transfer was quantified by employing Equation 4.11. This yielded a total convective heat loss of 17110 W. Therefore the sum of the energy lost through drying and convection must be extracted from an area in the computational domain in order to achieve the required pulveriser outlet temperature and associated air density pertaining to experimental test conditions.

The pulveriser temperature profile data outlined in the literature review (refer to Figure 2.1) was used in collaboration with the experimentally determined temperature profile (refer to Figure 3.20) as a guide to identify the most suitable location for the energy extraction. Notably from steep temperature gradient exhibited across the throat gap region in both these illustrations, it is apparent that a significant portion of the drying occurs in this region. Hence, the zone selected for the energy extraction is highlighted in Figure 5.16. The selection of this location for energy extraction is congruent with previous investigations (CD-Adapco, 2015).

The process followed for the selection of cells in the zone identified for the heat extraction was analogous to that presented in section 5.6.1.4. Furthermore, the volume of the cells in the extraction zone was acquired by generating a '*volume of energy zone*' report in StarCCM+. Subsequently, a user-defined field function was written to extract 1430270 W of energy from the total volume of cells in the zone described.

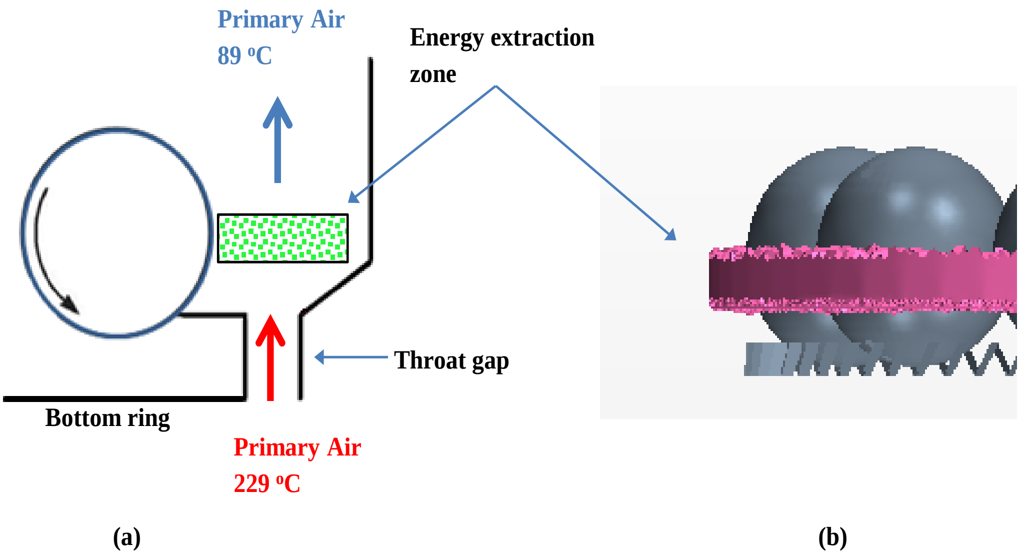

Figure 5.16 Schematic highlighting (a) coal drying zone and (b) threshold depicting the energy extraction zone created in StarCCM+

Figure 5.17 presents the resultant temperature contour plot exposing the cross sectional area of the pulveriser. Evidently, the application of the energy source option in extracting the specified amount of energy was successful as the pulveriser inlet and outlet temperatures displayed in the contour plot demonstrate close resemblance to the data obtained experimentally for the two-phase flow condition. Notably, there are areas above the throat region where the temperature reduced to 25 ^{o}C. This can be attributed to extracting too much energy from cells that exhibit a low velocity gradient.

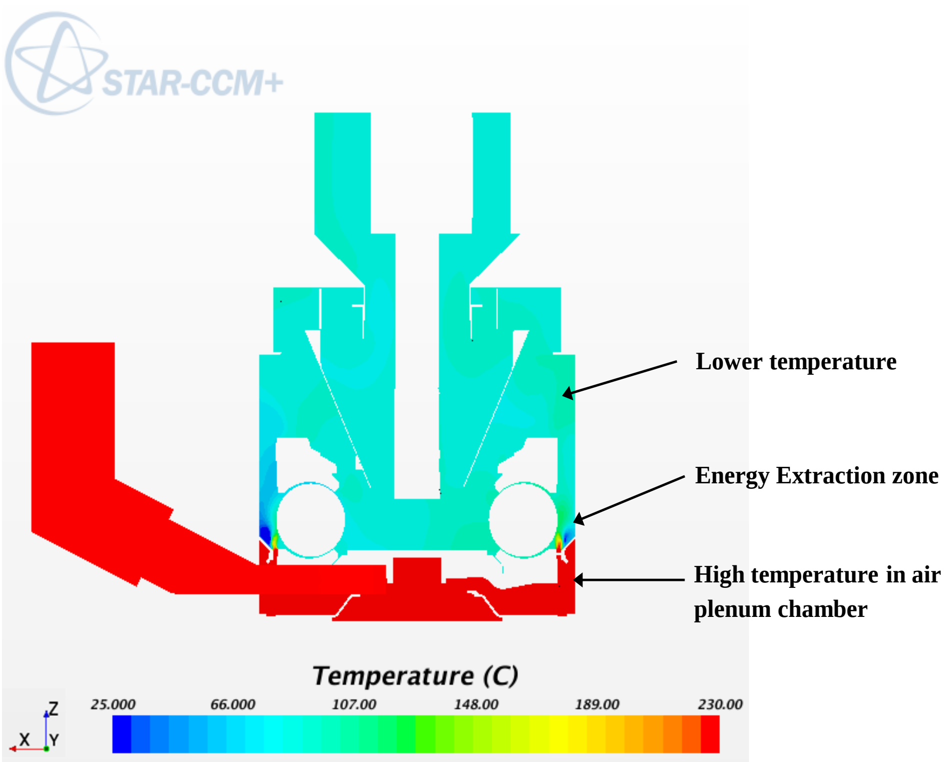

Figure 5.17 Temperature contour highlighting the effect of energy extraction

5.6.1.6 Solver settings

In StarCCM+, solvers that govern a solution are elected based on the physics models chosen for a particular simulation. The Under Relaxation Factor (URF) is a solver setting that dictates the degree to which a newly computed solution supplants the old solution as computation of the solution progresses. The default URF values for all variables in StarCCM+ are conservative and will in most cases lead to a converged solution. However there are certain cases where modifying the URF is a prerequisite to facilitate solution convergence (CD-Adapco, 2014).

Determining the optimal URF value is dependent on the particular solution being simulated. StarCCM+ recommends initiating a solution with the default URF settings and subsequently reducing the URF values as the solution develops. For the pulveriser multiphase flow simulation, it was necessary to reduce the URF values to obtain a stable solution. URF values employed in the final *coupled* multiphase solution are highlighted in Table 5.8. The adjusted URF values were within the StarCCM+ user guides prescribed range for multiphase flow conditions.

It must be noted that the engineering parameters and criteria employed to assess solution convergence for the two-phase flow simulation are analogous to those presented in section 5.5.4.

Table 5.8 Optimum URF values determined for the pulveriser multiphase simulation

Solver		**URF (default)**	**URF (adjusted)**
Two-Way coupling		1	0.25
Segregated Flow	Velocity	0.7	0.20
	Pressure	0.3	0.30
Segregated Energy	Fluid	0.99	0.90
	Solid	0.9	0.90
κ-ε Turbulence		1	0.40
κ-ε Turbulence Viscosity		1	0.50

5.6.1.7 Two-phase flow simulation results

Table 5.9 presents the static pressure results obtained through numerical simulation in StarCCM+ for the two-phase flow condition. The location of the measurement points (A to H) are referenced in Figure 3.14 and Figure 3.15.

Table 5.9 Static pressure simulation results obtained for the two-phase flow condition (Airflow: 9.8 kg/s; Particle count: 14076)

Measurement point	$\boldsymbol{P_{static,\ simulated}}$ $(\boldsymbol{Pa})$
A	7103.56
B	4048.35
C	4010.66
D	3954.77
E	2854.75
F	3104.28
G	7940.07
H	3302.52

5.6.1.8 Validation of the two-phase CFD model through experimental correlation

For the two-phase flow condition, CFD model validation was assessed analogously to the procedure described in section 5.5.6. The static pressure results predicted through CFD demonstrated a negative correlation to the static pressure results obtained experimentally for the two-phase coupled flow scenario, as depicted in Figure 5.18. An average disparity of 11 % (not shown) was calculated between the simulated and the experimental static pressure results. Evidently, the static pressure prediction across the throat region was the main contributor to the poor correlation achieved, where the individual variances at points G and A was computed to be 31 % and 25 %, respectively. Notably, areas higher up in the pulveriser (points B to F) revealed better correlation, and this may be attributed to the regions being dilute.

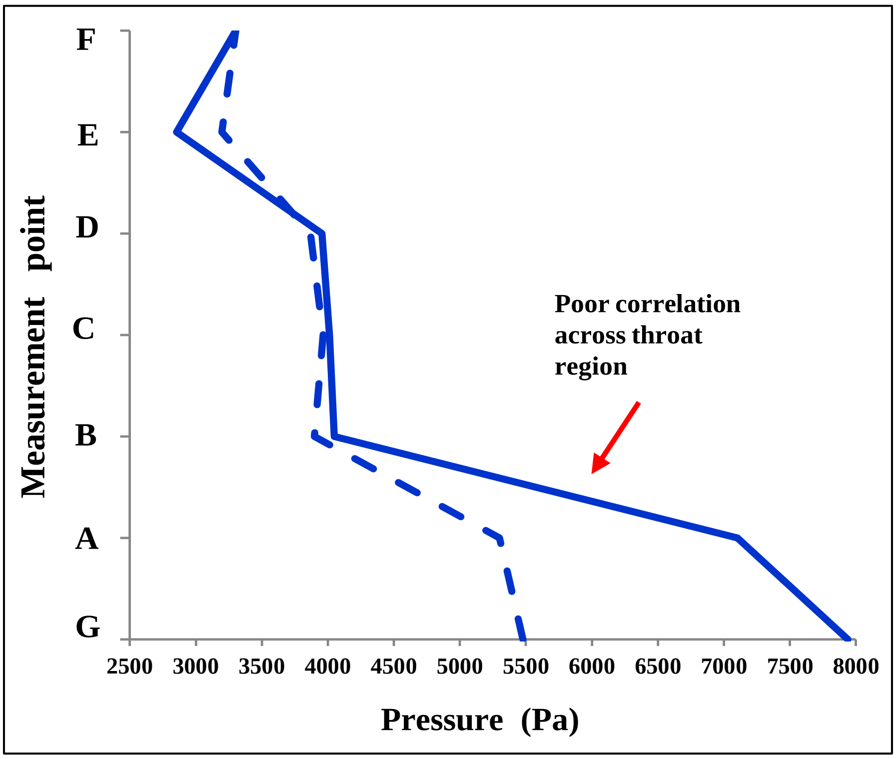

Figure 5.18 Experimental (solid) and simulated (dashed) static pressure profile

Recall from literature (refer to Figure 1.5 and Figure 2.2), during normal pulveriser operation the throat gap region was highlighted to exhibit fluidized bed phenomena as it is densely packed with finely ground coal particles. The poor correlation achieved across the throat region corroborates the limitation of the Lagrangian model to feasibly simulate high volume fraction flows. Factors which influence the pulveriser drop were presented in Chapter 1, section 1.4. As the pulveriser geometry, temperature profile and mass balance of air and coal were modelled accurately, the under-prediction in static pressure values across the throat region was primarily attributed to the computational limitation in simulating the actual number of particles present in an operational pulveriser.

Additionally, the coal analysis results highlighted in Chapter 3 demonstrated that the raw coal fed to the pulveriser comprised of coal particles with different sizes, typically from 3 mm to 40 mm. During pulveriser operation, it can be expected that not all of the coal particles will be ground to the required sized in the first circulation, hence different particle sizes present in the pulveriser will affect the two-phase static pressure profile. In the pulveriser simulation, one constant size particle (75 μm) was simulated as it was considered impractical to simulate the exact particle size distribution that exists in an operational pulveriser under two-phase flow conditions. This may have also had a negative influence on the predicted pressure profile.

5.6.2 Uncoupled approach

The pulveriser CFD model presented in section 5.6.1 considered Two-Way coupling between the fluid continuum and the particulate phase. However due to computational power limitations, it was considered impractical to simulate the actual number of particles in a pulveriser. Hence, the simulated pulveriser pressure drop results demonstrated poor correlation to the experimental results.

Without the Two-Way coupling model activated, the continuous phase influences the particle paths through terms such as drag in the momentum equation and heat transfer in the energy equation. Therefore, although the effect of the discrete phase on the continuous phase is neglected, the discrete phase pattern can be established and assessed in StarCCM+ based on a fixed continuous phase flow field (CD-Adapco, 2014). This approach in elucidating the behaviour of individual particles in the pulveriser domain is a key advantage of the Eulerian/Lagrangian methodology and is congruent with previous studies (Vuthaluru et al., 2006; Shah et al., 2009; CD-Adapco, 2015).

An important outcome of this section is to determine individual coal particle trajectories through the computational domain as a function of the continuous air phase. Therefore, simulation of the pulveriser using the uncoupled approach was instituted. The ensuing methodology applied for the continuous phase remained unchanged to that explicated in section 5.5. The approach followed for the solid-phase model was similar to that discussed in section 5.6.1 and relevant adjustments applied to the specified model are outlined below:

- The Two-Way coupling physics model under the Lagrangian phase was deactivated.

- Modelling of the pulveriser temperature profile through the employment of the volumetric heat source was excluded. Therefore the primary air temperature was simulated at ambient conditions (25 ^{o}C).
- For the addition of solid particles in to the continuous phase, 34 constant particle size injectors were manually set up to inject an equal number of coal particles ranging from 1 µm up to 400 µm.
- Physics solver settings remained unchanged from the default settings provided in StarCCM+.

5.6.2.1 Particle track results and discussion

As previously mentioned, the Track file model was chosen to track the path of each particle through the computational domain until the particle either escapes or reaches a maximum residence time. Best practice guidelines suggest injecting a considerably large amount of particles into the computational domain to proliferate confidence in the simulation results. Therefore approximately 14 000 particles were seeded into the domain and the path of each particle was subsequently followed from the point of injection. To obtain the particle track results for the pulveriser simulation, once the solid-phase model was set up, the simulation was only required to be stepped once. Conversely, when the Two-Way coupling model was active the simulation needed to be iterated until solution convergence.

A filtered scalar contour plot was created to establish the particle trajectories within the computational domain, as depicted in Figure 5.19. Evidently, by observation of the particle tracks, the particles travel from the injection point to the pulveriser exit, with varying velocities highlighted at different zones within the simulation domain. The majority of the particles exit the pulveriser with velocities between 22 m/s and 30 m/s which correspond well with the exit air flow velocity presented in Figure 5.10, thereby demonstrating particle entrainment. This corroborates well with results from an alternate study performed by Vuthaluru et al. (2006) and serves to verify the current model developed.

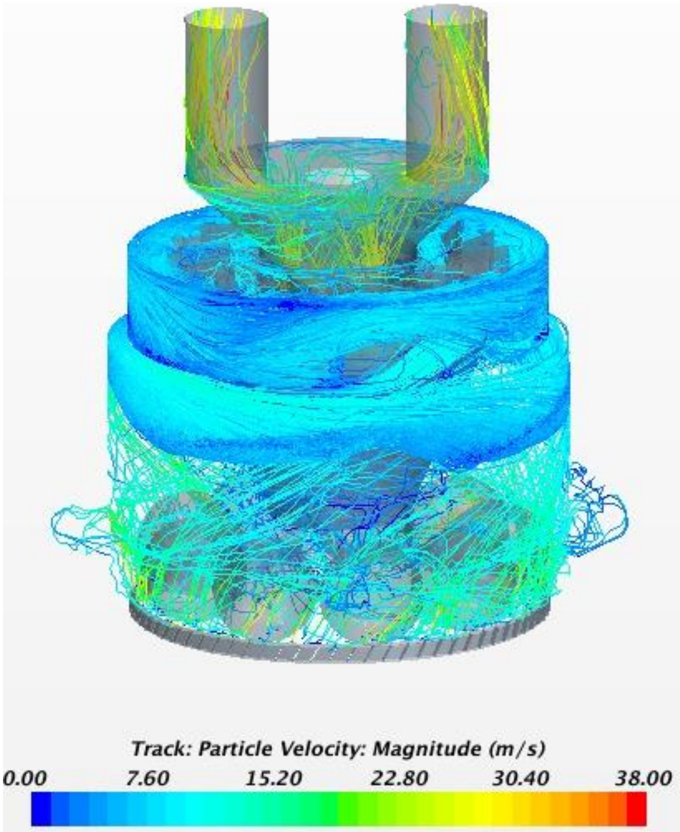

Figure 5.19 Particle trajectories illustrating particle velocities from injection point to pulveriser outlet

Figure 5.20 presents the particle tracks which outline the range of coal particle diameters simulated. While finer particles are easily entrained by the air stream toward the exit, larger particles experience difficulty and are observed to agglomerate in the computational domain. Particles near the throat region follow a slight helical pattern as a result of the angled throat vanes. Similar observations were discussed by Bhambare et al. (2010).

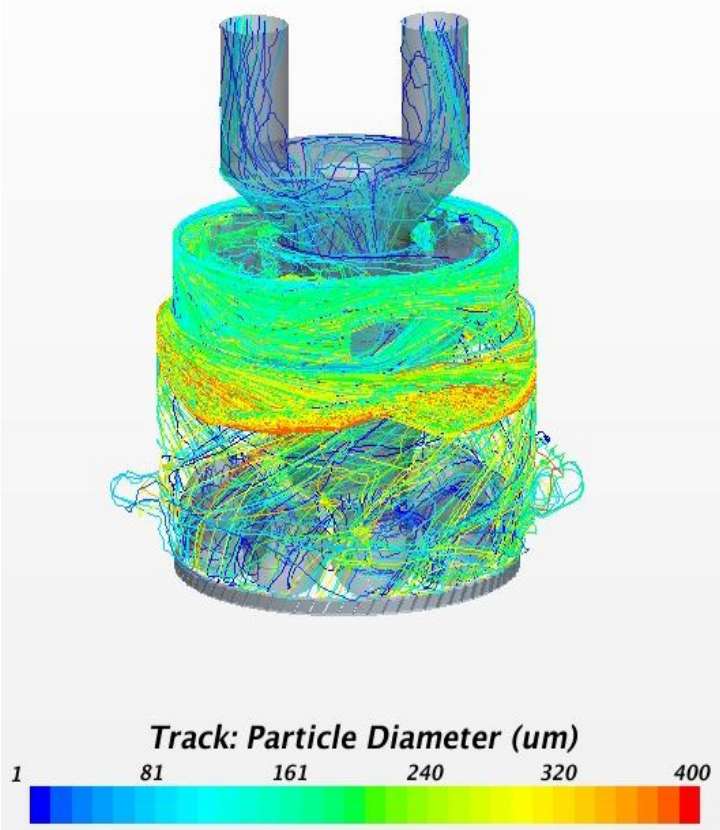

Figure 5.20 Particle trajectories illustrating particle diameters from injection point to pulveriser outlet

5.6.2.2 Particle size distribution results and discussion

As previously highlighted, the size of the coal particles which escape from the pulveriser after grinding is a critical parameter that needs to be within a specified range to ensure safe, reliable and efficient combustion. Larger particles which manage to escape tend to burn incompletely due to the limited residence time available in a coal furnace, this leads to high UBC in ash and high particulate emissions.

For the pulveriser simulation, the determination of the coal particle size distribution at the pulveriser exit was assessed quantitatively by completing a particle size count balance. Since a part type injector was defined for the coal injection point, the number of particles of each size injected is identifiable by the number of cells present on the part surface. More importantly, the primary objective of this section is to present the particle size distribution obtained at the pulveriser exit, therefore, an outlet plane section was created 10 mm upstream of the PF pipes as indicated in Figure 5.21. In order to quantify the number of particles exiting the pulveriser, particles which made contact with the said boundary plane were considered to have escaped from the pulveriser domain.

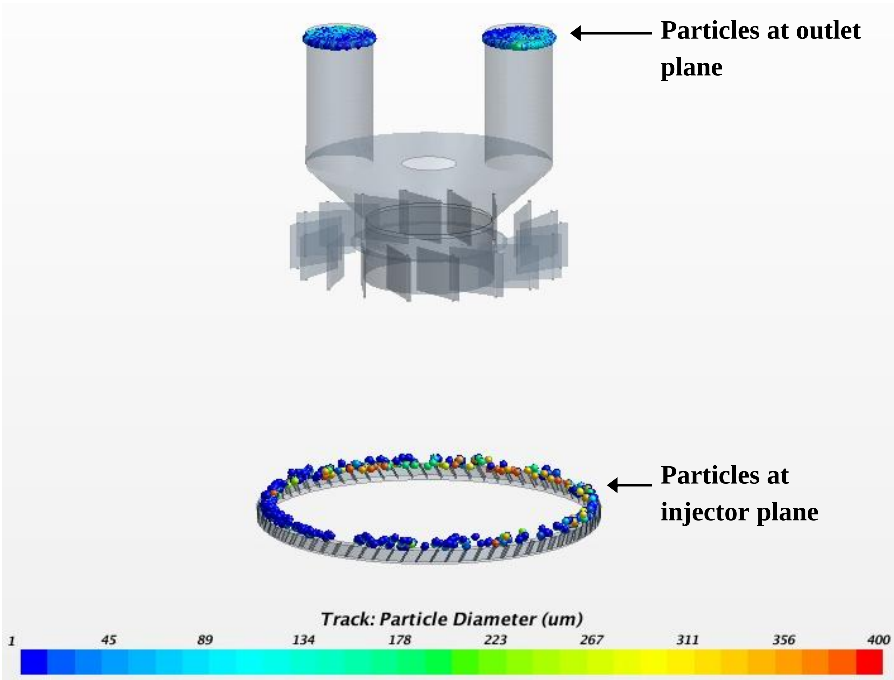

Figure 5.21 Contour plot indicating particle size distribution at the injector and outlet plane of the pulveriser

In a Lagrangian multiphase simulation, best practice guidelines suggest setting a maximum particle residence time for which the particles are tracked in the simulated domain. This recommendation prevents particles from becoming trapped within the fluid region indefinitely (CD-Adapco, 2014). An iterative approach was adopted to delineate the optimum particle residence time for the pulveriser simulation. An arbitrary value of 5s was used to initiate the process followed by incremental increases until the number of particles observed at the exit remained unchanged with any further proliferation of the residence time. Additionally, this approach ensured that the simulation was not stopped prematurely by allowing particles enough time to reach the exit if their size was satisfactory enough to do so with the prescribed air flow conditions. The optimum residence time was found to be 24 seconds. Particles which reached maximum residence time were assumed to be rejected by the pulveriser.

The percentage of coal passing the pulveriser outlet plane relative to the number of particles injected was determined by employing Equation 5.2. As illustrated in Figure 5.22, the particle size distribution at the pulveriser exit exhibits a higher percentage of fine particles with a gradual decrease in coarser particles. The quantity of particles greater than 250 μm was observed to be low at the pulveriser exit.

$$Coal\ passing\ (\%) = \frac{(Number\ of\ particles\ at\ exit\ )}{(Number\ of\ particles\ injected)} \times 100 \tag{5.2}$$

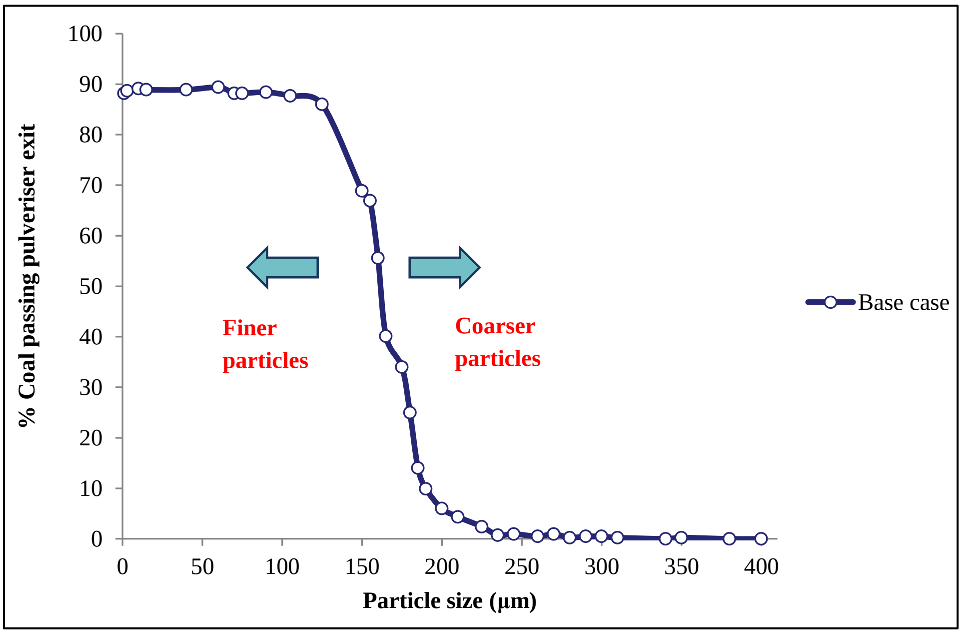

Figure 5.22 Graphical illustration of the particle size distribution at pulveriser exit

5.7 Concluding remarks

This chapter systematically presented the results of an in-depth investigation conducted to elucidate the flow profile in a full-scale 8.5E ball and ring pulveriser. The single-phase CFD model of the pulveriser was successfully developed and optimised. The mesh refinement study culminated in the selection of the most plausible mesh resolution for the simulation, this ensured a good compromise between solution accuracy and solution run time. A robust assessment of solution convergence was undertaken intimating a fully converged solution. The experimental and simulated static pressure values achieved good correlation, demonstrating the suitability of the numerical model to predict the single-phase static pressure profile of the pulveriser. The influence of the pulveriser geometrical characteristics and the magnitude of this influence on the measured outcomes proved different for each pulveriser zone analysed. The velocity profile highlighted through contour plots created across the cross sectional area of the pulveriser were congruent with previous studies, which served to verify the single-phase model.

In addition, this chapter employed the Lagrangian framework to investigate the static pressure profile for the two-phase flow condition of the pulveriser using a coupled approach. In this approach, the experimental and simulated static pressure profiles demonstrated negative correlation. As the CFD model generated made minimal assumption in relation to the geometrical characteristics and temperature profile of the pulveriser, the fundamental shortcomings of the two-phase flow (coupled) model appeared to be largely attributed to the computational limitation in simulating the actual number of particles in an operational pulveriser. Furthermore, simulating the exact particle size distribution during pulveriser operation was considered impractical. Hence, the suitability of the two-phase flow (coupled) model in predicting the static pressure profile demonstrated the poor potential of this model to be employed as a tool in the development of a viable monitoring philosophy, and no further studies employing the Two-Way coupling model were conducted.

The results of the single-phase model displayed good correlation in predicting the static pressure profile hence it exhibited promising potential for highlighting variations in pressure drop values measured across critical components as a result of modified pulveriser components. Furthermore, employment of the uncoupled approach revealed the individual particle paths through the computational domain and yielded the particle size distribution at the pulveriser exit. The graphical plots highlighting the static pressure profile (single-phase) and particle size distribution (two-phase uncoupled) was generated on the as-built geometrical characteristics of the pulveriser and is considered the benchmark case through which the ensuing pulveriser geometrically modified scenarios explored in Chapter 6 will be subsequently assessed.

Chapter 6: Development of a Condition-Based Monitoring Philosophy for a coal pulveriser

6.1 Introduction

Condition monitoring approaches, employing statistical evaluation of measured outcomes over a given period, are extensively practiced in industry to maintain a certain level of performance from processes, as it is an efficient and cost-effective tool that is able to provide early detection of damaged plant components. In order to ensure the successful development of a condition monitoring system for a given process, a sensing system that is able to monitor the system response to changes coalesced with an intelligent and rigorous data analysis procedure are fundamental prerequisites (Farrar and Worden, 2007). As the aim of this dissertation is related to the former requirement, the development of a MCMP will be the focal point of this chapter.

The undertaking of the pulveriser numerical study, as outlined in Chapter 5, provided vital data on the flow profile exhibited in the pulveriser. Subsequent to the identification of the single-phase flow model demonstrating the best potential for the development of a pulveriser condition monitoring philosophy, it provides a platform to assess the measured outcomes under conditions that mimic wear scenarios, typically those that cannot be adequately tested in real life. Hence, candidate damage scenarios were simulated to assess the viability of employing the static pressure measurements to achieve the aim. In line with this, common pulveriser damage conditions highlighted through engagement with experienced power plant personnel as well as associated literature culminated in the construction of a comprehensive pulveriser wear scenario matrix. The numerical results attained for the various wear scenarios simulated and the merits of employing the static pressure measurements to detect poor pulveriser condition for each scenario are presented herein.

6.2 Construction of a pulveriser wear scenario matrix

The review of an Eskom strategic report compiled by (Muller, 2015) highlighted common and recurring pulveriser mechanical deficiencies which appear to negatively influence the pulveriser performance. Moreover, the review facilitated the identification of candidate damage scenarios to be assessed through numerical simulation in StarCCM+. In addition, Visual Inspection (VI) of several Eskom pulverisers, conducted during time-based maintenance opportunities, substantiated the findings presented by Muller (2015), and other candidate damage scenarios were further elucidated. The degradation mechanism of internal components in a pulveriser is predominately caused by wear or impact damage influenced by component age or foreign material (EPRI, 2006.). Table 6.1 provides a succinct summary of the pulveriser wear matrix developed which describe eight potential scenarios that were identified.

Table 6.1 Pulveriser wear scenario matrix

Scenario	Component	Deficiency	Source	Candidate for simulation
1	Classifier vanes	Worn (30 %)	Muller (2015)/VI	Yes
2	Classifier vanes	Missing	VI	Yes
3	Classifier vanes	Holes (15 %)	Muller (2015)/VI	Yes
4	Inner cone	Large hole	VI	Yes
5	Inner cone	Multiple holes	Muller (2015)/VI	Yes
6	Vortex Finder	Damaged/worn	Muller (2015)/VI	Yes
7	Throat blades	Worn (60 %)	VI	Yes
8	Throat gap	Blocked (5 %)	Muller (2015)/VI	Yes

6.3 Simulation results and discussion

In order to ascertain to what extent the aforementioned scenarios have on the pulveriser static pressure profile, the deficiencies of respective components, as identified in Table 6.1, was deliberately applied individually to the CFD model by employing CAD and simulation tools available in StarCCM+.

It must be noted that the boundary conditions, physics models selection and physics input data, for each of the scenarios tested, is analogous to that described in Chapter 5 for single-phase flow modelling employing the uncoupled approach. This was to ensure a logical comparison could be performed with the CFD reference cases previously depicted in Table 5.6 (represented graphically in Figure 5.14, air flow of 9.8 kg/s) and Figure 5.22. The results for static pressure variations, observed for the ensuing scenarios, are presented as 'static pressure drop' across each respective zone. Each zone is identified by the measurement points as outlined in Figure 3.15 and Figure 3.16. In addition, comparison of the model-predicted outcomes for each candidate wear scenario is highlighted through the percentage variation value calculated in relation to the base case.

6.3.1 Classifier Modifications

6.3.1.1 Worn classifier vanes (Scenario 1)

In this scenario, each classifier vane was geometrically reduced by one third of its original height, as highlighted in Figure 6.1.

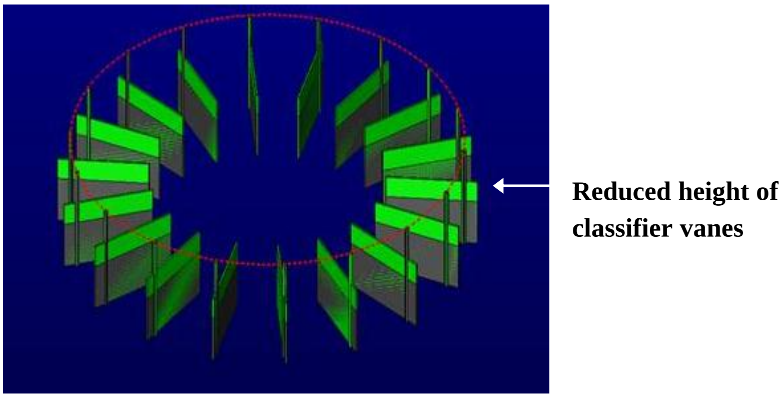

Figure 6.1 Classifier vane height reduction, original (green) and modified (grey)

Notably, a larger variation in static pressure drop is observed across the classifier region, demarcated through measurement points BF and CF, outlined in Table 6.2.

Since the vanes in the classifier influence the air flow resistance in that region, any reduction in vane height is expected to decrease the pressure drop across the said region. Hence, the results presented are congruent with this physical flow theory. Furthermore, the static pressure drop values across other regions demonstrated no outstanding differences.

Table 6.2 Simulated pressure drop results obtained for Scenario 1

Pressure drop	Base case (Pa)	Scenario 1 (Pa)	Variation (%)
ΔP_{GA}	168.41	168.20	0.13
ΔP_{AB}	865.39	875.60	1.18
ΔP_{BC}	-12.52	-12.48	0.30
ΔP_{BF}	371.03	329.78	11.12
ΔP_{CF}	383.55	342.27	10.76
ΔP_{GF}	1404.83	1373.58	2.22

6.3.1.2 Classifier vanes missing (Scenario 2)

Circulation of hard coal particles (HGI < 62, as highlighted in Table 3.11) is known to cause impact damage to components inside the pulveriser. As a result, classifier blades become loose and fall off, leaving a void in the classifier zone. The scenario simulated, highlighted in Figure 6.2, considered the removal of three vanes and the static pressure drop simulated results obtained are tabulated in Table 6.3. Removal of three classifier vanes resulted in a noticeable reduction in the static pressure calculated across the classifier, identified through points BF and CF. Whilst the removal of vanes is observed to have a smaller effect on the static pressure drop across the classifier in comparison to Scenario 1, the insignificant variation in pressure drop across the regions GA, AB and GF for both scenarios is noteworthy. In scenario 2, the change in static pressure drop across points BC was observed to be 5.48 % however, the pressure drop value only changes by approximately 1 Pa, hence, this result cannot be directly attributed to the missing vanes and can be regarded as insignificant.

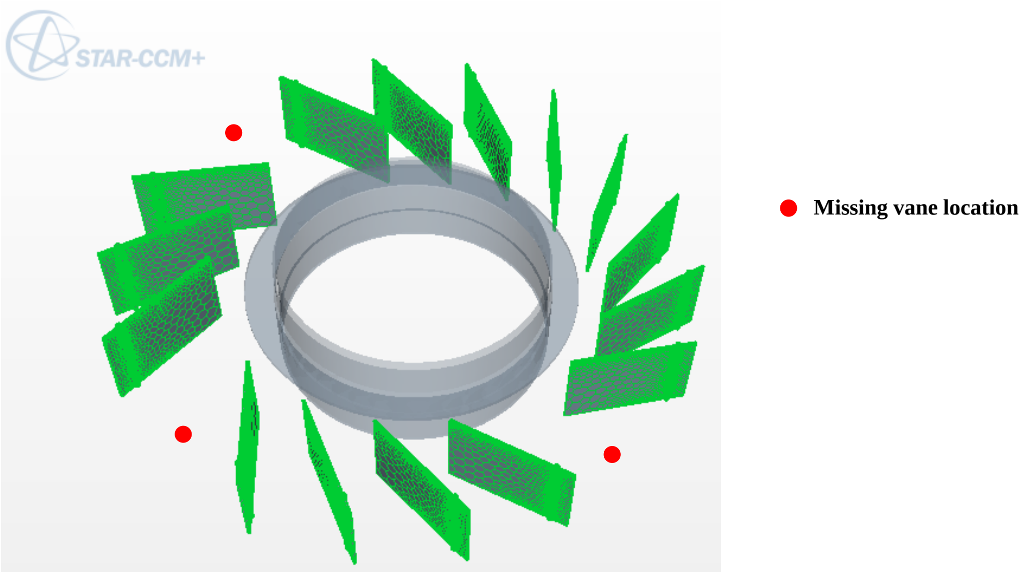

Figure 6.2 Schematic illustrating the top view of the classifier, highlighting the location of three missing classifier vanes

Table 6.3 Simulated pressure drop results obtained for Scenario 2

Pressure drop	Base case (Pa)	Scenario 2 (Pa)	Variation (%)
ΔP_{GA}	168.41	166.82	0.94
ΔP_{AB}	865.39	876.89	1.32
ΔP_{BC}	-12.52	-13.21	5.48
ΔP_{BF}	371.03	347.05	6.46
ΔP_{CF}	383.55	360.26	6.07
ΔP_{GF}	1404.83	1390.73	1

6.3.1.3 Classifier vanes with holes (Scenario 3)

Figure 6.3 displays three classifier blades with distinct holes created through the centre. The application of this modification to mimic impact wear on the vanes had no demonstrable effect on the measured outcomes, as depicted in Table 6.4, highlighting the unsuitability of employing the static pressure measurements to identify this particular deficiency. The lack of detection of such a condition may be directly attributed to the relatively small dimension of the worn area created.

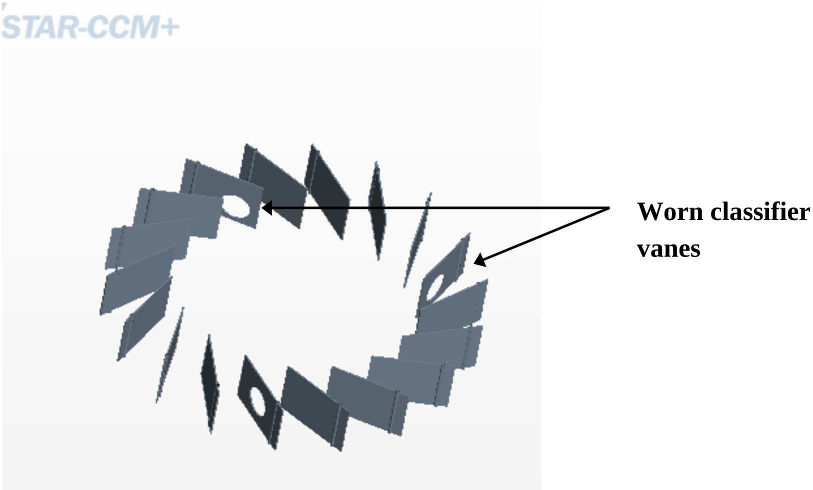

Figure 6.3 Schematic depicting three classifier vanes with holes

Table 6.4 Simulated pressure drop results obtained for Scenario 3

Pressure drop	**Base case (Pa)**	**Scenario 3 (Pa)**	**Variation (%)**
ΔP_{GA}	168.41	169.43	0.61
ΔP_{AB}	865.39	867.65	0.26
ΔP_{BF}	371.03	366.16	1.31
ΔP_{CF}	383.55	377.40	1.60
ΔP_{GF}	1404.83	1403.24	0.11

6.3.1.4 Particle size distribution analysis

Following the assessment of the static pressure drop caused by a deficient classifier, it is also of particular importance to establish the effects of the aforementioned conditions (refer to section 6.3.1) on the particle size distribution at the pulveriser exit. A particle 'size count' balance proved to be a suitable means to categorically elucidate the quantity of different sized particles that exit the pulveriser subsequent to the application of the worn components in the CFD model. Recall from section 5.6.2.2, the particle size distribution plot generated for the undamaged pulveriser was presented therein. Additionally, it must be noted that a brief analysis was undertaken to establish the effect of primary air temperature on the particle size distribution at the pulveriser exit. Two temperatures were evaluated, primary air at: (1) ambient temperature (25 ^{o}C) and (2) normal pulveriser operating outlet temperature (89 ^{o}C) for the base case (Figure 5.22) and scenario 1. As the particle size distribution curves (not presented) showed a relative indication between the base case and scenario 1 at both temperatures, a decision to save on solution run time was taken and the particle size distribution analysis was completed at ambient air temperature. Hence, the particle size distribution plots generated for the three classifier scenarios were compared to the base case (illustrated in Figure 5.22) in order to reveal the deviation in coal size distributions that can be expected at the pulveriser discharge, as displayed in Figure 6.4. Application of scenario 1 to the numerical domain demonstrated the greatest increase in coarser particles at the pulveriser exit, highlighting the importance of maintaining the correct height of the vanes in the classifier. Although the static pressure results indicated no significant variation for scenario 3, the size distribution plots generated for scenario 2 and scenario 3 are in general conformity with each other, with a notable increase in coal particles greater than 190 μm escaping the pulveriser domain in comparison to the base case.

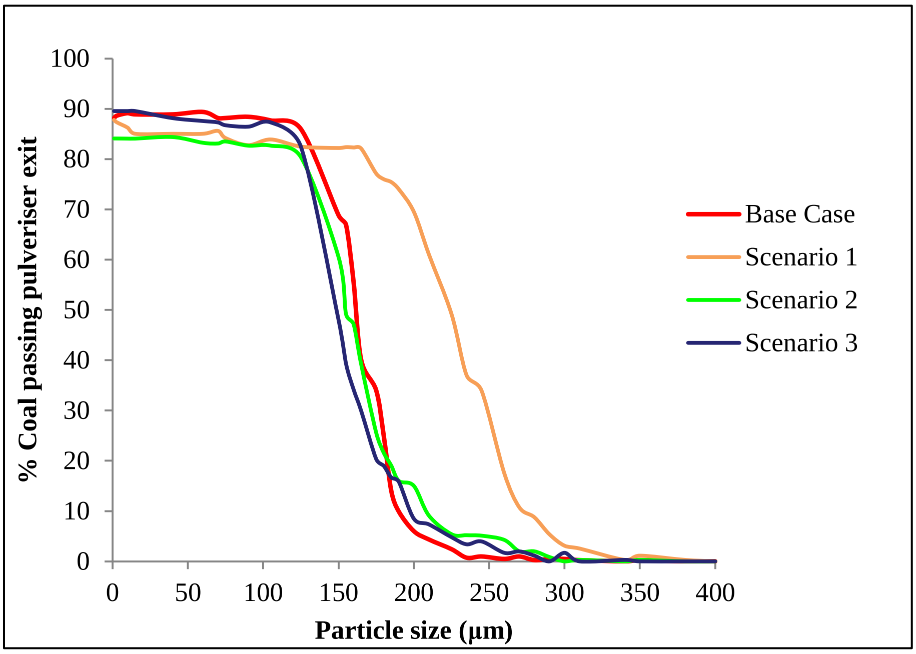

Figure 6.4 Comparison of the particle size distributions generated to elucidate the effect of the classifier modifications on the model output

6.3.2 Inner cone Modifications

6.3.2.1 Large hole in inner cone (Scenario 4)

The inner cone directs larger coal particles rejected by the classifier to the grinding zone. Therefore, it performs an important role in coal classification. Figure 6.5a presents the modified inner cone replicated in StarCCM+ to mimic the actual degradation. Mechanical deterioration of the inner cone, as highlighted in Figure 6.5b due to wear can be expected to alter the air flow pattern exhibited in the pulveriser by channelling air through the damaged portion, thereby causing coal entrained in the airflow to possibly bypass the classifier. Hence, larger particles may escape from the pulveriser. Furthermore during pulveriser operation, coal particles rejected by the classifier could potentially build-up inside the cone, only to be released into the area above the top grinding ring, hence regrinding of the coal particles may be circumvented.

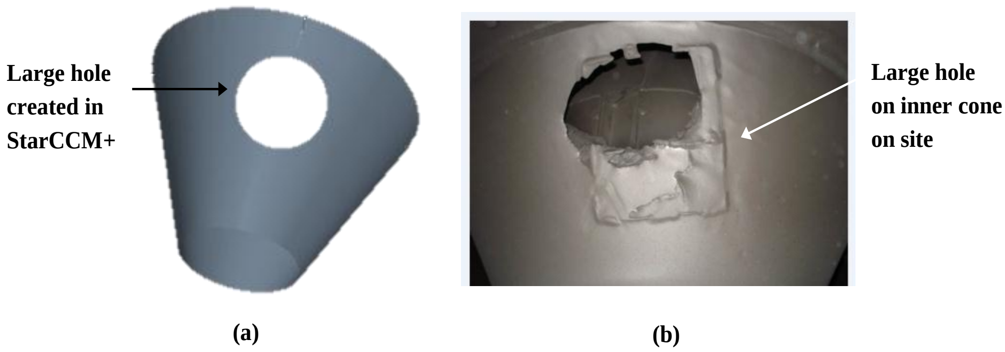

Figure 6.5 Large hole identified on inner cone, (a) simulated and (b) actual condition on site

Following the application of the modified inner cone in StarCCM+, the ensuing static pressure drop values presented in Table 6.5 highlight a considerable variation from the base case scenario for the classifier zone (BF and CF). Additionally, a notable change in pressure drop is highlighted across BC. As the deficiency was created adjacent to the measurement points BC, it can be concluded that the worn condition simulated contributed to the change in static pressure values sensed in the pulveriser domain. Relatively, the static pressure drop observed in other areas can be considered to be trivial.

Table 6.5 Simulated pressure drop results obtained for Scenario 4

Pressure drop	Base case (Pa)	Scenario 4 (Pa)	Variation (%)
ΔP_{GA}	168.41	162.11	3.74
ΔP_{AB}	865.39	881.57	1.87
ΔP_{BC}	-12.52	-8.51	32.06
ΔP_{BF}	371.03	247.48	33.30
ΔP_{CF}	383.55	255.99	33.26
ΔP_{GF}	1404.83	1291.16	8.09

6.3.2.2 Multiple holes in inner cone (Scenario 5)

In this scenario, multiple holes were created on the inner cone at the same location to that identified on site, illustrated in Figure 6.6. The pulveriser challenges associated with this scenario are analogous to those explicated in the preceding scenario.

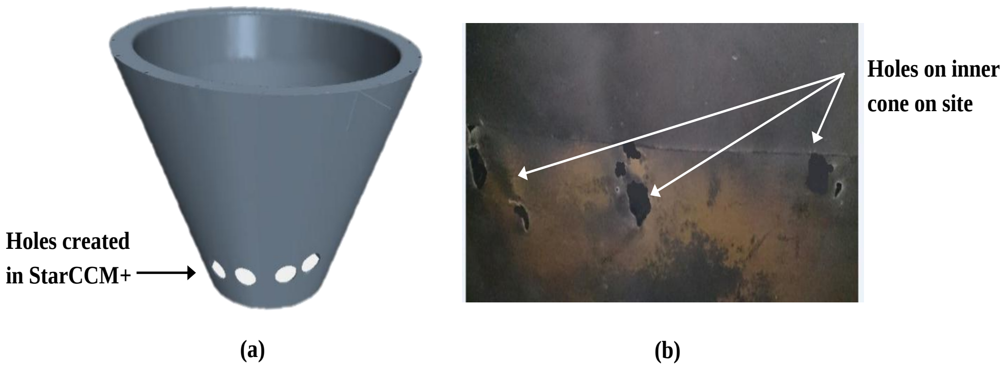

Figure 6.6 Multiple holes identified on inner cone, (a) simulated and (b) actual condition on site

Based on the pressure drop values reported in Table 6.6 it is evident that for multiple holes in the inner cone there is a complementary decrease in the predicted static pressure drop across the classifier zone (BF and CF) as well as a noteworthy change across measurement points BC. Therefore, it can be established that the zones that exhibited the greatest variation in pressure drop were indeed caused by a change in the geometric characteristic of the inner cone. This analysis further revealed statistically insignificant variation in pressure drop across other regions.

Table 6.6 Simulated pressure drop results obtained for Scenario 5

Pressure drop	Base case (Pa)	Scenario 5 (Pa)	Variation (%)
ΔP_{GA}	168.41	170.55	1.27
ΔP_{AB}	865.39	876.19	1.25
ΔP_{BC}	-12.52	-16.04	28.15
ΔP_{BF}	371.03	304.96	17.81
ΔP_{CF}	383.55	321	16.31
ΔP_{GF}	1404.83	1351.70	3.78

In addition, whilst the application of scenario 4 caused a significant variation in pressure drop across zones BF and CF, the relative disparity in the model-predicted pressure drop observed for scenario 5 was much lower, this can be primarily attributed to the larger dimension of the wear area created in scenario 4.

6.3.2.3 Particle size distribution analysis

The influence of mechanically defective inner cones on the particle size distribution at the pulveriser exit is visually explicated in the particle size distribution plots presented in Figure 6.7. By inspection, the quantity of particles larger than 150 µm exiting the pulveriser is more pronounced in both scenarios evaluated. In contrast, an inverse relationship is observed in relation to the base case for particle sizes below 150 µm, with scenario 4 producing a slightly finer product.

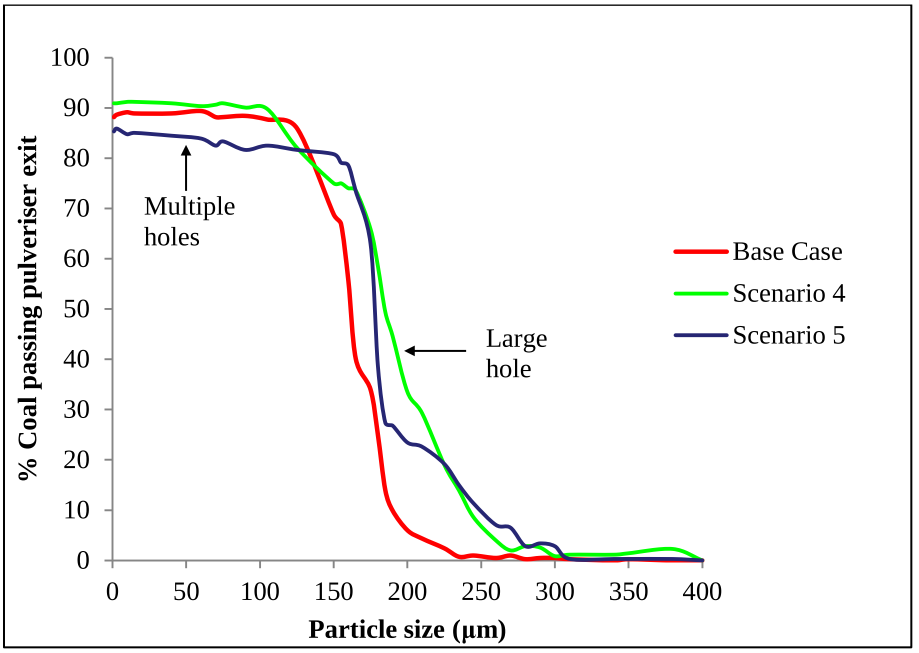

Figure 6.7 Comparison of the particle size distributions generated to elucidate the effect of the inner cone modifications on the model output

6.3.3 Vortex Finder Modification

6.3.3.1 Damaged vortex finder (Scenario 6)

The vortex finder is attached to the top plate of the classifier and is responsible for directing the ground coal particles from the classifier into the outlet plenum following which they are discharged into the PF pipes. More importantly, it assists the classifier vanes in providing the centrifugal forces required for PF delivery to the coal burners downstream the pulveriser exit. Due to the high swirl component present in the classifier zone, damages to the vortex finder are imminent due to impact. The image illustrated in Figure 6.8 highlights the damaged vortex finder created where part of the bottom right hand side was removed.

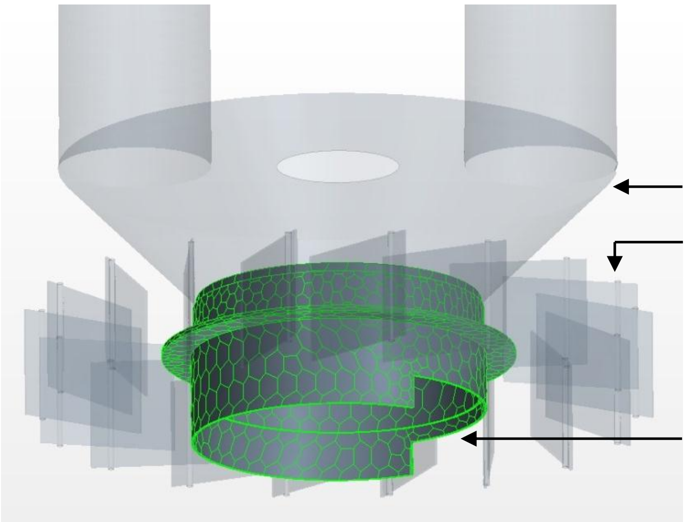

Figure 6.8 Schematic representation of a damaged vortex finder

Table 6.7 presents the simulated results obtained for scenario 6. In this scenario, while the variations in static pressure drop across other regions were relatively insignificant, approximate variations of 10 % was observed across the region containing the vortex finder, BF and CF. The benefit to perform a statistical evaluation of the static pressure drop values to distinctly discriminate variations from undamaged and damaged components is further highlighted.

Table 6.7 Simulated pressure drop results obtained for Scenario 6

Pressure drop	Base case (Pa)	Scenario 6 (Pa)	Variation (%)
ΔP_{GA}	168.41	163	3.21
ΔP_{AB}	865.39	900.21	4.02
ΔP_{BC}	-12.52	-12.67	1.20
ΔP_{BF}	371.03	331.03	10.78
ΔP_{CF}	383.55	343.70	10.39
ΔP_{GF}	1404.83	1394.23	0.75

Notably, the application of the mechanical conditions described by scenario 1, scenario 2 and scenario 6 revealed similar variations in static pressure drops across the classifier region (BF and CF). This result is attributed to implementing a geometric change in the same region. Hence, these results highlight the unsuitability of employing a statistical analysis of static pressure drop to decipher between a damaged classifier and a damaged vortex finder. However, this approach still provides useful information which can be utilised to narrow down the mechanically defective area of concern.

6.3.3.2 Particle size distribution analysis

The impact of a mechanically defective vortex finder on the particle size distribution at the pulveriser exit is visually elucidated in the particle size distribution plot presented in Figure 6.9. By inspection, the quantity of particles larger than 160 μm exiting the pulveriser is more pronounced for the damaged vortex condition hence, this profile exhibits a similar trend to the distribution plots presented for the previously discussed wear scenarios.

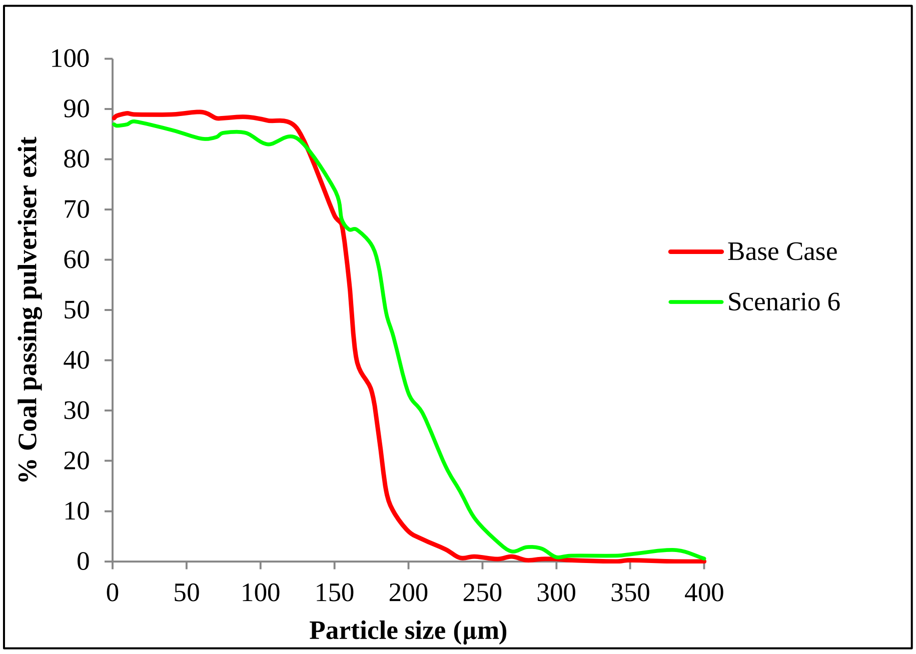

Figure 6.9 Comparison of the particle size distributions generated to elucidate the effect of vortex finder modifications on the model output

To this end, the scenarios presented explored the paradigms of poor component condition for components located in the upper region of the pulveriser. To more conclusively assess the viability of employing the static pressure drop values to predict changes in the mechanical condition of components, modifications were imposed to the lower area of the pulveriser domain, namely the throat region, and two possible scenarios were considered as outlined in the ensuing section.

6.3.4 Throat region Modifications

6.3.4.1 Worn throat blades (Scenario 7)

The 8.5E VSM has several throat vanes mechanically fitted to the outer perimeter of the bottom grinding ring. As previously highlighted, the vanes impart a swirl to the PA flow aiding in coal classification within the pulveriser. Figure 6.10 depicts the throat gap blade, illustrating the dimensions of the modified blade (highlighted in pink) in relation to the original. It must be noted that in this scenario the width of all 72 blades was geometrically reduced from 10 mm to 3 mm.

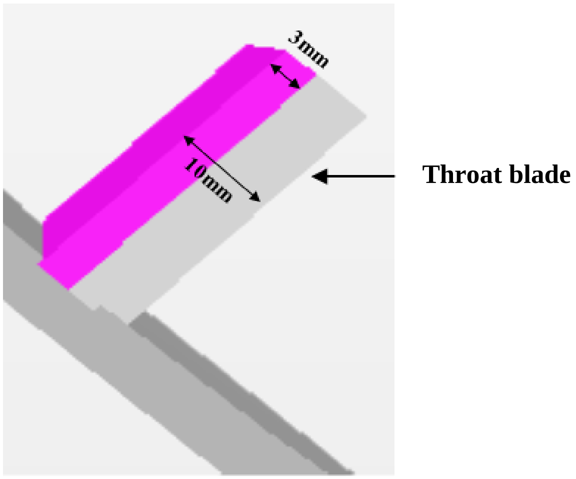

Figure 6.10 Schematic highlighting modified throat vane in relation to the original

As illustrated in Table 6.8, the variation in pressure drop displayed across the throat gap area (measurement point AB), in comparison to the other regions, was noted to be the largest, the difference of which, can be directly related to the modified throat vane dimensions. A significant disparity in pressure drop values measured across the classifier region (BF and CF) was distinctly absent, thereby successfully identifying the throat region as an area exhibiting changes have occurred. The variance in pressure visible across region GA may be attributed to the lower pressure experienced at point A as a result of the reduced resistance across the throat caused by the modification imposed. The 4.86 % change observed across points BC was regarded as insignificant as the pressure drop for scenario 7 only reduced by 0.61 Pa relative to the base case. Additionally, as can be expected, a change was observed across points GF mainly due to the pressure drop across the throat region being a large portion of the overall mill static pressure drop.

Table 6.8 Simulated pressure drop results obtained for Scenario 7

Pressure drop	Base case (Pa)	Scenario 7 (Pa)	Variation (%)
ΔP_{GA}	168.41	157.57	6.44
ΔP_{AB}	865.39	795.66	8.06
ΔP_{BC}	-12.52	-13.13	4.86
ΔP_{BF}	371.03	369.14	0.51
ΔP_{CF}	383.55	382.27	0.33
ΔP_{GF}	1404.83	1322.37	5.87

6.3.4.2 Air flow obstruction in between throat segments (Scenario 8)

Generally, large coal particles or foreign objects that are either too hard to grind, too heavy to be entrained by the primary air velocity passing through the gap and too large to pass through the throat gap to be rejected by the pulveriser may become wedged in the throat segments. The presence of a wedged object causes an obstruction thereby inhibiting free passage of primary air through the throat gap. In addition, impact damage to the bottom grinding ring plate as identified during visual inspections also creates a flow restriction, illustrated in Figure 6.11. The challenges associated with these two conditions are most likely unequal airflow distribution around the throat gap and as a consequence, it may lead to high wear rates in the throat region. The impact of unequal airflow on the wear profile adjacent to the throat region was investigated and highlighted by Vuthaluru et al. (2006), as previously explicated in Chapter 2, section 2.3.

To simulate a realistic scenario, 5 % of the 72 throat segments were obstructed, as displayed in Figure 6.12a. Application of the throat gap obstruction was achieved in StarCCM+ using a strategic part and a closer view of the part created is displayed in Figure 6.12b.

Figure 6.11 Digital image highlighting damaged grinding ring creating an obstruction above the throat gap

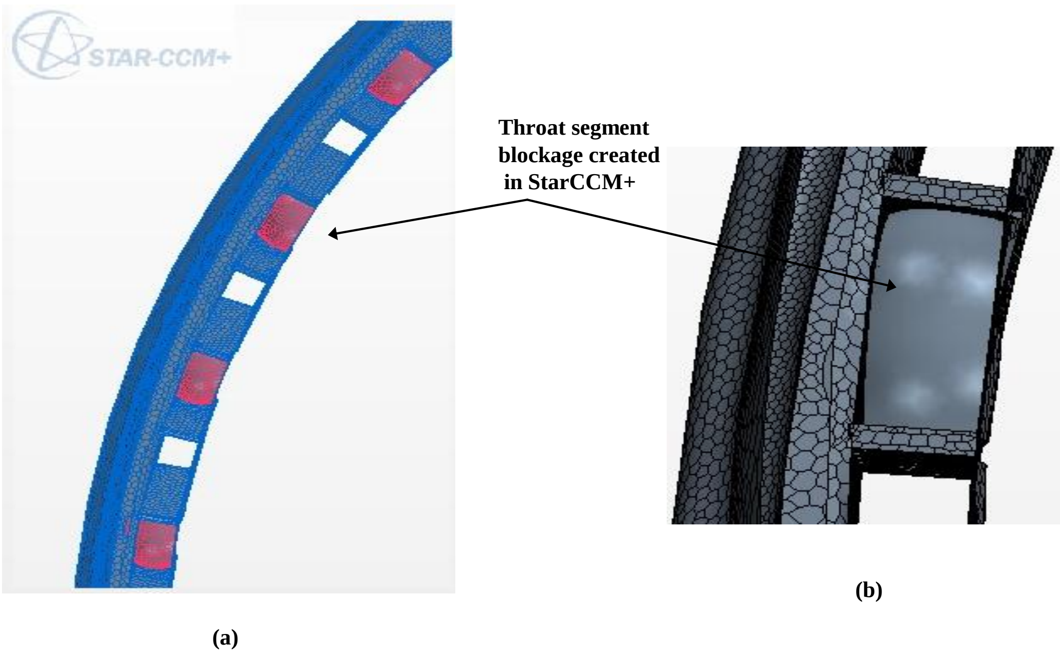

Figure 6.12 Schematic illustrating (a) 5 % blocked throat segments (b) closer view of segment blockage created

The presence of an obstruction in the throat gap region contributes significantly to the flow characteristics across the throat region, as depicted in Table 6.9. A significant rise in pressure drop of approximately 100 Pa is detected across points AB, emphasizing the added resistance created in the system by the blockage. A comparative assessment of the pressure drop results displayed for scenario 7 and scenario 8 revealed that worn blades lead to a reduced pressure drop across the throat whereas for a blocked throat, the pressure drop increases. In addition, the similarities observed between the measured outcomes across the classifier region (BF and CF) in relation to the other regions for both these scenarios emphasize the potential of isolating problem areas in the pulveriser by analysing the static pressure measurements.

Table 6.9 Simulated pressure drop results obtained for Scenario 8

Pressure drop	Base case (Pa)	Scenario 8 (Pa)	Variation (%)
ΔP_{GA}	168.41	156.96	6.80
ΔP_{AB}	865.39	968.75	11.94
ΔP_{BC}	-12.52	-13.12	4.81
ΔP_{BF}	371.03	364.83	1.67
ΔP_{CF}	383.55	377.95	1.46
ΔP_{GF}	1404.83	1490.54	6.10

6.3.4.3 Particle size distribution analysis

The particle size distribution was evidently affected by the modifications applied to the throat region, as illustrated in Figure 6.13. Assessment of these distribution plots revealed incongruity with the distribution plots presented in 6.3.1.4, 6.3.2.3 and 6.3.3.2, whereby both scenario 7 and 8 resulted in a higher percentage of finer particles (less than 165 µm) at the pulveriser exit. The slight increase in the percentage of finer particles observed for scenario 8 may be attributed to the increased PA velocity caused by the blocked throat segment. Furthermore, for particle sizes greater than 165 µm an inverse relationship exists between these scenarios, whereby a higher percentage of larger particles are observed to exit for scenario 7.

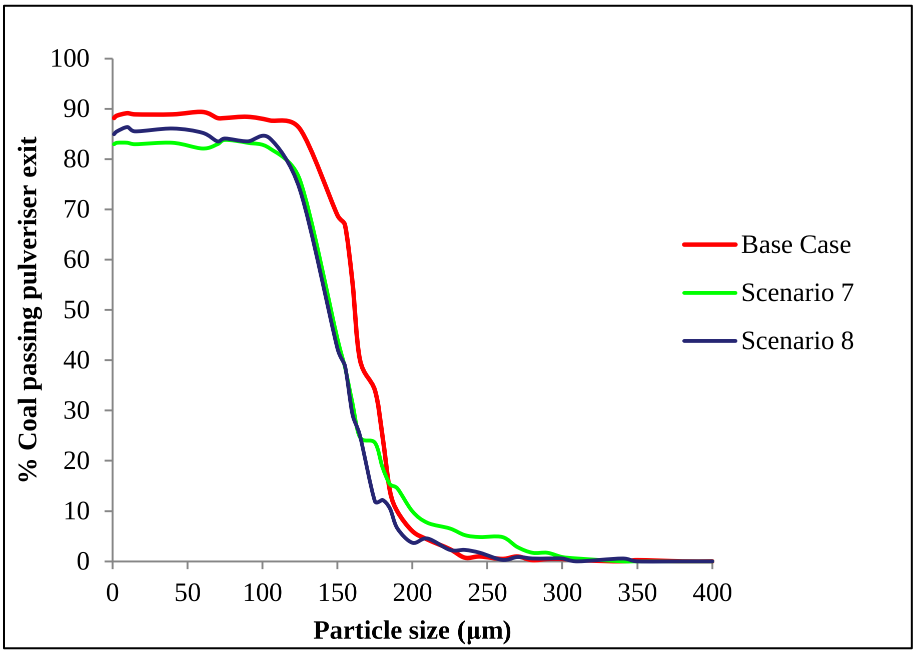

Figure 6.13 Comparison of the particle size distributions generated to elucidate the effect of the throat region modifications on the model output

6.4 Concluding remarks

The primary objective of this chapter was to determine whether the employment of static pressure drop values measured across critical pulveriser components would reveal the mechanical condition of the associated component. The array of pulveriser modifications applied to the baseline numerical model was dictated by paradigms of poor components explicated in literature as well as through visual inspections that was envisaged to potentially affect the overall pulveriser performance. The application of geometrically modified pulveriser internal components in CFD highlighted the definitive and statistically significant effect of sub-optimal pulveriser mechanical condition on the associated static pressure drop predicted. Modifications effected to the classifier region displayed a subsequent variation in the pressure drop calculated across the classifier (measurement points BF and CF) with statistically insignificant pressure variation displayed across the throat region. Modifications applied to the inner cone highlighted variations in the pressure drop values calculated across the classifier region supplemented by changes in pressure values measured across points BC. The implementation of modifications in the throat gap region highlighted variations in the pressure drop values measured across the throat gap region (measurement points AB) accompanied with statistically insignificant pressure drop variations across the classifier region. The assessment of the measured outcomes from the various modified scenarios investigated elucidates a general trend which highlights a reduction in the static pressure drop as the components deteriorates.

The success of any MCMP could not be fully established without assessing the quality of the pulveriser fuel product. Subsequently, particle size distribution analyses provided a means for comparison of changes in the particle size distributions resulting from each modification applied. Hence, the interplay between the mechanical condition of the pulveriser and the size of particles discharged by the pulveriser was established. The outcomes of this investigation provided evidence to substantiate the general tenet that as the pulveriser condition deteriorates, satisfactorily ground coal particles as required for efficient combustion is circumvented due to larger particles exiting the pulveriser.

Chapter 7: Conclusions and Recommendations

The present dissertation aimed to develop a comprehensive MCMP which is able to overcome the pulveriser performance challenges associated with conventional measurement and monitoring techniques, and subsequently lead to the development of a Mill Condition Monitoring System to improve combustion efficiency at coal-fired power utilities. The MCMP was developed in a logical step-wise manner. Firstly, an in-depth literature review aided in the elucidation of coal pulverisers which was supplemented by the challenges associated with coal pulverisation. The review culminated in the identification of significantly influential process variables as well as critical pulveriser internal components. Secondly, extensive experimental work was performed to quantify several pulveriser process variables that were deemed necessary for the assessment and validation of the mathematical models envisaged. Thirdly, two mathematical models, a global MMEB model and a numerically based model, were comprehensively developed for a commercial-scale 8.5E VSM (ball and ring). Finally, the validated mathematical models provided a platform to establish the practicality of employing measurement and monitoring techniques to successfully evaluate the pulveriser condition.

7.1 MMEB model Conclusions

For the MMEB model, all pulveriser energy input and output streams were identified and rigorously evaluated, following which the fundamental theories of mass and energy conservation, as well as the concepts of heat transfer, were applied to obtain a global energy balance. For simplification purposes, the model was developed with certain educated assumptions. The derivation was performed in steady state, whereas in industry coal pulverisation is a transient process. The model derivation highlighted the mass flow rate of coal to be dependent on several variables, some of which are not measured during normal pulveriser operation. The status of variables currently monitored was highlighted in Table A2. Therefore, the primary air flow traverse and the global pulveriser performance tests were undertaken as a means to quantify (unmeasured variables) and verify (DCS recorded variables) model dependent variables.

Several model input variables were quantified through acceptable experimental methods and measurement, and measurement errors were further minimized through engagement with best practice guidelines. However, experimental methods are accompanied by uncertainties as they are based on measurements. Therefore, a theoretical approach was employed to establish the uncertainty of each model input variable by utilizing the relative uncertainties of individual instruments employed. Following which, a theoretically simplified approach was adopted to ascertain the propagation of error on the model-predicted outcome, this yielded an overall coal mass flow rate uncertainty of 2.3 %. Variables such as the raw coal temperature and seal air temperature were identified to be the leading contributors to the overall measurement uncertainty with values of 4.9e-02 % and 1.74e-04 %, respectively. It can be concluded that a smaller propagation of error can be attained by employing instruments that are calibrated to a greater degree of accuracy.

A sensitivity analysis was performed to elucidate the sensitivity ranking of model input parameters on the model-predicted output. For a 10 % variation in input parameters, the primary air temperature was identified as the most sensitive variable, producing a 15 % variation in the model-predicted coal mass flow rate. This was sequentially followed by the primary air mass flow rate, pulveriser outlet temperature and raw coal moisture, each producing coal mass flow rate variations of 11.16 %, 9.77 % and 6.52 %, respectively. The analysis also identified parameters that produced statistically insignificant variation in coal mass flow rate, thereby providing vital information for model simplification through future research efforts. Moreover, the sensitivity results obtained were congruent with previous studies which served to verify the model developed.

In conclusion, the MMEB model-predicted coal mass flow rates demonstrated a close correlation to the experimentally determined value achieved through isokinetic sampling methods, achieving a variance of 4.31 %. This serves to validate the model developed. As the MMEB model is dependent on several pulveriser process variables, the model can at this time only be implemented on an industrial scale if it is supplemented with the necessary experiments, as required, to quantify variables that are currently not measured online.

Recommendations:

The sensitivity analysis highlighted the coal mass flow rate to be influenced by the raw coal moisture content. Furthermore, the heat capacity of coal was shown to be dependent on the volatile matter and ash content of raw coal, hence online monitoring of raw coal should be investigated in order to accurately quantify the aforementioned parameters.

The quantification of the raw coal mass flow rate using the DBM highlighted a consistently reproducible error in relation to the results obtained through the MMEB model, isokinetic sampling methods and gravimetric feeder (Power Station B). This finding warrants further investigation into the experimental technique as well as the errors associated with the raw coal bulk density determination. As the DBM is employed at several Eskom power stations, it is further recommended that a standard procedure be devised for employing the method once this investigation is complete.

As it is impractical to have online monitoring of raw coal temperature, a raw coal temperature survey should be undertaken with the aim of establishing a constant model input value. Additionally for MMEB model simplification purposes, air humidity may be excluded from the model derivation as it demonstrated a negligible effect on the model-predicted outcome.

7.2 Numerical model Conclusions

For the numerical study, a thorough literature review culminated in the identification of several geometric features and flow conditions that are significantly influential on the flow dynamic pattern exhibited within the pulveriser. In line with this, a full-scale highly detail 3D model of a typical Eskom coal VSM was prepared in CAD, following which the single-phase and two-phase static pressure flow profile was established through the employment of StarCCM+ CFD code.

Existing Eskom VSM static pressure measurement points are spatially biased hence, they were considered inadequate to establish a comprehensive picture of the flow dynamic pattern along the vertical height of the pulveriser. Therefore additional pressure measurement points were instituted, in accordance with best practice guidelines, at strategic locations on one VSM. Subsequently, quantification of the static pressure values, as well as the trend exhibited, was successfully accomplished through full-scale experiments (single and two-phase flow). For the single-phase experiment, three primary air mass flow rates were tested, all of which exhibited a similar trend, thereby highlighting the accuracy and precision of the measurement technique. The quantification of the two-phase flow static pressure profile was particularly challenging due to the frequent blockages experienced in the impulse lines and tapping points. This drawback was resolved with frequent air purging. However, only the maximum primary air flow rate (with its corresponding coal mass flow rate) was assessed. Although much higher in magnitude, the two-phase static pressure profile demonstrated a similar trend to the single-phase flow profile. The installation of additional pressure measurement points provided a means for a fundamental validation of the CFD model. In this regard, validation of the CFD models was assessed through the intensity of the correlation demonstrated between the experimentally determined and numerically calculated static pressure profiles.

For the single-phase flows, an excellent correlation was established between the CFD calculated and experimentally ascertained static pressure values for each flow condition. The measured outcomes from the simulation, at the experimental measurement locations, were within 5 % of the experimental data. This served to validate the model and the excellent correlation was attributed to the following: (1) the geometrical features of the pulveriser was captured correctly and minimal geometric assumptions were applied, (2) the magnitude of the static pressure sensed is strictly connected to the air mass flow rate and air temperature, a full-scale air flow traverse highlighted the actual mass flow rate and temperature of the primary air entering the pulveriser, hence, these physical quantities were implemented to the CFD model and, (3) the mesh refinement study culminated in the selection of the most plausible mesh resolution for areas identified with elevated velocity gradients, thereby solving the physics defined in the model accurately. The variation can be attributed to the CFD model being evaluated in steady state, whereas the experiment was performed under transient conditions. Furthermore, the CFD predicted velocities were agreeable with previous studies, which served to verify the current model developed.

During normal pulveriser operation, additional factors which influence the pressure drop are the presence of coal particles and heat transfer caused by moisture evaporation from coal. This necessitated the incorporation of a solid-phase model in collaboration with heat extraction into the fully converged single-phase CFD model to replicate the conditions conducive to two-phase flow. A Lagrangian coupled approach was selected to model the solid coal particles. In order to accurately model the thermal operating constraints of the pulveriser, a theoretical approach was employed to quantify the energy consumed during the pulverisation process, following which an absolute amount of energy was extracted from a selected volume within the computational domain. The reliability of this application was confirmed by comparison between the computed pulveriser temperature profile and the experimental measurement. Nonetheless, a negative correlation was achieved between the CFD predicted and experimentally ascertained static pressure profiles, with an average overall variation of 10 %. The largest contributor to the variation was the static pressure predictions around the throat region, achieving a variation of 31 %. The determinants responsible for achieving a better correlation in dilute areas higher up in the pulveriser can be attributed to the points highlighted in the aforementioned paragraph. The contributory factors responsible for the attaining a poor correlation at the throat region may be attributed to the following: (1) during two-phase flow operation, the throat and bottom grinding ring are in a constant state of rotation, the CFD model was simulated in steady state, (2) the computational limitation in simulating the actual number of particles in an operational pulveriser, in this model only 5000 particles could be injected, (3) simulating the exact particle size distribution during pulveriser operation was considered impractical and, in this model particles with a constant diameter of 75 µm were injected, (4) the limitations of the Lagrangian framework to accurately predict the static pressure drop across particle dense regions especially those exhibiting fluidized bed phenomena, as is the case across the throat region in a VSM.

The limitations of the two-phase flow (Two-Way coupling) CFD model not being able to accurately calculate the two-phase flow profile culminated in the selection of the adequately validated single-phase flow model to assess the viability of employing the static pressure measurements to identify changes in the mechanical condition of critical components.

By employing the tools available in StarCCM+ and CAD eight modifications, imitating typical wear conditions, were investigated through numerical simulation following which statistical analysis of the measured outcomes were performed. The influence of the modifications as well as the intensity of this influence on the measured outcomes (static pressure) proved different for each modification in comparison to the base case and in doing so areas prone to wear were simultaneously highlighted.

The success of any MCMP could not be fully established without assessing an important key performance indicator of the pulveriser, that being the quality (fineness) of the pulveriser product. Therefore, an uncoupled Lagrangian approach was employed to elucidate the discrete phase pattern based on the fully converged fixed continuous single-phase flow field. In this instance, 34 injectors were created to inject particles of various sizes between 1 µm and 400 µm into the computational domain. Subsequently, particle size distribution analyses provided a means for comparison of deviations in the particle size distributions resulting from each modification applied. Hence, the interplay between the mechanical condition of the pulveriser and the size of particles discharged by the pulveriser was established. The outcomes of this investigation provided evidence to substantiate the general tenet that as the pulveriser condition deteriorates, satisfactorily ground coal particles as required for efficient combustion is circumvented due to larger particles exiting the pulveriser.

In conclusion, the application of CFD in the pulveriser domain exhibited great potential in identifying worn pulveriser components through statistical analysis of the static pressure drop measured across specific components. Hence measuring and monitoring the single-phase static pressure drop along the vertical height of a VSM demonstrates a significant benefit for industrial application.

Recommendations:

The MCMP developed by the present dissertation is a simple and easy method which can be successfully applied to new and existing coal pulverisers. Application of the method requires a routine clean air test to be performed whilst the mill is offline. Continuous monitoring of the static pressure losses in the system will enable Engineers to establish if and in which region a faulty component might exist without the need to open a pulveriser and complete an internal inspection, thereby saving time and effort. It is recommended that at least three additional static pressure measurement points be installed on VSM's at locations delineated by points A, B and C (refer to Figure 3.14). Following which, fixed pressure probes must be installed to enable continuous recording and statistical analysis of data.

For the development of a successful condition monitoring system, it is recommended that benchmark cases be developed through experimentation to enable continuous evaluation of components during different process conditions. This will enable more educated and evidenced-based decisions to be taken, thereby reducing the uncertainties involved in early fault diagnosis. For example, in this dissertation, the clean air static pressure profile was acquired during winter hence, the ambient temperature was lower than if the test was performed during a summer month. As the temperature influences the static pressure measured, this necessitates the development of alternate static pressure profile 'benchmark cases' to be employed for component monitoring tests performed in summer months.

The particle size distribution analysis was assessed under steady state conditions. During typical pulveriser operation, the bottom grinding ring and throat gap are in a constant state of rotation. This rotation may alter the air flow distribution profile and consequently the particle size distribution at the pulveriser exit. A method to include this rotation, and the influence thereof, should be investigated under steady state conditions.

Subsequent to the identification of the Lagrangian two-phase model demonstrating poor potential in predicting the static pressure profile across the throat gap region, it is recommended that further analysis is conducted to determine the capability of the Eulerian approach to predict the pressure drop across the aforementioned fluidised bed region. It is further recommended that a field function be applied to only extract energy from cells within the throat gap region which demonstrate high velocity gradients in order to generate an improved two-phase temperature profile.

It is recommended that particle size distribution tests are undertaken on pulverisers with a known fault to establish the effect of worn pulveriser components on the pulverised fuel product.

The fully validated single-phase CFD model, employing the uncoupled Lagrangian approach, provides a platform to investigate a range of classifier and throat gap designs with the ultimate aim of improving the pulveriser performance.

References

Afolabi, L., Aroussi, A. & Isa, N., 2011. Numerical modelling of the carrier gas phase in a laboratory-scale coal classifier model. *Fuel Processing Technology,* Volume 92, pp. 556-562.

Agrawala, V., Panigrahia, B. & Subbarao, P., 2015. Review of control and fault diagnosis methods applied to coal mills. *Journal of Process Control,* Volume 32, pp. 138-153.

Andersen, P., Bendtsen, J. & Pedersen, T., 2006. Observer-based coal mill control using oxygen measurements. In: *Power Plants and Power Systems Control.* Kananaskis, Canada: Elsevier, pp. 171-176.

ANSYS, 2012. *Ansys Fluent User's Guide, Version 14.5.* United States of America: ANSYS, INC.

Archary, H., 2014. *Condition monitoring and performance optimisation of pulverised fuel vertical spindle type mills.* Johannesburg, EPPEI.

Benedict, R., 1977. *Fundamentals of temperature, pressure and air flow measurement.* Second ed. United Stated of America: John Wiley and Sons.

Bhambare, K., Ma, Z. & Lu, P., 2010. CFD modeling of MPS coal mill with moisture evaporation. *Fuel Processing Technology,* Volume 91, pp. 566-571.

Bhasker, C., 2002. Numerical simulation of turbulent flow in complex geometries used in power plants. *Advances in Engineering Software*, Volume 33, pp. 71-83.

British Standards, 1978. *Method for the measurement of the concentration of particulate material in ducts carrying gases.* United Kingdom: British Standards.

British Standards, 1991. *Method for testing and analysing coal and coke.* United Kingdom: British Standards.

British Standards, 2007. *BS EN 15259:2007: Air quality - Measurement of stationary source emissions - Requirements for measurement sections and sites and for the measurement objective plan and report.* United Kingdom: British Standards.

Burgess, W., Ellenbecker, M. & Treitman, R., 2004. *Ventilation for Control of the Work Environment.* Second ed. United States of America: John Wiley and Sons.

CD-Adapco, 2014. *StarCCM+ Version 9.02.*

CD-Adapco, 2015. *Improving the performance of the mill and classifier.* Aerotherm, StarCCM+ SA Conference, Pretoria, South Africa.

CMP, 2003. *Coal Milling Plant: Selection, Maintenance, Operation and Performance.* South Africa: Coal Milling Projects (CMP).

Coulson, J. & Richardson, R., 1999. *Chemical Engineering Design.* Third ed. Butterworth-Heinemann.

De Wet Krüger, J. I., 1977. *A study of the parameters affecting the design of Vertical Spindle Mills,* MSc. Dissertation (Eng), Johannesburg, South Africa: University of the Witwatersrand.

Dodds, D. et al., 2011. Experimental and numerical study of the pulverised-fuel distribution in the mill-duct system of the Loy Yang B lignite fuelled power station. *Powder Technology,* Volume 207, pp. 257-269.

Durbin, P. & Medic, G., 2007. *Fluid Dynamics with a Computational Perspective.* United States of America, Cambridge University Press.

Eccles, W., 2011. *Pragmatic Electrical Engineering.* Morgan and Claypool publishers.

EPRI, 2006. *Pulverizer maintenance guide,* Palo Alto, California,United States of America: EPRI.

Eskom, 2014. *About Electricity.* [Online]
Available at: http://www.eskom.co.za [Accessed 2015].

Fan, G. & Rees, N., 1997. An intelligent expert system (KBOSS)for power plant coal mill supervision and control. *Control Engineering Practice,* Volume 5, pp. 101-108.

Farrar, C. & Worden, K., 2007. An introduction to structural health monitoring. *Philosophical transactions of the royal society,* Volume 365, pp. 303-315.

Flynn, D., 2003. Modelling and control of pulverised fuel coal mills. In: *Thermal Power Plant Simulation and Control.* London, United Kingdom: The Institution of Electrical Engineers, pp. 63-99.

Fox, R., Pritchard, P. & McDonald, A., 2009. *Introduction to Fluid Mechanics.*

Hamby, D., 1994. A review of techniques for parameter sensitivity analysis of environmental models. *Environmental Monitoring and Assessment* , Volume 32, pp. 135-154.

Holman, J., 2012. *Experimental Methods for Engineers.* Eigth ed. United States of America: McGraw-Hill.

Holtshauzen, G., 2008. *Coal pulveriser maintenance performance enhancement through the application of a combination of technologies.* South Africa: University of Johannesburg.

Incropera, F., DeWitt, D., Bergman, T. & Lavine, A., 2006. *Fundamentals of Heat and Mass Transfer.* Sixth ed. United States of America: John Wiley & Sons.

International Energy Agency, 2015. *Topics: Coal.* [Online]
Available at: http://www.iea.org [Accessed 2015].

International Organisation for Standardization, 2007. *Fluid flow in closed conduits-Connections for pressure signal transmissions between primary and secondary elements.* International Organisation for Standardization.

International Organization for Standardization, 2006. *Hard coal and coke - Manual sampling.* International Organization for Standardization.

Kapakyulu, E., 2007. *Development of a model for temperature in a grinding mill,* MSc. Dissertation (Eng), Johannesburg, South Africa: University of the Witwatersrand.

Khan, M., 2011. *Advances in Clean Hydrocarbon Fuel Processing: Science and Technology.*Woodhead Publishing Limited.

Khare, A., Singh, A. & Nokam, K., 2009. *Best Practices in Grid Generation for CFD Applications Using HyperMesh.*

Kitto, J. & Schultz, S., 2005. *Steam/ Its generation and use.* 41st ed. Barberton, Ohio, U.S.A. The Babcock and Wilcox Company.

Lindsley, D., 2000. *Power-plant control and instrumentation.* London: The institute of Electrical Engineers.

Lipták, B., 2003. *Process Measurement and Analysis.* Fourth ed. United States of America: The Instrumentation, Systems and Automations Society.

Maharaj, A., 2014. *Experimental and Numerical studies of air preheater leakage,* MSc. Dissertation (Eng), Johannesburg, South Africa: University of the Witwatersrand.

Marvin, J., 1995. Perspective on computational fluid dynmics validation. *AIAA Journal,* Volume 33, pp. 1778-1787.

Messerschmidt, L., 1972. *Combustion Manual.* Eskom: Witbank, South Africa.

Michelis, C., 2011. *Condition monitoring and assessment of power plant components In: Chapter 2: Power plant life management and performance improvement.* John E. Oakney ed. Italy: Woodhead Publishing Limited.

Millen, M. et al., 2000. Plant tests of an on-line multiple-pipe pulverised coal mass flow measuring system. *Flow Measurement and Instrumentation,* Volume 11, pp. 153-158.

Miller, B. & Tillman, D., 2008. *Combustion Engineering Issues for Solid Fuel Systems.* Academic Press: London, United Kingdom.

Moffat, R., 1988. Describing the uncertainties in Experimental Results. *Experimental Thermal and Fluid Science,* Volume 1, pp. 3-17.

Mohanty, A., 2006. *Fluid Mechanics.* Second ed. India: Asoke K. Ghosh.

Muller, M., 2015. *Generation plant engineering strategic report for milling plant and burners for 2015.* Johannesburg, South Africa: Eskom.

Niemczyk, P., 2010. *Model-based fuel flow control for fossil-fired power plants,* PhD dissertation, Denmark: AAlborg University Denmark.

Niemczyk, P. et al., 2012. Derivation and validation o fa coal mill model for control. *Control Engineering Practice,* Volume 20, pp. 519-530.

Odgaard, P. & Mataji, B., 2006. Fault detection in coal mills used in power plants. In: D. D. Westwick, ed. *Power Plants and Power Systems Control.* Kananaskis, Canada: Elsevier, pp. 177-182.

Parham, J. & Easson, W., 2003. Flow visualisation and velocity measurements in a vertical spindle coal mill static classifier. *Fuel*, Volume 82, pp. 2115-2123.

Park, K., Asim, T. & Mishra, R., 2012. Computational fluid dynamics based fault simulations of a vertical axis wind turbine. *Procedia CIRP*, Volume 11, pp. 323-327.

Peta, S., 2014. *Ignition Characterstics of low volatile quality high ash coal ,* MSc. Dissertation (Eng), Johannesburg, South Africa: University of the Witwatersrand.

Postrzednik, S., 1981. *Analiza termodynamiczna procesu odgazowania paliw stałych,* Poland: Chemik International.

Pradeebha, P., Pappa, N. & Vasanthi, D., 2013. *Modelling and Control of a Coal Mill.* Mumbai, India, Preprints of the 10th IFAC International Symposium on Dynamics and Control of Process Systems.

Rathakrishnan, E., 2007. *Instrumentation, Measurements And Experiments in Fluids.* London, United Kingdom: Taylor and Francis Group, LLC.

Reader-Harris, M. & McNaught, J., 2005. *Impulse lines for differential pressure flowmeters, Best Practice Guide.* Glasglow, United Kingdom: The Department of Trade and Industry.

Rehman, A. et al., 2013. *CFD based condition monitoring of centrifugal pump.* Helsinki, Finland, Comaderm.

Salim, M. & Cheah, S., 2009. *Wall y+ strategy for Dealing with Wall-bounded Turbulent Flows.* Hong Kong, Proceedings of the International MultiConference of Engineers and Computer Scientists 2009 Vol II.

Shah, K. V., Vuthaluru, R. & & Vuthaluru, H. B., 2009. CFD based investigations into optimisation of coal pulveriser performance: Effect of classifer vane settings. *Fuel Processing Technology,* Volume 90, p. 1135–1141.

Shaw, R., 1960. The influence of hole dimensions on static pressure. *Journal of Fluid Mechanics,* Volume 7, pp. 550-564.

Siemens Energy & Automation, 2008. *User Manual- SITRANS P, Series DSIII Transmitters for Pressure, Differential Pressure,Flanged, Level, and Absolute Pressure Model, Revision 9.* Germany: Siemens Energy & Automation.

Stamboliadis, E. T., 2002. A contribution to the relationship of energy and particle size in the comminution of brittle particulate materials. *Minerals Engineering,* Volume 15, pp. 707-713.

Tu, J., Yeoh, G. & Liu, C., 2008. *Computational Fluid Dynamics: A Practical Approach.* Elsevier.

Van Der Merwe, J., 2013. *Pulverised fuel transport and balancing using 2-phase flow modelling and testing.* MSc Dissertation, Johannesburg, South Africa: University of the Witwatersrand.

Van Wyk, C., 2008. *Combustion Manual.* Eskom: South Africa.

Vuthaluru, H., Pareek, V. & Vuthaluru, R., 2005. Multiphase flow simulation of a simplified coal pulveriser. *Fuel processing technology,* Volume 86, pp. 1195-1205.

Vuthaluru, R. et al., 2006. Investigation of wear pattern in a complex coal pulveriser using CFD modelling. *Fuel Processing Technology,* Volume 87, pp. 687-694.

Wang, J., Wei, J. & Guo, S., 2010. *Condition monitoring of power plant milling process using intelligent optimisation and model based techniques,* United Kingdom: The University of Birmingham.

Wei, J., Wang, J. & Wu, Q., 2007. Development of a ultisegment coal mill model using an evolutionary computation technique. *IEEE Transactions on energy conversion,* Volume 22, pp. 718-727.

Zhang, Y. et al., 2002. Coal mill modeling by machine learning based on onsite measurements. *IEEE transactions on Energy Conversion,* Volume 17, pp. 549-555.

Appendix A

Table A1 Summary of Eskom pulverisation plants

Station	Unit	Commissioned date	Make	Type	No./ (ton/hr)	Unit Capacity (MW)
Komati	1-3 4&5 6&7 8&9	1967-1966	B&W 8.5E Mitchell Mitchell B&W 8.5E	VSM ball Tube Tube VSM ball	3/24 3/22 3/25 3/28	100 100 125 125
Camden	1-8	1966-1969	Loesche	VSM Roller/track	4/28	200
Grootvlei	1-4&6 5	1969-1977	B&W 8.5E Loesche	VSM ball VSM Roller/track	6/29 6/26	200 200
Hendrina	1-5 8-10	1970-1977	B&W 8.5E MPS	VSM ball VSM Tyre	6/24 6/21	200 200
Arnot	1 2-6	1971-1975	Stein Loesche LM	Tube VSM Roller/track	3/65 6/38	350 350
Kriel	1-3 4-6	1976-1979	B&W 10.8E B&W 12.0E	VSM ball VSM ball	6/50 6/62	500 500
Matla	1-6	1979-1983	B&W 12.9E	VSM ball	6/68	600
Duvha	1-4 5&6	1980-1984	B&W 12.9E Loesche	VSM ball VSM Roller/track	6/65 6/65	600 600
Tutuka	1-6	1985-1990	Stein	Tube	6/63	609
Lethabo	1-6	1985-1990	Riley	Tube	6/80	618
Matimba	1-6	1987-1991	Stein	Tube	4/105	665
Kendal	1-6	1988-1993	Kennedy van Saun	Tube	5/104	686
Majuba	1-6	1996-2001	Stein	Tube	5/105	685
Medupi	1-5 6	- 2015	MPS 265	VSM Tyre	5/115	800
Kusile	1-6	-	MPS 265	VSM Tyre	5/115	800

Table A2 Measurement status of pulveriser process variables at Power Station A

Pulveriser process variable	Measured online	Pulveriser process variable	Measured online
Raw coal flow at inlet	No	Pulverised coal/air temperature at outlet	Yes
Pulverised coal flow at outlet	No	Primary air differential pressure	Yes
Primary air flow at inlet	Yes	Pulveriser differential pressure	Yes
Primary air flow at outlet	No	Pulveriser motor current	Yes
Primary air flow temperature at inlet	Yes	Coal recirculation load	No
Seal air mass flow rate	No	Seal air temperature	No

Table A3 Eskom procedure employed to quantify process parameters

Test description	Procedure title	Reference number
Proximate analysis	Determination of calorific value	240-55195819
	Determination of total moisture	240-36547792
	Determination of ash content	240-36547751
	Determination of AI	240-36547788
	Determination of HGI	240-36547789
	Determination of volatile matter	240-36547761
Isokinetic PF sampling	Pulverised fuel sampling and size grading	240-30836576

Appendix B

CALIBRATION CERTIFICATES

L-type pitot-tube

Sampling Systems INTERNATIONAL

Tel: (011) 630-0119 Fax: (011) 907-9354 Cell: 082 851 0041

Unit 8 Jeanique Business Park, 168 Second Avenue, Alberton

PF SAMPLING SPECIALISTS, BOILER PLANT PERFORMANCE TESTING, DEVELOPMENT OF SAMPLING EQUIPMENT

OEM STANDARD

ISO-IEC 17025 COMPLIANT

No: SS 14 - 208 GV

DATE ISSUED: 30/07/2014

CALIBRATION CERTIFICATE

CLIENT DETAILS

COMPANY NAME: Eskom ADDRESS:

BRANCH:

DESCRIPTION OF INSTRUMENT

INSTRUMENT: Pitot Tube MODEL: 1.5m Prandel ADDITIONS: N/A

MAKE: Sampling Systems SERIAL NO: PT-P1.5-100 OTHER: N/A

TEST PARAMETERS

LOCATION: TEMPERATURE: 21°C BAROMETRIC PRESSURE: 1030mb

DATE RECIEVED: 18/07/2014 HUMIDITY: 28% PROCEDURE: SS-CAL-005

DATE COMPLETED: 30/07/2014 TECHNICIAN: F. MADUANE OTHER: N/A

INSTRUMENT ACCURACY TEST

UNIT OF MEASURE: Pa INSTRUMENT FOUND WITHIN TOLERANCE: YES

ITEM	SPEC	REFERENCE	INSTRUMENT	VARIANCE
1	-	-90	-92	2
2	-	-107	-101	6
3	-	-108	-105	3
4	-	-112	-112	0
5	-	-114	-113	1

PERFORMANCE SUMMARY

Visual inspection, leakage & blockage inspection was done. Instrument remains within the OEM specified tolerance.

Flow formula : Velocity (kg/s) = $K\sqrt{\frac{2 \times 1000 \times \Delta P}{\rho}}$ (where K= 1.01)

ΔP = Pressure Diff (kPa)

ρ = density (kg/m3)

K = 1.01

TRACEABILITY OF STANDARDS USED

ISO-IEC 17025

ISSUING

ISSUED BY: Julian Lopez ISSUED TO: Simon Phala

SIGNATURE: SIGNATURE:

DATE: 30/07/2014 DATE: 04/08/2014

Figure B1 Pitot-tube calibration certificate

Digital thermometer

InterCal **Certificate of Calibration** SANAS Calibration Laboratory

This certificate is issued without alteration, and in accordance with the conditions of accreditation granted by SANAS. It is a correct record of the measurements made at the time of calibration. Copyright of this certificate is owned by InterCal and may not be reproduced other than in full, except with the prior written approval of InterCal. The values given in this certificate were correct at the time of calibration. Subsequently the accuracy will depend on factors such as care exercised in handling the instrument and frequency of use. Recalibration should be performed after a period which has been chosen to ensure that, under normal circumstances, the instruments accuracy remains within the desired limits. The accuracies of all measurements were traceable to the national measuring standards as maintained in South Africa, unless otherwise noted. The reported expanded uncertainties are based on a standard uncertainty multiplied by a coverage factor k = 2 providing a level of confidence of approximately 95%. The uncertainties of measurement have been estimated in accordance with the principles defined in the GUM, Guide to Uncertainty of Measurement, ISO, Geneva, 1993

Certificate No : 61921

Manufacturer : Fluke
Description : Digital Thermometer
Model No : 54 IIB
Serial No : 17290118
Plant No : None

Calibrated for : Eskom Holdings SOC Ltd
Address :

Calibration Environment
Temperature : 21 °C (± 1°C)
Relative Humidity : 44 %rh (± 3%rh)

Date of calibration : 30 July 2014 **Print Date** : 30 July 2014
Expiry date : 30 July 2015

Calibrated by : T. Madiba **Checked by** :

ilac-MRA SANAS Calibration Laboratory

The South African National Accreditation System (SANAS) is a member of the International Laboratory Accreditation Cooperation (ILAC) Mutual Recognition Arrangement (MRA). This Arrangement allows for the mutual recognition of technical test and calibration data by the member accreditation bodies worldwide. For more information in the Arrangement please consult www.ilac.org

Technical Signatory
G. Snelling

Page 1 of 2

InterCal CC Reg: CK1992/28397/23
InterCal Test and Measurement Center, 907 Richards Drive, Halfway House, Midrand
PO Box 10907 Vorna Valley 1686
Tel: (011) 315 4321 Fax: (011) 312 1322 e-mail: intercal@intercal.co.za www.intercal.co.za

Members: PS Haarhoff GC Snelling

Figure B2 Digital thermometer calibration certificate, Page 1 of 2

Certificate of Calibration

Certificate No: 61921

1. Standards and equipment

Asset ID	Make	Model	Description	Serial Number	Due Date	Certificate No
1-152	Fluke	5500A	Calibrator	7380003	Oct 2015	79820

2. Procedure

2.1 The UUT was calibrated by simulation by using a relevant thermocouple wire in accordance with procedure **3/P/005.**

3. Results

3.1 Temperature: Simulation

Input (°C)	Tolerance (°C)	UUT Display T1 (°C)	UUT Display T2 (°C)	Uncertainty of measurement (°C)
-50	±0.3	-50.1	-50.0	±0. 2
0	±0.3	-0.2	0.0	± 0.2
50	±0.3	50.0	50.0	± 0.2
100	±0.4	99.9	100.0	± 0.2
200	±0.4	199.8	200.0	± 0.2
400	±0.5	399.8	400.1	± 0.2
600	±0.6	599.9	600.1	± 0.2
800	±0.7	799.8	800.1	± 0.2
1000	±0.8	999.9	999.9	± 0.2
1200	±1	1200	1201	± 0.2
1300	±1	1300	1301	± 0.2

4. Comments

4.1 The UUT was only calibrated at the above temperatures in accordance with the customer's instruction.

4.2 Temperature conversions were performed with reference to IEC 60751:2008 and/or EN 60584-1.

----- End of document ----

Technical Signatory

Page 2 of 3

Figure B3 Digital thermometer calibration certificate, Page 2 of 2

Thermo-vane Anemometer

Technology Solutions
Measurement Science Laboratory

ILAC-MRA | sanas Calibration Laboratory

Certificate of Calibration

The South African National Accreditation System (SANAS) is a member of the international Laboratory Accreditation Cooperation (ILAC) Mutual Recognition Agreement (MRA). This arrangement allows for the mutual recognition of technical test and calibration data by the member accreditation bodies worldwide. For more information on the arrangement please consult www.ilac.org. The accuracies of all measurements were traceable to the National Measuring Standards as maintained in South Africa, unless otherwise noted. The uncertainties of measurement were estimated for a coverage factor of k=2 which approximates a 95% confidence level.

Certificate No	L59221			
Manufacturer	Major Tech			
Description	Anemometer			
Model No	MT948			
Serial No	07057930			
Plant No	EELA13			
Calibrated for	Eskom Holdings Soc Ltd -			
Temperature	24	°C		
Relative humidity	27	% rh		
Barometric Pressure	863	mbar		
Date of calibration	23 September 2014			
Expiry date	23 September 2015		Issue Date	24 September 2014
Calibrated by	I. Jooste		Checked by	

This certificate is issued without alteration, and in accordance with the conditions of accreditation granted by the SANAS. Copyright of this certificate is owned by Technology Solutions and may not be reproduced other than in full, except with the prior written approval of Technology Solutions. It is a correct record of the measurements performed at the time of calibration. Subsequently the accuracy will depend on factors such as care exercised in handling the instrument and frequency of use. Recalibration should be performed after a period which has been chosen to ensure that, under normal circumstances, the instruments accuracy remains within the desired limits.

Technical Signatory *Luke W. Hards* Digitally signed by LAWtrust AESignCA, Luke William Hards DN: c=ZA, o=LAWtrust, cn=LAWtrust AESignCA, ou=LAWtrust AeSign, [illegible], cn=Luke William Hards, [illegible] Date: 2014.09.24 06:15:57 -07'00'

Page 1 of 3

Sales, Service, Training, Consultation and Calibration of Measurement Equipment
Setting New Standards in delivering Service Excellence to you.

Hards Laboratories cc T/A Technology Solutions. C3 Prospect Close, 311 Regency Drive, R21 Corporate Park, Irene
Tel: +27 (0) 12 345 5358 Fax +27 (0) 12 345 3263.

Figure B4 Thermo-vane anemometer calibration certificate, Page 1 of 2

Technology Solutions
Measurement Science Laboratory

sanas
Calibration Laboratory

Certificate of Calibration

Certificate No L59221

Standards and Equipment used

Description	Asset No	Cal due
Kanomax	TS-065	Nov 10, 2014
Testo Barometer	TS-021	30 June 2018
Wind Tunnel	TS-048	Source only

Procedure TS PL 005

Results

Standard velocity m/s	UUT velocity m/s	Correction m/s	UoM ± m/s
0.00	0.00	0.00	0.11
2.13	1.76	0.37	0.06
3.83	4.06	-0.23	0.11
5.82	6.13	-0.31	0.16
7.96	7.63	0.33	0.21
9.56	9.30	0.26	0.25
11.47	11.04	0.43	0.29
13.29	12.63	0.66	0.34
14.89	14.12	0.77	0.37
16.64	15.35	1.29	0.42
18.51	16.84	1.67	0.47

Parameter	Standard	UUT Reading	± UoM
Temperature (°C)	23.8	23.7	0.5
Humidity (% rh)	NA	NA	5

Status	Used
Repair details	None

Technical Signatory LW Hards

Page 2 of 3

Sales, Service, Training, Consultation and Calibration of Measurement Equipment
Setting New Standards in delivering Service Excellence to you.

Hards Laboratories cc T/A Technology Solutions. C3 Prospect Close, 311 Regency Drive, R21 Corporate Park, Irene
Tel: +27 (0) 12 345 5358 Fax +27 (0) 12 345 3263.

Figure B5 Thermo-vane anemometer calibration certificate, Page 2 of 2

Infrared Thermometer

REPCAL

Services cc

Reg. No. 2002/087115/23

sanas

Calibration Laboratory

146 308 1546 1446

CERTIFICATE OF CALIBRATION

South African National Accreditation System

Accredited Laboratory Number 146/308/1546/1446

CERTIFICATE NUMBER: 308-15644

Calibration of a	:	Infrared Thermometer
Manufacturer	:	Sentry
Model No	:	ST 672
Serial No	:	1109003066
Calibrated for	:	Eskom Holdings Soc Ltd
Address	:	

Issue Date	:	30 July 2014
Calibration Date	:	29 July 2014
Technical Signatory	:	JW Ysel
Calibrated by	:	J Ysel (Jnr)
Checked by	:	L Inama

The South African National Accreditation System (SANAS) is a member of the International Laboratory Accreditation Co-Operation (ILAC) for the Mutual Recognition Agreement (MRA). The MRA allows for the mutual recognition of technical test and calibration data by the member accreditation bodies worldwide. For more information on the MRA please refer to www.ilac.org

508 Nupen Crescent
Halfway House
Midrand

P.O. Box 6093
Halfway House
1685

Phone (011) 315 3134
Fax (011) 315 8726
e-mail : service@repcal.co.za

Figure B6 Infrared thermometer calibration certificate, Page 1 of 2

REPCAL SERVICES
SANAS CALIBRATION LABORATORY
LABORATORY NO 308

4. METHOD

The Infrared Thermometer was calibrated from 600°C to 1200°C against a Black Body furnace. The true temperature of the furnace was measured with a standard Pyrometer.

5. RESULTS

Actual Temperature (°C) ITS-90	UUT Temperature (°C)	UUT Correction (°C)
602	595.1	+6.9
899	896.5	+2.5
1199	1193.5	+5.5

**End of results*

6. UNCERTAINTY: The uncertainty of measurement was: ±5 °C

7. NOTES

7.1 Calibrated from: 600°C to 1200°C.

7.2 Cal distance: ±1m.

7.3 Emissivity set to 1.00

Signed : JW Ysel
Technical Signatory (Temperature)

Certificate No : 308-15644

Figure B7 Infrared thermometer calibration certificate, Page 2 of 2

PF Sampler

Sampling Systems
INTERNATIONAL

Tel: (011) 869-9119
Fax. (011) 907-8354
Cell: 082 651 0841

Unit 8 Jounique Business Park,
168 Second Avenue,
Alberton

PF SAMPLING SPECIALISTS, BOILER PLANT PERFORMANCE TESTING, DEVELOPMENT OF SAMPLING EQUIPMENT

OEM STANDARD
ISO-IEC 17025 COMPLIANT

CALIBRATION CERTIFICATE

No: SS 14 - 202 GV
DATE ISSUED: 29/07/2014

CLIENT DETAILS

COMPANY NAME: Eskom
ADDRESS:
BRANCH:

DESCRIPTION OF INSTRUMENT

INSTRUMENT: PF Sampler
MODEL: LC-4
ADDITIONS: N/A
MAKE: Sampling Systems
SERIAL NO: SSI 1985 041
OTHER: N/A

TEST PARAMETERS

LOCATION: Sampling Systems
TEMPERATURE: 17°C
BAROMETRIC PRESSURE: 1032mb
DATE RECIEVED: 18/07/2014
HUMIDITY: 70%
PROCEDURE: SS-CAL-010
ATE COMPLETED: 29/07/2014
TECHNICIAN: F. MADUANE
OTHER: N/A

INSTRUMENT ACCURACY TEST

UNIT OF MEASURE: NA
INSTRUMENT FOUND WITHIN TOLERANCE: YES

ITEM	SPEC	REFERENCE	INSTRUMENT	VARIANCE
1	-	NA	NA	NA
2	-			
3	-			
4	-			
5	-			

PERFORMANCE SUMMARY

Visual Inspection, Leakage and Blockage test done. Verification of U-tube functionality.
REPLACED: 2x Line Filters
6x Interception taps
1x 3/4" Ball valve and
Replaced missing labels and screws

TRACEABILITY OF STANDARDS USED

ISO-IEC 17025

ISSUING

ISSUED BY: Julian Lopez
SIGNATURE:
DATE: 29/07/2014
ISSUED TO: Simon Phala
SIGNATURE:
DATE: 04/08/2014

Figure B8 PF sampler calibration certificate

Pressure transducers

Unique Metrology

Eskom Research & Innovation Centre
Lower Germiston Road • Rosherville
P O Box 145296 • Bracken Gardens • 1452
Tel: 011 626 3808 • Cell: 083 254 3635 • Fax: 086 610 4196
Web: www.unimet.co.za

sanas Calibration Laboratory 306 205

CERTIFICATE OF CALIBRATION

Page 2 of 2 pages.

Certificate Number	:	1506P5810-1
Calibration of a	:	Pressure Transmitter
Manufacturer & Type	:	Siemens Sitrans P
Serial Number	:	N1-X914-9101876
Calibrated for	:	The University of the Witwatersrand, Johannesburg.
Procedure Number	:	53-124
Date of Calibration	:	02/06/2015
Date of Issue	:	02/06/2015
Laboratory Environment	:	22.4 °C
Reference Standards	:	205-S-01 Ruska 6200 PPG S/N 39478
	:	
	:	

Reference Pressure (kPa)	Indication (V) Rising	Falling
-0.5	0.499	0.500
0	0.594	0.593
2	0.971	0.971
4	1.348	1.348
6	1.724	1.724
8	2.103	2.104
10	2.339	2.339

Curve: $P\ (Pa) = (5.5308V - 3.3523)*1000$

The uncertainty of measurement is ± 0.025 kPa
The reported uncertainty is based on a standard uncertainty multiplied by a coverage factor of k=2, which unless specifically stated otherwise, provides a confidence level of 95%, in accordance with the Guide to the Expression of Uncertainty in Measurement, first edition, 1993.

Comments : The above readings were obtained using the customers data logging system. The transmitter was connected to channel 0.

Calibrated by : A Mathieson & R de Jager

M.Mat
Technical Signatory

Figure B9 Pressure transducer 1 calibration certificate, Page 1 of 6

Unique Metrology

Eskom Research & Innovation Centre
Lower Germiston Road • Rosherville
P O Box 145296 • Bracken Gardens • 1452
Tel: 011 626 3808 • Cell: 083 254 3635 • Fax: 086 610 4196
Web: www.unimet.co.za

sanas Calibration Laboratory 306 205

CERTIFICATE OF CALIBRATION

Page 2 of 2 pages.

Certificate Number	:	1506P5810-2
Calibration of a	:	Pressure Transmitter
Manufacturer & Type	:	Siemens Sitrans P
Serial Number	:	N1-X914-9101872
Calibrated for	:	The University of the Witwatersrand, Johannesburg.
Procedure Number	:	53-124
Date of Calibration	:	02/06/2015
Date of Issue	:	02/06/2015
Laboratory Environment	:	22.4 °C
Reference Standards	:	205-S-01 Ruska 6200 PPG S/N 39478
	:	
	:	

Reference Pressure (kPa)	Indication (V) Rising	Falling
-0.5	0.499	0.501
0	0.593	0.593
2	0.971	0.971
4	1.347	1.349
6	1.721	1.726
8	2.104	2.103
10	2.362	2.362

Curve: P (Pa) = (5.4972V - 3.3256)*1000

The uncertainty of measurement is ± 0.025 kPa
The reported uncertainty is based on a standard uncertainty multiplied by a coverage factor of k=2, which unless specifically stated otherwise, provides a confidence level of 95%, in accordance with the Guide to the Expression of Uncertainty in Measurement, first edition, 1993.

Comments : The above readings were obtained using the customers data logging system. The transmitter was connected to channel 1.

Calibrated by : A Mathieson & R de Jager

Technical Signatory

Figure B10 Pressure transducer 2 calibration certificate, Page 2 of 6

Unique Metrology

Eskom Research & Innovation Centre
Lower Germiston Road • Rosherville
P O Box 145296 • Bracken Gardens • 1452
Tel: 011 626 3808 • Cell: 083 254 3635 • Fax: 086 610 4196
Web: www.unimet.co.za

sanas Calibration Laboratory 306 205

CERTIFICATE OF CALIBRATION

Page 2 of 2 pages.

Certificate Number	:	1506P5810-3
Calibration of a	:	Pressure Transmitter
Manufacturer & Type	:	Siemens Sitrans P
Serial Number	:	N1-X914-9101875
Calibrated for	:	The University of the Witwatersrand, Johannesburg.
Procedure Number	:	53-124
Date of Calibration	:	02/06/2015
Date of Issue	:	02/06/2015
Laboratory Environment	:	22.4 °C
Reference Standards	:	205-S-01 Ruska 6200 PPG S/N 39478
	:	
	:	

Reference Pressure (kPa)	Indication (V) Rising	Falling
-0.5	0.499	0.499
0	0.595	0.595
2	0.972	0.973
4	1.347	1.350
6	1.722	1.727
8	2.104	2.104
10	2.370	2.370

Curve: P (Pa) = (5.4852V - 3.33189)*1000

The uncertainty of measurement is ± 0.025 kPa
The reported uncertainty is based on a standard uncertainty multiplied by a coverage factor of k=2, which unless specifically stated otherwise, provides a confidence level of 95%, in accordance with the Guide to the Expression of Uncertainty in Measurement, first edition, 1993.

Comments : The above readings were obtained using the customers data logging system. The transmitter was connected to channel 2.

Calibrated by : A Mathieson & R de Jager

Technical Signatory

Figure B11 Pressure transducer 3 calibration certificate, Page 3 of 6

Unique Metrology

Eskom Research & Innovation Centre
Lower Germiston Road • Rosherville
P O Box 145296 • Bracken Gardens • 1452
Tel: 011 626 3808 • Cell: 083 254 3635 • Fax: 086 610 4196
Web: www.unimet.co.za

sanas Calibration Laboratory 306 205

CERTIFICATE OF CALIBRATION

Page 2 of 2 pages.

Certificate Number	:	1506P5810-4
Calibration of a	:	Pressure Transmitter
Manufacturer & Type	:	Siemens Sitrans P
Serial Number	:	N1-X914-9101863
Calibrated for	:	The University of the Witwatersrand, Johannesburg.
Procedure Number	:	53-124
Date of Calibration	:	02/06/2015
Date of Issue	:	02/06/2015
Laboratory Environment	:	22.4 °C
Reference Standards	:	205-S-01 Ruska 6200 PPG S/N 39478
	:	
	:	

Reference Pressure (kPa)	Indication (V)	
	Rising	Falling
-0.5	0.499	0.501
0	0.596	0.596
2	0.973	0.973
4	1.349	1.350
6	1.723	1.727
8	2.106	2.105
10	2.375	2.375

Curve: P (Pa) = (5.4781V - 3.3173)*1000

The uncertainty of measurement is ± 0.025 kPa
The reported uncertainty is based on a standard uncertainty multiplied by a coverage factor of k=2, which unless specifically stated otherwise, provides a confidence level of 95%, in accordance with the Guide to the Expression of Uncertainty in Measurement, first edition, 1993.

Comments : The above readings were obtained using the customers data logging system. The transmitter was connected to channel 3.

Calibrated by : A Mathieson & R de Jager

Technical Signatory

Figure B12 Pressure transducer 4 calibration certificate, Page 4 of 6

Unique Metrology

Eskom Research & Innovation Centre
Lower Germiston Road • Rosherville
P O Box 145296 • Bracken Gardens • 1452
Tel: 011 626 3808 • Cell: 083 254 3635 • Fax: 086 610 4196
Web: www.unimet.co.za

sanas Calibration Laboratory 306 205

CERTIFICATE OF CALIBRATION

Page 2 of 2 pages.

Certificate Number	:	1506P5810-5
Calibration of a	:	Pressure Transmitter
Manufacturer & Type	:	Siemens Sitrans P
Serial Number	:	N1-X914-9101867
Calibrated for	:	The University of the Witwatersrand, Johannesburg.
Procedure Number	:	53-124
Date of Calibration	:	02/06/2015
Date of Issue	:	02/06/2015
Laboratory Environment	:	22.4 °C
Reference Standards	:	205-S-01 Ruska 6200 PPG S/N 39478
	:	
	:	

Reference Pressure (kPa)	Indication (V) Rising	Falling
-0.5	0.504	0.504
0	0.597	0.598
2	0.974	0.975
4	1.348	1.351
6	1.725	1.729
8	2.107	2.107
10	2.369	2.369

Curve: P (Pa) = (5.4937V - 3.3423)*1000

The uncertainty of measurement is ± 0.025 kPa
The reported uncertainty is based on a standard uncertainty multiplied by a coverage factor of k=2, which unless specifically stated otherwise, provides a confidence level of 95%, in accordance with the Guide to the Expression of Uncertainty in Measurement, first edition, 1993.

Comments : The above readings were obtained using the customers data logging system. The transmitter was connected to channel 4.

Calibrated by : A Mathieson & R de Jager

M-MXH

Technical Signatory

Figure B13 Pressure transducer 5 calibration certificate, Page 5 of 6

Unique Metrology

Eskom Research & Innovation Centre
Lower Germiston Road • Rosherville
P O Box 145296 • Bracken Gardens • 1452
Tel: 011 626 3808 • Cell: 083 254 3635 • Fax: 086 610 4196
Web: www.unimet.co.za

sanas Calibration Laboratory 306 205

CERTIFICATE OF CALIBRATION

Page 2 of 2 pages.

Certificate Number	:	1506P5810-6
Calibration of a	:	Pressure Transmitter
Manufacturer & Type	:	Siemens Sitrans P
Serial Number	:	N1-X914-9101861
Calibrated for	:	The University of the Witwatersrand, Johannesburg.
Procedure Number	:	53-124
Date of Calibration	:	02/06/2015
Date of Issue	:	02/06/2015
Laboratory Environment	:	22.4 °C
Reference Standards	:	205-S-01 Ruska 6200 PPG S/N 39478
	:	
	:	

Reference Pressure (kPa)	Indication (V) Rising	Falling
-0.5	0.4992	0.4995
0	0.5923	0.5917
2	0.9697	0.9707
4	1.3459	1.3473
6	1.7213	1.7267
8	2.1041	2.1048
10	2.3553	2.3553

Curve: P (Pa) = (5.5034V - 3.3269)*1000

The uncertainty of measurement is ± 0.025 kPa
The reported uncertainty is based on a standard uncertainty multiplied by a coverage factor of k=2, which unless specifically stated otherwise, provides a confidence level of 95%, in accordance with the Guide to the Expression of Uncertainty in Measurement, first edition, 1993.

Comments : The above readings were obtained using the customers data logging system. The transmitter was connected to channel 5.

Calibrated by : A Mathieson & R de Jager

M.Math

Technical Signatory

Figure B14 Pressure transducer 6 calibration certificate, Page 6 of 6

Appendix C

C1 PRIMARY AIR FLOW TRAVERSE

Test conditions

Date: 20/07/2015
Unit: 4
Unit load: 200 MW
Mills in service: B, C, D, E, F (A on standby)
Start time: 10:00 am
End time 1:30 pm
Barometric pressure: 85200 Pa

Left Hand Duct

Table C1 Measured and calculated data for measurement point 1

Duct Depth (mm)	P_{static} (Pa)	Δp (Pa)	$T_{measured}$ (°C)	ρ (kg/m^3)	v_{air} (m/s)	A_i (m^2)	$\dot{m}_i$ (kg/s)	$\sum_{i=95mm}^{855} \dot{m}_i$ (kg/s)
95	2532	19.68	24.70	1.02	6.19	0.039	0.253	1.280
285	2755	20.67	25.50	1.02	6.34	0.039	0.259	
475	2986	19.61	24.60	1.03	6.16	0.039	0.254	
665	1983	20.58	25.20	1.01	6.35	0.039	0.258	
855	2485	19.88	24.90	1.02	6.22	0.039	0.255	

Table C2 Measured and calculated data for measurement point 2

Duct Depth (mm)	P_{static} (Pa)	Δp (Pa)	$T_{measured}$ (°C)	ρ (kg/m^3)	v_{air} (m/s)	A_i (m^2)	$\dot{m}_i$ (kg/s)	$\sum_{i=95mm}^{855} \dot{m}_i$ (kg/s)
95	2758	17.68	25.66	1.03	5.87	0.038	0.229	1.193
285	2395	20.69	25.32	1.02	6.36	0.038	0.247	
475	2664	19.62	24.96	1.02	6.18	0.038	0.241	
665	2195	18.66	25.21	1.02	6.04	0.038	0.235	
855	2386	19.75	24.78	1.02	6.20	0.038	0.242	

Table C3 Measured and calculated data for measurement point 3

Duct Depth (mm)	P_{static} (Pa)	Δp (Pa)	$T_{measured}$ (℃)	ρ (kg/m^3)	v_{air} (m/s)	A_i (m^2)	$\dot{m}_i$ (kg/s)	$\sum_{i=95mm}^{855} \dot{m}_i$ (kg/s)
95	2268	14.86	24.9	1.02	5.39	0.038	0.210	1.195
285	1896	20.68	25.5	1.02	6.38	0.038	0.246	
475	2569	18.71	25.7	1.02	6.05	0.038	0.235	
665	2735	22.85	24.9	1.03	6.67	0.038	0.261	
855	2618	19.97	25.9	1.02	6.25	0.038	0.243	

Table C4 Measured and calculated data for measurement point 4

Duct Depth (mm)	P_{static} (Pa)	Δp (Pa)	$T_{measured}$ (℃)	ρ (kg/m^3)	v_{air} (m/s)	A_i (m^2)	$\dot{m}_i$ (kg/s)	$\sum_{i=95mm}^{855} \dot{m}_i$ (kg/s)
95	2301	15.88	25.6	1.02	5.58	0.040	0.227	1.268
285	2465	21.05	24.9	1.03	6.41	0.040	0.262	
475	2216	20.54	25.0	1.02	6.34	0.040	0.259	
665	2569	18.2	24.7	1.03	5.95	0.040	0.244	
855	2158	23.52	25.8	1.02	6.80	0.040	0.276	

Right Hand Duct

Table C5 Measured and calculated data for measurement point 1

Duct Depth (mm)	**P_{static} $(\boldsymbol{Pa})$**	**Δp $(\boldsymbol{Pa})$**	**$T_{measured}$ (℃)**	**ρ $(\mathbf{kg}/\boldsymbol{m}^3)$**	**$\boldsymbol{v_{air}}$ $(\mathbf{m/s})$**	**$\boldsymbol{A_i}$ $(\boldsymbol{m}^2)$**	**$\dot{\boldsymbol{m}}_i$ $(\mathbf{kg/s})$**	**$\sum_{i=95mm}^{855} \dot{m}_i$ $(\mathbf{kg/s})$**
95	2680	17.85	24.1	1.03	5.89	0.040	0.242	1.229
285	2510	18.63	25.7	1.02	6.03	0.040	0.246	
475	2239	17.45	25.0	1.02	5.84	0.040	0.238	
665	2050	19.66	25.1	1.02	6.21	0.040	0.253	
855	2389	19.18	25.0	1.02	6.12	0.040	0.250	

Table C6 Measured and calculated data for measurement point 2

Duct Depth (mm)	**P_{static} $(\boldsymbol{Pa})$**	**Δp $(\boldsymbol{Pa})$**	**$T_{measured}$ (℃)**	**ρ $(\mathbf{kg}/\boldsymbol{m}^3)$**	**$\boldsymbol{v_{air}}$ $(\mathbf{m/s})$**	**$\boldsymbol{A_i}$ $(\boldsymbol{m}^2)$**	**$\dot{\boldsymbol{m}}_i$ $(\mathbf{kg/s})$**	**$\sum_{i=95mm}^{855} \dot{m}_i$ $(\mathbf{kg/s})$**
95	2250	19.65	25.69	1.02	6.21	0.038	0.241	1.213
285	2569	19.68	25.78	1.02	6.20	0.038	0.241	
475	2489	20.85	24.86	1.03	6.38	0.038	0.249	
665	2258	19.92	24.34	1.02	6.24	0.038	0.243	
855	2596	19.48	25.45	1.02	6.17	0.038	0.240	

Table C7 Measured and calculated data for measurement point 3

Duct Depth (mm)	P_{static} (Pa)	Δp (Pa)	$T_{measured}$ (°C)	ρ (kg/m^3)	v_{air} (m/s)	A_i (m^2)	$\dot{m}_i$ (kg/s)	$\sum_{i=95mm}^{855} \dot{m}_i$ (kg/s)
95	2794	18.56	25.05	1.029	6.01	0.038	0.235	1.186
285	2658	19.52	25.54	1.025	6.17	0.038	0.240	
475	2421	18.69	24.08	1.028	6.03	0.038	0.236	
665	2387	19.66	25.66	1.022	6.20	0.038	0.241	
855	2396	18.58	24.84	1.025	6.02	0.038	0.234	

Table C8 Measured and calculated data for measurement point 4

Duct Depth (mm)	P_{static} (Pa)	Δp (Pa)	$T_{measured}$ (°C)	ρ (kg/m^3)	v_{air} (m/s)	A_i (m^2)	$\dot{m}_i$ (kg/s)	$\sum_{i=95mm}^{855} \dot{m}_i$ (kg/s)
95	2558	19.65	25.6	1.024	6.20	0.040	0.253	1.235
285	2397	17.96	25.1	1.024	5.92	0.040	0.242	
475	2663	20.58	25.06	1.027	6.33	0.040	0.259	
665	2786	14.87	24.23	1.031	5.37	0.040	0.221	
855	2550	20.69	25.21	1.025	6.35	0.040	0.260	

C2 GLOBAL PULVERISER PERFORMANCE TESTS

Day Two

Test conditions

Date:	22/07/2015
Unit:	4
Unit load:	200 MW
Mills in service:	A, B, C, D, E
Start time:	12:00 pm
End time	4:30 pm

Table C9 Proximate analysis results, air dried

		Day Two
Measured Parameter	**Units**	**Value**
Calorific Value	MJ/kg	20.21
Total moisture	%	8.36
Volatiles	%	20.89
Ash	%	31.27
HGI	-	58
AI	-	160

Table C10 Measured data and calculated results for PF mass flow rate

PF Pipe	M_{pf} (kg)	N	t (s)	D_{pipe} (mm)	d_{probe} (mm)	$\dot{m}_{pf,\ calculated}$ (kg/s)	$\sum_{i=1}^{4} \dot{m}_{pf,calculated}$ (kg/s)
1	0.648	32	15	387	12.5	1.29	6.84
2	1.041	32	15	387	12.5	2.08	
3	0.972	32	15	387	12.5	1.94	
4	0.768	32	15	387	12.5	1.53	

Table C11 Measured and calculated PF moisture content results

PF Pipe	Mass of sample before drying (g)	Mass of sample after drying (g)	w_1 (g/g)
1	60	58.20	0.030
2	60	59.21	0.013
3	60	58.70	0.022
4	60	58.51	0.025
		Average	0.023

Table C12 Measured data and calculated results for the DBM test, mill 4A

Test number	L (m)	B (m)	H (m)	V_{duct} (m^3)	$t_{measured}$ (s)	ρ_{bulk} (kg/m^3)	$\dot{m}_{coal,\ calculated}$ $(\mathrm{kg/s})$
Test 1	0.63	0.63	3	1.17	155	892.91	6.74
Test 2					161		6.47
Test 3					169		6.18
						Average	6.46

Day Three

Test conditions

Date:	23/07/2015
Unit:	4
Unit load:	200 MW
Mills in service:	A, B, C, D, E
Start time:	1:30 pm
End time	4:30 pm

Table C13 Proximate analysis results, air dried

Measured Parameter	Units	Value
Calorific Value	MJ/kg	20.85
Total moisture	%	8.17
Volatiles	%	23.84
Ash	%	29.08
HGI	-	57
AI	-	161

Table C14 Measured data and calculated results for PF mass flow rate

PF Pipe	M_{PF} (kg)	N	t (s)	D_{pipe} (mm)	d_{probe} (mm)	$\dot{m}_{PF,\ calculated}$ (kg/s)	$\sum_{i=1}^{4} \dot{m}_{PF,calculated}$ (kg/s)
1	0.976	32	15	387	12.5	1.95	6.63
2	0.588	32	15	387	12.5	1.17	
3	0.715	32	15	387	12.5	1.43	
4	1.041	32	15	387	12.5	2.08	

Table C15 Measured and calculated PF moisture content results

PF Pipe	Mass of sample before drying (g)	Mass of sample after drying (g)	w_1 (g/g)
1	60	58.40	0.027
2	60	59.62	0.006
3	60	59.50	0.008
4	60	58.81	0.020
		Average	0.015

Table C16 Measured data and calculated results for the DBM test, mill 4A

Test number	L (m)	B (m)	H (m)	V_{duct} (m^3)	$t_{measured}$ (s)	ρ_{bulk} (kg/m^3)	$\dot{m}_{coal,\ calculated}$ $(\mathrm{kg/s})$
Test 1	0.63	0.63	3	1.17	171	895.92	6.13
Test 2					157		6.68
Test 3					177		5.92
						Average	6.24

C4 STATIC PRESSURE TESTS

Test conditions

Date: 20/07/2015
Unit: 4
Unit load: 200 MW
Mills in service: B, C, D, E, F (A on standby)
Start time: 10:00 am
End time 1:30 pm

Table C17 Measured data and calculated results for primary air mass flow rate 2, 7 kg/s

Measurement point	**Pressure transducer**	$V_{measured,\ avg}$ (V)	$P_{static,\ calculated}$ (Pa)
A	6	0.797	1062.82
B	5	0.710	517.77
C	2	0.699	515.23
D	4	0.700	519.36
E	3	0.674	376.75
F	4	0.678	395.58
G	1	0.805	1101.60
H	2	0.680	438

Table C18 Measured data and calculated results for primary air mass flow rate 3, 8 kg/s

Measurement point	**Pressure transducer**	$V_{measured,\ avg}$ (V)	$P_{static,\ calculated}$ (Pa)
A	6	0.878	1507.81
B	5	0.752	787.62
C	2	0.751	805
D	4	0.751	799.31
E	3	0.708	562.75
F	4	0.720	628.41
G	1	0.890	1569.33
H	2	0.728	678.01

Appendix D

Coal bulk density determination

The bulk density of raw coal is defined as the mass of a collection of coal particles in a container divided by the volume of the container. BS 1016:1991 was employed as a guide to determine the bulk density of raw coal. Table D1 highlights the requirements of BS 1016:1991. Equation D1 presents the basic relationship employed for the bulk density calculation.

$$\rho_{bulk} = \frac{Mass\ of\ coal}{Volume\ of\ container} \qquad \text{(D1)}$$

Table D1 BS 1016:1991 specifications for bulk density determination

Volume of container required (m^3)	**Maximum particle size (mm)**	**Method of levelling**
0.057	120	Eye

As a container with the exact volume specified in Table D1 was unavailable, it was difficult to comply with the specifications in full and a cylinder with a volume of 0.0503 m^3 was utilised. The measured and calculated results obtained for the bulk density tests are displayed in Table D2.

Table D2 Measured and calculated data for the raw coal bulk density test

Power Station	**Volume of container (m^3)**	**Mass of empty container (kg)**	**Mass of container filled with coal (kg)**	**Mass of coal (kg)**	**ρ_{bulk} (kg/m^3)**
A, day 1	0.0503	0.73	48.33	47.59	946.28
A, day 2	0.0503	0.73	45.64	44.91	892.91
A, day 3	0.0503	0.73	45.76	45.06	895.92
B	0.0503	0.73	47.20	46.47	923.91

Appendix E

Raw coal flow validation using DBM

A preliminary investigation was conducted at Power Station B to evaluate the validity of the DBM. Figure E1 presents the duct configuration upstream of the raw coal gravimetric feeder, highlighting the location of the port hole at Power Station B. With reference to Figure E1, ideally the location of the port is required in the constant area zone marked ‘Feeder inlet standpipe’. Notably, the location of the port hole was in an area not conducive for the DBM. Therefore, a minor modification to the general technique was applied in this instance to accommodate the unique duct configuration. The height from the port hole to the entrance of the feeder inlet standpipe was measured to be 1500 mm.

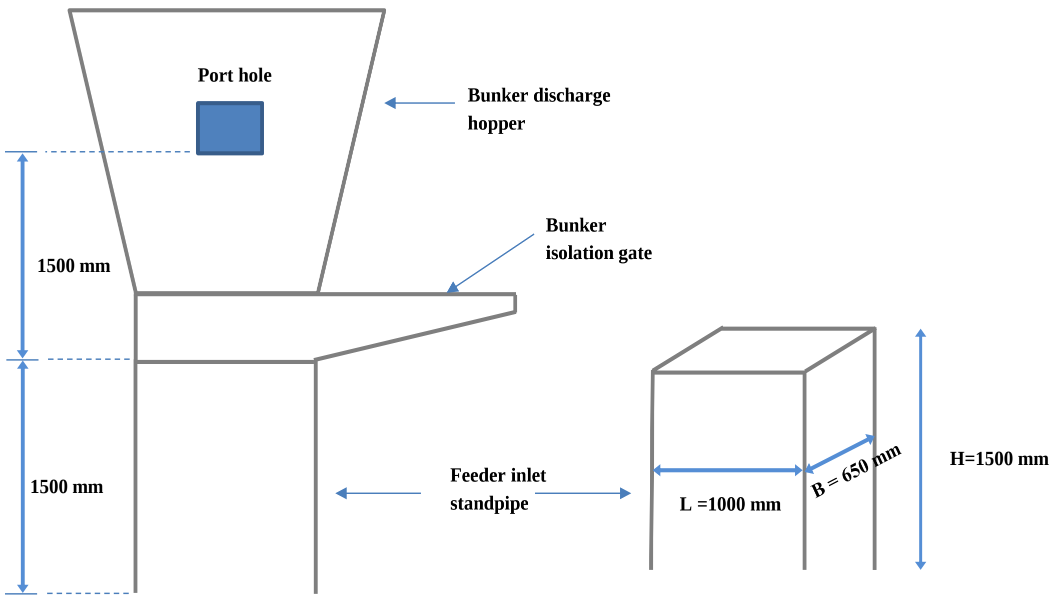

Figure E1 Front view highlighting raw coal chute configuration at Power Station B (Drawing is not to scale)

Consider the DBM technique, as illustrated in Figure E2. A wooden ball, approximately 40 mm in diameter (to resemble a piece of raw coal) is attached to a piece of string threaded through a pipe. The pipe and wooden ball are then inserted through the port hole to the midpoint of the duct. Given that the coal flow is influenced by gravity, the wooden ball was allowed to travel freely down the raw coal pipe. The time taken for the wooden ball to travel a known distance was then recorded. Since the height measured from the port hole to the feeder inlet standpipe was measured to be 1500 mm, the length of string used in this instance was increased by 1500 mm. The required lengths on the string were marked as X, A and B, as illustrated in Figure E2. Once point A travelled to point X, it was assumed that the wooden ball was now at the entrance to the constant area zone (feeder inlet standpipe) and the stop watch starts recording the time. The time was recorded until point B reached point X. This essentially indicates the time the wooden ball travelled a height of 1500 mm in the feeder inlet stand pipe. It must be noted that the duct configuration alters further downstream and, therefore, it was not possible to use a height of 3000 mm, as completed at Power Station A. Additionally, a sample of coal was taken and analysed for its bulk density at the local laboratory using the method explicated in Appendix D.

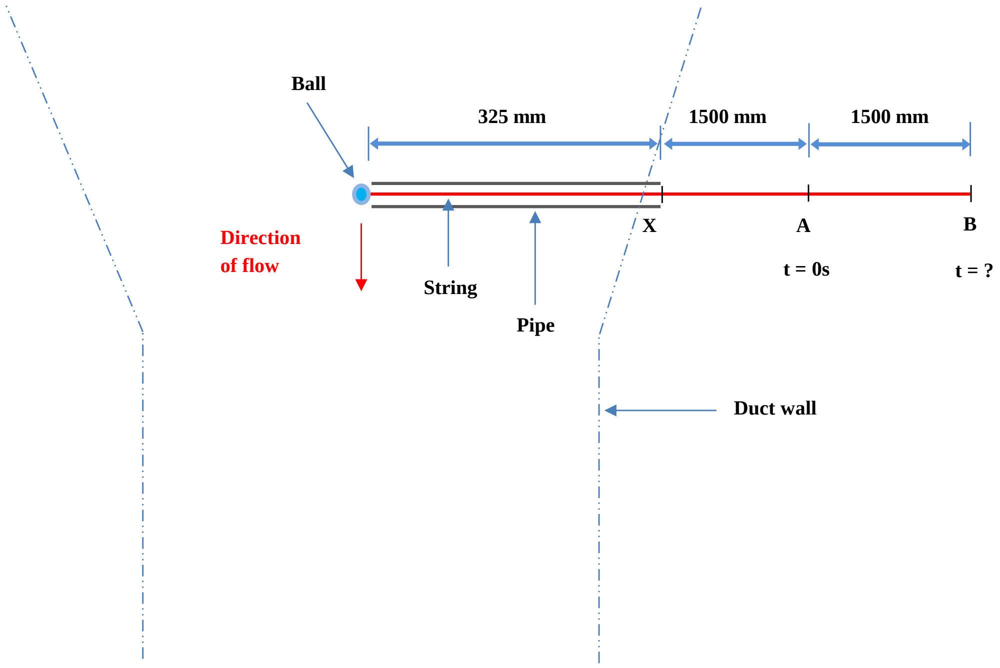

Figure E2 Side view of raw coal chute highlighting the DBM (Drawing is not to scale)

The calculations related to the DBM, as described in Chapter 3, section 3.3.2.3, was analogously applied at Power Station B and is therefore not represented. The test was conducted in quadruplicate to determine the reproducibility of the results. Table E1 presents the measured data and the calculated results for DBM. The length, width and height of the feeder inlet standpipe (as highlighted in Figure E1) used to calculate the internal duct volume are presented as L, B and H respectively in Table E1.

Table E1 Measured data and calculated results for the DBM, mill 1F, Power Station B

Test number	L (m)	B (m)	H (m)	V_{duct} (m^3)	$t_{measured}$ (s)	ρ_{bulk} (kg/m^3)	$\dot{m}_{coal,\ calculated}$ (kg/s)
1	1	0.65	1.5	0.975	81	923.91	11.12
2					78		11.55
3					80		11.26
4					77		11.70

The ability of the DBM to accurately measure the coal mass flow rate can be assessed by the intensity of the correlation between the experimentally determined and DCS recorded coal mass flow rates. A noteworthy correlation is evident between the DBM and DCS measured coal mass flow rates, as outlined in Table E2. The correlation established between the two measured outcomes highlight that the DBM consistently under-predicts the coal mass flow rate by an average of 8.74 %. The uncertainties associated with the DBM can be largely attributed to the following:

- The assumption that the drop ball falls vertically and is not swayed to the left or the right while in motion in the duct.
- The assumption that the coal flow velocity throughout the cross section of the duct is uniform.
- The assumption that the coal flow rate is independent of the coal particle size.
- Uncertainty in the raw coal bulk density measurement.

Table E2 Comparison between the measured coal flow and DCS recorded values

Test number	$\dot{m}_{coal,\ calculated}$ (kg/s)	$\dot{m}_{coal,\ DCS}$ (kg/s)	Variance (%)
1	11.12	12.5	11.03
2	11.55		7.61
3	11.26		9.92
4	11.70		6.41
Average	11.41		8.74

Appendix F

F1 20th Southern African Conference on Research in Coal Science and Technology, Fossil Fuel Foundation

GOVENDER, ANDRÉ
Schmitz Walter, Naidoo Reshendren
School of Mechanical, Industrial and Aeronautical Engineering

The development of a condition monitoring philosophy for a pulverised fuel vertical spindle pulveriser

The quantity and quality (fineness) of pulverised fuel supplied to combustion equipment downstream of coal pulverising plants are critical to achieve safe, reliable and efficient combustion. These two key performance indicators are largely dependent on the mechanical condition of the pulveriser. A Computational Fluid Dynamic (CFD) model based on actual geometry of a coal pulveriser used in the power generation industry was developed to predict the static pressure drop across major internal components of the pulveriser as a function of the air flow through the pulveriser. Air flow rates under normal pulveriser operating conditions were applied to the numerical model created in StarCCM+. A steady three-dimensional flow model was solved using the Eulerian approach for air only. Turbulence was modelled using the realizable κ-ε turbulence model. The results of the simulation produced contour plots of static pressure and velocity distributions across the computational domain. CFD model results were validated against experimental data from an industrial pulveriser. Static pressure drop predictions of the CFD model came within 7% error of calibrated plant measurements. Three geometrical modifications were investigated with the intention of relating the wear of the pulveriser to the static pressure drop predicted by the CFD model. It was found that as the pulveriser condition deteriorates the static pressure drop across the pulveriser decreases. An un-coupled Lagrangian approach will be utilised to simulate coal particle trajectories following a Rosin-Rammler size distribution for each of the three geometrically modified scenarios to investigate the pulveriser throughput based on coal particle size. A Lagrangian approach with Two-Way coupling and the ideal gas model was modelled for the above described pulveriser computational domain. This model was generated to predict the static pressure drop across the pulveriser domain as a function of the mass flowrate of air and coal input. The results of the simulation showed a substantially lower pressure drop prediction as compared to experimental results of a commercial-scale pulveriser. Predicted results were 56 % lower than the experimental results. The discrepancies between the CFD predicted and experimental pressure drop can be attributed to many physical parameters that were excluded in the CFD model. These include the moisture content of raw coal, a wider range of particle sizes and largely due to the number of particles simulated. A steady-state mass and energy balance was developed from first principles for a commercial-scale coal pulveriser. The model energy streams account for energy input from the primary air, seal air, pulveriser motor power and raw coal. Moisture evaporation from coal is included in the model derivation and moisture content of pulverised fuel is considered. The model accounts for heat loss due to convection to the environment. Heat loss due to conduction and radiation was considered to be negligible. The model predicts the coal flow to within 3 % of acceptance test data. Model sensitivity analysis revealed that the predicted coal flow results are largely influenced by the pulveriser primary air input temperature, output temperature, primary air flow rate and raw coal moisture content. Experimental work to validate the mass and energy balance model is underway.

GOVENDER, ANDRÉ
Schmitz Walter, Naidoo Reshendren
School of Mechanical, Industrial and Aeronautical Engineering

Numerical studies on a Vertical Spindle Mill employed in the power generation industry

The quantity and quality (fineness) of pulverised fuel supplied to combustion equipment downstream of coal pulverising plants are critical to achieve safe, reliable and efficient combustion. These two key performance indicators are largely dependent on the mechanical condition of the pulveriser. A Computational Fluid Dynamic (CFD) model based on actual geometry of a coal pulveriser used in the power generation industry was developed to predict the static pressure drop across major internal components of the pulveriser. Air flow rates under normal pulveriser operating conditions were applied to the numerical model created in StarCCM+. A steady three-dimensional un-coupled flow model was solved using the Eulerian approach. Turbulence was modelled using the standard κ-ε turbulence model. The results of the simulation produced contours of static pressure and velocity distributions across the computational domain. The results of the CFD model were validated against experimental data from an industrial pulveriser. Static pressure drop predictions of the CFD model came within 7% error of calibrated plant measurements. Three geometrical modifications were investigated with the intention of relating the wear of the pulveriser to the static pressure drop predicted by the CFD model. It was found that as the pulveriser condition deteriorates the static pressure drop across the pulveriser decreases. A Lagrangian approach was utilised to simulate coal particle trajectories following a Rosin-Rammler size distribution for each of the three geometrically modified scenarios. The results of the simulations showed that different particle sizes follow different trajectories and are influenced by the pulveriser internal condition.